NANOCOMPOSITE ELECTRODES FOR STRUCTURAL ENERGY STORAGE

A Dissertation

by

PARASKEVI FLOUDA

Submitted to the Office of Graduate and Professional Studies of
Texas A&M University
in partial fulfillment of the requirements for the degree of

DOCTOR OF PHILOSOPHY

Chair of Committee,	Jodie L. Lutkenhaus
Co-Chair of Committee,	Dimitris C. Lagoudas
Committee Members,	Micah J. Green
	James G. Boyd
	Terry S. Creasy
Head of Department,	Ibrahim Karaman

May 2021

Major Subject: Materials Science and Engineering

ABSTRACT

Structural energy storage devices combine the energy storage properties of batteries and supercapacitors with the mechanical properties of structural composites. Such multifunctional devices may allow for energy to be stored within the body panels of electric vehicles, leading to mass and volume savings. However, energy storage and mechanical properties come at a trade-off, making it challenging to develop electrodes that can both store energy and bear mechanical loads. To balance this trade-off, here, we demonstrate how selected materials, such as reduced graphene oxide (rGO) and Kevlar® aramid nanofibers (ANFs), can be processed into structural electrodes with enhanced mechanical properties (*i.e.* ultimate tensile strength and Young's modulus) by engineering interfacial interactions.

Structural supercapacitor electrodes composed of rGO and ANFs were fabricated through vacuum-assisted filtration. rGO and ANFs interact with each other mainly through hydrogen bonding interactions. GO was chemically modified to enhance these interfacial interactions, and the effect of the GO modifications on mechanical and energy storage performance was investigated. Significant improvements on the mechanical performance (up to five-fold increase in Young's modulus and four-fold increase in tensile strength compared to pure rGO (no ANFs)) were observed due to the enhanced interfacial interactions. Small deteriorations in energy storage were observed due to the introduction of defects and ion-diffusion limitations induced by the more compact structures. This work demonstrates that synergistic interfacial interactions can lead to significant improvements

in mechanical properties of structural supercapacitor electrodes while maintaining good energy storage.

Motivated by our prior work on rGO/ANF structural supercapacitor electrodes, we extended this concept to structural lithium-ion battery electrodes using branched ANFs (BANFs) and battery active materials. We combined BANFs with lithium iron phosphate (LFP, cathode) or silicon (Si, anode) particles, and rGO. Overall, we obtained up to two orders of magnitude improvements in Young's modulus and tensile strength compared to commercial battery electrodes while maintaining comparable energy storage properties. As an alternative to the LFP-containing cathodes, structural cathodes based on polyaniline, BANFs, and carbon nanotubes were also fabricated. This work demonstrates an efficient route for developing structural lithium-ion battery cathodes and anodes with enhanced mechanical properties using Kevlar® aramid nanofibers.

DEDICATION

To my uncle.

ACKNOWLEDGEMENTS

First and foremost, I would like to thank my advisors, Dr. Jodie L. Lutkenhaus and Dr. Dimitris C. Lagoudas, for their endless guidance, support, and patience during my graduate studies. I will be forever grateful for the opportunity they gave me to be a part of their lab families. Their mentoring, encouragement, and experience were instrumental to my growth, both academically and personally.

I would like to thank my committee members, Dr. Micah J. Green, Dr. James G. Boyd, and Dr. Terry S. Creasy, for their guidance and advice. Their feedback was always valuable and concise for completing this dissertation.

Special thanks to Se Ra Kwon, Anish Patel, Dimitrios Loufakis, Smit Shah, Tianyang Zhou, Sarah Aderayani, and Wanmei Sun for all their help with the project. Additionally, I would like to thank Alex Quinn and Suyash Oka for being excellent mentees, always supportive and enthusiastic. I would also like to thank all my colleagues and friends at Texas A&M for making this experience fun and sometimes even embarrassing.

Finally, I would like to thank my family. Specifically, my parents and my big brother, for their continuous love, support, and encouragement. Special thanks to my family in Texas for all their support during my graduate studies.

CONTRIBUTORS AND FUNDING SOURCES

Contributors

This work was supervised by a dissertation committee consisting of Dr. Jodie Lutkenhaus (chair) of the Chemical Engineering Department, Dr. Dimitris C. Lagoudas (co-chair) of the Aerospace Engineering Department, Dr. Micah J. Green of the Chemical Engineering Department, Dr. James G. Boyd of the Aerospace Engineering Department, and Dr. Terry S. Creasy of the Materials Science and Engineering Department.

High-resolution scanning electron microscopy images for Chapter 2 were provided by Dr. Xueyan Feng and Prof. Edwin L. Thomas of the Department of Materials Science and NanoEngineering, Rice University. Thermal gravimetric analysis for Chapters 3 and 4, X-ray diffraction and Raman spectroscopy for Chapter 5, and preliminary work for Chapter 6 were conducted by Smit S. Shah and Prof. Micah J. Green, Suyash Oka, and Alex Quinn of the Chemical Engineering Department, respectively. Chapter's 4 solid-state supercapacitor was fabricated in collaboration with Dr. Junyeong Yun of the Chemical Engineering Department. All four-point probe measurements were conducted by Dimitrios Loufakis of the Materials Science and Engineering Department. All other work conducted for the dissertation was completed by the student independently.

Funding Sources

This work was supported by the Air Force Office of Scientific Research (grant numbers: FA9550-16-1-0230 and FA9550-19-1-0170). Its contents are solely the

responsibility of the authors and do not necessarily represent the official views of the Air Force Office of Scientific Research.

TABLE OF CONTENTS

Page

LIST OF FIGURES

Page

LIST OF TABLES

Page

1. INTRODUCTION

1.1. Introductory Remarks and Background

Structural energy storage aims at the development of supercapacitors and batteries that simultaneously store energy and bear mechanical loads.[1, 2] Structural supercapacitors and batteries can lead to significant mass and volume savings in ground and areal transportation as energy may be stored within structural body panels, Figure 1.1.[3, 4] However, the major challenge is that traditional electrodes are optimized for energy storage (*e.g.* capacitance or capacity, specific energy, and specific power) and not for mechanical performance (*e.g.* Young's modulus and tensile strength) leading to unacceptably low mechanical properties (Young's modulus < 5 GPa and tensile strength < 35 MPa) for structural applications.[1, 2] Multifunctional electrodes with both good energy storage and mechanical performance are necessary to utilize such technologies in real-life applications.

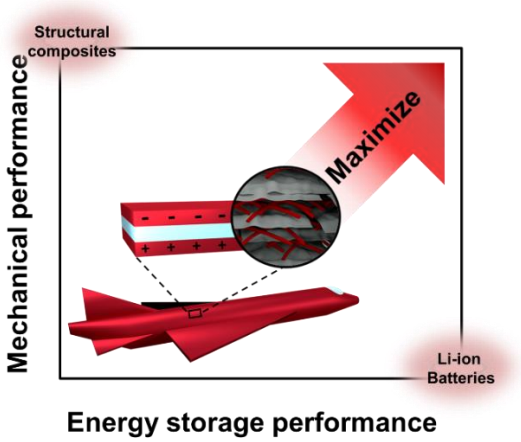

Figure 1.1 Schematic representation of structural energy storage. Adapted with permission.[5] Copyright 2019, Wiley-VCH GmbH.

The simplest approach to develop structural electrodes is by the utilization of mechanically strong materials that can also store energy. However, there is only a limited choice of such materials (*i.e.* carbon fibers).[6, 7] Carbon fibers (CF) have gained much interest due to their high mechanical performance (strength of 3 – 6 GPa and modulus of 200 – 300 GPa) and ability to store energy.[6] Despite the exceptional mechanical properties of the CF-based electrodes, energy storage is extremely poor (*e.g.* specific capacitance < 10 F/g).[6, 8, 9] As an alternative, nanocomposites of electrochemically active and structural materials have been developed.[3, 10-12] The major challenge, here, is to balance the two functionalities as they come at a trade-off.[3, 10-12] This trade-off may be tuned by varying the interfacial interactions between the nanocomposite's components, however, the role of interfacial interactions in structural energy storage is not yet well understood.

This dissertation focuses on the development of nanocomposite structural supercapacitor and lithium-ion battery electrodes reinforced with Kevlar® aramid nanofibers with emphasis on the effect of different interfacial interactions (hydrogen bonding and coordination bonding) on the multifunctional performance.

1.2. Electrochemical Energy Storage

Conventional electrochemical energy storage devices can be classified into supercapacitors (Figure 1.2a) and batteries (Figure 1.2b).[13, 14] Supercapacitors and batteries are both composed of two electrodes, an electrolyte (ions and solvent), and a separator (permeable membrane).[13] Despite their similarities, supercapacitors and batteries exhibit different energy storage mechanisms resulting in significant differences

in their performance (*e.g.* specific energy and specific power). Supercapacitors store energy through the formation of an electric double layer (EDL) due to reversible ion adsorption onto the surface of each electrode or through a combination of EDL with redox reactions limited at the surface of each electrode (pseudo-capacitance).[15] In contrast, batteries consist of an anode and cathode and store energy chemically, through redox reactions occurring within the electrodes.[13, 15, 16]

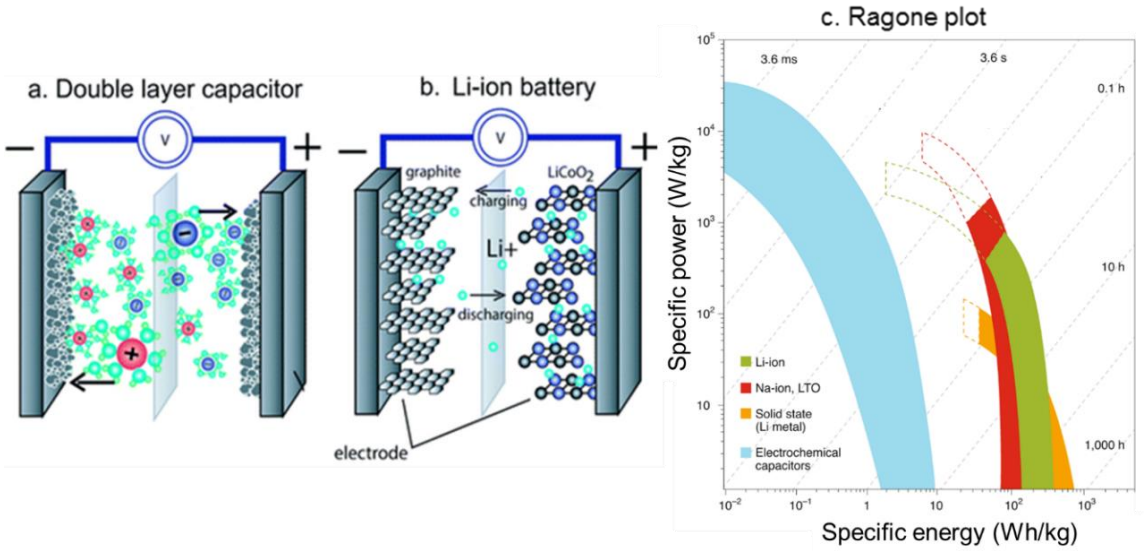

Figure 1.2 Schematic representation of a typical a) supercapacitor and b) lithium-ion battery. c) Ragone plot for specific power (W/kg) *vs.* specific energy (Wh/kg). Reprinted and modified with permission.[14, 15] Copyright 2014, Royal Society of Chemistry and Copyright 2020, Springer Nature Limited.

To evaluate the energy storage performance of supercapacitors and batteries, electrochemical tests such as galvanostatic cycling, cyclic voltammetry, and electrochemical impedance spectroscopy are conducted.[15] Important performance metrics

include the capacitance (amount of charge stored per given potential window) or capacity (amount of charge stored), energy (amount of energy stored), power (how fast energy can be delivered), as well as cycling life.[15] For a supercapacitor, capacitance (C), energy (E), and power (P) are derived from the generalized expressions:

$$C = \frac{I \cdot t}{\Delta V} \tag{1.1}$$

$$E = \frac{1}{2} \cdot C \cdot \Delta V^2 \tag{1.2}$$

$$P = E/\Delta t \tag{1.3}$$

where *I*, *t*, and ΔV are the discharge current, discharge time, and potential window, respectively.[15] Out of those, capacitance represents the most widely used metric to evaluate the performance of a supercapacitor and is usually normalized by the electrodes' mass (F/g) or area (F/cm^2).[6] Capacitance is typically depicted as a function of scan rate (cyclic voltammetry) or as a function of specific current and cycling number (galvanostatic charge-discharge). For batteries, similar expressions are used, however, capacity (mAh/g) is the preferred metric.[15, 17]

The performance of supercapacitors and batteries in terms of specific energy and power is shown in Figure 1.2c. Supercapacitors demonstrate high specific power with intermediate specific energy values due to the fast EDL formation, limited/absent redox reactions, and surface limited charge storage.[13, 16] Batteries exhibit superior specific energy values with low specific power values due to redox reactions occurring throughout the entire electrodes, which are also ion-diffusion limited.[13, 16] As a result, supercapacitors are more suitable for high power applications (*e.g.* regenerative braking and pulsed

power), while batteries are preferred for high energy applications (*e.g.* consumer electronics and transportation).

At this point, it is worth mentioning that the performance (*e.g.* specific capacitance/capacity, specific energy, specific power) of an electrochemical energy storage device depends on the electrolyte used and the testing conditions (*e.g.* current density and scan rate). The electrolyte characteristics must encompass a high voltage window, electrochemical stability, high concentration of ions, and low resistivity.[15, 17] Electrolytes can be classified into three main categories: aqueous, organic, and ionic liquids (IL). Aqueous electrolytes exhibit a low voltage window of about 1.2 V, organic electrolytes can reach up to ~3.5 V, whereas ionic liquids operate at 2-6 V.[15, 17] Additionally, the electrolyte ion size is important. For example, in supercapacitors, electrolytes with larger ions can lead to lower specific capacitance values as ions may not be able to access all available electrode surface area.[15, 17] As a result, the selection of the electrolyte may affect the specific capacitance, specific energy, and specific power values.

Another important performance characteristic for supercapacitors and batteries is their cycling life. Supercapacitors have a lifetime of 100,000 – 1,000,000 cycles, whereas batteries are limited to 1,000 – 10,000 cycles.[7] Cycling stability is evaluated mainly from galvanostatic cycling tests and is represented in plots of specific capacitance or capacity *vs.* number of cycles.[7]

1.2.1. Supercapacitors

Supercapacitors were commercialized in the 1980s and since then have garnered significant attention due to their fast charging, increased cycle life, and enhanced safety.[13, 18-20] Supercapacitors require electrode materials that are conductive and have large electrolyte-accessible (electrochemically active) surface area.[21, 22] Electrode materials that have been extensively explored for supercapacitors include carbon nanotubes (CNTs), reduced graphene (rGO), and activated carbons.[23, 24] Porous CNT-based composites possessed specific capacitance values of 40 – 100 F/g.[25] rGO-based supercapacitors, reported first by Ruoff *et al.* in 2008, exhibited specific capacitance values of 135 F/g and 99 F/g in aqueous and organic electrolytes, respectively.[21] Finally, activated carbons have been explored due to their high surface area (> 2000 m^2/g) leading to high specific capacitance values (120 – 200 F/g).[26, 27]

Apart from the traditional carbon-based electrode materials, pseudocapacitive materials such as metal oxides (*e.g.* MnO_2, RuO_2, and Fe_2O_3) and conjugated polymers (*e.g.* polyaniline and polypyrrole) have also been investigated.[14] Pseudocapacitive electrodes involve both reversible ion adsorption/desorption and Faradaic redox reactions at the electrodes' surface, leading to higher capacitance values and lower cycling life.[14] Polyaniline (PANI) is among the most widely used pseudocapacitive materials due to its good electrical conductivity, ease of synthesis, and unique redox chemistry.[28] PANI-based electrodes have demonstrated superior capacitance values, for example, PANI/CNT composite electrodes demonstrated specific capacitance values up to 424 F/g.[29]

1.2.2. Batteries

Lithium-ion batteries were commercialized in 1991 and became the most widely used power source for portable electronics and electric vehicles.[30] Graphite was one of the first anode materials investigated for lithium-ion batteries and remains the most widely used anode material due to its good theoretical capacity (372 mAh/g) and high electrochemical stability.[30] During discharge, oxidation takes place at the anode:

$$LiC_6 \rightarrow Li_{1-x}C_6 + xLi^+ + xe^- \quad (1.4)$$

Recently, research efforts have focused on the development of alloy-forming anodes (*e.g.* Si, Ge, Al, and Sn) due to their higher capacity values. Out of those, silicon has gathered lots of attention resulting from its high theoretical capacity values (3579 mAh/g, for $Li_{3.7}Si$). However, several issues arising from large volumetric expansions (> 300%) during charging/discharging hinder the widespread use of silicon.[30] Different binder materials have been developed to address this issue such as polyacrylic acid (PAA), alginate, and carboxymethyl cellulose (CMC).[31] For example, Si/polyacrylic acid (PAA)/carbon black (CB) electrodes showed a good cycling stability with capacity values above 2400 mAh/g after 100 galvanic cycles, owing to the hydrogen bonding interactions between the Si surface hydroxyl groups and PAA.[30]

Typical cathode-materials include layered lithium metal oxides such as lithium cobalt oxide ($LiCoO_2$ or LCO). LCO (theoretical capacity of 274 mAh/g) was the first metal oxide cathode investigated and consists the most widely used cathode material in

commercial lithium-ion batteries.[32] During discharge, reduction takes place at the LCO cathode:

$$xLi^{+} + xe^{-} + CoO_2 \rightarrow Li_xCoO_2 \quad (1.5)$$

LCO faces issues with fast capacity fade at high current rates, low thermal stability, and high cost.[32] Olivine lithium iron phosphate ($LiFePO_4$ or LFP) consists a promising alternative due to its high theoretical capacity (170 mAh/g), high electrochemical stability, and abundancy.[32] Additionally, conjugated polymers and radical polymers have been investigated as alternatives to the lithium metal oxides.[33, 34]

1.3. Structural Energy Storage

Several reports on structural energy storage devices focused on the development of mechanically strong electrodes, separators, and solid polymer electrolytes. As discussed in the following paragraphs, structural electrodes based on carbon fiber (CF) fabrics have been extensively studied for both supercapacitors and batteries.[1, 2, 8, 9, 35, 36] Significant efforts have also been made on structural separators and electrolytes.[36-41] Kotov *et al.* reported separators using poly(ethylene oxide) (PEO)/aramid nanofibers (ANF) membranes for lithium-ion batteries.[37] Ionic conductivities of 1.7×10^{-4} S/cm with a Young's modulus of 5 GPa and tensile strength of 170 MPa were achieved.[37] Similarly, Yuan *et al.* reported on boron nitride (BN)/polyvinylidene fluoride (PVdF) composite separators with ionic conductivities of 3.6×10^{-4} S/cm, a Young's modulus of 1.2 GPa, and a tensile strength of 13 MPa.[36]

More recently, the development of mechanically strong polymer-based solid electrolytes was reported. Yang *et al.* reported nacre-inspired ceramic/polymer solid composite electrolytes composed of a PEO matrix with $Li_{1.5}Al_{0.5}Ge_{1.5}(PO_4)_3$ (LAGP) embedded particles.[40] The composite electrolytes demonstrated ionic conductivities of 1.25×10^{-4} S/cm with enhanced mechanical properties compared to pure PEO-based electrolytes.[40] Additionally, significant efforts have focused on epoxy-based phase separated electrolytes.[42-44] These electrolytes combined high ionic conductivities (~10^{-3} – 10^{-4} S/cm) with comparable mechanical properties to epoxy.[42-44]

1.3.1. Structural Supercapacitor Electrodes

Early work on structural electrodes focused on CF-based electrodes due to their high mechanical performance and their ability to store charge.[1,] Typical CF-based energy storage systems consist of activated CF fabrics, glass fiber cloths as the separator, and polyethylene glycol diglycidylether (PEGDGE) with ionic liquids as the solid electrolyte (Figure 1.3a).[1, 42, 45, 46] Wetzel *et al.* designed structural supercapacitors based on CF fabrics that exhibited a compressive Young's modulus of ~3.6 GPa with a specific capacitance of 0.093 F/g.[47] Similarly, Asp, Greenhalgh, and co-workers obtained low capacitance values using the CF-based systems, as shown in Figure 1.3b.[1, 46, 48, 49] Despite the superior mechanical properties of the CF-based electrodes, the electrochemical performance is poor mainly due to the low electrochemically active surface area (0.2 – 25 m^2/g).[46] In order to improve the energy storage properties of the CF-based supercapacitors, recent studies focused on the introduction of 3D porous structures, as well as the addition

of pseudocapacitive materials such as MnO_2 and heteroatoms such as nitrogen.[50-54] However, such modifications typically lead to deteriorations in mechanical properties due to the disruption of the CFs.[50-54]

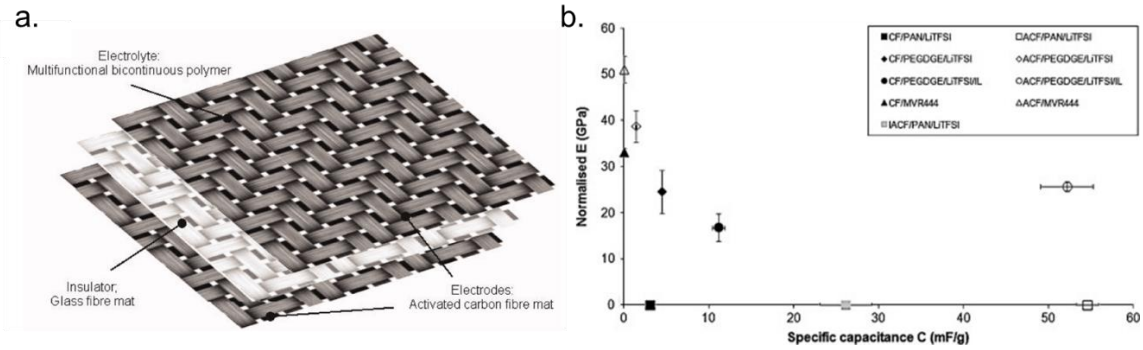

Figure 1.3 a) Schematic representation and b) normalized Young's modulus *vs.* specific capacitance for structural supercapacitors based on carbon fibers. Reprinted with permission.[46] Copyright 2013, Elsevier.

Yushin *et. al* followed a different approach by utilizing CNT veils coated with other electrochemically active materials.[55-58] CNT veils offered structural support and energy storage while the coating served to store energy. CNT veils coated with polyaniline, exhibited a specific capacitance of 200 F/g, tensile strength of 484 MPa, and Young's modulus of 19 GPa.[55] Due to the promising results, the same technique was used for the fabrication of structural batteries using Si nanoparticles, FeF_2 nanoparticles, and $FePO_4$ as the active materials.[56-58] Additionally, Pint *et. al* also investigated the use of CNTs in structural supercapacitors and batteries.[59-61] The performance of the whole device was investigated under tensile, compressive, shear stresses, and even under impact conditions.[59]

More recently, nanocomposite structural supercapacitor electrodes based on reduced graphene oxide (rGO) and MXenes were reported.[10, 12] Specifically, rGO combined with cellulose demonstrated specific capacitance values of 65.9 F/g, a Young's modulus of ~5 GPa, and a tensile strength of 204 MPa.[12] The improved mechanical performance compared to pure rGO was attributed to the hydrogen bonding interactions between rGO and cellulose.[12] Similarly, MXene/cellulose nanofibril (CNF) electrodes with a CNF loading up to 20%, showed a Young's modulus of 41 GPa, mechanical strength of 341 MPa (*vs.* 29 MPa for pristine MXene films) with a specific capacitance of 298 F/g.[10] Hydrogen bonding interactions between the CNF oxygen-containing groups and the MXene hydroxyl groups, as well as geometric effects led to the enhanced mechanical properties. The reported studies on nanocomposite electrodes show great promise for their utilization as structural supercapacitor electrodes.

1.3.1.1. rGO/ANF Structural Electrodes

Prior work from the Lutkenhaus group on structural energy storage focused on the development of nanocomposite supercapacitor electrodes composed of rGO and ANFs.[3, 62] rGO was selected as the energy storage component, while ANFs as the structural component.[3, 62] The effect of different rGO/ANF electrode architectures on mechanical and energy storage performance has been investigated.[3, 62-64] Overall, the rGO/ANF electrodes exhibited a good combination of electrochemical and mechanical properties. In

this section, the different rGO/ANF structural electrode architectures are discussed as these nanocomposites will be the primary focus of this dissertation.

Different architectures of rGO/ANF structural supercapacitor electrodes have been investigated such as layer-by-layer, 'brick and mortar', and 'house of cards'.[3, 62-68] Layer-by-layer assemblies of rGO/ANF exhibited areal capacitances of 211 μF cm^{-2} with stable electrical conductivity values under bending.[62] Despite the interesting properties of these composites, the high ANF content (~ 25 wt%) and the discontinuous rGO structure hindered energy storage leading to low energy storage perfromance.[62]

'Brick and mortar' paper-like architectures were realised using vacuum filtration.[3] In this architecture, rGO acted as the 'brick' and ANF as the 'mortar' in a well-layered, organized structure (Figure 1.4a). The incorporation of ANFs led to a dramatic improvement in tensile strength (~ 209 %) and Young's modulus (~ 350 %) compared to pure rGO (no ANFs) electrodes. Overall, the rGO/ANF electrodes with ANF compositions of 0 – 25 wt% exhibited specific capacitance values of 120 - 190 F/g, tensile strength values of 30 - 100 MPa, and Young's moduli of 4 - 13 GPa depending on composition.[3] The improvement in mechanical performance with ANF addition was attributed to the non-covalent interactions, hydrogen bonding and π-π stacking, between the ANFs and rGO sheets.[3] However, the addition of ANFs led to lower capacitance values, as ANFs are not conductive and do not contribute in energy storage.[3] In addition, the densely packed 'brick and mortar' rGO/ANF structures may impede ion-diffusion as indicated from

physics based models.[65] Addition of CNTs improved ion transport leading to enhancements in capacitance at higher discharge rates.[69]

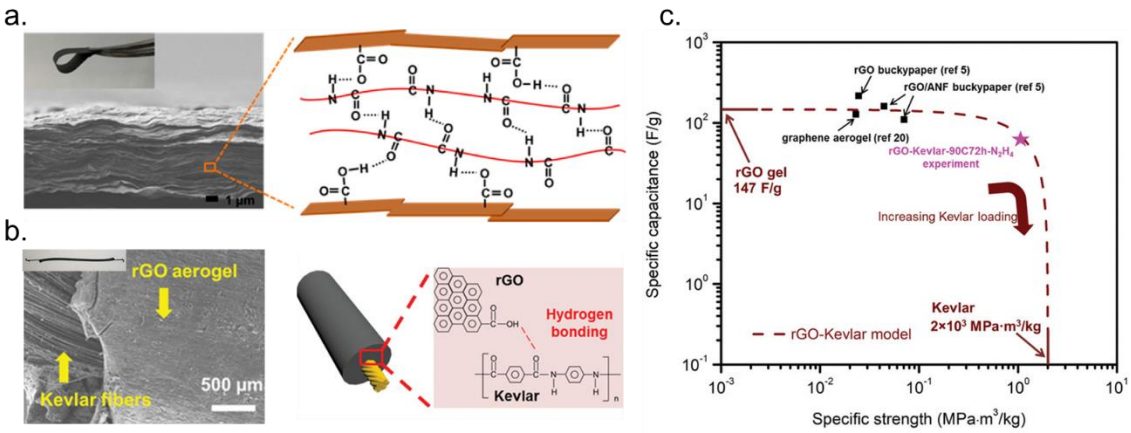

Figure 1.4 a) Cross-sectional scanning electron microscopy image of rGO/ANF 'brick-and-mortar' electrode. Insets show a digital image of the electrode under bending and a schematic representation of the non-covalent interactions between rGO and ANFs. b) Top view electron microscopy image of rGO-gel on Kevlar electrode. Insets show digital images of the electrodes and schematic representations of the non-covalent interactions within the composites. c) Ashby plot for specific capacitance *vs.* specific strength. Reprinted with permission.[3, 64] Copyright 2017, American Chemical Society and Copyright 2019, John Wiley and Sons.

To further improve ion transport and energy storage, 'house of cards' architectures were developed.[63, 64] More specifically, rGO gels containing randomly oriented ANFs were fabricated.[63] ANFs improved the shear elastic modulus of the composite hydrogel by 80% with respect to neat rGO hydrogels. However, addition of ANFs resulted in reduction

in specific capacitance from 190 F/g for neat graphene hydrogel to 128 F/g for an ANF loading of 15 wt%. In a different study, rGO gel structures were coated onto Kevlar fibers and cloths.[64] The Kevlar fibers and cloths served as the mechanical support while the rGO gels contributed to the energy storage function (Figure 1.4b).[64] These structural electrodes exhibited similar mechanical properties to pure Kevlar fibers with a specific capacitance of 57 F/g.[64] Finally, computational studies were developed to assess the rGO/ANF electrodes' modulus, conductivity, and ion-transport properties.[65, 68, 70, 71] Despite the well balanced properties of the rGO/ANF electrodes, the role of the interface and its effect on energy storage and mechanical performance hasn't been investigated.

1.3.2. Structural Battery Electrodes

Despite the progressive studies on structural supercapacitors, the development of structural batteries is at a less advanced stage. In supercapacitors, most electrode materials are also mechanically robust, however, this is not the case for most battery electrodes. For example, commercial graphite-based anodes exhibit capacity values of 330 $mAh/g_{graphite}$ (at 0.1 C, *vs.* a theoretical capacity of 372 mAh/g), but with a low Young's modulus of 0.7 GPa and a tensile strength of 3.7 MPa.[72] Similarly, commercial LFP-based cathodes exhibit capacity values of 124 mAh/g_{LFP} (at 0.5 C, *vs.* a theoretical capacity of 170 mAh/g), with a Young's modulus of only 0.02 GPa and a tensile strength of 0.2 MPa.[73] As a result, there are only a handful reports on structural battery electrodes.

Several of the concepts presented for supercapacitors have also been proven useful for the development of structural battery electrodes, such as the utilization of CF-fabrics.

More specifically, Pint *et al.* recently reported the development of CF-based electrodes coated with graphite for the anode and LFP for the cathode, as shown in Figure 1.5.[8, 35] Full cell battery cells were fabricated using the CF-based electrodes and bi-continuous epoxy-based electrolytes. The structural batteries exhibited superior mechanical properties with a Young's modulus of 2.6 GPa and a tensile strength of 228 MPa.[8] However, poor capacity values were obtained (< 20 mAh/g at 0.1 C) due to delamination of the electrochemically active material and ion-diffusion limitations.[8] Similar observations have also been reported by Asp and Grenhalgh, as well as Yang *et al.* for lithium-ion and lithium-sulfur batteries, respectively.[2, 9, 36, 44, 74]

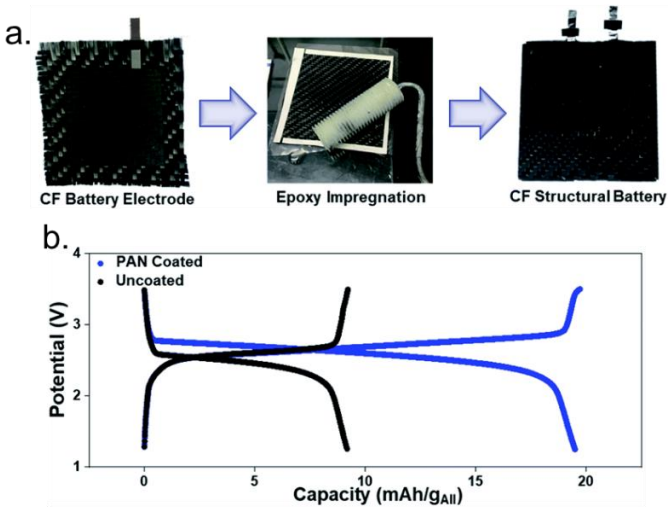

Figure 1.5 a) Digital images and b) charge-discharge voltage profiles for structural lithium-ion batteries based on carbon fibers. Reprinted with permission.[8] Copyright 2020, Royal Society of Chemistry.

Another approach for designing mechanically strong battery electrodes is by developing nanocomposite electrodes containing binder materials that strongly interact,

covalently or non-covalently, with the battery active materials. For example, Si-based anodes using crosslinked chitosan (CS) with dialdehyde of glutaraldehyde (GA) as a binder demonstrated a capacity of 1969 mAh/g_{Si} (at 0.1 C) with a Young's modulus of 4.7 GPa, and a tensile strength of 68.8 MPa.[75] The improved mechanical performance was attributed to the CS-GA crosslinkers that strongly bind with the Si particles.[75]

1.3.3. Multifunctional Efficiency

To assess the ability of a structural energy storage electrode for mass savings, Wetzel *et al.* developed a metric that combines mechanical and energy storage properties, the multifunctional efficiency (n_{mf}).[47, 76, 77] The multifunctional efficiency, for both supercapacitors and batteries, is expressed as a sum of the energy (n_e) and the structural (n_s) efficiency:

$$n_{mf} \equiv n_e + n_s > 1 \text{ where } n_e = \frac{\bar{\Gamma}_{mf}}{\bar{\Gamma}} \text{ and } n_s = \frac{\bar{E}_{mf}}{\bar{E}} \text{ or } n_s = \frac{\overline{UTS}_{mf}}{\overline{UTS}} \quad (1.6)$$

where $\bar{\Gamma}_{mf}$, $\bar{E}_{mf}$, and $\overline{UTS}_{mf}$ represent the specific energy, specific Young's modulus, and specific tensile strength for the structural electrode. Similarly, $\bar{\Gamma}$, $\bar{E}$, and $\overline{UTS}$ represent the specific energy, specific Young's modulus, and specific tensile strength for a monofunctional/conventional device. Here, specific energy is the preferred metric for calculating the energy efficiency instead of specific capacitance as both metrics are highly dependent on the testing conditions and specific energy is more universal as it can be utilized both for the case of supercapacitors and batteries. Mass savings can be realized when the multifunctional efficiency (n_{mf}) is higher than one.[47, 76, 77]

Wetzel's expression for the multifunctional efficiency represents a simplified tool to account for mass savings. However, this expression equally weights the structural and energy efficiency, does not take into account the need for simultaneously good mechanical and electrochemical performances in one device, highly depends on the benchmark materials, and assumes simplified loading conditions and electrode structures. Recently, other researchers developed different expressions for the multifunctional efficiency to tackle these discrepancies. Patel *et. al* developed a utility function that weights structural and energy efficiency according to the desired application.[66] Sun *et al.* proposed a modified equation that requires simultaneously good mechanical and electrochemical performance ($n_{mf} = 2 \cdot \sqrt{n_e \cdot n_s}$).[64] Zhou *et al.* developed a multifunctional efficiency metric using micromechanics that takes into consideration the shape of the components and loading conditions.[78] In this dissertation, we will be using Wetzel's expression as it is currently the most widely used in the field.

1.4. Structural Energy Storage Materials

This dissertation mainly focuses on the development of nanocomposite electrodes containing reduced graphene oxide (rGO), aramid nanofibers (ANFs), or polyaniline (PANI). Properties and synthetic routes for these materials are discussed in this section.

1.4.1. Reduced Graphene Oxide (rGO)

Graphene, a two dimensional sheet of sp^2-hybridized carbon atoms, possesses high electrical conductivity (~10^6 S/cm), large surface area (~2630 m^2/g), and exceptional mechanical properties (Young's modulus of ~ 1.1 TPa and fracture strength of ~ 125 GPa

for a graphene monolayer).[79-83] The most common way to obtain rGO is through the oxidation of graphite, followed by ultrasonication to exfoliate the GO sheets, and reduction (Figure 1.6).[79, 80] Reduction steps are necessary to restore the sp^2-hybridized carbon atoms and the electrical conductivity.[80, 84] The most widely used reduction methods are: thermal, chemical, and electrochemical reduction.[80, 84] Out of these methods, thermal reduction is typically preferred as it is gentler and does not require the use of harsh reducing agents.[80, 83, 84] rGO has been extensively studied as an electrode material both in supercapacitor and batteries due to its ability to electrostatically store energy and host lithium ions.[85-90]

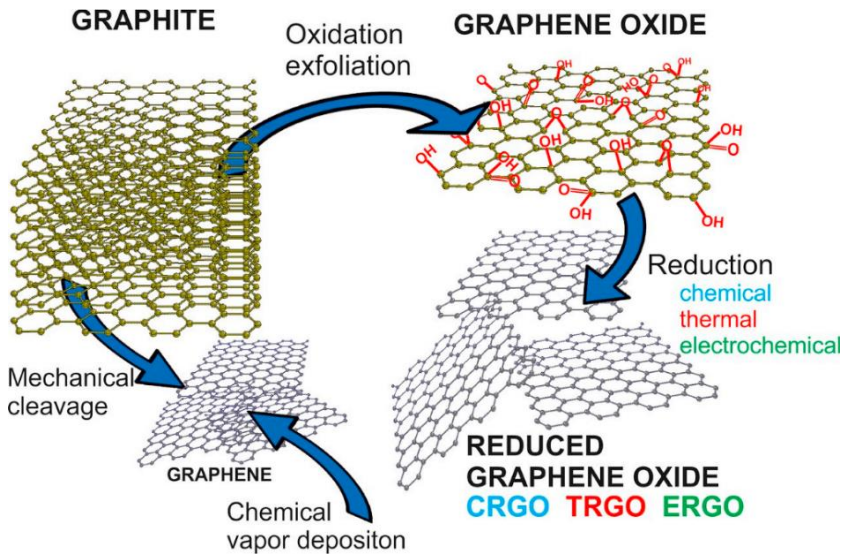

Figure 1.6 Schematic representation of different ways to produce graphene. Reprinted with permission.[90] Copyright 2018, Elsevier.

1.4.2. Aramid Nanofibers (ANFs)

ANFs and branched aramid nanofibers (BANFs) are nanoscale Kevlar® fibers, as shown in Figure 1.7.[91-97] Kevlar® is composed of poly(paraphenylene terephthalamide)

(PPTA) aligned chains and is known for its exceptional mechanical properties such as high Young's modulus (*e.g.* 129 GPa) and high tensile strength (*e.g* 4.1 GPa).[91, 92, 98] The superior mechanical properties of Kevlar® result from the strong hydrogen bonding and π-π stacking interactions between the PPTA chains.[91-93]

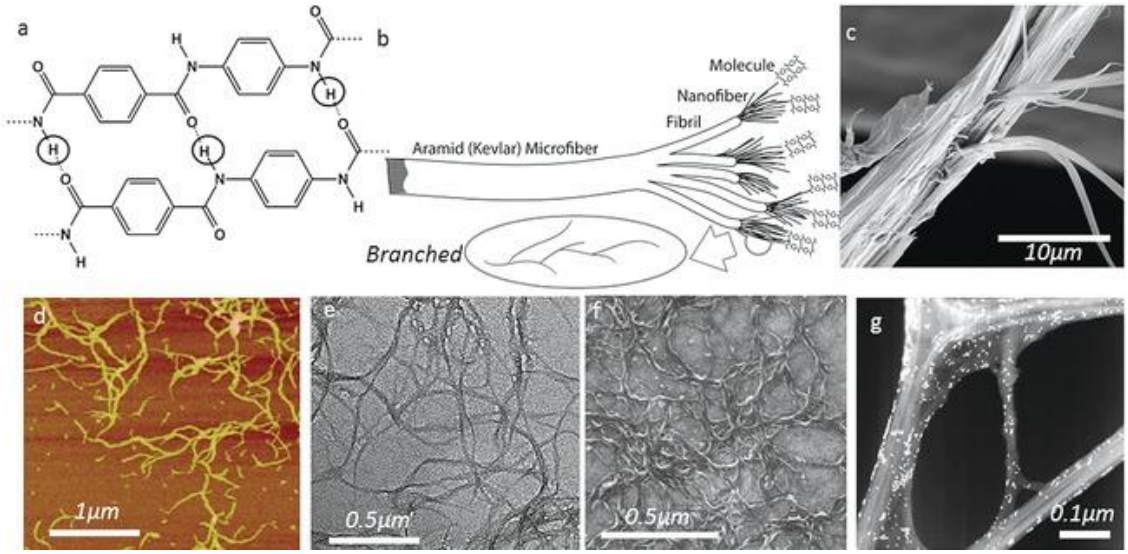

Figure 1.7 a) Chemical structure of PPTA chains. b) Schematic representation of the hierarchical structure of Kevlar® microfibers. c) Scanning electron microscopy (SEM) image of fractured Kevlar® microfibers. d) Atomic force microscopy (AFM) image and e) transmission electron microscopy (TEM) image of branched ANFs (BANFs). f) SEM image of BANFs. Reprinted with permission. [97] Copyright 2017, John Wiley and Sons.

Kotov *et al.* reported the fabrication of ANFs using a top-down procedure in 2011.[95] More specifically, ANFs were obtained by the dissolution of chopped bulk Kevlar® fibers in a polar aprotic environment (dimethyl sulfoxide, DMSO) and potassium

hydroxide (KOH).[95] KOH served to deprotonate the amide groups of PPTA leading to stable red dispersions of the aramid nanofibers.[95] Typically ANFs have diameters of 5-30 nm and lengths up to 10 μm.[3, 97] ANFs can be further processed and incorporated in nanocomposites using methods such as layer-by-layer or vacuum-assisted assembly for various applications such as structural, energy storage, and electromagnetic interference (EMI) shielding.[3, 41, 62, 99-101]

1.4.3. Polyaniline (PANI)

PANI is a p-conjugated polymer and possesses good electrical conductivity (2-5 S/cm in emeraldine form) and high capacity values (theoretical capacity of 147 mAh/g).[33, 102-106] Additionally, PANI can be used as an electrode material in both aqueous and non-aqueous energy storage systems.[28] PANI is redox active, stores charge through a doping/de-doping mechanism, and has five different oxidation states (emeraldine base, emeraldine salt, leucoemeraldine base, prenigraniline base, and prenigraniline salt), as shown in Figure 1.8.[107] Among them, emeraldine salt is electrically conductive.[107] PANI can be easily synthesized *via* oxidative polymerization.[107]

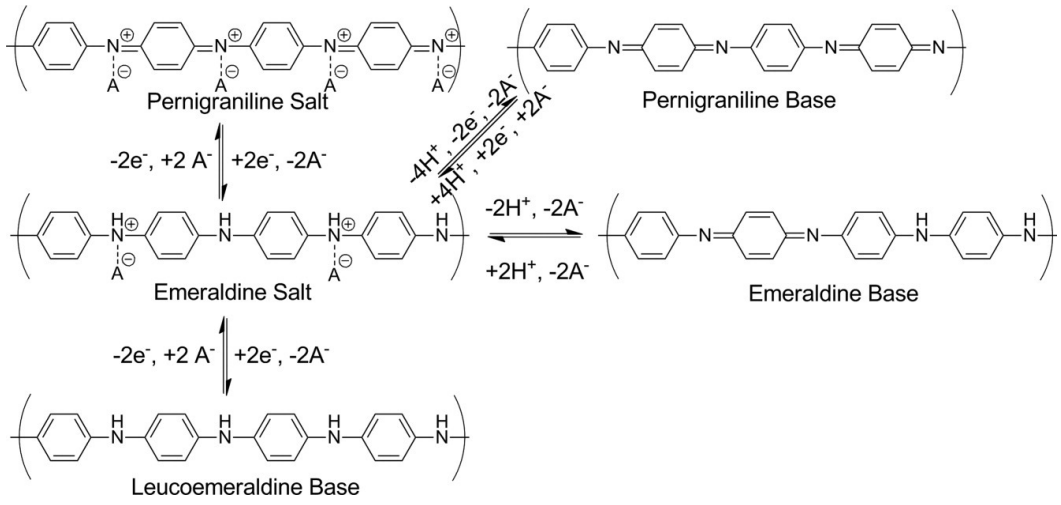

Figure 1.8 Schematic representation of PANI's redox states. Reprinted with permission.[107] Copyright 2013, John Wiley and Sons.

1.5. Dissertation Overview

In this dissertation, structural nanocomposite electrodes for supercapacitors and lithium-ion batteries were developed. We mainly focused on rGO/ANF 'brick and mortar' architectures with emphasis on the effect of different interfacial interactions on mechanical and energy storage performance. rGO and ANFs interact with each other through hydrogen bonding interactions between the rGO oxygen-containing groups and the ANF amide groups. Interfacial interactions (enhanced hydrogen bonding interactions and coordination bonding) were engineered as means to improve the mechanical performance of these structural electrodes.

Figure 1.9 depicts a summary of the different modifications explored to enhance hydrogen bonding interactions and induce coordination bonding. More specifically,

functionalizing GO with -COOH, -NH_2, dopamine, and tannic acid, as well as branching the ANFs were investigated to increase hydrogen bonding interactions. Coordination bonding was induced by the addition of divalent (Ca^{2+}) and trivalent (Fe^{3+}) ions and the effect of metal ion valency was investigated. **Chapters 2**, **3**, and **4** discuss these modifications separately as standalone chapters. **Chapters 5** and **6** translate some of these concepts in structural lithium-ion battery electrodes, while in **Chapter 7** all results are discussed holistically.

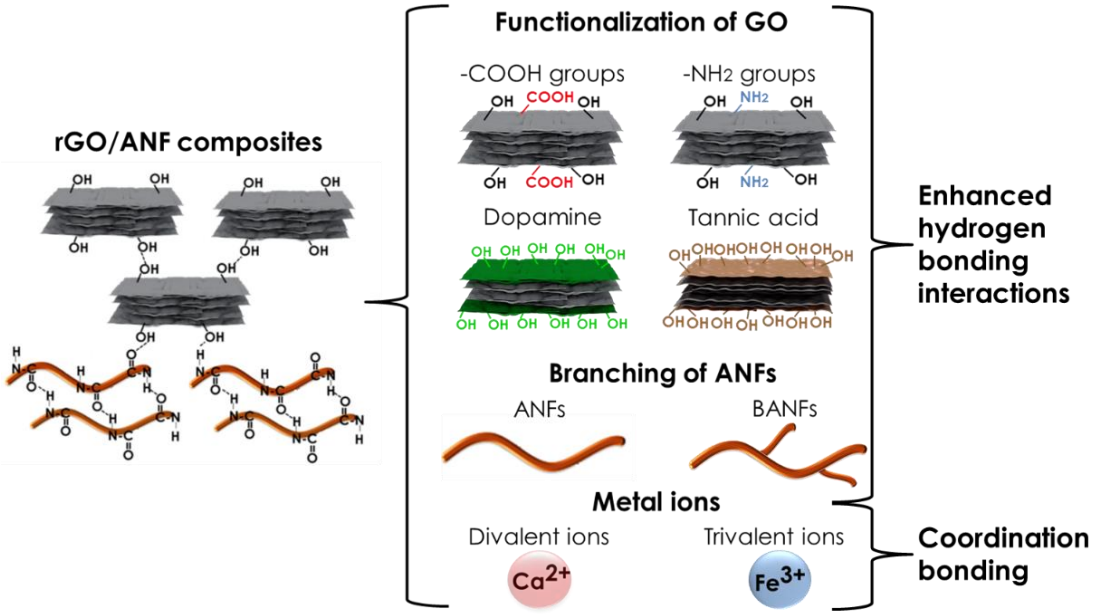

Figure 1.9 Summary of the different modifications investigated to enhance hydrogen bonding interactions and induce coordination bonding in rGO/ANF structural electrodes.

In **Chapter 2**, the effect of enhanced hydrogen bonding interactions in rGO/ANF electrodes was investigated. To enhance these interactions, GO was functionalized with

carboxylic acid (-COOH) and amine (-NH_2) groups. Structural supercapacitor electrodes were fabricated using vacuum-assisted filtration. -NH_2 functionalization and addition of ANFs (25 wt%) led to 200 % and 150 % improvements in tensile strength and Young's modulus, respectively, compared to pure rGO without significantly compromising the energy storage performance. –COOH functionalization did not lead to such improvements due to the introduction of defects in the graphitic structure during the functionalization process. The results demonstrate that gentler interfacial modifications can lead to even further enhancements in mechanical performance with good energy storage.

In **Chapter 3**, we investigated the synergistic effect of hydrogen bonding interactions and coordination bonding between rGO and branched ANFs (BANFs). GO was functionalized with dopamine, a highly adhesive molecule that mimics the adhesive proteins of mussels. Furthermore, divalent ions (Ca^{2+}) were added to induce coordination bonding between the rGO flakes. Ca^{2+} ions coordinate with the oxygen containing groups of the dopamine functionalized rGO. BANFs and non-covalent interactions resulting from the dopamine functionalization and the addition of divalent ions led to enhancements in ultimate tensile strength and Young's modulus of 255 % and 220 %, respectively, as compared to pure rGO. Electrochemical performance deteriorated due to the more compact structures that introduced ion-diffusion limitations. However, high multifunctional efficiency values of 5-13.6 were achieved. This work underlines the synergistic effect of hydrogen and coordination bonding for realizing multifunctional structural electrodes.

We further investigated the effect of coordination bonding in more depth in **Chapter 4**. More specifically, we functionalized GO with tannic acid – a molecule composed of catechol and galloyl groups – and introduced divalent (Ca^{2+}) and trivalent (Fe^{3+}) ions. The effect of coordination bonding induced by divalent and trivalent ions on both mechanical properties and energy storage properties was investigated. Addition of trivalent ions led to superior mechanical performance compared to the divalent ion-containing composites resulting from the higher valency that leads to stronger attraction. Finally, we built a prototype structural supercapacitor to demonstrate the good energy storage capabilities of these electrodes under mechanical loads.

From the previous studies, it was found that rGO/BANF composites exhibited the highest multifunctional efficiency values. In **Chapter 5**, we investigated the utilization of the rGO/BANF composites in structural lithium-ion battery electrodes. Structural cathodes and anodes were fabricated by the incorporation of lithium iron phosphate (LFP) and silicon (Si) particles in rGO/BANF composites, respectively. It was shown that the BANF-containing electrodes demonstrated improved multifunctional performance as a result of the strong BANFs that acted as binder and allowed for higher active material contents while maintaining the electrodes' mechanical integrity. Overall, up to two orders of magnitude improvements in tensile strength and Young's modulus were achieved compared to commercial lithium-ion battery anodes and cathodes.

In **Chapter 6**, we utilized BANFs for the development of structural supercapacitor electrodes and lithium-ion battery cathodes using PANI. PANI is a promising conjugated

polymer for energy storage but its brittle nature has hindered the fabrication of mechanically strong PANI electrodes. Here, aniline was polymerized in the presence of single-walled carbon nanotubes (SWCNTs) and BANFs. CNTs and BANFs created continuous networks that allowed for high electrical conductivities and efficient load transfer within the composites. Overall, promising energy storage performance both in supercapacitors and lithium-ion batteries was achieved with good mechanical properties.

Finally, in **Chapter 7**, we discuss the effect of all modifications on the multifunctional efficiency of the structural electrodes and present future directions.

1.6. References

1. Asp, L. E.; Greenhalgh, E. S., Structural power composites. *Composites Science and Technology* **2014,** *101*, 41-61.
2. Asp, L. E.; Johansson, M.; Lindbergh, G.; Xu, J.; Zenkert, D., Structural battery composites: a review. *Functional Composites and Structures* **2019,** *1* (4), 042001.
3. Kwon, S. R.; Harris, J.; Zhou, T.; Loufakis, D.; Boyd, J. G.; Lutkenhaus, J. L., Mechanically Strong Graphene/Aramid Nanofiber Composite Electrodes for Structural Energy and Power. *ACS Nano* **2017,** *11* (7), 6682-6690.
4. Chan, K.-Y.; Jia, B.; Lin, H.; Hameed, N.; Lee, J.-H.; Lau, K.-T., A critical review on multifunctional composites as structural capacitors for energy storage. *Composite Structures* **2018,** *188*, 126-142.
5. Flouda, P.; Feng, X. Y.; Boyd, J. G.; Thomas, E. L.; Lagoudas, D. C.; Lutkenhaus, J. L., Interfacial Engineering of Reduced Graphene Oxide for Aramid Nanofiber-Enabled Structural Supercapacitors. *Batteries Supercaps* **2019,** *2* (5), 464-472.
6. Chen, Y.; Amiri, A.; Boyd, J. G.; Naraghi, M., Promising Trade-Offs Between Energy Storage and Load Bearing in Carbon Nanofibers as Structural Energy Storage Devices. *Advanced Functional Materials* **2019,** *29* (33), 1901425.
7. Rana, M.; Ou, Y.; Meng, C.; Sket, F.; González, C.; Vilatela, J. J., Damage-tolerant, laminated structural supercapacitor composites enabled by integration of carbon nanotube fibres. *Multifunctional Materials* **2020,** *3* (1), 015001.
8. Moyer, K.; Ait Boucherbil, N.; Zohair, M.; Eaves, J.; Pint, C., Polymer Reinforced Carbon Fiber Interfaces for High Energy Density Structural Lithium-Ion Batteries. *Sustainable Energy & Fuels* **2020**.

9. Giulia, F.; Steffen, J.; Athmane, B.; Joachim, W.; Masoud, R.; Fang, L.; Ross, H.; Dan, Z.; Johan, H.; Göran, L.; Patrik, J.; Lorenzo, S.; Leif, E. A., Graphitic microstructure and performance of carbon fibre Li-ion structural battery electrodes. *Multifunctional Materials* **2018,** *1* (1), 015003.
10. Tian, W.; VahidMohammadi, A.; Reid, M. S.; Wang, Z.; Ouyang, L.; Erlandsson, J.; Pettersson, T.; Wågberg, L.; Beidaghi, M.; Hamedi, M. M., Multifunctional Nanocomposites with High Strength and Capacitance Using 2D MXene and 1D Nanocellulose. *Advanced Materials* **2019,** *31* (41), 1902977.
11. Yin, Q.; Jia, H.; Mohamed, A.; Ji, Q.; Hong, L., Highly flexible and mechanically strong polyaniline nanostructure @ aramid nanofiber films for free-standing supercapacitor electrodes. *Nanoscale* **2020,** *12* (9), 5507-5520.
12. Guan, F.; Chen, S.; Sheng, N.; Chen, Y.; Yao, J.; Pei, Q.; Wang, H., Mechanically robust reduced graphene oxide/bacterial cellulose film obtained via biosynthesis for flexible supercapacitor. *Chem. Eng. J.* **2019,** *360*, 829-837.
13. Simon, P.; Gogotsi, Y.; Dunn, B., Where Do Batteries End and Supercapacitors Begin? *Science* **2014,** *343* (6176), 1210-1211.
14. Simon, P.; Gogotsi, Y., Perspectives for electrochemical capacitors and related devices. *Nature Materials* **2020,** *19* (11), 1151-1163.
15. Jost, K.; Dion, G.; Gogotsi, Y., Textile energy storage in perspective. *Journal of Materials Chemistry A* **2014,** *2* (28), 10776-10787.
16. Simon, P.; Gogotsi, Y., Materials for electrochemical capacitors. *Nature Materials* **2008,** *7* (11), 845-854.
17. Mathis, T. S.; Kurra, N.; Wang, X.; Pinto, D.; Simon, P.; Gogotsi, Y., Energy Storage Data Reporting in Perspective—Guidelines for Interpreting the Performance of Electrochemical Energy Storage Systems. *Advanced Energy Materials* **2019,** *9* (39), 1902007.
18. Huang, L.; Santiago, D.; Loyselle, P.; Dai, L., Graphene-Based Nanomaterials for Flexible and Wearable Supercapacitors. *Small 0* (0), 1800879.
19. Qu, D.; Shi, H., Studies of activated carbons used in double-layer capacitors. *Journal of Power Sources* **1998,** *74* (1), 99-107.
20. Huang, S.; Zhu, X.; Sarkar, S.; Zhao, Y., Challenges and opportunities for supercapacitors. *APL Materials* **2019,** *7* (10), 100901.
21. Stoller, M. D.; Park, S.; Zhu, Y.; An, J.; Ruoff, R. S., Graphene-Based Ultracapacitors. *Nano Letters* **2008,** *8* (10), 3498-3502.
22. Stoller, M. D.; Ruoff, R. S., Best practice methods for determining an electrode material's performance for ultracapacitors. *Energy & Environmental Science* **2010,** *3* (9), 1294-1301.
23. Liu, W.; Song, M.-S.; Kong, B.; Cui, Y., Flexible and Stretchable Energy Storage: Recent Advances and Future Perspectives. *Advanced Materials* **2017,** *29* (1), 1603436.

24. Wen, L.; Li, F.; Cheng, H.-M., Carbon Nanotubes and Graphene for Flexible Electrochemical Energy Storage: from Materials to Devices. *Advanced Materials* **2016,** *28* (22), 4306-4337.
25. Izadi-Najafabadi, A.; Yamada, T.; Futaba, D. N.; Yudasaka, M.; Takagi, H.; Hatori, H.; Iijima, S.; Hata, K., High-Power Supercapacitor Electrodes from Single-Walled Carbon Nanohorn/Nanotube Composite. *ACS Nano* **2011,** *5* (2), 811-819.
26. Zhu, Y.; Murali, S.; Stoller, M. D.; Ganesh, K. J.; Cai, W.; Ferreira, P. J.; Pirkle, A.; Wallace, R. M.; Cychosz, K. A.; Thommes, M.; Su, D.; Stach, E. A.; Ruoff, R. S., Carbon-Based Supercapacitors Produced by Activation of Graphene. *Science* **2011,** *332* (6037), 1537-1541.
27. Kim, T.; Jung, G.; Yoo, S.; Suh, K. S.; Ruoff, R. S., Activated Graphene-Based Carbons as Supercapacitor Electrodes with Macro- and Mesopores. *ACS Nano* **2013,** *7* (8), 6899-6905.
28. Eftekhari, A.; Li, L.; Yang, Y., Polyaniline supercapacitors. *Journal of Power Sources* **2017,** *347*, 86-107.
29. Meng, C.; Liu, C.; Fan, S., Flexible carbon nanotube/polyaniline paper-like films and their enhanced electrochemical properties. *Electrochem. Commun.* **2009,** *11* (1), 186-189.
30. Parikh, P.; Sina, M.; Banerjee, A.; Wang, X.; D'Souza, M. S.; Doux, J.-M.; Wu, E. A.; Trieu, O. Y.; Gong, Y.; Zhou, Q.; Snyder, K.; Meng, Y. S., Role of Polyacrylic Acid (PAA) Binder on the Solid Electrolyte Interphase in Silicon Anodes. *Chemistry of Materials* **2019,** *31* (7), 2535-2544.
31. Zuo, X.; Zhu, J.; Müller-Buschbaum, P.; Cheng, Y.-J., Silicon based lithium-ion battery anodes: A chronicle perspective review. *Nano Energy* **2017,** *31*, 113-143.
32. Manthiram, A., A reflection on lithium-ion battery cathode chemistry. *Nature Communications* **2020,** *11* (1), 1550.
33. Jeon, J.-W.; O'Neal, J.; Shao, L.; Lutkenhaus, J. L., Charge Storage in Polymer Acid-Doped Polyaniline-Based Layer-by-Layer Electrodes. *ACS Applied Materials & Interfaces* **2013,** *5* (20), 10127-10136.
34. Wang, S.; Park, A. M. G.; Flouda, P.; Easley, A. D.; Li, F.; Ma, T.; Fuchs, G. D.; Lutkenhaus, J. L., Solution-Processable Thermally Crosslinked Organic Radical Polymer Battery Cathodes. *ChemSusChem* **2020,** *13* (9), 2371-2378.
35. Moyer, K.; Meng, C.; Marshall, B.; Assal, O.; Eaves, J.; Perez, D.; Karkkainen, R.; Roberson, L.; Pint, C. L., Carbon fiber reinforced structural lithium-ion battery composite: Multifunctional power integration for CubeSats. *Energy Storage Materials* **2020,** *24*, 676-681.
36. Huang, W.; Wang, P.; Liao, X.; Chen, Y.; Borovilas, J.; Jin, T.; Li, A.; Cheng, Q.; Zhang, Y.; Zhai, H.; Chitu, A.; Shan, Z.; Yang, Y., Mechanically-robust structural lithium-sulfur battery with high energy density. *Energy Storage Materials* **2020,** *33*, 416-422.

37. Tung, S.-O.; Ho, S.; Yang, M.; Zhang, R.; Kotov, N. A., A dendrite-suppressing composite ion conductor from aramid nanofibres. *Nature Communications* **2015,** *6*, 6152.
38. Wang, M.; Emre, A.; Tung, S.; Gerber, A.; Wang, D.; Huang, Y.; Cecen, V.; Kotov, N. A., Biomimetic Solid-State Zn2+ Electrolyte for Corrugated Structural Batteries. *ACS Nano* **2019,** *13* (2), 1107-1115.
39. Wang, M.; Vecchio, D.; Wang, C.; Emre, A.; Xiao, X.; Jiang, Z.; Bogdan, P.; Huang, Y.; Kotov, N. A., Biomorphic structural batteries for robotics. *Science Robotics* **2020,** *5* (45), eaba1912.
40. Li, A.; Liao, X.; Zhang, H.; Shi, L.; Wang, P.; Cheng, Q.; Borovilas, J.; Li, Z.; Huang, W.; Fu, Z.; Dontigny, M.; Zaghib, K.; Myers, K.; Chuan, X.; Chen, X.; Yang, Y., Nacre-Inspired Composite Electrolytes for Load-Bearing Solid-State Lithium-Metal Batteries. *Adv. Mater.* **2020,** *32* (2), 1905517.
41. Yang, Y.; Huang, C.; Gao, G.; Hu, C.; Luo, L.; Xu, J., Aramid nanofiber/bacterial cellulose composite separators for lithium-ion batteries. *Carbohydr. Polym.* **2020,** *247*, 116702.
42. Shirshova, N.; Bismarck, A.; Carreyette, S.; Fontana, Q. P. V.; Greenhalgh, E. S.; Jacobsson, P.; Johansson, P.; Marczewski, M. J.; Kalinka, G.; Kucernak, A. R. J.; Scheers, J.; Shaffer, M. S. P.; Steinke, J. H. G.; Wienrich, M., Structural supercapacitor electrolytes based on bicontinuous ionic liquid–epoxy resin systems. *Journal of Materials Chemistry A* **2013,** *1* (48), 15300-15309.
43. Ihrner, N.; Johannisson, W.; Sieland, F.; Zenkert, D.; Johansson, M., Structural lithium ion battery electrolytes via reaction induced phase-separation. *Journal of Materials Chemistry A* **2017,** *5* (48), 25652-25659.
44. Johannisson, W.; Ihrner, N.; Zenkert, D.; Johansson, M.; Carlstedt, D.; Asp, L. E.; Sieland, F., Multifunctional performance of a carbon fiber UD lamina electrode for structural batteries. *Composites Science and Technology* **2018,** *168*, 81-87.
45. Shirshova, N.; Bismarck, A.; Greenhalgh, E. S.; Johansson, P.; Kalinka, G.; Marczewski, M. J.; Shaffer, M. S. P.; Wienrich, M., Composition as a Means To Control Morphology and Properties of Epoxy Based Dual-Phase Structural Electrolytes. *The Journal of Physical Chemistry C* **2014,** *118* (49), 28377-28387.
46. Shirshova, N.; Qian, H.; Shaffer, M. S. P.; Steinke, J. H. G.; Greenhalgh, E. S.; Curtis, P. T.; Kucernak, A.; Bismarck, A., Structural composite supercapacitors. *Composites Part A: Applied Science and Manufacturing* **2013,** *46*, 96-107.
47. Snyder, J.; Gienger, E.; Wetzel, E. J. J. o. C. M., Performance metrics for structural composites with electrochemical multifunctionality. *J. Compos. Mater.* **2015,** *49* (15), 1835-1848.
48. Qian, H.; Diao, H.; Shirshova, N.; Greenhalgh, E. S.; Steinke, J. G. H.; Shaffer, M. S. P.; Bismarck, A., Activation of structural carbon fibres for potential applications in multifunctional structural supercapacitors. *Journal of Colloid and Interface Science* **2013,** *395*, 241-248.

49. Greenhalgh, E.; Ankersen, J.; Asp, L.; Bismarck, A.; Fontana, Q.; Houlle, M.; Kalinka, G.; Kucernak, A.; Mistry, M.; Nguyen, S.; Qian, H.; Shaffer, M.; Shirshova, N.; Steinke, J.; Wienrich, M., Mechanical, electrical and microstructural characterisation of multifunctional structural power composites. *Journal of Composite Materials* **2015,** *49* (15), 1823-1834.
50. Sha, Z.; Huang, F.; Zhou, Y.; Zhang, J.; Wu, S.; Chen, J.; Brown, S. A.; Peng, S.; Han, Z.; Wang, C.-H., Synergies of vertical graphene and manganese dioxide in enhancing the energy density of carbon fibre-based structural supercapacitors. *Composites Science and Technology* **2021,** *201*, 108568.
51. Mofokeng, T. P.; Tetana, Z. N.; Ozoemena, K. I., Defective 3D nitrogen-doped carbon nanotube-carbon fibre networks for high-performance supercapacitor: Transformative role of nitrogen-doping from surface-confined to diffusive kinetics. *Carbon* **2020,** *169*, 312-326.
52. Javaid, A.; Ho, K.; Bismarck, A.; Steinke, J.; Shaffer, M.; Greenhalgh, E., Improving the multifunctional behaviour of structural supercapacitors by incorporating chemically activated carbon fibres and mesoporous silica particles as reinforcement. *Journal of Composite Materials* **2018,** *52* (22), 3085-3097.
53. Reece, R.; Lekakou, C.; Smith, P. A., A High-Performance Structural Supercapacitor. *ACS Applied Materials & Interfaces* **2020,** *12* (23), 25683-25692.
54. Ganguly, A.; Karakassides, A.; Benson, J.; Hussain, S.; Papakonstantinou, P., Multifunctional Structural Supercapacitor Based on Urea-Activated Graphene Nanoflakes Directly Grown on Carbon Fiber Electrodes. *ACS Applied Energy Materials* **2020,** *3* (5), 4245-4254.
55. Benson, J.; Kovalenko, I.; Boukhalfa, S.; Lashmore, D.; Sanghadasa, M.; Yushin, G., Multifunctional CNT-Polymer Composites for Ultra-Tough Structural Supercapacitors and Desalination Devices. *Adv. Mater.* **2013,** *25* (45), 6625-6632.
56. Evanoff, K.; Benson, J.; Schauer, M.; Kovalenko, I.; Lashmore, D.; Ready, W. J.; Yushin, G., Ultra Strong Silicon-Coated Carbon Nanotube Nonwoven Fabric as a Multifunctional Lithium-Ion Battery Anode. *ACS Nano* **2012,** *6* (11), 9837-9845.
57. Huang, Q.; Turcheniuk, K.; Ren, X.; Magasinski, A.; Song, A.-Y.; Xiao, Y.; Kim, D.; Yushin, G., Cycle stability of conversion-type iron fluoride lithium battery cathode at elevated temperatures in polymer electrolyte composites. *Nature Materials* **2019,** *18* (12), 1343-1349.
58. Ren, X.; Turcheniuk, K.; Lewis, D.; Fu, W.; Magasinski, A.; Schauer, M. W.; Yushin, G., Iron Phosphate Coated Flexible Carbon Nanotube Fabric as a Multifunctional Cathode for Na-Ion Batteries. *Small* **2018,** *14* (43), 1703425.
59. Davis, B. F.; Yan, X.; Muralidharan, N.; Oakes, L.; Pint, C. L.; Maschmann, M. R., Electrically Conductive Hierarchical Carbon Nanotube Networks with Tunable Mechanical Response. *ACS Applied Materials & Interfaces* **2016,** *8* (41), 28004-28011.
60. Meng, C.; Muralidharan, N.; Teblum, E.; Moyer, K. E.; Nessim, G. D.; Pint, C. L. J. N. l., Multifunctional Structural Ultrabattery Composite. *Nano Lett.* **2018,** *18* (12), 7761-7768.

61. Cohn, A. P.; Oakes, L.; Carter, R.; Chatterjee, S.; Westover, A. S.; Share, K.; Pint, C. L., Assessing the improved performance of freestanding, flexible graphene and carbon nanotube hybrid foams for lithium ion battery anodes. *Nanoscale* **2014,** *6* (9), 4669-4675.
62. Kwon, S. R.; Elinski, M. B.; Batteas, J. D.; Lutkenhaus, J. L., Robust and Flexible Aramid Nanofiber/Graphene Layer-by-Layer Electrodes. *ACS Appl Mater Interfaces* **2017,** *9* (20), 17125-17135.
63. Shah, S. A.; Kulhanek, D.; Sun, W.; Zhao, X.; Yu, S.; Parviz, D.; Lutkenhaus, J. L.; Green, M. J., Aramid nanofiber-reinforced three-dimensional graphene hydrogels for supercapacitor electrodes. *Journal of Colloid and Interface Science* **2019**.
64. Sun, W.; Shah, S. A.; Lowery, J. L.; Oh, J. H.; Lutkenhaus, J. L.; Green, M. J., Lightweight Kevlar-Reinforced Graphene Oxide Architectures with High Strength for Energy Storage. *Advanced Materials Interfaces* **2019,** *6* (21), 1900786.
65. Aderyani, S.; Flouda, P.; Lutkenhaus, J. L.; Ardebili, H., The effect of nanoscale architecture on ionic diffusion in rGo/aramid nanofiber structural electrodes. *Journal of Applied Physics* **2019,** *125* (18), 185106.
66. Patel, A. G.; Johnson, L.; Arroyave, R.; Lutkenhaus, J. L., Design of multifunctional supercapacitor electrodes using an informatics approach. *Mol Syst Des Eng* **2019,** *4*, 654-663.
67. Tianyang, Z.; James, G. B.; Dimitrios, L.; Jodie, L.; Dimitris, C. L., Fabrication, characterization and micromechanics modeling of the electrical conductivity of reduced graphene oxide/aramid nanofiber nanocomposites. *Smart Materials and Structures* **2019**.
68. Zhou, T.; Boyd, J. G.; Lutkenhaus, J. L.; Lagoudas, D. C., Micromechanics modeling of the elastic moduli of rGO/ANF nanocomposites. *Acta Mech* **2018,** *230* (1), 265-280.
69. Patel, A.; Loufakis, D.; Flouda, P.; George, I.; Shelton, C.; Harris, J.; Oka, S.; Lutkenhaus, J. L., Carbon Nanotube/Reduced Graphene Oxide/Aramid Nanofiber Structural Supercapacitors. *ACS Applied Energy Materials* **2020,** *3* (12), 11763-11771.
70. Zhou, T.; Boyd, J. G.; Loufakis, D.; Lutkenhaus, J. L.; Lagoudas, D. C., Fabrication, characterization and micromechanics modeling of the electrical conductivity of reduced graphene oxide/aramid nanofiber nanocomposites. *Smart Materials and Structures* **2019,** *28* (9), 094001.
71. Aderyani, S.; Shah, S. A.; Masoudi, A.; Green, M. J.; Lutkenhaus, J. L.; Ardebili, H., Comparison of Nanoarchitecture to Porous Media Diffusion Models in Reduced Graphene Oxide/Aramid Nanofiber Electrodes for Supercapacitors. *ACS Nano* **2020,** *14* (5), 5314-5323.
72. Zheng, H.; Zhang, L.; Liu, G.; Song, X.; Battaglia, V. S., Correlationship between electrode mechanics and long-term cycling performance for graphite anode in lithium ion cells. *Journal of Power Sources* **2012,** *217*, 530-537.
73. Boaretto, N.; Almenara, J.; Mikhalchan, A.; Marcilla, R.; Vilatela, J. J., A Route to High-Toughness Battery Electrodes. *ACS Applied Energy Materials* **2019,** *2* (8), 5889-5899.

74. Carlstedt, D.; Marklund, E.; Asp, L. E., Effects of state of charge on elastic properties of 3D structural battery composites. *Composites Science and Technology* **2019,** *169*, 26-33.
75. Chen, C.; Lee, S. H.; Cho, M.; Kim, J.; Lee, Y., Cross-Linked Chitosan as an Efficient Binder for Si Anode of Li-ion Batteries. *ACS Applied Materials & Interfaces* **2016,** *8* (4), 2658-2665.
76. O'Brien, D.; Baechle, D.; Wetzel, E. J. J. o. C. M., Design and performance of multifunctional structural composite capacitors. *J. Compos. Mater.* **2011,** *45* (26), 2797-2809.
77. Snyder, J. F.; Wetzel, E. D.; Watson, C. M. J. P., Improving multifunctional behavior in structural electrolytes through copolymerization of structure-and conductivity-promoting monomers. *Polymer* **2009,** *50* (20), 4906-4916.
78. Zhou, T.; Dickinson, E.; Boyd, J. G.; Lutkenhaus, J. L.; Lagoudas, D. C., Multifunctional efficiency metric for structural supercapacitors. *Multifunctional Materials* **2021,** *3* (4), 044002.
79. Kuila, T.; Bose, S.; Mishra, A. K.; Khanra, P.; Kim, N. H.; Lee, J. H., Chemical functionalization of graphene and its applications. *Prog. Mater Sci.* **2012,** *57* (7), 1061-1105.
80. Dreyer, D. R.; Park, S.; Bielawski, C. W.; Ruoff, R. S., The chemistry of graphene oxide. *Chem. Soc. Rev.* **2010,** *39* (1), 228-240.
81. Geim, A. K.; Novoselov, K. S., The rise of graphene. *Nat. Mater* **2007,** *6* (3), 183-91.
82. Dikin, D. A.; Stankovich, S.; Zimney, E. J.; Piner, R. D.; Dommett, G. H. B.; Evmenenko, G.; Nguyen, S. T.; Ruoff, R. S., Preparation and characterization of graphene oxide paper. *Nature* **2007,** *448*, 457.
83. Bai, H.; Li, C.; Shi, G., Functional Composite Materials Based on Chemically Converted Graphene. *Advanced Materials* **2011,** *23* (9), 1089-1115.
84. Park, S.; An, J.; Potts, J. R.; Velamakanni, A.; Murali, S.; Ruoff, R. S., Hydrazine-reduction of graphite- and graphene oxide. *Carbon* **2011,** *49* (9), 3019-3023.
85. Ma, Y.; Li, P.; Sedloff, J. W.; Zhang, X.; Zhang, H.; Liu, J., Conductive Graphene Fibers for Wire-Shaped Supercapacitors Strengthened by Unfunctionalized Few-Walled Carbon Nanotubes. *ACS Nano* **2015,** *9* (2), 1352-1359.
86. He, Y.; Chen, W.; Li, X.; Zhang, Z.; Fu, J.; Zhao, C.; Xie, E., Freestanding Three-Dimensional Graphene/MnO2 Composite Networks As Ultralight and Flexible Supercapacitor Electrodes. *ACS Nano* **2013,** *7* (1), 174-182.
87. Weng, Z.; Su, Y.; Wang, D. W.; Li, F.; Du, J.; Cheng, H. M., Graphene–cellulose paper flexible supercapacitors. *Adv Energy Mater* **2011,** *1* (5), 917-922.
88. De, S.; Purcell, C.; Murley, J.; Flouda, P.; Shah, S.; Green, M.; Lutkenhaus, J., Spray-On Reduced Graphene Oxide-Poly(vinyl alcohol) Supercapacitors for Flexible Energy and Power. *Adv Mater Interfaces* **2018,** *5* (23), 1801237.
89. Peng, X.; Peng, L.; Wu, C.; Xie, Y., Two dimensional nanomaterials for flexible supercapacitors. *Chemical Society Reviews* **2014,** *43* (10), 3303-3323.

90. Rowley-Neale, S. J.; Randviir, E. P.; Abo Dena, A. S.; Banks, C. E., An overview of recent applications of reduced graphene oxide as a basis of electroanalytical sensing platforms. *Applied Materials Today* **2018,** *10*, 218-226.
91. Reis, P. N. B.; Ferreira, J. A. M.; Santos, P.; Richardson, M. O. W.; Santos, J. B., Impact response of Kevlar composites with filled epoxy matrix. *Compos. Struct.* **2012,** *94* (12), 3520-3528.
92. Tanner, D.; Fitzgerald, J. A.; Phillips, B. R., The Kevlar Story—an Advanced Materials Case Study. *Angewandte Chemie International Edition in English* **1989,** *28* (5), 649-654.
93. Sun, W.; Shah, S. A.; Lowery, J. L.; Oh, J. H.; Lutkenhaus, J. L.; Green, M. J., Lightweight Kevlar-Reinforced Graphene Oxide Architectures with High Strength for Energy Storage. *Advanced Materials Interfaces 0* (0), 1900786.
94. Yang, M.; Cao, K. Q.; Yeom, B.; Thouless, M. D.; Waas, A.; Arruda, E. M.; Kotov, N. A., Aramid nanofiber-reinforced transparent nanocomposites. *J Compos Mater* **2015,** *49* (15), 1873-1879.
95. Yang, M.; Cao, K.; Sui, L.; Qi, Y.; Zhu, J.; Waas, A.; Arruda, E. M.; Kieffer, J.; Thouless, M. D.; Kotov, N. A., Dispersions of aramid nanofibers: a new nanoscale building block. *ACS Nano* **2011,** *5* (9), 6945-54.
96. Lyu, J.; Wang, X. Z.; Liu, L. H.; Kim, Y.; Tanyi, E. K.; Chi, H.; Feng, W. C.; Xu, L. Z.; Li, T. H.; Noginov, M. A.; Uher, C.; Hammig, M. D.; Kotov, N. A., High Strength Conductive Composites with Plasmonic Nanoparticles Aligned on Aramid Nanofibers. *Adv Funct Mater* **2016,** *26* (46), 8435-8445.
97. Zhu, J.; Yang, M.; Emre, A.; Bahng, J. H.; Xu, L.; Yeom, J.; Yeom, B.; Kim, Y.; Johnson, K.; Green, P.; Kotov, N. A., Branched Aramid Nanofibers. *Angewandte Chemie* **2017,** *129* (39), 11906-11910.
98. Young, R. J.; Lu, D.; Day, R. J.; Knoff, W. F.; Davis, H. A., Relationship between structure and mechanical properties for aramid fibres. *Journal of Materials Science* **1992,** *27* (20), 5431-5440.
99. Cao, W. X.; Yang, L.; Qi, X. D.; Hou, Y.; Zhu, J. Q.; Yang, M., Carbon Nanotube Wires Sheathed by Aramid Nanofibers. *Advanced Functional Materials* **2017,** *27* (34), 1701061.
100. Patterson, B. A.; Malakooti, M. H.; Lin, J.; Okorom, A.; Sodano, H. A., Aramid nanofibers for multiscale fiber reinforcement of polymer composites. *Composites Science and Technology* **2018,** *161*, 92-99.
101. Weng, C.; Xing, T.; Jin, H.; Wang, G.; Dai, Z.; Pei, Y.; Liu, L.; Zhang, Z., Mechanically robust ANF/MXene composite films with tunable electromagnetic interference shielding performance. *Composites Part A: Applied Science and Manufacturing* **2020,** *135*, 105927.
102. Jeon, B. H.; Kim, S.; Choi, M. H.; Chung, I. J., Synthesis and characterization of polyaniline–polycarbonate composites prepared by an emulsion polymerization. *Synth. Met.* **1999,** *104* (2), 95-100.

103. Jeon, J.-W.; Kwon, S. R.; Li, F.; Lutkenhaus, J. L., Spray-On Polyaniline/Poly(acrylic acid) Electrodes with Enhanced Electrochemical Stability. *ACS Applied Materials & Interfaces* **2015,** *7* (43), 24150-24158.
104. MacDiarmid, A. G.; Epstein, A. J., The concept of secondary doping as applied to polyaniline. *Synth. Met.* **1994,** *65* (2), 103-116.
105. MacDiarmid, A. G.; Yang, L. S.; Huang, W. S.; Humphrey, B. D., Polyaniline: Electrochemistry and application to rechargeable batteries. *Synth. Met.* **1987,** *18* (1), 393-398.
106. Yun, J.; Echols, I.; Flouda, P.; Wang, S.; Easley, A.; Zhao, X.; Tan, Z.; Prehn, E.; Zi, G.; Radovic, M.; Green, M. J.; Lutkenhaus, J. L., Layer-by-Layer Assembly of Polyaniline Nanofibers and MXene Thin-Film Electrodes for Electrochemical Energy Storage. *ACS Applied Materials & Interfaces* **2019**.
107. Mike, J. F.; Lutkenhaus, J. L., Recent advances in conjugated polymer energy storage. *J. Polym. Sci., Part B: Polym. Phys.* **2013,** *51* (7), 468-480.

2. INTERFACIAL ENGINEERING OF REDUCED GRAPHENE OXIDE FOR ARAMID-ENABLED STRUCTURAL SUPERCAPACITORS*

2.1. Introduction

Recently, our group demonstrated, for the first time, the fabrication of reduced graphene oxide (rGO)/aramid nanofiber (ANF) nanocomposite paper electrodes for structural supercapacitors using vacuum-assisted filtration.[1] Extensive hydrogen bonding and π-π interactions between ANFs and rGO sheets were harnessed, resulting in high strength electrodes.[1] However, a trade-off between mechanical and electrochemical properties was observed, with the incorporation of ANFs leading to a 350% and 290% increase in Young's modulus and tensile strength, respectively, while slightly reducing the capacitance.[1] Although encouraging, these results led us to speculate that the mechanical properties might be improved even further without sacrificing energy storage through engineering the interfacial interactions between rGO sheets and ANFs.[2-5] However, studies of the interfacial engineering of rGO/ANF electrodes are still in an initial stage.

---

*Modified and reprinted with permission from "Interfacial Engineering of Reduced Graphene Oxide for Aramid Nanofiber-Enabled Structural Supercapacitors" by Paraskevi Flouda, Xueyan Feng, James G. Boyd, Edwin L. Thomas, Dimitris C. Lagoudas, and Jodie L. Lutkenhaus, *Batteries & Supercaps* 2019**,** *2* (5), 464-472, Copyright 2019, Wiley-VCH GmbH.

Here, we explore how functionalization (-COOH and $–NH_2$) of rGO sheets influences the mechanical and energy storage properties of rGO/ANF structural supercapacitor electrodes. ANFs and rGO sheets were selected as the structural components, whereas rGO sheets were used as the electrochemically active component. These two were processed into free-standing flexible electrodes using vacuum-assisted filtration, Figure 2.1. The hydrogen bonding interactions between the functional groups and the ANFs were examined using X-ray photoelectron spectroscopy (XPS). Electrodes of three different compositions (0 wt%, 10 wt%, and 25 wt% ANF) were characterized using tensile testing, cyclic voltammetry, and galvanostatic cycling to evaluate the mechanical and electrochemical properties. We discuss the results in the context of interfacial interactions and then we compare the trade-off using a multifunctional efficiency metric. These results favorably demonstrate that interfacial interactions can indeed improve mechanical properties, while still maintaining electrochemical activity.

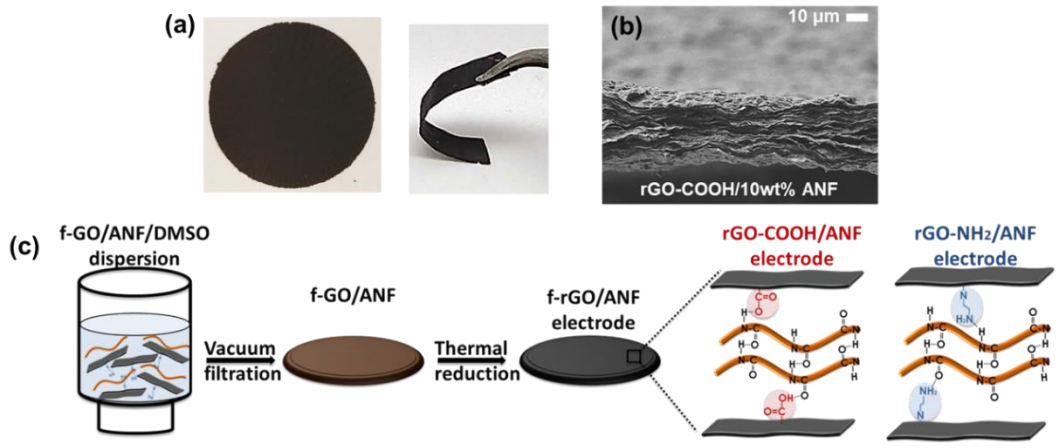

Figure 2.1 (a) Digital images and (b) cross-sectional scanning electron microscopy images for functionalized rGO (f-rGO)/ANF composite electrodes (c) Schematic representation

of the fabrication f-rGO/ANF composite electrodes. f-GO sheets were mixed with ANF in dimethylsulfoxide (DMSO), followed by vacuum filtration. The obtained f-GO/ANF electrodes were thermally reduced to yield f-rGO/ANF, where ANF interact with f-rGO through extensive hydrogen bonding and π-π stacking interactions.

2.2. Materials and Methods

Graphite (SP-1) and Kevlar®69 thread were purchased from Bay Carbon and Thread Exchange, respectively. Dimethyl sulfoxide (DMSO), potassium permanganate, and sodium nitrate were purchased from Sigma Aldrich. Potassium hydroxide (KOH) was provided by Amresco. Hydrobromic acid (HBr) and ethylenediamine were purchased from BDH. Oxalic acid and carbon paper were purchased by Alfa Aesar. Microporous poly(propylene) separator (Celgard 3501) was purchased from Celgard.

In dimethyl sulfoxide DMSO (500 ml), Kevlar®69 thread (1 g) and potassium hydroxide KOH (1.5 g) were added, followed by magnetic stirring for 14 days at room temperature.[6] A dark red dispersion of ANF/DMSO (2 mg/ml) was obtained. Graphene oxide was prepared using the modified Hummers method.[7] More specifically, in a cold solution of H_2SO_4 (120 ml), graphite powder (3 g) and $NaNO_3$ (2.5 g) were added. The mixture was stirred in an ice water bath for 5 hours. Next, $KMnO_4$ (15 g) was gradually added while the temperature was kept below 20 ^oC. Then, the mixture was heated at 35 ^oC for 2 h followed by the addition of of deionized water (250 ml). The mixture was diluted further with the addition of deionized water (700 ml) and stirred for 30 min. Subsequently, 30 wt% H_2O_2 (20 ml) was added and the color of the mixture turned black from green.

Finally, the mixture was washed with 5 wt% HCl solution, filtered through a Whatman filter paper (55 mm diameter and 2.5 μm pore size) and dialyzed to remove metal ions and acids. The resulting dispersion was dried overnight, and graphite oxide powder was obtained. The powder was dissolved in deionized water and ultrasonicated to exfoliate the graphene oxide sheets. Graphene oxide was then dispersed in water (2 mg/ml) and further sonicated. Solvent exchange was used to obtain a GO/DMSO dispersion.

To obtain GO functionalized with carboxylic acid groups (-COOH), GO (100 mg) was dispersed in de-ionized water (50 ml) and hydrobromic acid (6.67 ml) was added. The mixture was stirred vigorously for 24 h at room temperature. Then, oxalic acid (2 g) was added under magnetic stirring for 4 h at room temperature. The dispersion was filtrated, dried at 60 ^{o}C under vacuum overnight and re-dispersed in DMSO (1 mg/ml).[8, 9] To obtain GO functionalized with amine groups (-NH_2), ethylenediamine (300 mg) was dissolved in ethanol (50 ml) and added dropwise to an aqueous GO (100 ml of 2 mg/ml) dispersion. The mixture was stirred vigorously at room temperature for 24 h. The functionalized GO was isolated by filtration and washed three times with 1:1 (v/v) ethanol/water. The precipitate was dried in vacuum overnight at 60 ^{o}C and re-dispersed in DMSO (1 mg/ml).[10, 11]

Vacuum-assisted filtration was used to fabricate the f-GO/ANF composite films. The total mass of the film was held constant at 40 mg. ANF/DMSO dispersion (0.2 mg/ml) and f-GO/DMSO dispersion (1 mg/ml) at the desired amounts were stirred for 1 h. Then deionized water was added to the mixture and stirred further for 2 h at 80 ^{o}C in order to

reprotonate the amide groups of the ANFs. The mixture was vacuum-filtered on nylon filter membrane (47 mm diameter, 0.2 μm pore size). The resulting composite films were then rinsed with water, air-dried and dried at 80 ^{o}C in vacuum for 3 days. The films were thermally reduced at 200 ^{o}C in vacuum for 2 h to yield reduced f-GO/ANF composite films. During the reduction step, films were placed between glass slides and heavy tiles to prevent bubble formation. Finally, the free-standing films were cut into rectangular strips (2 mm x 20 mm) using a razor blade for tensile testing and circles of 16 mm in diameter by punching the films for electrochemical testing.

The morphology and thickness of the composite films were investigated using scanning electron microscopy (SEM) (JSM-7500F, JEOL and Helios). Raman spectra were obtained by a Horiba Jobin Yvon spectrometer with 514 nm excitation and XPS spectra by an Omicron ESCA Probe (Omicron Nanotechnology) with a monochromated Mg Ka radiation (hm = 1253.6 eV). XPS survey scans were performed with an analyzer pass energy of 100-1100 eV (1.0 eV steps, 50 ms dwell time), while high resolution scans of carbon (C1s) and nitrogen (N1s) were performed with a pass energy of 150 eV (0.05 eV steps, 200 ms dwell time). All spectra were calibrated with the C1s photoemission peak for sp^2-hybridized carbons at 284.5 eV and the FWHM was constrained. Curve fitting of C1s and N1s spectra was conducted using a Gaussian-Lorentzian peak shape after Shirley-type background correction.

Static uniaxial in-plane tensile tests and cyclic loading were performed using a dynamic mechanical analyzer (DMA Q800, TA Instruments). A film tension clamp with

a compliance of 1.8 μm/N was used. The tensile tests were conducted in controlled strain rate mode with a preload force of 0.02 N and a strain ramp rate of 0.1 %/min. The toughness was calculated from the area underneath the stress-strain curves up to the point of fracture. All tensile tests were conducted in room conditions (temperature: 22-25 ^{o}C and humidity: 40-50%).

Two electrode symmetric coin cells were used to evaluate the electrochemical performance of the composite films. The coin cells consisted of a top and bottom stainless-steel covering, two current collectors (carbon paper), two electrodes, the electrolyte (6M KOH), two spacers, a spring, and the separator (polypropylene). The electrochemical tests (cyclic voltammetry and galvanostatic charge/discharge) were conducted using a Gamry Potentiostat/Galvanostat Instrument (Gamry Interface 1000, Gamry Instruments). Cyclic voltammetry was conducted at various scan rates in a potential window of 0-1 V. The specific capacitance (F/g) of the electrode was calculated from cyclic voltammetry curve using the equation, $C = 2\cdot \frac{\int_{V-}^{V+} IdV}{v\cdot\Delta V\cdot M}$, where I is the current (A), V+ and V- the high and low voltage (V) cut-off respectively, M the total mass (g) of the two electrodes, ΔV the potential window, and v the scan rate. Galvanostatic charge/discharge tests were performed at variant current densities (A/g). The specific capacitance was calculated by the equation, $C = \frac{4\cdot I\cdot\Delta t}{M\cdot\Delta V}$, where Δt is the discharge time (s).

2.3. Results and Discussion

Graphene oxide (GO) prepared by the modified Hummers method was firstly reduced with hydrobromic acid (HBr) to open the epoxide groups (-O-) and convert them into hydroxyl groups (-OH).[12, 13] Subsequently, an esterification reaction took place by the introduction of oxalic acid that interacts with the -OH groups. The obtained functionalized GO (GO-COOH) contained -COOH not only on the edges but also on the basal planes.[8, 9] For the second functionalization, graphene oxide was reacted with ethylenediamine. The amine groups of ethylenediamine chemically graft to GO (GO-NH_2) *via* nucleophilic substitution reactions on the epoxide groups.[14] The carboxylic acid (–COOH) and amine (–NH_2) functionalizations lead to an increase in the d-spacing by ~1.7% and ~14.6%, respectively.[8-10, 15]

Successful functionalizations were verified using Raman spectroscopy and XPS. Raman spectra of GO, GO-COOH, and GO-NH_2 are shown in Figure 2.2. Characteristic D and G bands were observed at 1352 and 1600 cm^{-1}, respectively. The D band is associated with defects leading to sp^3-hybridized carbon atoms, whereas the G band arises from the in-plane bond stretching vibration of sp^2-hybridized carbon atoms.[16, 17] The relative intensity of the two bands (I_D/I_G) reveals the amount of disorder. The relative intensity I_D/I_G for GO was 1.09, while the value for GO-COOH was 1.19. The increase of the D/G ratio indicates the introduction of defects during –COOH functionalization.[18] The D/G ratio for GO-NH_2 also increased, but only slightly (1.12) indicating that

ethylenediamine reacted with the epoxide groups on the surface of GO without significantly affecting the aromatic carbon-carbon bonds.[18]

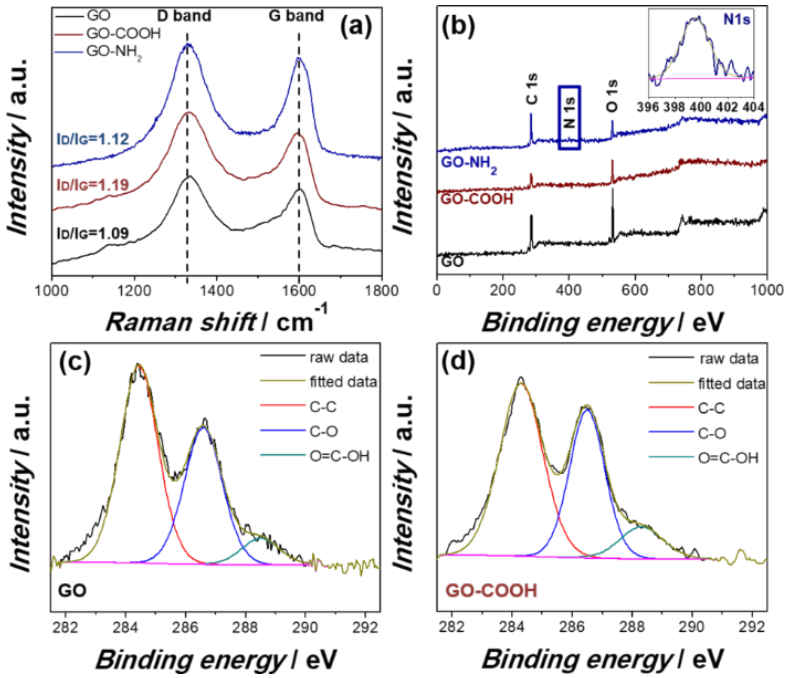

Figure 2.2 (a) Raman spectra and (b) XPS survey scans of GO, GO-COOH, and GO-NH_2. The inset shows the high resolution N1s peak for GO-NH_2. High resolution XPS spectra for the C1s peak for (c) GO and (d) GO-COOH.

Functionalization was also confirmed using XPS. Figure 2.2b illustrates the XPS survey scans of GO, GO-COOH, and GO-NH_2. GO had 74 atomic percent (at%) carbon and 26 at% oxygen to yield a C/O ratio of 2.85. In GO-COOH the C/O ratio decreased to 2.20, whereas in GO-NH_2 the C/O ratio increased to 4.91, while an N1s peak (2.5 at%) appeared at 399.9 eV (Figure 2.2b, inset), indicating the successful -NH_2 modification. Moreover, the C1s XPS spectrum for GO (Figure 2.2c) shows three distinct peaks at 284.5,

286.6 and 288.7 eV attributed to sp^2-hybridized carbon, C-O and -COOH groups, respectively.[19] In GO-COOH (Figure 2.2d), the peak attributed to the carboxylic acid groups (-COOH) slightly increased from 7.4% to 9.8%, indicating the successful addition of the -COOH groups. From here, we generically term GO-NH_2 and GO-COOH as functionalized GO (f-GO),

f-GO/ANF electrodes of varying compositions were fabricated using vacuum filtration, Figure 2.1. Desired amounts of ANF/DMSO and f-GO/DMSO dispersions were mixed and stirred together, followed by the addition of water and vacuum filtration. The addition of water serves to reprotonate the ANF amide bonds, leading to extensive hydrogen bonding with the oxygen-containing and/or the amine functional groups on f-GO.[20] Moreover, ANFs and f-GO interact with each other through π-π interactions between ANF's aromatic rings and f-GO graphitic basal planes.[21, 22]

The as-prepared f-GO/ANF composite films were reduced thermally at 200 ^{o}C under vacuum for 2 h to yield functionalized reduced graphene oxide (f-rGO). Cross-sectional SEM images of f-rGO/10 wt% ANF composite films revealed a highly layered and compact structure, Figure 2.3. The films containing functionalized rGO exhibited a slightly wavy morphology and had thicknesses varying from 8 to 15 μm. ANFs were not directly observed from the cross-sectional SEM images due to their small size and low content. To observe the ANFs, high resolution cross-sectional SEM was conducted on rGO/25 wt% ANF films after tensile testing, Figure 2.3d, which shows ANFs spanning the fracture surfaces of the electrode.

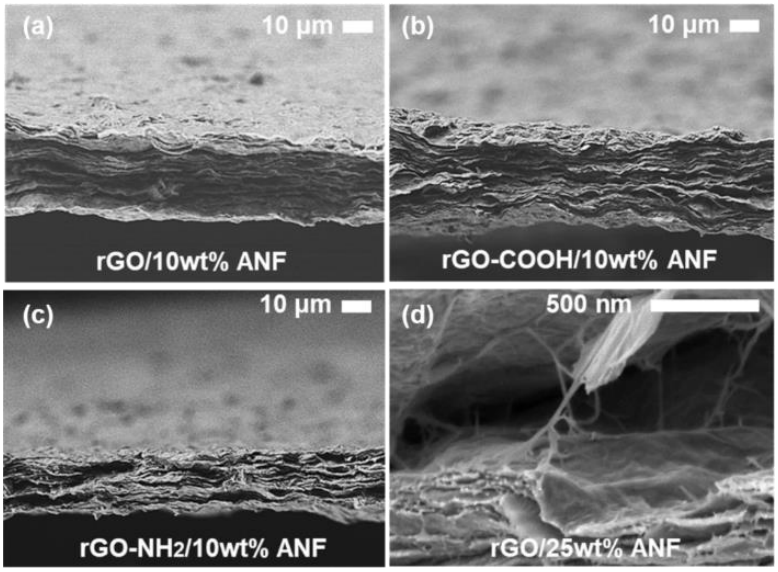

Figure 2.3 Low magnification cross-sectional SEM images of (a) rGO/10 wt% ANF, (b) rGO-COOH/10 wt% ANF, and (c) rGO-NH_2/10 wt% ANF. High resolution cross-sectional SEM image of (d) rGO/25 wt% ANF after tensile testing. Both wavy rGO platelets and taut load bearing ~10 nm diameter ANF adhering and spanning the rGO layers are evident.

Reduction was verified using Raman spectroscopy and XPS of rGO/10 wt% ANF, rGO-COOH/10 wt% ANF, and rGO-NH_2/10 wt% ANF composite films. The characteristic D and G bands were observed for all three cases (Figure 2.4a, 2.4b, and 2.4c). After thermal reduction the D/G ratio increased from 1.07 to 1.19 for rGO/10 wt% ANF, 1.15 to 1.23 for rGO-COOH/10 wt% ANF, and 1.01 to 1.03 for rGO-NH_2/10 wt% ANF. The increased D/G ratio is derived from the smaller, newly created sp^2-hybridrized graphitic domains upon reduction.[23]

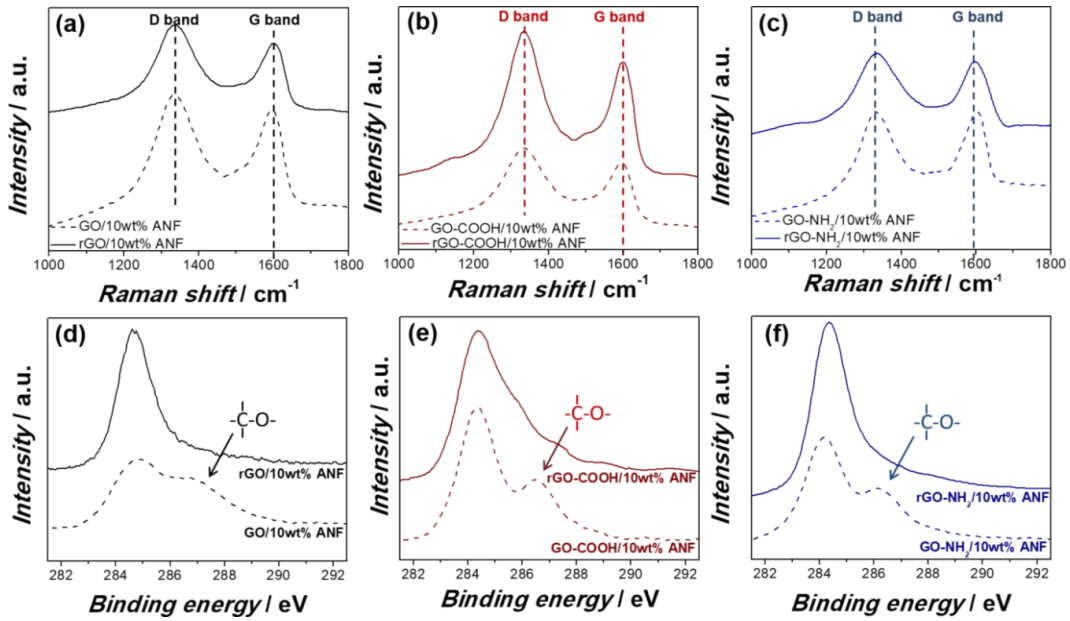

Figure 2.4 Raman spectra of (a) GO/10 wt% ANF and rGO/10 wt% ANF, (b) GO-COOH/10 wt% ANF and rGO-COOH/10 wt% ANF, and (c) GO-NH_2/10 wt% ANF and rGO-NH_2/10 wt% ANF. High resolution XPS spectra for the C1s peak for (d) GO/10 wt% ANF and rGO/10 wt% ANF, (e) GO-COOH/10 wt% ANF and rGO-COOH/10 wt% ANF, and (f) GO-NH_2/10 wt% ANF and rGO-NH_2/10 wt% ANF.

Figures 2.4d-2.4f show the C1s high resolution spectra for the composite films before and after reduction. Before reduction, two distinct peaks were observed, corresponding to the sp^2-hybridized carbon atoms (284.5 eV) and the oxygen-containing functional groups (286.1 eV). After thermal reduction, the peak assigned to the oxygen-containing functional groups disappeared, indicating the successful reduction.[24] XPS was also utilized to verify that the previously added functional groups remained grafted on GO even after reduction. For rGO-COOH/10 wt% ANF, the deconvolution of the C1s peak

was necessary to determine the ratio of the carboxylic acid (–COOH) groups after reduction. The C1s peak was deconvoluted to C-C (284.5 eV), C-N/C-O (286.1 eV), N-C=O (287.8 eV), O=C-OH (289 eV), and π-π interactions (291 eV).[1] It was found that the amount of carboxylic acid (-COOH) groups for rGO-COOH/10 wt% ANF (5.6%) was higher than rGO/10 wt% ANF (3.4%) (Figure 2.5). Moreover, 4.78 at% nitrogen was found in rGO-NH_2/10 wt% ANF composite films, whereas only 1.25 at% nitrogen was apparent in the rGO/10 wt% ANF films, indicating that after reduction the amine functional groups remained grafted on GO.

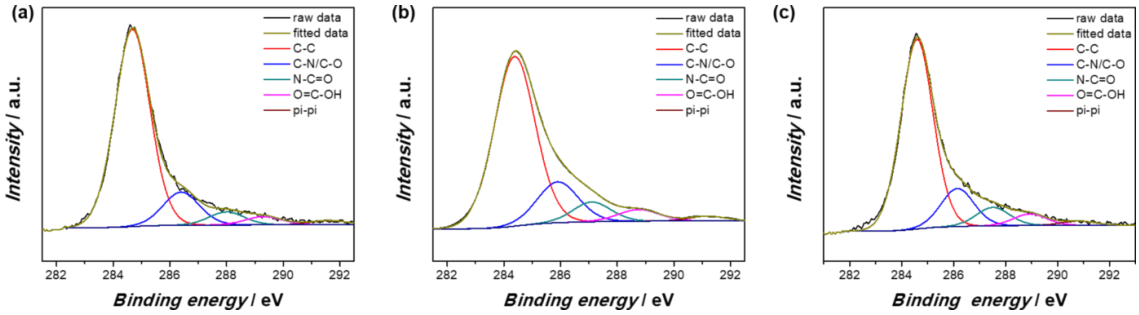

Figure 2.5 High resolution C1s peak XPS spectra for (a) rGO/10 wt% ANF, (b) rGO-COOH/10 wt% ANF, and (c) rGO-NH_2/10 wt% ANF.

We hypothesized that hydrogen bonding would be enhanced through the introduction of –COOH and –NH_2 groups to the rGO sheets. Evidence of hydrogen bonding was confirmed from the high resolution N1s spectra for the composite films (Figure 2.6). Two peaks were observed, the amide peak N-C=O at 399.9 eV and a second peak at 401.8 eV attributed to hydrogen bonding interactions between the ANF amide

bonds and the oxygen-containing and/or amine groups of f-GO.[25] Moreover, a slight increase in the hydrogen bonding peak was apparent with functionalization, indicating the enhancement of hydrogen bonding interactions due to the addition of functional groups such as -COOH and -NH_2, confirming the extensive non-covalent interactions between rGO and ANFs.

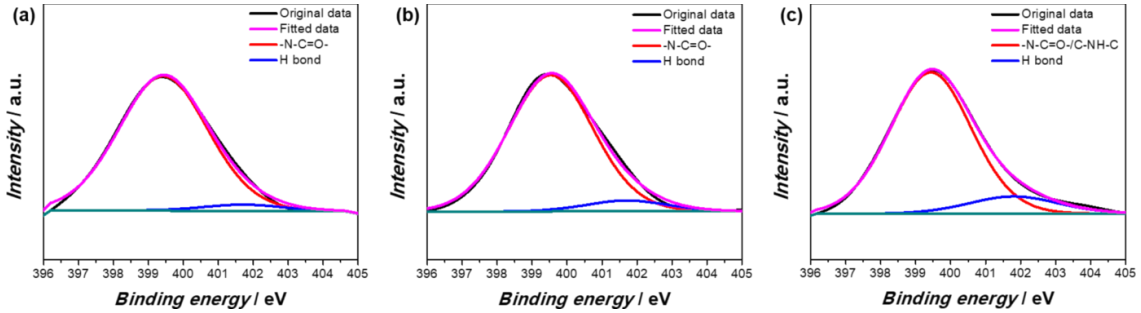

Figure 2.6 High resolution N1s spectra for (a) rGO/10 wt% ANF, (b) rGO-COOH/10 wt%, and (c) rGO-NH_2/10 wt% ANF.

To better understand the reinforcement effect, the mechanical properties of the rGO/ANF, rGO-COOH/ANF and rGO-NH_2/ANF composite films were evaluated (Figure 2.7). Stress-strain curves typically exhibited three regimes: initial (E_i), straightening (E_s), and "elastic" (E_e).[26, 27] The initial and straightening regions are attributed to straightening geometric wrinkles and structural sliding of the reduced functionalized graphene sheets to adopt a more favorable structure. This behavior was apparent in the composite electrodes, as shown in Figure 2.7a.

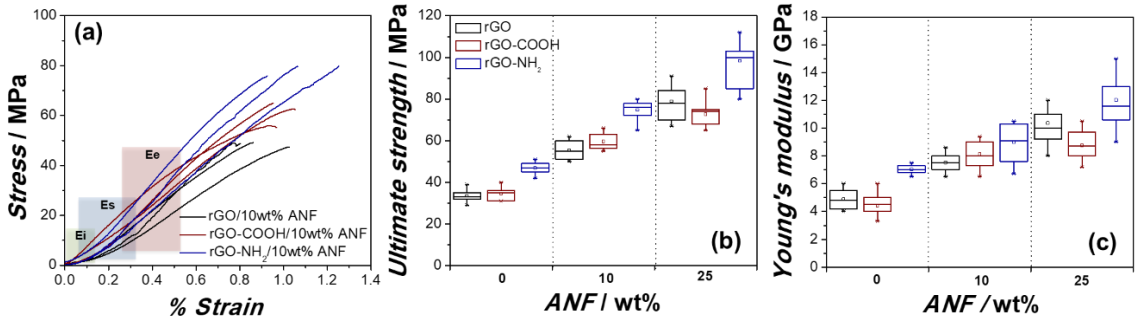

Figure 2.7 (a) Typical stress-strain curves of rGO/10 wt% ANF, rGO-COOH/10 wt% ANF, and rGO-NH_2/10 wt% ANF. Three regimes were observed: initial (E_i), straightening (E_s), and "elastic" (E_e), labeled in green, blue, and red, respectively. Box plots of (b) ultimate tensile strength and (c) Young's modulus. The rectangular shapes extend from the first to the third quartile. The open squares represent the mean, whereas the lines inside the rectangular shapes represent the median. The whiskers indicate the maximum and minimum values. Each box corresponds to 12-15 data points.

The ultimate tensile strength and Young's modulus increased significantly with ANF content for all three cases, Figure 2.7b and 2.7c. The Young's modulus of rGO/25 wt% ANF was 9.9 ± 2.0 GPa, 115% higher than the Young's modulus of pure rGO films (4.8 ± 1.2 GPa), as calculated from the "elastic" regimes. The ultimate tensile strength and toughness also increased by 139% (from 33 ± 6.2 to 79 ± 12.1 MPa) and 172% (from 123 ± 30.0 to 335 ± 105 kJ/m^3), respectively. The enhancement of the mechanical properties is attributed to the increased hydrogen bonding and the π-π interactions that facilitate load transfer between the reduced graphene oxide sheets and the 2D randomly oriented ANFs.

The reported values are comparatively lower from our previous studies since the tests were conducted at different strain rates. As shown in Figure 2.8, f-rGO/ANF films exhibited strong strain rate dependency. At lower strain rates there is more time for the f-rGO sheets to slide and to reform hydrogen bonds, leading to lower stiffness and higher energy absorption.[28]

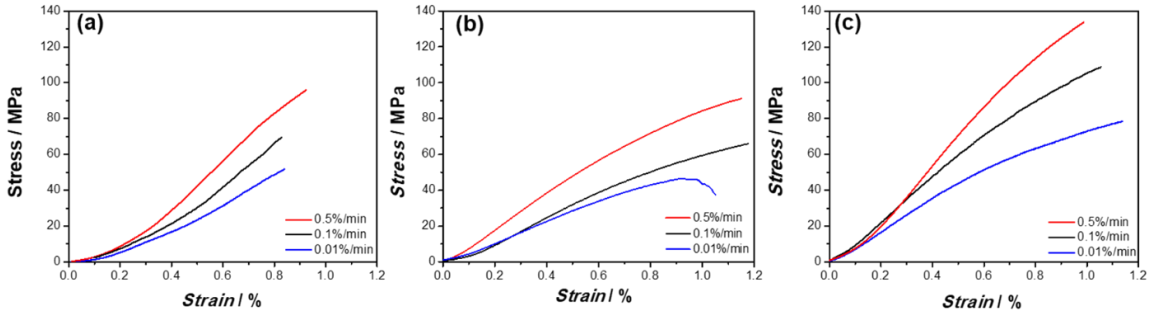

Figure 2.8 Strain rate dependency tests for (a) rGO/25 wt% ANF, (b) rGO-COOH/25 wt% ANF, and (c) rGO-NH_2/25 wt% ANF.

Furthermore, the effect of functionalization with carboxylic acid (–COOH) and amine (-NH_2) functional groups was compared. rGO-COOH composite electrodes exhibited a slightly worse performance that resulted from two competing mechanisms. More specifically, the functionalization of GO with carboxylic acid (-COOH) groups led to enhanced hydrogen bonding with the ANF amide groups but also led to a decrease in the stiffness of the functionalized GO sheets due to the introduction of defects, as shown previously from the Raman and XPS spectra.[29] Amine (-NH_2) functionalized electrodes exhibited a better mechanical performance as a result of the enhanced hydrogen bonding

interactions and not as harsh functionalization process. The stiffness and ultimate strength increased by 18% (12.2 ± 3.0 GPa) and 24% (98 ± 18 MPa) for the rGO-NH_2/25 wt% ANF electrodes, respectively, when compared to the non-functionalized electrodes of the same composition. Moreover, a remarkable amelioration on toughness was observed, with the toughness increasing by 119% (732 ± 232 kJ/m^3). The improvement on toughness can be attributed to two main mechanisms. On the one hand, energy dissipates to break the extensive hydrogen bonding at the interface, but on the other hand, hydrogen bonds reform which then facilitate increased extensibility.[20] Overall, the addition of ANFs and the amine (-NH_2) functionalization of the graphene sheets (rGO *vs.* rGO-NH_2/25 wt% ANF) led to increases in Young's modulus, ultimate tensile strength, and toughness by 154%, 197%, and 495%, respectively.

Cyclic loading experiments were performed on all electrodes with a composition of 25 wt% ANF, Figure 2.9. An increase in the stiffness after 4 cycles was observed for all three cases. Repeated cyclic loading at small forces (0.15 Nt) under slow rates (0.2 Nt/min) allows the functionalized graphene sheets to slide and lock so that they "mechanically anneal" to the energetically favorable structure.[26] Stiffness of the non-functionalized electrodes did not change significantly for the same number of cycles, whereas the stiffness for rGO-COOH/25 wt% and rGO-NH_2/25 wt% increased by 24% (10.9 GPa) and 44% (17.6 GPa), respectively, with cycling loading. These results show that small mechanical perturbations allow the hydrogen bonding interactions to reconfigure to adopt more favorable interactions, leading to enhanced stiffness. This

mechanism explains the strain-stiffening behavior of the functionalized samples following cycling loading.

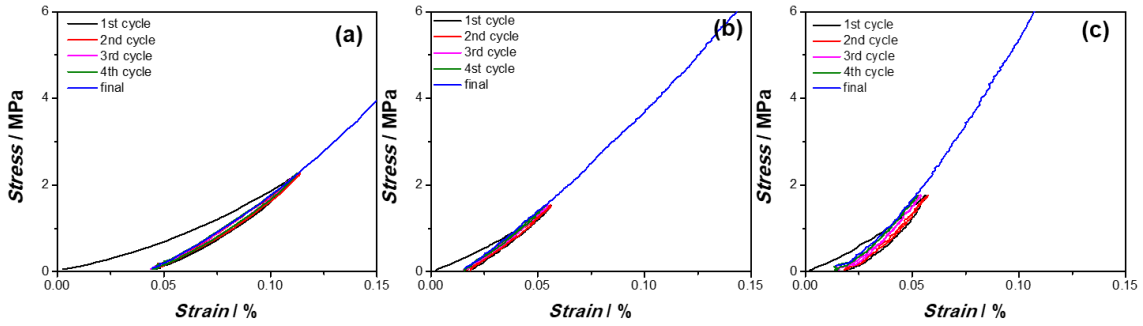

Figure 2.9 Cycling loading for (a) rGO/25 wt% ANF, (b) rGO-COOH/25 wt% and (c) rGO-NH_2/25 wt% ANF.

The electrochemical performance of the composite electrodes was evaluated using cyclic voltammetry and galvanostatic cycling. Two-electrode symmetric coin cells were assembled and 6M KOH was used as the electrolyte. Cyclic voltammetry was performed at varying scan rates from 1 to 100 mV/s for each electrode type and the results are depicted in Figure 2.10a. The obtained cyclic voltammograms exhibited a rectangular shape indicating an ideal capacitive behavior where energy is stored through the formation of an electric double layer.[30]

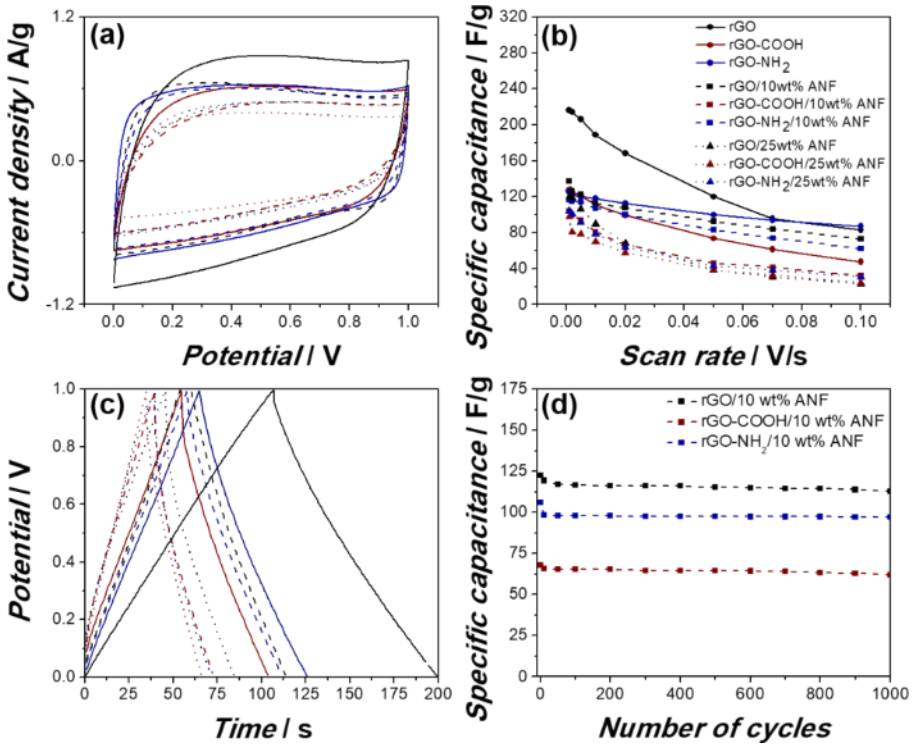

Figure 2.10 (a) CV curves of rGO, rGO-COOH and rGO-NH_2 composite electrodes at 20 mV/s. (b) Specific capacitance *vs.* scan rate. (c) Galvanostatic charge/discharge curves of rGO, rGO-COOH and rGO-NH_2 composite electrodes at a current density of 0.5 A/g. The legend in (b) also applies to (a) and (c). (d) Cycling behavior of rGO, rGO-COOH, and rGO-NH_2 composite electrodes up to 1000 cycles at 0.5 A/g.

The specific capacitance for each electrode was calculated at different scan rates, as shown in Figure 2.10b. The specific capacitance decreased with the addition of ANF for all electrodes, since ANFs are electrochemically inactive. The highest values of specific capacitance for the rGO, rGO/10 wt% ANF and rGO/25 wt% ANF electrodes were 216, 138 and 120 F/g at 1 mV/s, respectively. Moreover, functionalized composite

electrodes exhibited diminished performance compared to non-functionalized electrodes. The lowest values of specific capacitance were obtained for the rGO-COOH electrodes with specific capacitances of 127, 104, and 98 F/g, for compositions of 0 wt%, 10 wt%, and 25 wt% ANF at 1 mV/s, respectively. rGO-NH_2 composite electrodes exhibited a slightly better performance with specific capacitances of 126, 116, and 104 F/g for the same compositions at 1 mV/s. The decrease in specific capacitance can be attributed to the introduction of defects during the functionalization step.

Galvanostatic cycling was also performed at 0.5 A/g, Figure 2.10c. The galvanostatic charge/discharge tests were in agreement with the results obtained by cyclic voltammetry, with a decreasing specific capacitance with ANF content. The specific capacitances were 187, 122, and 82 F/g for rGO, rGO/10 wt% ANF, and rGO/25 wt% ANF electrodes, respectively. Whereas, the electrodes with the same compositions for the rGO-COOH case exhibited specific capacitances of 98, 68, and 60 F/g. Similarly, rGO-NH_2, composite electrodes had specific capacitances of 122, 106, and 62 F/g. The iR drop was 70 mV for rGO/10 wt% ANF, 180 mV for rGO-COOH/10wt% ANF, and 80 mV for rGO-NH_2/10 wt%, following the same trend with the specific capacitance. Similar trends with ANF composition and functionalization were made from the Ragone plots (Specific energy *vs.* specific power and energy density *vs.* power density), as shown in Figure 2.11. Furthermore, prolonged cycling up to 1000 cycles was performed on the composite electrodes containing 10 wt% ANF, Figure 2.10d. All electrodes exhibited excellent stability as a result of the extensive hydrogen bonding. The specific capacitance of the

rGO/10 wt% ANF electrode retained 92% of the initial specific capacitance after 1000 cycles. In comparison, the rGO-COOH/10 wt% ANF and rGO-NH_2/10 wt% ANF retained 90% and 92% of the initial capacitance.

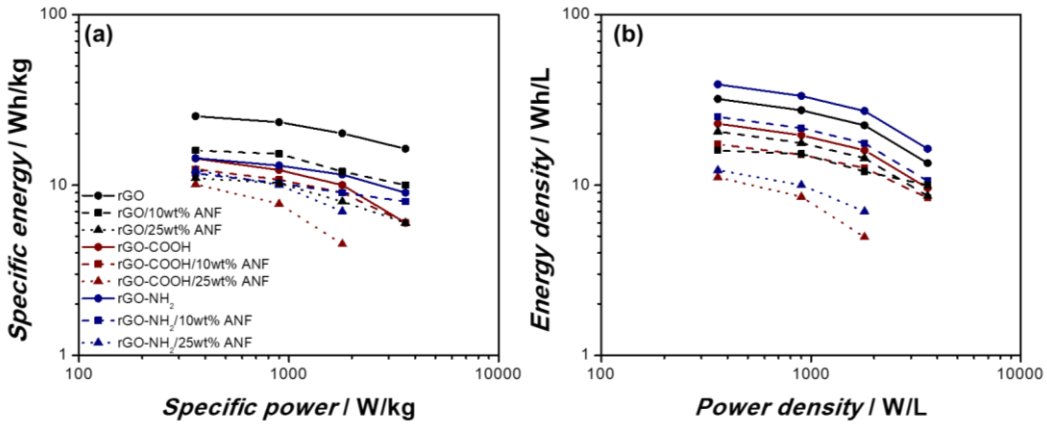

Figure 2.11 Ragone plot of (a) specific energy (Wh/kg) *vs.* specific power (W/kg) and (b) energy density (Wh/L) *vs.* power density (W/L). Legend in panel (a) also applies in panel (b).

In order to visualize the multifunctional nature of the composite electrodes, an Ashby plot of the specific capacitance *vs.* ultimate strength *vs.* Young's modulus of our results compared against other free-standing structural electrodes from the literature was constructed, Figure 2.12a. The plot includes multi- and single- walled carbon nanotube (MWCNT and SWCNT) buckypapers, rGO/MnO_2, rGO/MnO_2/CNTs, polypyrrole (Ppy)/rGO, rGO-cellulose, and SWCNT-Ppy-cyanate ester (CE).[1, 31, 32] It can be observed that f-rGO/ANF electrodes exhibit a good combination of mechanical and electrochemical properties compared to other carbon-based structural electrodes. Even though, other

electrodes, such as rGO/MnO_2/CNT, Ppy/rGO, and SWCNT-Ppy-CE, displayed higher specific capacitance, the f-rGO/ANF electrodes exhibited higher ultimate tensile strength with similar or even higher Young's modulus values. This is attributed to the extensive hydrogen bonding and π-π interactions between the functionalized graphene sheets and ANFs. Moreover, a trade-off between the mechanical and electrochemical properties is apparent. Specifically, increasing the ANF content improves the mechanical properties at the expense of the specific capacitance. It was also observed that the functionalization of the graphene oxide sheets affected this trade-off. More specifically, the rGO-NH_2/ANF electrodes displayed enhanced mechanical performance due to the enhanced hydrogen bonding at the cost of the electrochemical performance because of the introduction of defects in the rGO sheets.

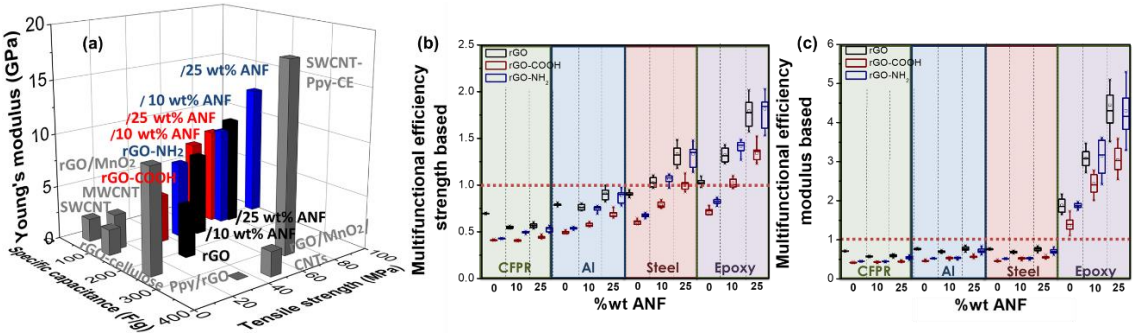

Figure 2.12 (a) Ashby plot of specific capacitance *vs.* ultimate strength *vs.* Young's modulus. Grey bars correspond to data obtained from the literature, black bars to rGO composites, red bars to rGO-COOH composites, and blue bars to rGO-NH_2 composite electrodes. (b) Multifunctional efficiency (strength based) and (c) multifunctional efficiency (Young's modulus based) for four different structural benchmark materials.

This trade-off can be better demonstrated by the multifunctional efficiency.[33-35] The multifunctional efficiency (n_{mf}) is expressed as the summation of the energy (n_e) and the structural (n_s) efficiencies:

$$n_{mf} \equiv n_e + n_s > 1 \text{ where } n_e = \frac{\bar{\Gamma}_{mf}}{\bar{\Gamma}} \text{ and } n_s = \frac{\bar{E}_{mf}}{\bar{E}} \text{ or } n_s = \frac{\overline{UTS}_{mf}}{\overline{UTS}} \quad (2.1)$$

where $\bar{\Gamma}$, $\bar{E}$, and $\overline{UTS}$ are the specific energy, specific Young's modulus, and specific tensile strength of the monofunctional/conventional device, respectively, whereas $\bar{\Gamma}_{mf}$, $\bar{E}_{mf}$, and $\overline{UTS}_{mf}$ are the same quantities for the multifunctional system. In order to obtain savings in mass and volume the multifunctional efficiency (n_{mf}) should be higher than unity.[33-35]

Here, the multifunctional efficiency was calculated using carbon aerogel (specific energy 12.5 Wh/kg) as the monofunctional energy storage material.[36, 37] The structural efficiency was calculated for four different monofunctional structural materials: carbon fiber reinforced epoxy (specific Young's modulus of 43.75 GPa cm^3/g and specific tensile strength of 375 MPa cm^3/g),[38] aluminum (specific Young's modulus of 25.5 GPa cm^3/g and specific tensile strength of 153.7 MPa cm^3/g),[39] steel (specific Young's modulus of 26.5 GPa cm^3/g and specific tensile strength of 88.5 MPa cm^3/g),[40] and epoxy (specific Young's modulus of 2.8 GPa cm^3/g and specific tensile strength of 60.18 MPa cm^3/g).[1] All four materials are currently used in automobile and aerospace applications. Figure 2.12b demonstrates that the f-rGO/ANF multifunctional electrodes have the potential to be employed in such applications as multifunctional/structural electrodes leading to mass and volume savings for steel or epoxy.

2.4. Conclusions

Structural electrodes for supercapacitors containing ANFs and reduced functionalized graphene sheets were fabricated using vacuum filtration to exploit the extensive hydrogen bonding interactions between the ANF amide groups and the –COOH or $–NH_2$ groups on f-rGO through interfacial engineering. The addition of ANFs, as well as the functionalization of GO led to a compromise between the mechanical and electrochemical properties. An improvement of 115%, 140%, and 170% in Young's modulus, ultimate tensile strength, and toughness was achieved by the incorporation of ANF to the pure rGO composite electrodes, whereas the specific capacitance decreased (~45%). Functionalization with $-NH_2$ groups also led to an enhancement in the mechanical properties, with the Young's modulus, ultimate tensile strength, and toughness increasing by 18%, 24%, and 120%, compared to pure rGO/ANF films. In all cases, the capacitance was affected by the functionalization. This was attributed to two competing mechanisms, the enhanced hydrogen bonding interactions *vs.* the introduction of defects during functionalization. The introduction of defects disrupts the sp^2-hybridized network of carbon atoms leading to lower f-rGO sheet stiffness and conductivity. Overall, the addition of ANF and the amine ($-NH_2$) functionalization of the graphene oxide sheets (rGO *vs.* rGO-NH_2/25 wt% ANF) gave the best mechanical improvement; Young's modulus, ultimate tensile strength and toughness increased by 150%, 200%, and 500%, respectively. The f-rGO/ANF supercapacitors exhibited a good combination of mechanical and electrochemical properties compared to other state-of-the-art carbon-based structural

electrodes. This was further demonstrated by the multifunctional efficiency that was above unity, suggesting the potential of these structural electrodes in real-life applications, such as in the transportation, satellites, or aircraft.

2.5. References

1. Kwon, S. R.; Harris, J.; Zhou, T.; Loufakis, D.; Boyd, J. G.; Lutkenhaus, J. L., Mechanically Strong Graphene/Aramid Nanofiber Composite Electrodes for Structural Energy and Power. *ACS Nano* **2017,** *11* (7), 6682-6690.
2. Wagner, H. D.; Vaia, R. A., Nanocomposites: issues at the interface. *Materials Today* **2004,** *7* (11), 38-42.
3. Fu, S.-Y.; Feng, X.-Q.; Lauke, B.; Mai, Y.-W., Effects of particle size, particle/matrix interface adhesion and particle loading on mechanical properties of particulate–polymer composites. *Composites Part B: Engineering* **2008,** *39* (6), 933-961.
4. Palermo, V.; Kinloch, I. A.; Ligi, S.; Pugno, N. M., Nanoscale Mechanics of Graphene and Graphene Oxide in Composites: A Scientific and Technological Perspective. *Advanced Materials* **2016,** *28* (29), 6232-6238.
5. Chhetri, S.; Adak, N. C.; Samanta, P.; Mallisetty, P. K.; Murmu, N. C.; Kuila, T., Interface engineering for the improvement of mechanical and thermal properties of covalent functionalized graphene/epoxy composites. *Journal of Applied Polymer Science* **2018,** *135* (15), 46124.
6. Yang, M.; Cao, K.; Sui, L.; Qi, Y.; Zhu, J.; Waas, A.; Arruda, E. M.; Kieffer, J.; Thouless, M. D.; Kotov, N. A., Dispersions of aramid nanofibers: a new nanoscale building block. *ACS Nano* **2011,** *5* (9), 6945-54.
7. Hummers, W. S.; Offeman, R. E., Preparation of Graphitic Oxide. *Journal of the American Chemical Society* **1958,** *80* (6), 1339-1339.
8. Liu, Y.; Deng, R. J.; Wang, Z.; Liu, H. T., Carboxyl-functionalized graphene oxide-polyaniline composite as a promising supercapacitor material. *Journal of Materials Chemistry* **2012,** *22* (27), 13619-13624.
9. Fang, X.; Liu, X.; Cui, Z.-K.; Qian, J.; Pan, J.; Li, X.; Zhuang, Q., Preparation and properties of thermostable well-functionalized graphene oxide/polyimide composite films with high dielectric constant, low dielectric loss and high strength via in situ polymerization. *Journal of Materials Chemistry A* **2015,** *3* (18), 10005-10012.
10. Bourlinos, A. B.; Gournis, D.; Petridis, D.; Szabó, T.; Szeri, A.; Dékány, I., Graphite Oxide: Chemical Reduction to Graphite and Surface Modification with Primary Aliphatic Amines and Amino Acids. *Langmuir* **2003,** *19* (15), 6050-6055.
11. Georgakilas, V.; Otyepka, M.; Bourlinos, A. B.; Chandra, V.; Kim, N.; Kemp, K. C.; Hobza, P.; Zboril, R.; Kim, K. S., Functionalization of Graphene: Covalent and Non-Covalent Approaches, Derivatives and Applications. *Chemical Reviews* **2012,** *112* (11), 6156-6214.

12. He, H.; Klinowski, J.; Forster, M.; Lerf, A., A new structural model for graphite oxide. *Chemical Physics Letters* **1998,** *287* (1), 53-56.
13. Dreyer, D. R.; Park, S.; Bielawski, C. W.; Ruoff, R. S., The chemistry of graphene oxide. *Chemical Society Reviews* **2010,** *39* (1), 228-240.
14. Loh, K. P.; Bao, Q.; Ang, P. K.; Yang, J., The chemistry of graphene. *Journal of Materials Chemistry* **2010,** *20* (12), 2277-2289.
15. Yan, J.-l.; Chen, G.-j.; Cao, J.; Yang, W.; Xie, B.-h.; Yang, M.-b., Functionalized graphene oxide with ethylenediamine and 1,6-hexanediamine. *Carbon* **2013,** *52*, 624.
16. Shen, J.; Hu, Y.; Shi, M.; Lu, X.; Qin, C.; Li, C.; Ye, M., Fast and Facile Preparation of Graphene Oxide and Reduced Graphene Oxide Nanoplatelets. *Chemistry of Materials* **2009,** *21* (15), 3514-3520.
17. Tuinstra, F.; Koenig, J. L., Raman Spectrum of Graphite. *The Journal of Chemical Physics* **1970,** *53* (3), 1126-1130.
18. Kudin, K. N.; Ozbas, B.; Schniepp, H. C.; Prud'homme, R. K.; Aksay, I. A.; Car, R., Raman Spectra of Graphite Oxide and Functionalized Graphene Sheets. *Nano Letters* **2008,** *8* (1), 36-41.
19. Yang, D.; Velamakanni, A.; Bozoklu, G.; Park, S.; Stoller, M.; Piner, R. D.; Stankovich, S.; Jung, I.; Field, D. A.; Ventrice, C. A.; Ruoff, R. S., Chemical analysis of graphene oxide films after heat and chemical treatments by X-ray photoelectron and Micro-Raman spectroscopy. *Carbon* **2009,** *47* (1), 145-152.
20. Xu, L.; Zhao, X.; Xu, C.; Kotov, N. A., Water-Rich Biomimetic Composites with Abiotic Self-Organizing Nanofiber Network. *Advanced Materials* **2018,** *30* (1), 1703343-n/a.
21. Potts, J. R.; Dreyer, D. R.; Bielawski, C. W.; Ruoff, R. S., Graphene-based polymer nanocomposites. *Polymer* **2011,** *52* (1), 5-25.
22. Ghislandi, M.; Tkalya, E.; Schillinger, S.; Koning, C. E.; de With, G., High performance graphene- and MWCNTs-based PS/PPO composites obtained via organic solvent dispersion. *Composites Science and Technology* **2013,** *80*, 16-22.
23. Eda, G.; Fanchini, G.; Chhowalla, M., Large-area ultrathin films of reduced graphene oxide as a transparent and flexible electronic material. *Nature Nanotechnology* **2008,** *3*, 270.
24. Park, S.; An, J.; Potts, J. R.; Velamakanni, A.; Murali, S.; Ruoff, R. S., Hydrazine-reduction of graphite- and graphene oxide. *Carbon* **2011,** *49* (9), 3019-3023.
25. Byon, H. R.; Lee, S. W.; Chen, S.; Hammond, P. T.; Shao-Horn, Y., Thin films of carbon nanotubes and chemically reduced graphenes for electrochemical micro-capacitors. *Carbon* **2011,** *49* (2), 457-467.
26. Park, S.; Lee, K.-S.; Bozoklu, G.; Cai, W.; Nguyen, S. T.; Ruoff, R. S., Graphene Oxide Papers Modified by Divalent Ions—Enhancing Mechanical Properties via Chemical Cross-Linking. *ACS Nano* **2008,** *2* (3), 572-578.
27. Dikin, D. A.; Stankovich, S.; Zimney, E. J.; Piner, R. D.; Dommett, G. H. B.; Evmenenko, G.; Nguyen, S. T.; Ruoff, R. S., Preparation and characterization of graphene oxide paper. *Nature* **2007,** *448*, 457.

28. Xu, L.; Zhao, X.; Xu, C.; Kotov, N. A., Water-Rich Biomimetic Composites with Abiotic Self-Organizing Nanofiber Network. *Adv. Mater* **2018,** *30* (1), 1703343-n/a.
29. Wang, G.; Dai, Z.; Liu, L.; Hu, H.; Dai, Q.; Zhang, Z., Tuning the Interfacial Mechanical Behaviors of Monolayer Graphene/PMMA Nanocomposites. *ACS Appl. Mater. Interfaces* **2016,** *8* (34), 22554-62.
30. Stoller, M. D.; Ruoff, R. S., Best practice methods for determining an electrode material's performance for ultracapacitors. *Energy & Environmental Science* **2010,** *3* (9), 1294-1301.
31. Cheng, Y.; Lu, S.; Zhang, H.; Varanasi, C. V.; Liu, J., Synergistic Effects from Graphene and Carbon Nanotubes Enable Flexible and Robust Electrodes for High-Performance Supercapacitors. *Nano Letters* **2012,** *12* (8), 4206-4211.
32. Lee, W. S. V.; Peng, E.; Choy, D. C.; Xue, J. M., Mechanically robust glucose strutted graphene aerogel paper as a flexible electrode. *Journal of Materials Chemistry A* **2015,** *3* (37), 19144-19147.
33. Brien, D. J. O.; Baechle, D. M.; Wetzel, E. D., Design and performance of multifunctional structural composite capacitors. *Journal of Composite Materials* **2011,** *45* (26), 2797-2809.
34. O'Brien, D. J.; Baechle, D. M.; Wetzel, E. D., Performance Metrics for Structural Composite Capacitiors. **2010,** (44168), 215-221.
35. Baechle, D.; O'Brien, D.; Wetzel, E. In *STRUCTURAL DIELECTRICS FOR MULTIFUNCTIONAL CAPACITORS*, Proc. of SPIE Vol, pp 69292L-1.
36. Zhang, L. L.; Zhao, X. S., Carbon-based materials as supercapacitor electrodes. *Chemical Society Reviews* **2009,** *38* (9), 2520-2531.
37. Qu, D.; Shi, H., Studies of activated carbons used in double-layer capacitors. *Journal of Power Sources* **1998,** *74* (1), 99-107.
38. Soutis, C., Fibre reinforced composites in aircraft construction. *Progress in Aerospace Sciences* **2005,** *41* (2), 143-151.
39. Suganuma, K.; Fujita, T.; Suzuki, N.; Niihara, K., Aluminium composites reinforced with a new aluminium borate whisker. *Journal of Materials Science Letters* **1990,** *9* (6), 633-635.
40. Ledbetter, H., Stainless-steel elastic constants at low temperatures. *Journal of Applied Physics* **1981,** *52* (3), 1587-1589.

3. HIGHLY MULTIFUNCTIONAL DOPAMINE-FUNCTIONALIZED REDUCED GRAPHENE OXIDE SUPERCAPACITORS*

3.1. Introduction

Nature-inspired materials could transform the poor mechanical properties of supercapacitor electrodes into those mimicking nacre, bone, or wood to realize exceptionally high values of multifunctional efficiency. The most widely accepted strategy for improving the mechanical performance of reduced graphene oxide (rGO) nacre-mimicking structures, such as the 'brick and mortar' rGO/aramid nanofiber (ANF) composites presented in the previous chapter, is by functionalizing rGO or adding a third component to improve the adhesion between the 'hard' rGO and the 'soft' polymeric phase. Dopamine - known as a hormone and a neurotransmitter - comprises an attractive candidate due to its ability to functionalize GO and self-polymerize into the highly adhesive polymer, poly(dopamine) (PDA).[1-3] More specifically, dopamine is a molecule mimicking the structure of adhesive proteins in mussels and owes its adhesive properties to the catechol and amine functional groups. PDA was first reported as a coating material in 2007 and since then has been of great interest as a tool to modify surfaces due to its incredible adhesive properties.[4-6]

---

*Reprinted with permission from "Highly Multifunctional Dopamine-Functionalized Reduced Graphene Oxide Supercapacitors" by Paraskevi Flouda, Smit A. Shah, Dimitris C. Lagoudas, Micah J. Green and Jodie L. Lutkenhaus, *Matter* 2019, *1* (6), 1532-1546, Copyright 2019, Elsevier

PDA has been utilized in Li-ion batteries and supercapacitors as an electrode material, separator modifier, and binder. PDA-coated FWNTs (53 wt% PDA) Li-ion battery electrodes exhibited a capacity of 133 mAh/g resulting from the double layer capacitance of the FWNTs and redox-reactions of PDA.[7] PDA has also been used to modify traditional polyethylene separators for enhanced hydrophilicity while restraining the Li dendrite formation in Li-ion batteries.[8] PDA, used as a shell to encapsulate Si nanoparticles forming a 'yolk-shell' structure, allowed for large volumetric expansion of Si during lithiation/de-lithiation due to PDA's intrinsic elasticity.[9] The reports on battery systems have demonstrated PDA's redox activity, good cycling, and thermal stability. However, the performance of PDA in high power, energy systems with sub-second charging and longer cycle life such as supercapacitors is under-examined. As for supercapacitors, GO-PDA/poly(3,4-ethylenedioxythiophene) (PEDOT) and PDA/MnO_2 composites exhibited enhanced specific capacitance of 126 F/g and 193 F/g, respectively.[10, 11]

To date, only a handful of studies have focused on incorporating PDA in rGO composites. For example, rGO/PDA composites exhibited a tensile strength of ~205 MPa and Young's modulus of ~6 GPa, which corresponds to a 75% and 140% improvement compared to the pure rGO films.[1] The mechanical properties of the rGO/PDA composites can be further improved by the addition of metal ions (Ca^{2+}, Cu^{2+}, Mn^{2+}, etc.) as the catechol groups of poly(dopamine) interact with metal ions through coordination and chelation bonding interactions.[4] Furthermore, graphene oxide is also known to chelate with metal ions.[12, 13] This has been demonstrated by the addition of Ni^{2+} ions on rGO/PDA

composites. The nanocomposites exhibited a tensile strength of ~420 MPa and Young's modulus of ~4 GPa.[14] From this prior work, it is clear that dopamine modification can enhance mechanical properties, but dopamine has not yet been investigated for enhancing the multifunctional efficiency parameter in energy storage devices.

We sought to combine the excellent mechanical properties of PDA-modified rGO with high-modulus, high-tensile strength Kevlar® aramid nanofiber for the first time to improve the multifunctional efficiency. Aramid nanofibers are obtained by the deprotonation of the aramid chains (poly(*p*-phenylene terephthalamide) (PPTA)) of Kevlar® using a base in an aprotic environment.[15] ANFs have been used in a variety of applications including energy storage.[16-24, 25-28] ANF/Poly(3,4-ethylenedioxythiophene):poly(styrene sulfonate) (PEDOT:PSS) electrodes exhibited specific capacitance of 112 F/g, Young's modulus of 5 GPa, and tensile strength of 76 MPa.[24] Last year, branched aramid nanofibers (BANFs) were first reported and were shown to bear further improved mechanical properties over ANFs.[29] The use of BANFs in structural as well as in energy storage applications is still unexplored due to their very recent development.

Here, we explore bio-inspired rGO-BANF structural electrodes modified with dopamine (rGO-DOPA) and divalent ions. Dopamine functionalization and Ca^{2+} ions were used to improve the interfacial interactions between rGO sheets and BANFs through hydrogen bonding and chelation. The composite electrodes were fabricated utilizing vacuum filtration to achieve a nacre-like 'brick-and-mortar' structure. The interactions between dopamine-functionalized rGO and BANFs were proven using X-ray

photoelectron spectroscopy, Raman, and X-ray diffraction. Structural electrodes containing 10 and 25 wt% BANF were investigated using tensile testing, cyclic voltammetry and galvanostatic charge-discharge, and were compared to pure rGO (no BANFs) electrodes. Comparisons with literature show that this approach yields structural electrodes of exceptionally high modulus, tensile strength, and multifunctional efficiency. This work shows that mechanical properties for structural electrodes may be greatly improved by using a nature-inspired structure (brick-and-mortar, nacre-like) and nature-inspired chemistries (dopamine).

3.2. Materials and Methods

Kevlar®69 thread and graphite (SP-1) were purchased from Thread Exchange and Bay Carbon, respectively. Potassium hydroxide (KOH), dimethyl sulfoxide (DMSO), potassium permanganate ($KMnO_4$), sulfuric acid (H_2SO_4), and sodium nitrate ($NaNO_3$) were purchased from Sigma Aldrich. Carbon paper and dopamine hydrochloride were purchased by Alfa Aesar. Celgard 3501separator was purchased from Celgard.

Chopped bulk Kevlar® thread (0.5 g) was dissolved in DMSO (50 ml) and KOH (0.5 g). The mixture was stirred for 7 days at room temperature and a dark red viscous dispersion of 10 mg/ml BANF/DMSO was obtained.[29] The modified Hummers method was used to synthesize graphene oxide.[30] Graphite powder (3 g) was dissolved in H_2SO_4 (120 ml) and $NaNO_3$ (2.5 g), followed by stirring for 5h in a cold ice bath. Subsequently, $KMnO_4$ (15 g) was slowly added and the temperature was set below 20 ^oC. The mixture was stirred for 2h at 35 ^oC, followed by the addition of deionized water (250 ml). Then, deionized water (700 ml) was added, and the mixture was stirred for 30 more min. In

addition, 30 wt% H_2O_2 (20 ml) was added and as a result the original green mixture turned black. The dispersion was washed with 5 wt% HCl aqueous solution, filtered using a porous membrane (Whatman filter paper, 55 mm diameter and 2.5 μm pore size) and dialyzed. Finally, the dispersion was dried overnight in a vacuum oven at 60 ^oC to obtain graphite oxide powder. The graphite oxide powder was dissolved in deionized water followed by ultrasonication. To obtain GO/DMSO dispersion, solvent exchange was performed.

Desired amounts of dopamine hydrochloride were added to 50 ml Tris Buffer (pH = 8.5) and stirred vigorously for 15 min. Then, the mixture was mixed with a 2 mg/ml GO dispersion, followed by magnetic stirring and heating at 60 ^oC for 24h.[1, 3] Finally, the mixture was washed and filtered with water:ethanol (1:1 v/v mixture), and the resulting powder was dried under vacuum overnight at 60 ^oC. GO-DOPA powder was then dispersed in DMSO to yield a 1 mg/ml dispersion.

The composite electrodes were fabricated using vacuum filtration, and the total solids mass was kept constant at 40 mg. Desired amounts of GO/DMSO or GO-DOPA/DMSO and BANF/DMSO were mixed together for 1 h. The mixture was then heated at 80 ^oC and stirred for 2h. During this step, deionized water was added to reprotonate the BANF amide groups. The resulting mixture was filtered using a nylon membrane (diameter: 47 mm and pore size: 0.2 μm). $CaCl_2$ was added (10 ml of 0.2 mmol) while the films were still wet.[12] The films were peeled off the nylon membrane, rinsed with deionized water, air dried and dried in a vacuum oven for 3 days at 80 ^oC. Finally,

the composite films were thermally reduced at 200 ^{o}C under vacuum while heavy tiles were used to avoid the formation of bubbles.

Chemical characterization was conducted using X-ray photoelectron spectroscopy (XPS). The XPS spectra were obtained using an Omicron ESCA Probe with a monochromated Mg Kα radiation. The survey scans were conducted using a pass energy of 100-1100 eV with steps of 1.0 eV and 50 ms dwell time. High resolution scans were conducted at a pass energy of 150 eV with steps of 0.05 eV and 500 ms dwell time. A Shirley-type background correction was applied, and curve fitting was performed using a Gaussian-Lorentzian peak shape. The electrodes were further characterized using scanning electron microscopy (SEM) (JSM-7500F, JEOL). Dispersions of BANFs (0.02 mg/ml) drop-cast on mica were investigated using atomic force microscopy (AFM), (Nanoscope IIIa, Digital Instruments) in tapping mode. Thermogravimetric analysis (TGA) was conducted using a TGA Q50 analyzer. The samples were heated at a rate of 10 ^{o}C/min, isothermally held at 80 ^{o}C for 2 h, followed by heating to 700 ^{o}C. X-ray diffraction (XRD) measurements were conducted using a Bruker D8 X-ray diffractometer (Cu Ka, λ = 1.541 Å) with 2θ range 5^{o} – 50^{o}. UV-Vis was conducted using Shimazu SolidSpec-3700 over a wavelength of 250-800 nm.

Tensile tests were conducted using a dynamic mechanical analyser (DMA Q800, TA Instruments). The tests were conducted using film tension clamps with a torque force of 1.6 μm/N, a strain rate of 0.1 %/min, and a preload force of 0.02 N. The tests were conducted under lab room conditions (temperature: 22-25 ^{o}C and humidity: 55-60%). The Young's modulus was calculated from the slope of the "linear" regimes and the toughness

was calculated from the area underneath the stress-strain curves until failure. The ultimate tensile strength was defined as the strength at failure.[12]

Cyclic voltammetry and galvanostatic charge/discharge tests were conducted using a Gamry Potensiostat/Galvanostat Instrument (Gamry Interface 1000, Gamry Instruments). Two-electrode symmetric coin cells were used with 6M KOH as the electrolyte. The coin cells consisted of two stainless steel coverings, two spacers, a spring, two carbon paper current collectors, the two electrodes (mass loading: 1.5 - 2 mg/cm^2) and a Celgard separator. Cyclic voltammetry (CV) was performed at a voltage window of 0-1V at variant scan rates (1-100 mV/s). The CV curves were used to calculate the specific gravimetric capacitance at different scan rates ($C = 2\cdot \frac{\int_{V-}^{V+} IdV}{v\cdot\Delta V\cdot M}$, where I is the current, V+ and V- the high and low potential cut-off respectively, v the scan rate, M the total mass of the two electrodes, and ΔV the voltage window). Galvanostatic charge/discharge tests (CCCD) were performed at a voltage window of 0-1V at variant current densities (0.1-2 A/g). The CCCD curves were used to calculate the specific gravimetric capacitance at different current densities ($C = \frac{4\cdot I\cdot\Delta t}{M\cdot\Delta V}$, where Δt is the discharge time).

3.3. Results and Discussion

Aqueous dispersions of graphene oxide (GO) were mixed with dopamine in a basic solution (pH = 8.5). The amine groups of dopamine react with the epoxide groups of the basal planes of GO to yield dopamine-functionalized GO (GO-DOPA). Moreover, the dopamine molecules self-polymerize under weak alkaline environments to yield poly(dopamine).[4] GO-DOPA was mixed with BANFs to fabricate composite films using

vacuum filtration, followed by the addition of Ca^{2+} ions and thermal reduction. rGO-DOPA interacts with BANFs through hydrogen bonding interactions, while the Ca^{2+} ions cause chelation between the rGO-DOPA flakes. Qualitatively it was observed that rGO-DOPA/BANF/Ca^{2+} exhibited good tensile strength capabilities with highly layered structures with, as shown in Figure 3.1a and 3.1b, respectively. Figure 3.1c illustrates the structure of the obtained electrodes.

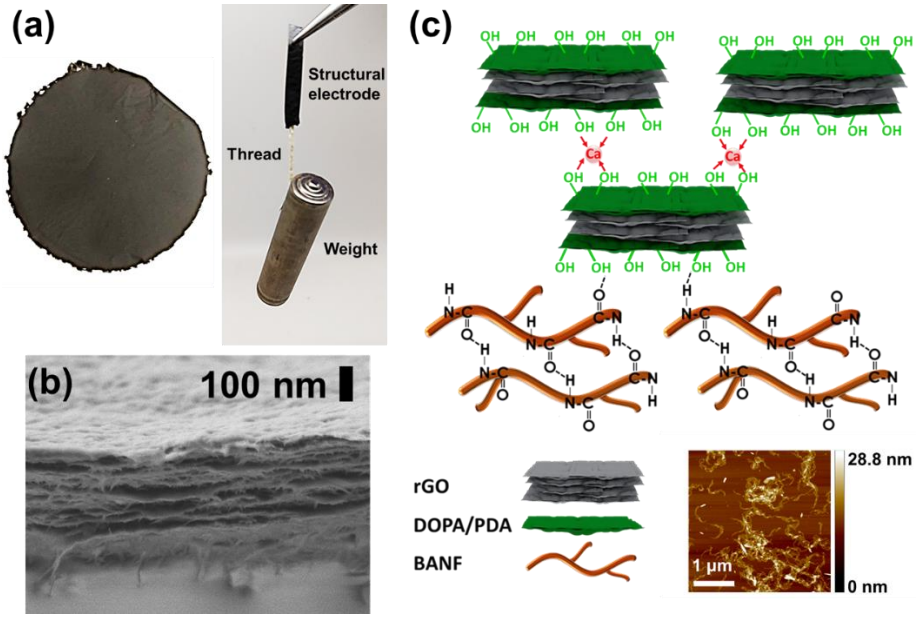

Figure 3.1 (a) Digital images and (b) cross-sectional scanning electron microscopy images of rGO-DOPA/BANF/Ca^{2+} electrodes. (c) Schematic representation of the structure of the structural electrodes. Inset shows an atomic force microscope phase image of BANFs drop-cast on mica.

Raman spectroscopy and X-ray photoelectron spectroscopy (XPS) were utilized to verify the dopamine functionalization. Figure 3.2a illustrates the Raman spectra of GO

and GO-1wt% DOPA, where the wt% DOPA indicates the composition at the functionalization step. The relative intensity of the two bands (I_D/I_G) indicates the amount of disorder as the D band (1350 cm^{-1}) results from the sp^3-hybridized carbon atoms and the G band (1600 cm^{-1}) from the sp^2-hybridized carbon atoms.[31-33] Dopamine functionalization caused a decrease in I_D/I_G from 1.09 to 0.89 due to the partial reduction of the GO sheets induced by the dopamine polymerization.[4] The XPS survey scans for GO and GO-1 wt% DOPA (Figure 3.2b) were used to calculate the C/O ratio. More specifically, GO exhibited a C/O ratio of 2.9, while GO-1wt% DOPA had a C/O ratio of 3.9 and a N1s peak appeared at 399.9 eV resulting from the dopamine functionalization.

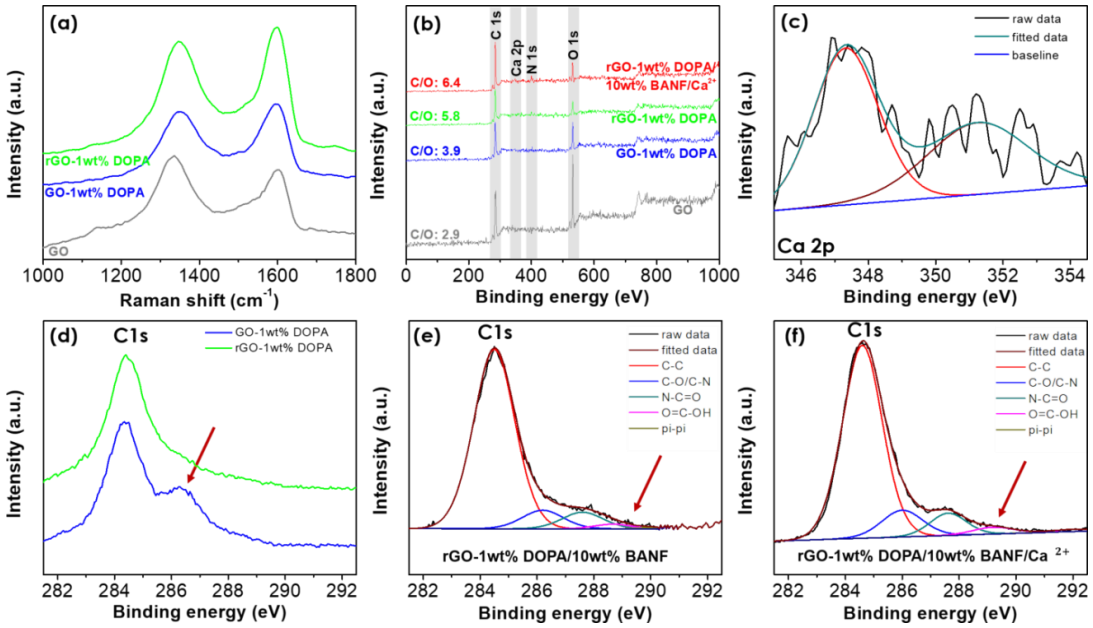

Figure 3.2 (a) Raman spectra and (b) XPS survey scans of GO, GO-1 wt% DOPA, rGO-1 wt% DOPA, and rGO-1 wt% DOPA/10 wt% BANF/Ca^{2+}. (c) High resolution XPS spectra for Ca 2p peak for rGO-1 wt% DOPA/10 wt% BANF/Ca^{2+}. High resolution XPS spectra for the C1s peak for (d) GO-1 wt% DOPA and rGO-1 wt% DOPA, (e) rGO-1 wt%

DOPA/10 wt% BANF and (f) rGO-1 wt% DOPA/10 wt% BANF/Ca^{2+}. The arrow indicates the O=C-OH peak.

Dispersions of GO-DOPA/DMSO and BANF/DMSO were mixed together while deionized water was added to reprotonate the BANF amide bonds. This leads to extensive hydrogen bonding between the BANF amide bonds and the dopamine hydroxyl groups as well as the oxygen-containing groups of graphene oxide.[4, 18] Additionally, BANFs interact with GO-DOPA through π-π stacking interactions between the BANF backbone and the GO-DOPA basal planes.[26] GO-DOPA and BANFs were processed into free-standing films using vacuum-assisted filtration. Finally, metal ion modification was employed by passing an aqueous $CaCl_2$ solution through the pre-made composites under vacuum to avoid any uncontrollable agglomeration of the sheets due to the cross-linking of the dopamine functionalized graphene sheets by the Ca^{2+} ions.[12]

Thermal reduction was performed to restore the sp^2-hybridized carbon atoms and improve the electrode's conductivity.[34] Cross-sectional SEM images of the reduced dopamine functionalized graphene oxide (rGO-DOPA) electrodes revealed the 'brick-and-mortar' morphology, as shown in Figure 3.3. The thickness of the non-functionalized composite electrodes was 10-15 μm, while the dopamine functionalized electrodes were consistently thinner (rGO-DOPA/BANF: 5-9 μm and rGO-DOPA/BANF/Ca^{2+}: 2-5 μm). Figure 3.3b-3.3g shows cross-sections of the electrodes after tensile testing and electrochemical testing.

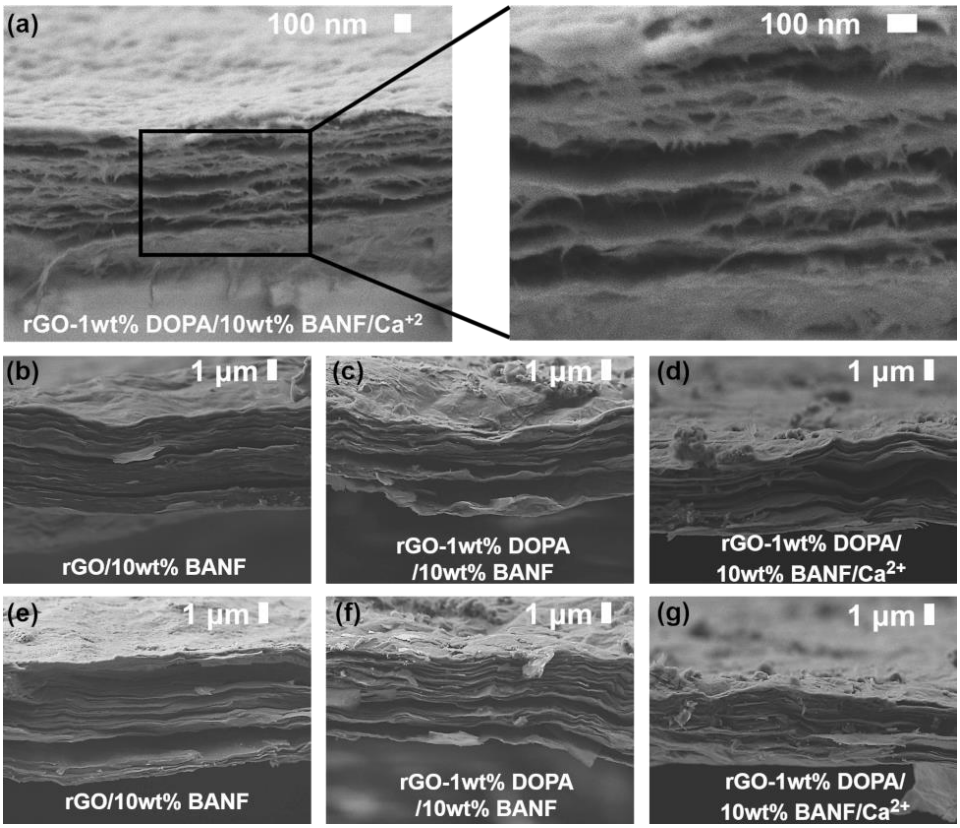

Figure 3.3 (a) High resolution cross-sectional SEM images of rGO-1 wt% DOPA/10 wt% BANF/Ca^{2+}. Cross-sectional SEM images after (b, c, d) tensile testing for the composite electrodes and (e, f, g) electrochemical testing.

Thermal reduction was confirmed using Raman and XPS for rGO-1 wt% DOPA (no BANFs). The relative intensity (I_D/I_G) slightly increased from 0.89 to 0.92, indicating the successful reduction, as shown in Figure 3.2a.[35] This was also confirmed from the C/O ratio which increased from 3.9 to 5.8 as calculated from the XPS survey scans (Figure 3.2b). Moreover, the C1s high resolution spectra exhibited two peaks at 284.5 eV and 286.1 eV attributed to the sp^2-hybridized carbon atoms and the oxygen-containing functional groups, respectively (Figure 3.2d).[36] Reduction caused the disappearance of the

second peak.[37] The N1s peak was still apparent after reduction indicating that dopamine molecules were not reduced from the GO sheets.

XPS of rGO/10 wt% BANF and rGO-1 wt% DOPA/10 wt% BANF was utilized to explore the interactions between rGO-DOPA and the BANFs. These materials interact through π-π stacking interactions between the rGO-DOPA basal planes and the BANF aromatic rings, as shown by the pi-pi contribution to the C1s peak in Figure 3.2e. Moreover, hydrogen bonding was observed from the high resolution N1s peak, Figure 3.4. The N1s peak was deconvoluted into two peaks at 399.9 eV and 401.6 eV, attributed to the BANF amide groups and the hydrogen bonding interactions, respectively.[25]

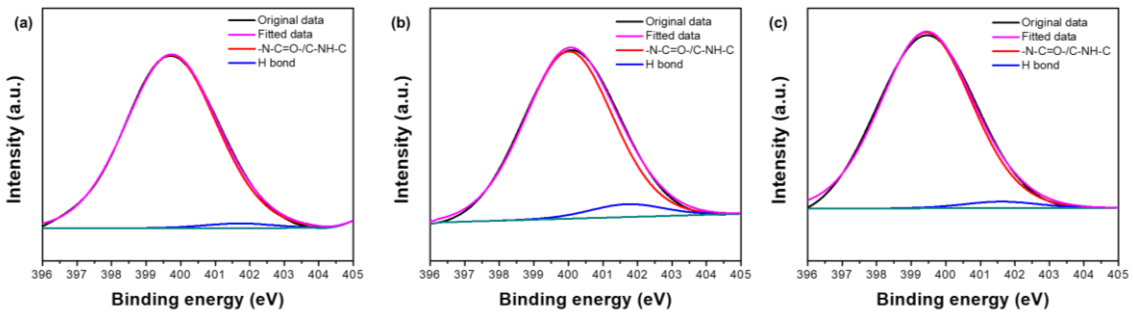

Figure 3.4 High resolution N1s peak XPS spectra for (a) rGO/10 wt% BANF, (b) GO-1 wt% DOPA/10 wt% BANF, and (c) rGO-1 wt% DOPA/10 wt% BANF/Ca^{2+}.

XPS of rGO-1 wt% DOPA/10 wt% BANF/Ca^{2+} (Figure 3.2a and Figure 3.2c) revealed the existence of a small amount of Ca^{2+} (0.5 at%), indicating the successful addition of the Ca^{2+} ions. The addition of Ca^{2+}ions was also verified from thermogravimetric analysis (TGA). Moreover, the high resolution C1s peak (Figure 3.2e and 3.2f) revealed a small shift of the -COOH peak from 288.7 eV to 289.1 eV, suggestive

of chelation and the formation of coordination bonding.[12, 14] The Ca^{2+} ions chelate with the carboxylic acid groups of rGO, bridging the edges of the functionalized graphene sheets and also interacting through weak alkoxide or dative bonds with the carbonyl and hydroxyl groups of rGO and the dopamine catechol groups.[38]

X-ray diffractograms revealed a decrease in d-spacing as a result of the dopamine functionalization and Ca^{2+} addition, Figure 3.5. The decrease in d-spacing indicates that the GO sheets stack to form flakes. Dopamine functionalizes mainly the external sheets of the flakes that are rich in oxygen-containing groups, as there was no evidence of intercalation by dopamine. The addition of Ca^{2+} leads to a further decrease in d-spacing.[39]

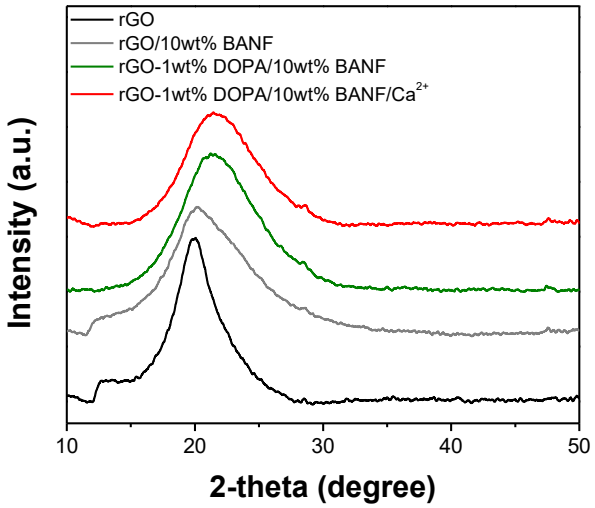

Figure 3.5 XRD diffractograms for rGO, rGO /10wt% BANF, rGO-1wt% DOPA/10wt% BANF, and rGO-1wt% DOPA/10wt% BANF/Ca^{2+}.

The mechanical properties of the composite electrodes were evaluated using uniaxial tensile testing, as shown in Figure 3.6. The addition of BANFs led to an increase in ultimate tensile strength and Young's modulus. More specifically, the ultimate tensile

strength and the Young's modulus of rGO/25 wt% BANF was 100 ± 11 MPa and 11 ± 2 GPa, which is ~200% and ~120% higher than the pure rGO (no BANFs) electrodes, respectively. This improvement results from the hydrogen bonding interactions between the BANF amide bonds and the rGO oxygen-containing groups, as well as the π-π stacking interactions between the BANF aromatic rings and the rGO basal planes. These interactions mitigate the load transfer from the rGO sheets to the stiff BANFs.[26]

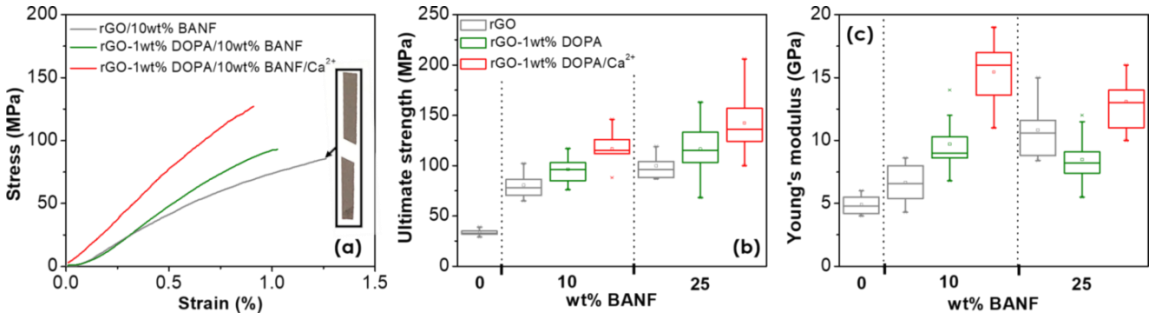

Figure 3.6 (a) Stress-strain curves of rGO/10 wt% BANF, rGO-1 wt% DOPA/10 wt% BANF, and rGO-1 wt% DOPA/10 wt% BANF/Ca^{2+}. Inset shows the sample after tensile testing. Box plots of (b) ultimate tensile strength, and (c) Young's modulus. The boxes extend from the first to third quartile, while the whiskers extend from the minimum to the maximum values. The lines inside the boxes represent the median and the internal open squares the mean.

rGO was functionalized with three different dopamine loadings (0.5 wt%, 1 wt%, and 2.5 wt%) to determine the loading that leads to the best mechanical properties for this system. This was necessary since a low loading may not result in the anticipated improvement and high loadings can lead to a deterioration of the mechanical performance

due to possible aggregation of the BANFs at the dopamine rich locations. A loading of 1 wt% DOPA was selected since these samples exhibited the best mechanical properties (ultimate tensile strength and Young's modulus). Only rGO-1 wt% DOPA electrodes with 10 wt% BANF and 25 wt% BANF were fabricated since the fabrication of pure rGO-DOPA electrodes (no BANFs) was unsuccessful due to the strong adhesion of the electrodes to the Nylon filter membrane. The ultimate tensile strength and Young's modulus of the rGO-1 wt% DOPA/10 wt% BANF was 96 ± 12 MPa and 10 ± 2 GPa, respectively, which is ~20% and ~60% higher than the same properties of the rGO/10 wt% BANF electrodes. The enhancement is attributed to the enhanced hydrogen bonding interactions due to the dopamine functionalization and the hydrogen bonded poly(dopamine) chains that act as a bridge and facilitate load transfer between rGO-DOPA and BANF. [1, 14] Increased addition of BANFs led to a slight decrease in Young's modulus due to possible BANF aggregation with the dopamine/poly(dopamine) molecules.

Next, the effect of the addition of divalent ions was investigated. rGO-1 wt% DOPA/10 wt% BANF/Ca^{2+} exhibited an ultimate tensile strength of 117 ± 17 MPa and a Young's modulus of 15 ± 3 GPa, which corresponded to a ~45% and ~60% enhancement compared to the rGO-1 wt% DOPA/10 wt% BANF electrodes. In total, rGO-1wt% DOPA/10 wt% BANF/Ca^{2+} exhibited enhanced ultimate tensile strength and Young's modulus of ~255% and ~220% compared to the pure rGO (no BANFs) electrodes. While ultimate tensile strength and Young's modulus increased, toughness and ultimate tensile strain were not significantly impacted. Therefore, the enhanced mechanical performance results from the dynamic hydrogen bonding and coordination bonding that can break and

reform within the timescale of the experiment.[12, 18] This clearly demonstrates the strong effects of non-covalent interactions on the mechanical properties of these electrodes.

Additionally, tensile testing on electrolyte-wetted electrodes was conducted (Figure 3.7a). The electrodes were soaked overnight in 6M KOH and the electrolyte uptake was 170-200 wt%. Tensile strength and Young's modulus decreased while ultimate tensile strain increased for all cases. rGO (no BANFs) exhibited the larger decrease in tensile strength (~ 46 %) and decrease in Young's modulus (~ 60 %), followed by rGO/10 wt% BANF (~ 28 % in tensile strength and ~ 43 % in Young's modulus), and rGO-DOPA/10 wt% BANF (~ 15 % in tensile strength and ~ 20 % in Young's modulus). The Ca^{2+}-modified electrodes exhibited only a ~ 14 % decrease in both properties resulting from the synergistic effect of the enhanced hydrogen bonding interactions and coordination bonding. Furthermore, tensile testing was conducted after electrochemical testing (galvanostatic charge/discharge tests at 0.5 A/g for 5000 cycles), as shown in Figure 3.7b. The electrodes exhibited small decreases in tensile strength and Young's modulus when compared to the wet electrodes with electrolyte. The reduction is attributed to the structural changes in the electrodes, as observed from the cross-sectional SEM images after electrochemical testing (Figure 3.3b-g).

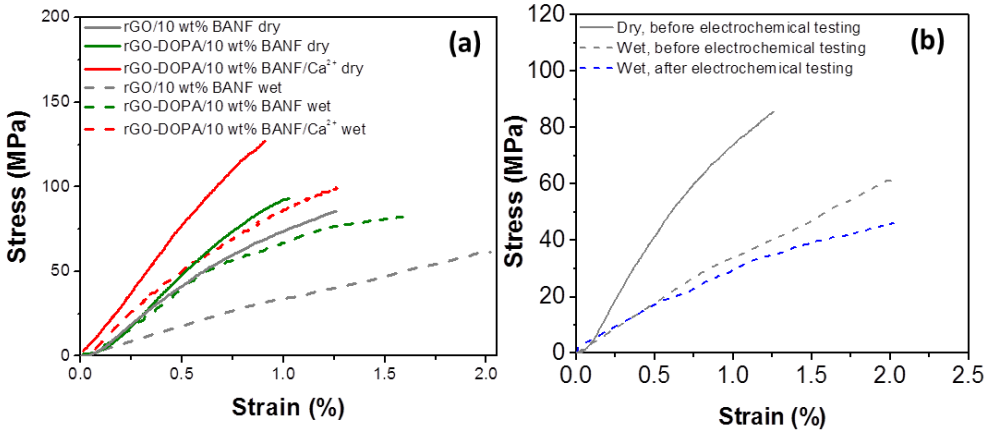

Figure 3.7 (a) Stress-strain curves of rGO/10 wt% BANF, rGO-DOPA/10 wt% BANF, and rGO-DOPA/10 wt% BANF/Ca^{2+} dry (solid lines) and electrolyte-wetted (dashed lines) electrodes. (b) Stress-strain curves of rGO/10 wt% BANF before and after electrochemical testing (galvanostatic charge/discharge tests at 0.5 A/g for 5,000 cycles).

Figure 3.8a shows cyclic voltammograms (CV) of composite electrodes containing 10 wt% BANFs at a scan rate of 20 mV/s. The voltammograms exhibited rectangular shapes with no redox peaks, indicative of the formation of the electric double layer.[40] Voltammograms at different scan rates (1 mV/s – 100 mV/s) were used to calculate the specific capacitance of the structural electrodes (Figure 3.8b). rGO electrodes (no BANFs) exhibited the highest specific capacitance (216.2 F/g) at a scan rate of 1 mV/s. Addition of 10 wt% and 25 wt% BANFs led to a decrease of 37% and 50% in specific capacitance, respectively, since BANFs do not contribute to the electric double layer. The d-spacing values (0.41-0.45 nm) of the partially reduced electrodes indicate that the electrolyte ions (K^+, radius: 0.138 nm and hydrated radius: 0.331 nm and OH^-, radius: 0.133 nm and hydrated radius: 0.3 nm) may not access the rGO sheets within the flakes.[41 42, 43] Therefore,

energy storage primarily occurs at electrical double layers generated at the rGO flakes' surfaces.

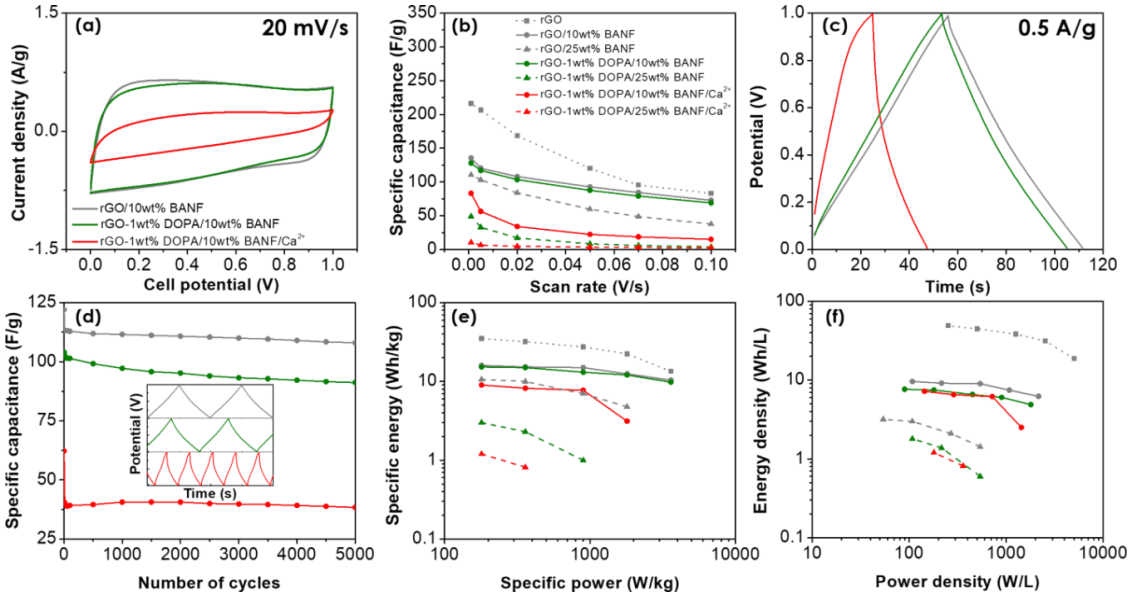

Figure 3.8 (a) Cyclic voltammograms of rGO/10 wt% BANF, rGO-1wt% DOPA/10 wt% BANF and rGO-1 wt% DOPA/10 wt% BANF/Ca^{2+} electrodes at a scan rate of 20 mV/s. (b) Specific capacitance *vs.* scan rate for all composite electrodes. The legend in (b) applies to all the figures. (c) Galvanostatic charge/discharge curves of rGO/10wt% BANF, rGO-1 wt% DOPA/10 wt% BANF and rGO-1 wt% DOPA/10 wt% BANF/Ca^{2+} electrodes at 0.5 A/g. (d) Specific capacitance *vs*. number of cycles for rGO/10 wt% BANF, rGO-1 wt% DOPA/10 wt% BANF and rGO-1 wt% DOPA/10 wt% BANF/Ca^{2+} at 0.5 A/g for 5000 cycles. Inset shows a portion of the charge/discharge cycling starting from the 500th

cycle. Ragone plots of (e) specific energy *vs.* specific power and (f) energy density *vs.* power density.

Dopamine functionalization led to only a slight decrease in specific capacitance. More specifically, rGO-1 wt% DOPA/10 wt% BANF exhibited a specific capacitance of 127.9 F/g. However, further increase of the BANF content to 25 wt% led to a significant decline (49.1 F/g), which supports the observations from the mechanical performance. The specific capacitance of rGO-1 wt% DOPA/10 wt% BANF/Ca^{2+} and rGO-1 wt% DOPA/25 wt% BANF/Ca^{2+} was 83.2 F/g and 10.6 F/g, respectively. The introduction of Ca^{2+} ions results in more compact and dense electrodes. The decreased capacitance values are also attributed to the existence of the Ca^{2+} (radius: 0.100 nm and hydrated radius: 0.412 nm) ions that may hinder the movement of the solvated K^+ and OH^- ions due to their similar sizes.[41-43] Moreover, the Ca^{2+} ions are strongly attached to the rGO-1 wt% DOPA sheets through coordination bonding, as indicated also by similar studies on Ca^{2+}-alginate battery binders.[44, 45]

The CV results were also supported by galvanostatic cycling conducted at a current density of 0.5 A/g, Figure 3.8c, for which the specific capacitance of rGO/10 wt% BANF was ~122.0 F/g. Dopamine functionalization led to a decreased in specific capacitance of 13%, whereas addition of Ca^{2+} led to a reduction of almost 50%. Cycling up to 5000 cycles was performed to determine the cycling stability of the composite electrodes, as shown in Figure 3.8d. The capacitance retention starting from the second cycle was 95%, 89%, and 95% for rGO/10 wt% BANF, rGO-1 wt% DOPA/10 wt% BANF, and rGO-1 wt%

DOPA/10 wt% BANF/Ca^{2+}, respectively. The galvanostatic charge discharge data from different current densities (0.1, 0.2, 0.5, 1, and 2 A/g) were used to construct the Ragone plots (specific energy *vs.* specific power and energy density *vs.* power density), as shown in Figure 3.8e and 3.8f. In general, pure rGO (no BANFs) exhibited the highest specific energy values. This is to be expected, as BANFs are not electrochemically active and Ca^{2+} ions increase the packing of rGO sheets. Even so, a holistic assessment of the mechanical and electrochemical properties is required to determine the best multifunctional efficiency.

The mechanical performance of the rGO-DOPA/BANF/Ca^{2+} structural electrodes is demonstrated in an Ashby plot of Young's modulus *vs.* tensile strength, Figure 3.9a. The rGO-DOPA/BANF/Ca^{2+} composites were compared against natural materials such as bone, nacre, and wood.[46, 47] rGO-DOPA/BANF/Ca^{2+} structural electrodes exhibited similar tensile strength to these natural materials, while the Young's modulus was higher than wood but lower than natural nacre. Moreover, the composite electrodes were compared against other nacre-mimicking structures such as graphene oxide (GO)/chitosan and montmorillonite (MTM)/chitosan composites.[46] GO/chitosan and MTM/chitosan utilize the 'brick-and-mortar' structure as well as the extensive hydrogen bonding interactions. However, the rGO-DOPA/BANF/Ca^{2+} exhibited higher Young's modulus as a result of the strong interfacial interactions with the stiff BANFs and the chelation of Ca^{2+} ions.

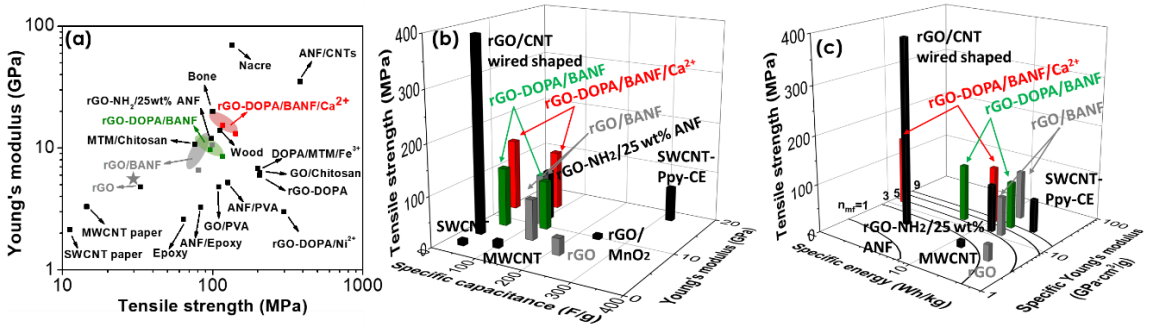

Figure 3.9 Ashby plot of (a) Young's modulus *vs.* ultimate tensile strength for mechanically strong composites, (b) Young's modulus *vs.* specific capacitance *vs.* tensile strength for structural supercapacitor electrodes, and (c) specific Young's modulus *vs.* specific energy *vs.* tensile strength structural supercapacitor electrodes. The lines represent constant multifunctional efficiency (η_{mf}) traces.

Furthermore, comparison against literature reveals that the rGO-DOPA/10 wt% BANF/Ca^{2+} composites exhibit Young's moduli higher than reported values for other rGO-DOPA structures. For example, the next highest modulus as compared to ours was for an rGO-DOPA composite with a Young's modulus of 6 GPa,[1] which is 60% less. Here, the increased Young's modulus originates from the synergistic effect of the strong interfacial interactions with the stiff BANFs. rGO-DOPA interacts with BANFs through extensive hydrogen bonding and π-π stacking interactions, and the Ca^{2+} ions create dative bonds that strongly bridge the components, leading to higher Young's modulus.

We next compared the mechanical properties of the rGO/BANF electrodes to other aramid nanofiber-containing structures. The rGO-DOPA/10 wt% BANF/Ca^{2+} composites exhibited a better combination of mechanical properties than other ANF based composites

such as ANF/epoxy and ANF/PVA.[20, 22] To-date, the best combination was achieved using 95 wt% ANF / 5wt% carbon nanotubes (CNTs).[48] However, the rGO-DOPA/BANF/Ca^{2+} exhibited the highest reported modulus using the lowest content of ANFs in electrically conductive composites, which is important for maintaining good capacity.[48, 19, 21, 49-51]

The performance of rGO-DOPA/BANF/Ca^{2+} composites as structural electrodes for supercapacitors is demonstrated in Figure 3.9b. The structural electrodes are compared against single-walled carbon nanotube buckypaper (SWCNT paper), multi-walled carbon nanotube buckypaper (MWCNT paper), rGO/CNT wire shaped composites, SWCNT-Ppy-cyanate ester (CE), and rGO/MnO_2.[52-58] SWCNT-Ppy-CE and rGO/MnO_2 exhibited the highest specific capacitance. However, these electrodes display a pseudocapacitive performance that is known to lead to higher capacitance values. In general, all rGO/BANF electrodes showed a satisfactory combination of both mechanical and electrochemical properties. We observe that the addition of the stiff BANFs led to increased mechanical properties but led also to a deterioration in the specific capacitance due to the incorporation of an electrochemically inactive material. Dopamine functionalization led to enhanced Young's modulus and tensile strength, while the specific capacitance was not severely affected. This is attributed to the enhanced hydrogen bonding interactions and the more compact structure. Addition of Ca^{2+} ions led to a significant increase in Young's modulus and tensile strength resulting from the synergistic effect of hydrogen bonding and chelation. However, the specific capacitance decreased as a result of the much more compact structure and the existent of Ca^{2+} ions that may hinder the electrolyte ion movement.

Up to now, the best rGO/aramid nanofiber containing structural electrodes were the rGO-NH_2/25 wt% ANFs, in which rGO sheets had been modified with amine functional groups.[27] These electrodes exhibited Young's modulus of ~12 GPa and ultimate tensile strength of ~100 MPa. In that report, the increased mechanical performance was attributed to the enhanced hydrogen bonding interactions between the ANF amide bonds and the GO amine groups caused by the amine functionalization. Moreover, these electrodes exhibited a specific capacitance of ~105 F/g.[27] In this work, we obtained higher specific capacitance (23%) while maintaining similar mechanical properties and while using only 10 wt% BANFs and dopamine functionalization.

Figure 3.9c illustrates the specific Young's modulus (GPa·cm³/g) *vs.* specific energy (W·h/kg) *vs.* tensile strength, where the lines represent the multifunctional efficiency. The multifunctional efficiency was calculated using Wetzel *et al.'s* model where epoxy (specific Young's modulus: 2.8 GPa·cm³/g) and carbon aerogel (specific energy: 12.5 W·h/kg) were used as the structural and energy storage monofunctional materials, respectively.[59-62] The structural electrodes studied here exhibited multifunctional efficiencies in the range of η_{mf} = 5 to 13.6, where values above unity indicate a desired mass and volume savings. Specifically, rGO/25 wt% BANF structural electrodes exhibited the best performance in terms of multifunctional efficiency (η_{mf} = 13.6) out of rGO, rGO-NH_2/25 wt% ANF, MWCNT paper, rGO/CNT wire shaped, and SWCNT-Ppy-CE (η_{mf} = 3.4, 5.4, 2.5, 2.0, and 9.7, respectively). Figure 3.9 shows that inclusion of dopamine and Ca^{2+} ions are beneficial when Young's modulus, tensile

strength, and capacitance are priorities, while still maintaining multifunctional efficiencies >5.

3.4. Conclusions

Nacre-mimicking structural supercapacitor electrodes based on branched aramid nanofibers and dopamine-functionalized reduced graphene oxide sheets were fabricated using vacuum filtration. The effect of BANF addition, dopamine functionalization as well as that of Ca^{2+} ions on the mechanical and electrochemical performance was investigated. These modifications led to a significant increase of 220% in Young's modulus and 255% in ultimate tensile strength relative to pure rGO electrodes (no BANFs). The excellent mechanical properties were a result of the synergetic effect of the increased hydrogen bonding caused by the dopamine functionalization and the chelation caused by the Ca^{2+} ions. The improvements in the mechanical properties lead to extremely high values of multifunctional efficiency >5 and up to 13.6. This approach is applicable to other nacre-mimicking structures leading to a new stronger multifunctional family of nature-inspired materials. Future work should focus on improving the electrochemical performance, either by adding porosity to improve the ionic mobility or by adding a pseudocapacitive material to enhance energy density. To the best of our knowledge, the obtained Young's modulus and multifunctional efficiency is the highest among the low aramid nanofiber content electrically conductive composites. This leads to strong structural supercapacitor electrodes with high electrochemical performance.

3.5. References

1. Cui, W.; Li, M.; Liu, J.; Wang, B.; Zhang, C.; Jiang, L.; Cheng, Q., A strong integrated strength and toughness artificial nacre based on dopamine cross-linked graphene oxide. *ACS Nano* **2014,** *8* (9), 9511-7.
2. Xu, L. Q.; Yang, W. J.; Neoh, K. G.; Kang, E. T.; Fu, G. D., Dopamine-Induced Reduction and Functionalization of Graphene Oxide Nanosheets. *Macromolecules* **2010,** *43* (20), 8336-8339.
3. Li, W.; Shang, T.; Yang, W.; Yang, H.; Lin, S.; Jia, X.; Cai, Q.; Yang, X., Effectively Exerting the Reinforcement of Dopamine Reduced Graphene Oxide on Epoxy-Based Composites via Strengthened Interfacial Bonding. *ACS Appl. Mater. Interfaces* **2016,** *8* (20), 13037-50.
4. Liu, Y.; Ai, K.; Lu, L., Polydopamine and its derivative materials: synthesis and promising applications in energy, environmental, and biomedical fields. *Chem. Rev.* **2014,** *114* (9), 5057-115.
5. Ryu, J. H.; Messersmith, P. B.; Lee, H., Polydopamine Surface Chemistry: A Decade of Discovery. *ACS Appl. Mater. Interfaces* **2018,** *10* (9), 7523-7540.
6. Jiang, B.; He, Y.; Li, B.; Zhao, S.; Wang, S.; He, Y. B.; Lin, Z., Polymer-Templated Formation of Polydopamine-Coated SnO2 Nanocrystals: Anodes for Cyclable Lithium-Ion Batteries. *Angew. Chem.* **2017,** *56* (7), 1869-1872.
7. Liu, T.; Kim, K. C.; Lee, B.; Chen, Z. M.; Noda, S.; Jang, S. S.; Lee, S. W., Self-polymerized dopamine as an organic cathode for Li- and Na-ion batteries. *Energ Environ Sci* **2017,** *10* (1), 205-215.
8. Ryou, M. H.; Lee, D. J.; Lee, J. N.; Lee, Y. M.; Park, J. K.; Choi, J. W., Excellent Cycle Life of Lithium-Metal Anodes in Lithium-Ion Batteries with Mussel-Inspired Polydopamine-Coated Separators. *Adv Energy Mater* **2012,** *2* (6), 645-650.
9. Liu, N.; Wu, H.; McDowell, M. T.; Yao, Y.; Wang, C.; Cui, Y., A yolk-shell design for stabilized and scalable li-ion battery alloy anodes. *Nano Lett.* **2012,** *12* (6), 3315-21.
10. Cha, I.; Lee, E. J.; Park, H. S.; Kim, J.-H.; Kim, Y. H.; Song, C., Facile electrochemical synthesis of polydopamine-incorporated graphene oxide/PEDOT hybrid thin films for pseudocapacitive behaviors. *Synthetic Metals* **2014,** *195*, 162-166.
11. Hou, D.; Tao, H.; Zhu, X.; Li, M., Polydopamine and MnO2 core-shell composites for high-performance supercapacitors. *Appl Surf Sci* **2017,** *419*, 580-585.
12. Park, S.; Lee, K.-S.; Bozoklu, G.; Cai, W.; Nguyen, S. T.; Ruoff, R. S., Graphene Oxide Papers Modified by Divalent Ions—Enhancing Mechanical Properties via Chemical Cross-Linking. *ACS Nano* **2008,** *2* (3), 572-578.
13. Chen, K.; Tang, X.; Yue, Y.; Zhao, H.; Guo, L., Strong and Tough Layered Nanocomposites with Buried Interfaces. *ACS Nano* **2016,** *10* (4), 4816-27.
14. Wan, S.; Xu, F.; Jiang, L.; Cheng, Q., Superior Fatigue Resistant Bioinspired Graphene-Based Nanocomposite via Synergistic Interfacial Interactions. *Adv. Funct. Mater.* **2017,** *27* (10), 1605636.

15. Yang, M.; Cao, K.; Sui, L.; Qi, Y.; Zhu, J.; Waas, A.; Arruda, E. M.; Kieffer, J.; Thouless, M. D.; Kotov, N. A., Dispersions of aramid nanofibers: a new nanoscale building block. *ACS Nano* **2011,** *5* (9), 6945-54.
16. Lyu, J.; Hammig, M. D.; Liu, L. H.; Xu, L. Z.; Chi, H.; Uher, C.; Li, T. H.; Kotov, N. A., Stretchable conductors by kirigami patterning of aramid-silver nanocomposites with zero conductance gradient. *Appl Phys Lett* **2017,** *111* (16), 161901.
17. Lyu, J.; Wang, X. Z.; Liu, L. H.; Kim, Y.; Tanyi, E. K.; Chi, H.; Feng, W. C.; Xu, L. Z.; Li, T. H.; Noginov, M. A.; Uher, C.; Hammig, M. D.; Kotov, N. A., High Strength Conductive Composites with Plasmonic Nanoparticles Aligned on Aramid Nanofibers. *Adv. Funct. Mater.* **2016,** *26* (46), 8435-8445.
18. Xu, L.; Zhao, X.; Xu, C.; Kotov, N. A., Water-Rich Biomimetic Composites with Abiotic Self-Organizing Nanofiber Network. *Adv. Mater* **2018,** *30* (1), 1703343-n/a.
19. Yang, M.; Cao, K. Q.; Yeom, B.; Thouless, M. D.; Waas, A.; Arruda, E. M.; Kotov, N. A., Aramid nanofiber-reinforced transparent nanocomposites. *J. Compos. Mater.* **2015,** *49* (15), 1873-1879.
20. Lin, J.; Bang, S. H.; Malakooti, M. H.; Sodano, H. A., Isolation of Aramid Nanofibers for High Strength and Toughness Polymer Nanocomposites. *ACS Appl Mater Interfaces* **2017,** *9* (12), 11167-11175.
21. Fan, J.; Shi, Z.; Tian, M.; Yin, J., Graphene–aramid nanofiber nanocomposite paper with high mechanical and electrical performance. *RSC Adv.* **2013,** *3* (39), 17664.
22. Guan, Y.; Li, W.; Zhang, Y. L.; Shi, Z. Q.; Tan, J.; Wang, F.; Wang, Y. H., Aramid nanofibers and poly (vinyl alcohol) nanocomposites for ideal combination of strength and toughness via hydrogen bonding interactions. *Compos. Sci. Technol.* **2017,** *144*, 193-201.
23. Kuang, Q. X.; Zhang, D.; Yu, J. C.; Chang, Y. W.; Yue, M. L.; Hou, Y.; Yang, M., Toward Record-High Stiffness in Polyurethane Nanocomposites Using Aramid Nanofibers. *J Phys Chem C* **2015,** *119* (49), 27467-27477.
24. Li, Y. N.; Ren, G. Y.; Zhang, Z. Q.; Teng, C.; Wu, Y. Z.; Lu, X. Y.; Zhu, Y.; Jiang, L., A strong and highly flexible aramid nanofibers/PEDOT:PSS film for all-solid-state supercapacitors with superior cycling stability. *J Mater Chem A* **2016,** *4* (44), 17324-17332.
25. Kwon, S. R.; Elinski, M. B.; Batteas, J. D.; Lutkenhaus, J. L., Robust and Flexible Aramid Nanofiber/Graphene Layer-by-Layer Electrodes. *ACS Appl Mater Interfaces* **2017,** *9* (20), 17125-17135.
26. Kwon, S. R.; Harris, J.; Zhou, T.; Loufakis, D.; Boyd, J. G.; Lutkenhaus, J. L., Mechanically Strong Graphene/Aramid Nanofiber Composite Electrodes for Structural Energy and Power. *ACS Nano* **2017,** *11* (7), 6682-6690.
27. Flouda, P.; Feng, X. Y.; Boyd, J. G.; Thomas, E. L.; Lagoudas, D. C.; Lutkenhaus, J. L., Interfacial Engineering of Reduced Graphene Oxide for Aramid Nanofiber-Enabled Structural Supercapacitors. *Batteries & Supercaps* **2019,** *2* (5), 464-472.
28. Patel, A. G.; Johnson, L.; Arroyave, R.; Lutkenhaus, J. L., Design of multifunctional supercapacitor electrodes using an informatics approach. *Mol Syst Des Eng* **2019,** *4*, 654-663.

29. Zhu, J.; Yang, M.; Emre, A.; Bahng, J. H.; Xu, L.; Yeom, J.; Yeom, B.; Kim, Y.; Johnson, K.; Green, P.; Kotov, N. A., Branched Aramid Nanofibers. *Angewandte Chemie* **2017,** *129* (39), 11906-11910.
30. Hummers, W. S.; Offeman, R. E., Preparation of Graphitic Oxide. *J. Am. Chem. Soc.* **1958,** *80* (6), 1339-1339.
31. Shen, J. F.; Hu, Y. Z.; Shi, M.; Lu, X.; Qin, C.; Li, C.; Ye, M. X., Fast and Facile Preparation of Graphene Oxide and Reduced Graphene Oxide Nanoplatelets. *Chem Mater* **2009,** *21* (15), 3514-3520.
32. Tuinstra, F.; Koenig, J. L., Raman Spectrum of Graphite. *J. Chem. Phys.* **1970,** *53* (3), 1126-1130.
33. Kudin, K. N.; Ozbas, B.; Schniepp, H. C.; Prud'homme, R. K.; Aksay, I. A.; Car, R., Raman spectra of graphite oxide and functionalized graphene sheets. *Nano Lett.* **2008,** *8* (1), 36-41.
34. Stankovich, S.; Dikin, D. A.; Piner, R. D.; Kohlhaas, K. A.; Kleinhammes, A.; Jia, Y.; Wu, Y.; Nguyen, S. T.; Ruoff, R. S., Synthesis of graphene-based nanosheets via chemical reduction of exfoliated graphite oxide. *Carbon* **2007,** *45* (7), 1558-1565.
35. Eda, G.; Fanchini, G.; Chhowalla, M., Large-area ultrathin films of reduced graphene oxide as a transparent and flexible electronic material. *Nat Nanotechnol* **2008,** *3* (5), 270-274.
36. Yang, D.; Velamakanni, A.; Bozoklu, G.; Park, S.; Stoller, M.; Piner, R. D.; Stankovich, S.; Jung, I.; Field, D. A.; Ventrice, C. A.; Ruoff, R. S., Chemical analysis of graphene oxide films after heat and chemical treatments by X-ray photoelectron and Micro-Raman spectroscopy. *Carbon* **2009,** *47* (1), 145-152.
37. Park, S.; An, J.; Potts, J. R.; Velamakanni, A.; Murali, S.; Ruoff, R. S., Hydrazine-reduction of graphite- and graphene oxide. *Carbon* **2011,** *49* (9), 3019-3023.
38. Zhang, Y.; Gong, S.; Zhang, Q.; Ming, P.; Wan, S.; Peng, J.; Jiang, L.; Cheng, Q., Graphene-based artificial nacre nanocomposites. *Chem Soc Rev* **2016,** *45* (9), 2378-95.
39. Rodríguez-Pérez, L.; Herranz, M. a. Á.; Martín, N., The chemistry of pristine graphene. *Chem Commun* **2013,** *49* (36), 3721-3735.
40. Stoller, M. D.; Ruoff, R. S., Best practice methods for determining an electrode material's performance for ultracapacitors. *Energ Environ Sci* **2010,** *3* (9), 1294-1301.
41. Marcus, Y., A Simple Empirical-Model Describing the Thermodynamics of Hydration of Ions of Widely Varying Charges, Sizes, and Shapes. *Biophys Chem* **1994,** *51* (2-3), 111-127.
42. Nightingale, E. R., Phenomenological Theory of Ion Solvation - Effective Radii of Hydrated Ions. *J Phys Chem-Us* **1959,** *63* (9), 1381-1387.
43. Huang, J.; Sumpter, B. G.; Meunier, V., A universal model for nanoporous carbon supercapacitors applicable to diverse pore regimes, carbon materials, and electrolytes. *Chem* **2008,** *14* (22), 6614-26.
44. Liu, J.; Zhang, Q.; Wu, Z. Y.; Wu, J. H.; Li, J. T.; Huang, L.; Sun, S. G., A high-performance alginate hydrogel binder for the Si/C anode of a Li-ion battery. *Chem. Commun. (Camb.)* **2014,** *50* (48), 6386-9.

45. Yoon, J.; Oh, D. X.; Jo, C.; Lee, J.; Hwang, D. S., Improvement of desolvation and resilience of alginate binders for Si-based anodes in a lithium ion battery by calcium-mediated cross-linking. *Phys Chem Chem Phys* **2014,** *16* (46), 25628-35.
46. Wang, J.; Cheng, Q.; Tang, Z., Layered nanocomposites inspired by the structure and mechanical properties of nacre. *Chem. Soc. Rev.* **2012,** *41* (3), 1111-29.
47. Ji, B. H.; Gao, H. J., Mechanical properties of nanostructure of biological materials. *J Mech Phys Solids* **2004,** *52* (9), 1963-1990.
48. Zhu, J.; Cao, W.; Yue, M.; Hou, Y.; Han, J.; Yang, M., Strong and stiff aramid nanofiber/carbon nanotube nanocomposites. *ACS Nano* **2015,** *9* (3), 2489-501.
49. Patterson, B. A.; Malakooti, M. H.; Lin, J. J.; Okorom, A.; Sodano, H. A., Aramid nanofibers for multiscale fiber reinforcement of polymer composites. *Compos Sci Technol* **2018,** *161*, 92-99.
50. Wang, F.; Wu, Y. D.; Huang, Y. D., Novel application of graphene oxide to improve hydrophilicity and mechanical strength of aramid nanofiber hybrid membrane. *Compos Part a-Appl S* **2018,** *110*, 126-132.
51. Cao, W. X.; Yang, L.; Qi, X. D.; Hou, Y.; Zhu, J. Q.; Yang, M., Carbon Nanotube Wires Sheathed by Aramid Nanofibers. *Adv. Funct. Mater.* **2017,** *27* (34), 1701061.
52. Rigueur, J. L.; Hasan, S. A.; Mahajan, S. V.; Dickerson, J. H., Buckypaper fabrication by liberation of electrophoretically deposited carbon nanotubes. *Carbon* **2010,** *48* (14), 4090-4099.
53. Kim, S. Y.; Hong, J.; Kavian, R.; Lee, S. W.; Hyder, M. N.; Shao-Horn, Y.; Hammond, P. T., Rapid fabrication of thick spray-layer-by-layer carbon nanotube electrodes for high power and energy devices. *Energ Environ Sci* **2013,** *6* (3), 888-897.
54. Whitten, P. G.; Spinks, G. M.; Wallace, G. G., Mechanical properties of carbon nanotube paper in ionic liquid and aqueous electrolytes. *Carbon* **2005,** *43* (9), 1891-1896.
55. Barisci, J. N.; Wallace, G. G.; Baughman, R. H., Electrochemical studies of single-wall carbon nanotubes in aqueous solutions. *J. Electroanal. Chem* **2000,** *488* (2), 92-98.
56. Sumboja, A.; Foo, C. Y.; Wang, X.; Lee, P. S., Large areal mass, flexible and free-standing reduced graphene oxide/manganese dioxide paper for asymmetric supercapacitor device. *Adv. Mater* **2013,** *25* (20), 2809-15.
57. Ma, Y.; Li, P.; Sedloff, J. W.; Zhang, X.; Zhang, H.; Liu, J., Conductive Graphene Fibers for Wire-Shaped Supercapacitors Strengthened by Unfunctionalized Few-Walled Carbon Nanotubes. *ACS Nano* **2015,** *9* (2), 1352-1359.
58. Li, S.; Zhao, C.; Shu, K.; Wang, C.; Guo, Z.; Wallace, G. G.; Liu, H., Mechanically strong high performance layered polypyrrole nano fibre/graphene film for flexible solid state supercapacitor. *Carbon* **2014,** *79*, 554-562.
59. O'Brien, D. J.; Baechle, D. M.; Wetzel, E. D., Design and performance of multifunctional structural composite capacitors. *J. Compos. Mater* **2011,** *45* (26), 2797-2809.

60. Snyder, J. F.; Gienger, E. B.; Wetzel, E. D., Performance metrics for structural composites with electrochemical multifunctionality. *J. Compos. Mater.* **2015,** *49* (15), 1835-1848.
61. Zhang, L. L.; Zhao, X. S., Carbon-based materials as supercapacitor electrodes. *Chem. Soc. Rev.* **2009,** *38* (9), 2520-31.
62. Qu, D.; Shi, H., Studies of activated carbons used in double-layer capacitors. *J. Power Sources* **1998,** *74* (1), 99-107.

4. STRUCTURAL REDUCED GRAPHENE OXIDE SUPERCAPACITORS MECHANICALLY ENHANCED WITH TANNIC ACID*

4.1. Introduction

The previous chapters described the development of functionalized reduced graphene oxide (rGO)/aramid nanofiber (ANF) and branched ANF (BANF) composite structural supercapacitor electrodes. The composites exhibited a specific capacitance of 80-220 F/g, a tensile strength of 35-142 MPa, and Young's moduli up to 15 GPa.[1-4] Hydrogen bonding interactions were enhanced and coordination bonding was introduced by the incorporation of metal divalent ions (Ca^{2+}). Despite the good electrochemical performance of the rGO-based electrodes, there remains a challenge to further improve mechanical performance without compromising capacitance. To this end, here, we further investigate the effect of enhanced hydrogen and coordination bonding, as well as the effect of metal ions with different valency (Ca^{2+} and Fe^{3+}).

Hydrogen bonding interactions may be improved by functionalizing GO with tannic acid (TA), a highly adhesive molecule. TA is a polyphenol with catechol and pyrogallol units that is extracted from natural plants such as wood, tea leaves, and berries.[5, 6] TA-functionalized GO (GO-TA) improved the mechanical and electrical properties of PVA-based humidity sensors.[7] Addition of 1 wt% GO-TA in PVA led to a 31 % increase in tensile strength, a 34 % increase in Young's modulus, and 57 % in ultimate strain.[7]

---

* Adapted with permission from "Structural reduced graphene oxide supercapacitors mechanically enhanced with tannic acid" by Paraskevi Flouda, Junyeong Yun, Dimitrios Loufakis, Smit A. Shah, Dimitris C. Lagoudas, Micah J. Green and Jodie L. Lutkenhaus, *Sustainable Energy & Fuels* 2020**,** 4 (5), 2301-2308, Copyright 2020, Royal Society of Chemistry

Coordination bonding through the addition of Fe^{3+} ions to GO-TA films led to a remarkable increase in tensile strength and Young's modulus up to 150 % and 520 %, respectively.[5] However, ultimate strain decreased by 70 %.[5] TA alone has been examined as a redox-active molecule for supercapacitors and batteries.[6, 8, 9] rGO/carbonized paper/TA supercapacitor electrodes exhibited a specific capacitance of 186 F/g, with a capacitance retention of 83% after 500 bending cycles.[8] However, none of these cases quantified *both* the mechanical and energy storage properties for TA-containing electrodes.

Here, we investigate the effect of hydrogen and coordination bonding on the mechanical, electrical, and electrochemical properties of rGO/ANF-based electrodes. GO was functionalized with TA and mixed with branched aramid nanofibers (BANFs) to improve the mechanical properties. The nanocomposites were further modified with divalent (Ca^{2+}) and trivalent (Fe^{3+}) ions. The resulting composites exhibited a maximum Young's modulus of 25 GPa and a tensile strength of 140 MPa, which are five-fold and four-fold improvements compared to pure rGO paper, respectively. The electrochemical performance of the composites in a symmetric supercapacitor configuration was investigated. To demonstrate the electrochemical stability under mechanical loads a flexible device was fabricated. This work demonstrates that synergistic interfacial interactions lead to large improvements in mechanical properties while maintaining superior electrical and electrochemical properties.

4.2. Materials and Methods

Graphite and Kevlar®69 thread were purchased from Bay Carbon and Thread Exchange, respectively. Sulfuric acid (H_2SO_4), potassium hydroxide (KOH), dimethyl sulfoxide (DMSO), potassium permanganate ($KMnO_4$), sodium nitrate ($NaNO_3$), Tris buffer solution (pH 8.5) and Poly(vinyl alcohol) (PVA, Mw 89,000-98,000, 99+% hydrolysed) were purchased from Sigma-Aldrich. Celgard 3501 was provided by Celgard. Carbon paper and phosphoric acid (H_3PO_4, 85% aqueous solution) were purchased from Alfa Aesar. Electrically conductive double-sided tape (XYZ-Axis, 6.35 mm x 32.9 mm) was purchased from 3M.

Graphene oxide (GO) was synthesized from graphite using a modified Hummers method as previously reported.[10] To functionalize GO with tannic acid, desirable amounts of GO aqueous dispersion (1 mg/ml) were mixed with tannic acid in a basic solution of Tris buffer (pH: 8.5). The mixture was stirred for 24 h at room temperature. Finally, the mixture was filtered using Whatman filter paper (2.5 pore size and 55 mm diameter) and washed in ethanol:water (1:1 v:v mixture).[7] The obtained powder was dried at 60 ^oC overnight under vacuum and re-dispersed in DMSO. Branched aramid nanofibers (BANF) were produced by the dissolution of chopped Kevlar® fiber (0.5 g) in DMSO (50 ml) and KOH (0.5 g).[11] Composite thin films of GO-TA and BANF were fabricated using vacuum filtration as described in previous reports. The composites were further dried at 80 ^oC for three days and thermally reduced at 200 ^oC under vacuum.[2, 4]

First a H_3PO_4-PVA gel electrolyte was synthesized. PVA (5 g) and milli-Q-water (50 ml) were mixed and stirred at 130 ^oC until a clear solution was obtained. The solution

was then cooled to room temperature. H_3PO_4 (3.46 ml) was added and stirred for 1 hour at room temperature. The composite electrodes (rGO-TA/10 wt% BANF/Fe^{3+}) were cut into 0.5 cm x 3 cm strips and were attached to commercial conductive tape used as a current collector, respectively. A pre-cured at room temperature H_3PO_4-PVA film was cut into a 0.7 cm x 3.5 cm strip. Then, we applied uncured H_3PO_4-PVA gel electrolyte to both sides of this pre-cured H_3PO_4-PVA film and the prepared electrodes were carefully attached to each side. The all-solid-state flexible supercapacitor was obtained after drying for 20 ^oC at room temperature. The flexible device had a total thickness of ~0.64 cm and mass of ~18.5 mg (current collector, electrodes, and electrolyte).

The morphology of the composite films was examined using scanning electron microscopy (JEOL, SEM). X-ray photoelectron spectroscopy (XPS) was conducted using an Omicron ESCA Probe with Mg Ka radiation (hm = 1253.6 eV). Survey scans were collected at 100-1100 eV with steps of 1.0 eV and 50 ms dwell time. High resolution scans were collected with steps of 0.05 eV and 200 ms dwell time. The C1s peak for sp^2-hybridized carbon atoms (284.5 eV) was used to calibrate all spectra. Shirley background correction, gaussian-lorentzian peak shape fitting were applied and the FWHM of the peaks was constrained. Raman spectroscopy was conducted using a Horiba Jobin-Yvon Lab Ram HR with 514 nm excitation. X-ray diffraction was conducted using a Brucker D8 X-ray. The X-ray source was Cu (Ka, λ = 1.541 Å) and the diffractograms were obtained at 2θ range $5^o - 50^o$. A TA Q50 analyzer was used to conduct thermogravimetric analysis under N_2 gas (TGA). The samples were heated and isothermally held at 80 ^oC with a rate of 10 ^oC/min for 2 h, followed by heating to 600 ^oC.

4.3. Results and Discussion

Graphene oxide was functionalized with tannic acid by the reaction of GO's epoxide groups with TA's galloyl and catechol groups. GO-TA of different TA contents (1, 3, 5, and 7 wt%) were synthesized. GO-TA dispersions were mixed with branched aramid nanofiber dispersions in dimethyl sulfoxide and free-standing films were fabricated using vacuum filtration. The premade films were modified with metal chloride solutions of Ca^{2+} and Fe^{3+}. The nanocomposites were thermally reduced[12] to yield reduced GO-TA/BANF (rGO-TA/BANF) electrodes.

Digital images of the composites are shown in Figure 4.1a. Scanning electron microscopy (SEM) images (Figure 4.1b and 4.1c) revealed a highly layered structure with thicknesses of 5-10 μm. rGO-TA flakes interact with BANFs through extensive hydrogen bonding interactions while the Ca^{2+} and Fe^{3+} ions interact with the rGO oxygen groups and the TA galloyl and catechol groups though coordination bonding, as shown in Figure 4.1d. The electrodes made from GO with a TA content of 5 wt% were selected for further studies since it led to the optimum mechanical performance for rGO-TA papers (without BANFs). From this point on "GO-TA" implies to a content of 5 wt% TA.

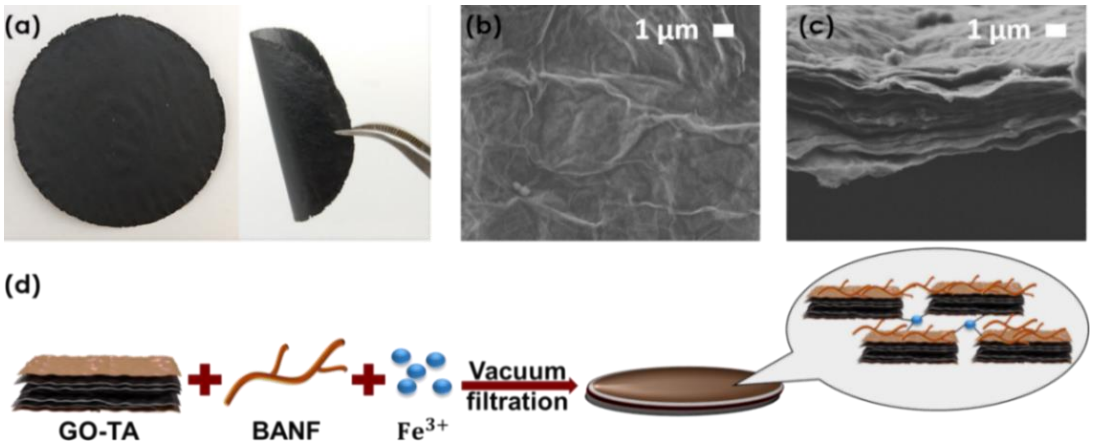

Figure 4.1 (a) Digital images of the composite electrodes. Scanning electron microscopy images of the (b) top and (c) cross-section of rGO-TA/10 wt% BANF. (d) Schematic representation of the rGO-TA/BANF composites.

X-ray photoelectron spectroscopy (XPS), energy dispersive X-ray spectroscopy (EDS), Raman spectroscopy, and X-ray diffraction (XRD) were utilized to verify the chemical modifications and interactions. Figure 4.2a shows the XPS survey scans for rGO/10 wt% BANF, rGO-TA/10 wt% BANF, rGO-TA/10 wt% BANF/Ca^{2+}, and rGO-TA/10 wt% BANF/Fe^{3+}. TA functionalization caused a decrease in the C/O ratio from 4.6 to 3.1 (rGO/10 wt% BANF *vs.* rGO-TA/10 wt% BANF) resulting from the TA oxygen moieties.[7] Addition of Ca^{2+} and Fe^{3+} ions led to a slightly decreased C/O ratio of 2.9 and 2.7, respectively, due to the acidic nature of the metal chlorides.[5, 13] Moreover, Ca^{2+} and Fe^{3+} peaks appeared in the survey scans, indicating the successful addition of the metal ions corresponding to 1.5 at % and 2.9 at %, respectively (Figure 4.2a). Fe^{3+} addition was verified also using SEM-EDS mapping, as shown in Figure 4.2c and 4.2d.

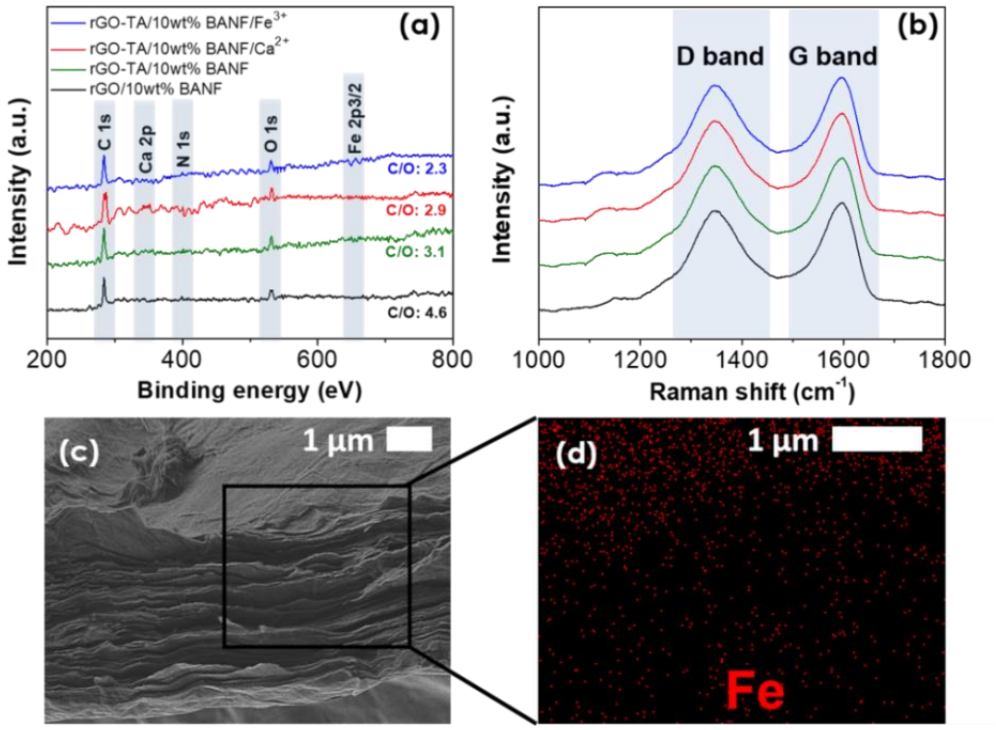

Figure 4.2 (a) XPS survey scans and (b) Raman spectra for rGO/10 wt% BANF, rGO-TA/10 wt% BANF, rGO-TA/10 wt% BANF/Ca^{2+}, and rGO-TA/10 wt% BANF/Fe^{3+}. Legend in (a) applies also for (b). (c) Cross-sectional SEM image and (d) EDS mapping of Fe for rGO-TA/10 wt% BANF/Fe^{3+}.

The characteristic D (1347 cm^{-1}) and G (1602 cm^{-1}) bands for carbon-based materials were apparent in the Raman spectra, Figure 4.2b.[14, 15] The D band is attributed to defects such as sp^3-hybridized carbon atoms, whereas the G band derives from the sp^2-hybridized carbon atoms. The D/G intensity ratio is used to qualitatively characterize defects.[15] TA functionalization led to an increase in I_D/I_G from 0.93 to 0.95 resulting from the partial reduction of the GO flakes.[16] Ca^{2+} and Fe^{3+} modifications did not cause significant changes in the I_D/I_G values.

High-resolution XPS N1s and C1s peaks were used to verify the interfacial interactions between rGO-TA and BANFs. TA functionalization led to an increase in the hydrogen bonding peak of the N1s spectra at 401.8 eV (Figure 4.3).[17] More specifically, rGO-TA and BANFs interact with each other through extensive hydrogen bonding interactions between the rGO oxygen groups, the TA galloyl and catechol groups, and the BANF amide groups. Metal ions interact with the rGO oxygen groups and the TA galloyl and catechol groups though coordination bonding.[5] These interactions were verified from the shift of the -COOH peak of the C1s peak after the addition of the Ca^{2+} and Fe^{3+} ions from 288.7 eV to 289.0 eV and 289.2 eV, respectively (Figure 4.4).

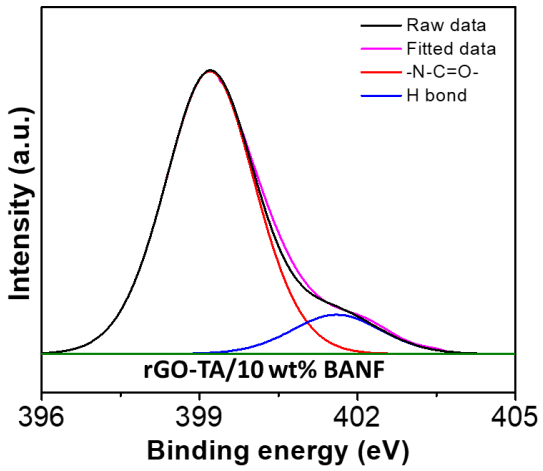

Figure 4.3 High resolution XPS N1s peak for rGO-TA/10 wt% BANF. Amide peak at 399.9 eV and H-bond peak at 401.8 eV.

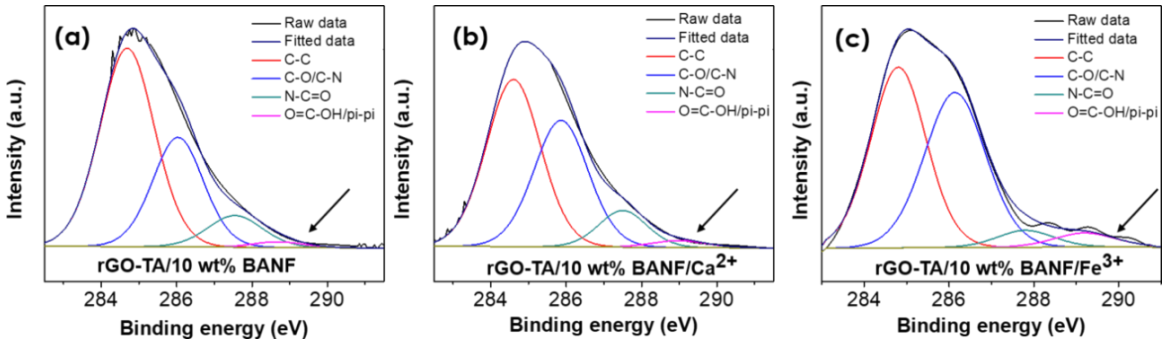

Figure 4.4 High resolution C1s XPS peaks for (a) rGO-TA/10 wt% BANF, (b) rGO-TA/10 wt% BANF/Ca^{2+}, and (c) rGO-TA/10 wt% BANF/Fe^{3+}.

Typical stress-strain curves of the composite films are shown in Figure 4.5a. Those curves were used to calculate the ultimate tensile strength and Young's modulus, are shown in Figure 4.5b and 4.5c. TA functionalization led to an 80 % increase (from 5 GPa to 9 GPa) in Young's modulus and 123 % increase (from 35 to 78 MPa) in ultimate tensile strength compared to rGO. Ultimate strain and toughness increased by 25 % (from 0.8 to 1.0 %) and 250 % (from 120 to 420 kJ/m^3), respectively. Such increases result from the enhanced hydrogen bonding interactions between the galloyl and catechol groups of the TA functionalized rGO flakes.[5, 7] Addition of BANFs up to 10 wt% led to a further increase in Young's modulus of ~90 % (17 GPa) and an 80 % (140 MPa) increase in ultimate tensile strength, due to the stiff and load-bearing BANFs.[4] Toughness and ultimate strain exhibited a similar trend. Further increase in the BANF composition (to 15 wt% and 25 wt%) did not lead to improvements in the mechanical properties due to possible aggregation of the BANFs.

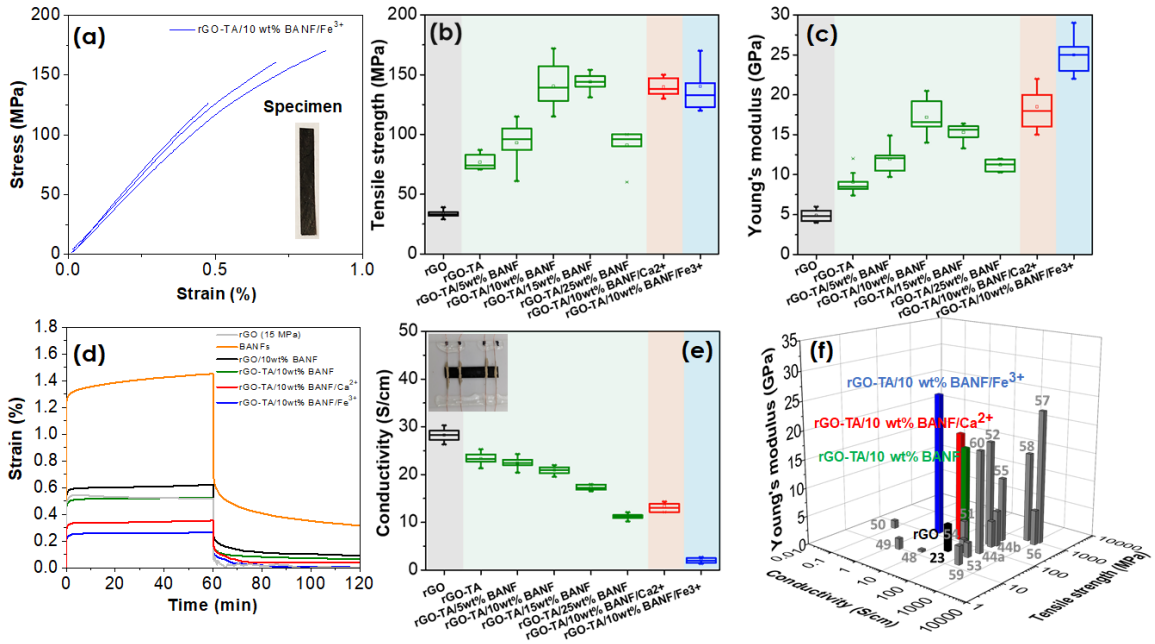

Figure 4.5 (a) Typical stress-strain curves for rGO-TA/10 wt% BANF/Fe^{3+}. Inset shows a specimen used for tensile testing. Box plots of (b) tensile strength and (c) Young's modulus. (d) Creep and recovery curves for BANFs (orange), rGO/10 wt% BANF (black), rGO-TA/10 wt% BANF (green), rGO-TA/10 wt% BANF/Ca^{2+} (red), and rGO-TA/10 wt% BANF/Fe^{3+} (blue) electrodes at 40 MPa and rGO (grey) at 15 MPa. (e) Box plots of electrical conductivity. Inset shows the sample preparation for the conductivity measurements. (f) Ashby plot of Young's modulus *vs.* electrical conductivity vs. tensile strength for mechanically strong conductive materials (not necessarily energy storage materials). Grey bars represent data obtained from the literature and the numbers correspond to references from this chapter.

Additionally, the rGO-TA/10 wt% BANF composites were modified with divalent (Ca^{2+}) and trivalent ions (Fe^{3+}). Young's modulus increased further by ~12 % (19 GPa,

within error) and ~70 % (25 GPa) when Ca^{2+} and Fe^{3+} ions were added, respectively. No changes were observed in the ultimate tensile strength, and the toughness retained its high values whereas the ultimate strain decreased up to 10 % for Ca^{2+} and 37 % for Fe^{3+}. The TA hydroxyl groups provide binding sites for the metal ions to bind and coordinate leading to extensive cross-linking between the functionalized rGO flakes.[5] These modifications prevent the rGO flakes from sliding leading to lower ultimate strains but significantly higher Young's moduli.[5, 18] The Fe^{3+}-containing composites exhibited superior mechanical performance compared to the Ca^{2+}-containing composites resulting from the higher valency that leads to stronger attraction.[19] Therefore, we focus on the Fe^{3+} containing composites.

To further elucidate the mechanism for the improved mechanical performance, additional tensile testing on rGO/Fe^{3+} (without BANFs) and rGO/10 wt% BANF/Fe^{3+} was conducted, as shown in Figure 4.6. The rGO/Fe^{3+} electrodes exhibited a Young's modulus of 6.5 GPa and tensile strength of 40 MPa, which corresponds to a 30 % and 14 % increase compared to the pure rGO films (without BANFs).[2] However, these properties are lower than the rGO-TA composites due to the absences of the extensive hydrogen bonding afforded by the TA. rGO/10 wt% BANF/Fe^{3+} films exhibited a Young's modulus and tensile strength of 12 GPa and 97 MPa, which is 70 % and 21 % more than the rGO/10 wt% BANF, and 52 % and 31 % less than the TA modified films (rGO-TA/10 wt% BANF/Fe^{3+}).[17] The results reveal the synergistic effect of the enhanced hydrogen and coordination bonding due to the TA functionalization and multivalent ion modification that leads to enhanced mechanical properties.

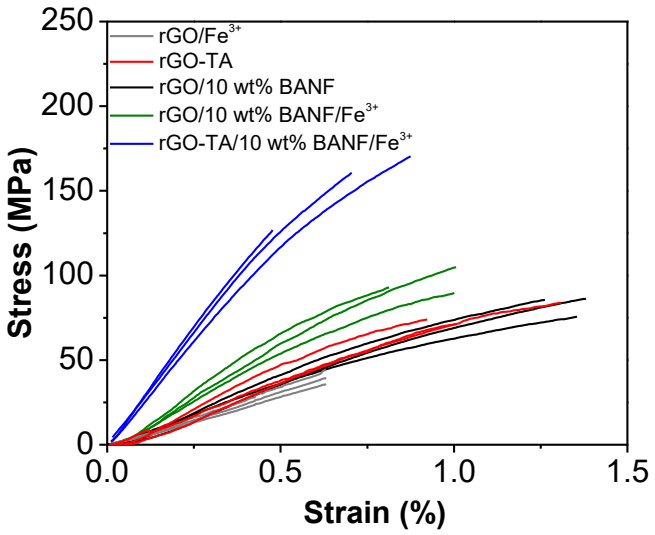

Figure 4.6 Typical stress-strain curves for rGO/Fe^{3+}, rGO-TA, rGO/10 wt% BANF, rGO/10 wt% BANF/Fe^{3+}, and rGO-TA/10 wt% BANF/Fe^{3+}.

Furthermore, creep testing was conducted for BANF, rGO, rGO/10 wt% BANF, rGO-TA/10 wt% BANF, rGO-TA/10 wt% BANF/Ca^{2+}, and rGO-TA/10 wt% BANF/Fe^{3+} electrodes, Figure 4.5d. Creep tests are used to study the relative slipping of the rGO flakes within the composite.[20] The unmodified composites (rGO/10 wt% BANF) and pure BANF films exhibited the highest creep and residual recovery strains, followed by rGO-TA/10 wt% BANF and the metal ion modified composites. The results indicate that the TA and Fe^{3+} modifications led to stronger adhesion between the rGO flakes that restrained their slippage.[21]

The electrical conductivity of the rGO and rGO-TA composites was measured using a 4-point sensing method, as shown in Figure 4.5e. The 4-point probe measurements were utilized to evaluate the effect of the different modifications in electrical conductivity,

as well as a way to select the most promising (high electrical conductivity and mechanical performance) compositions for structural energy storage to proceed with more advanced characterization techniques (*i.e.* electrochemical testing). TA functionalization led to an 18 % decrease in conductivity (from 28 S/cm to 23 S/cm) due to the addition of a non-conductive molecule (TA).[22] The conductivity further decreased by 9 % (21 S/cm) as a result of the addition of 10 wt% BANFs, since BANFs are not electrically conductive and disrupt the conductive rGO pathways.[23] Further addition of BANF (15-25 wt%) led to a significant drop in conductivity (11 S/cm). The metal ion modifications also led to deteriorated electrical conductivity resulting from the metal chloride treatment and the disruption of the conductive pathways.[22]

Figure 4.5f illustrates an Ashby plot of the Young's modulus *vs.* electrical conductivity *vs.* tensile strength for mechanically strong conductive nanocomposites. Trade-offs due to TA functionalization and metal ion modification are apparent. More specifically, these modifications (<10 wt% BANF) led to an increased Young's modulus, tensile strength but deteriorated electrical conductivity. The properties of the TA composites were compared against other state-of-the-art conductive nanocomposites.[24-27] More specifically, rGO-polyacrylic acid (PAA),[28] rGO-polydopamine (PDA),[18] rGO-PDA/Ni^{2+},[18] polypyrrole (PPy)/rGO,[29] rGO/MnO_2/carbon nanotube (CNTs),[30] rGO-10,12-pentacosadiyn-1-ol (PCO)/Zn^{2+},[31] rGO-cellulose nanocrystal (CNC),[32] pBG,[33] SBG,[34] mutli-walled CNTs (MWCNTs),[35] and single-walled CNTs (SWCNTs)-PPy-cyanate ester (CE)[36] exhibited higher conductivity values. However, the TA composites maintained high conductivities, tensile strength, and exhibited significantly higher

Young's moduli as a result of the strong interactions with the stiff BANFs and coordination bonding.

The electrochemical performance of selected composite films as supercapacitor electrodes was investigated. More specifically, the composites with the highest electrical conductivity (rGO), highest Young's modulus and tensile strength (rGO-TA/10 wt% BANF/Fe^{3+}), and best combination of these properties (rGO-TA/10 wt% BANF) were examined. Two-electrode symmetric coin cells with 6M KOH as the electrolyte were assembled (Figure 4.7a). Figure 4.7b shows the cyclic voltammograms for rGO-TA/10 wt% BANF/Fe^{3+} at different scan rates (1-100 mV/s). rGO exhibited the highest specific capacitance (216 ± 11 F/g) at 1 mV/s.[2] TA functionalization and BANF addition (10 wt%) led to a deteriorated specific capacitance of 120 ± 8 F/g, resulting from the decreased electrical conductivity and diffusion limitations due to the more compact structure.[37] Addition of Fe^{3+} ions led to an improved specific capacitance (145 ± 9 F/g), despite the low electrical conductivity of the composites. To better understand the unexpected improvement in specific capacitance, contact angle experiments were conducted. The improvement is attributed to the better wettability of the Fe^{3+} ion modified electrodes, as observed from the contact angle experiments (Figure 4.8). Better electrode wettability from the electrolyte, may lead to a larger ion-accessible surface area leading to higher capacitance values. Increasing the scan rate led to a decrease in specific capacitance due to diffusion limitations for all electrodes investigated.[37]

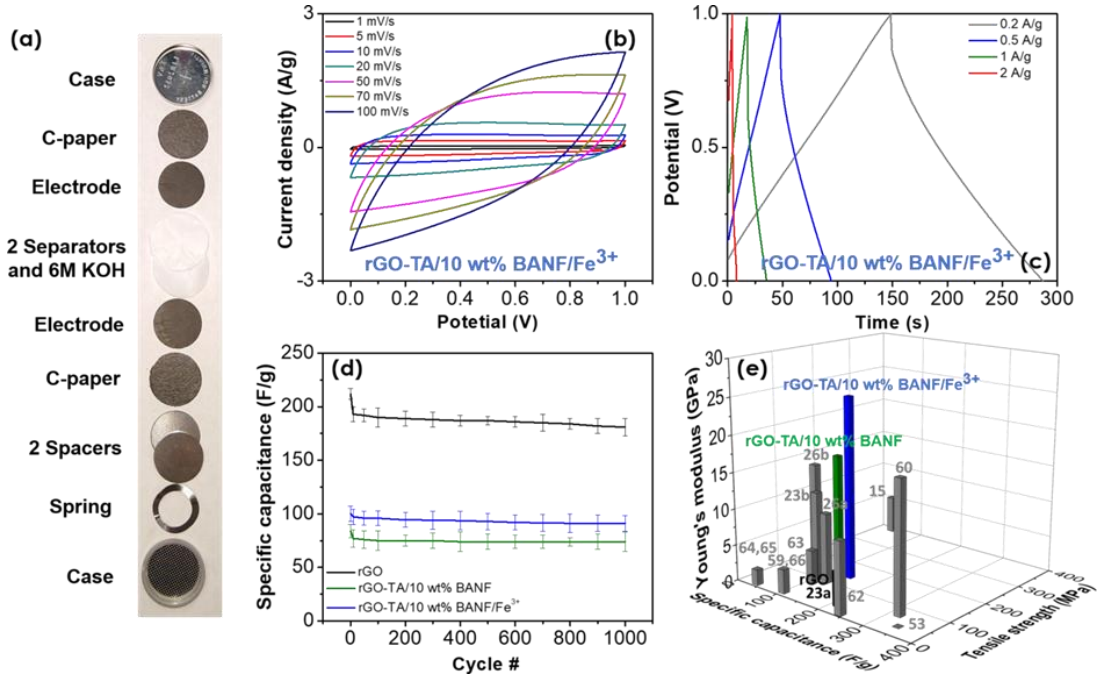

Figure 4.7 (a) Digital image of the parts of a 2-electrode symmetric coin cell. (b) Cyclic voltammetry curves at different scan rates (1-100 mV/s) and (c) galvanostatic charge-discharge curves at different current densities (0.2-2 A/g) for rGO-TA/10 wt% BANF/Fe^{3+}. (d) Specific capacitance *vs.* cycle number at 0.5 A/g for 1000 cycles. (e) Ashby plot of Young's modulus vs. specific capacitance *vs.* tensile strength for mechanically strong supercapacitor electrodes. Grey bars represent data obtained from the literature and the numbers correspond to references from this chapter.

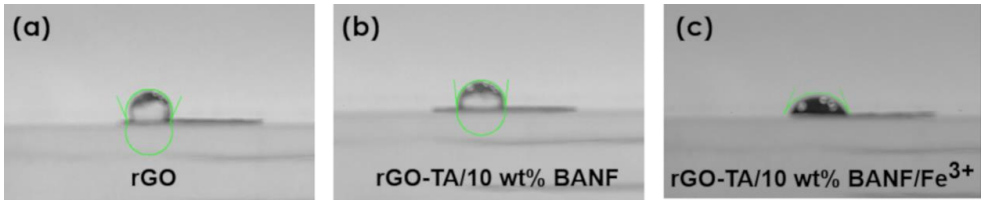

Figure 4.8 Contact angle images for (a) rGO, (b) rGO-TA/10 wt% BANF, and (c) GO-TA/10 wt% BANF/ Fe^{3+} electrodes using 10 µl of 6M KOH.

Galvanostatic charge-discharge tests at variant current densities (0.2-2 A/g) were also conducted, as shown in Figure 4.7c. The curves exhibited triangular shapes and the discharge time decreased with current density. Prolonged charge-discharge tests at 0.5 A/g for 1000 cycles were conducted (Figure 4.7d). The electrodes exhibited good electrochemical stability with a capacitance retention of 85 % for rGO, 89 % for rGO-TA/10 wt% BANF, and 91 % rGO-TA/10 wt% BANF/Fe^{3+}. Similar trends were observed from the Ragone plots, Figure 4.9.

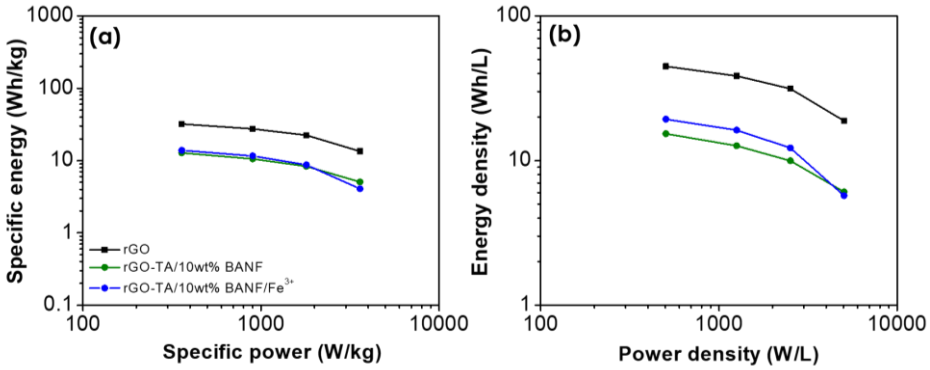

Figure 4.9 Ragone plots of (a) Specific energy (Wh/kg) *vs.* specific power (W/kg) and (b) energy density (Wh/L) *vs.* power density (W/L) for rGO, rGO-TA/10 wt% BANF, and rGO-TA/10 wt% BANF/Fe^{3+}.

Figure 4.7e illustrates Ashby plots of the Young's modulus *vs.* specific capacitance *vs.* tensile strength for mechanically strong supercapacitor electrodes.[2, 29, 35, 36, 38-43] The TA composites exhibited a better combination of properties compared against other rGO containing composites such as rGO/CNT,[39] rGO-NH_2/ANF,[2] and rGO-dopamine (DOPA)[17] because of the stronger synergistic interfacial interactions. rGO,[2] rGO/MnO_2[38] and SWCNT-PPy-CE[36] exhibited higher specific capacitance than the rGO-TA/10 wt%

BANF composites. However, the rGO-TA/10 wt% BANF/Fe^{3+} electrodes maintained high specific capacitance and tensile strength values with a superior Young's modulus. To demonstrate the combination of mechanical and electrochemical properties the multifunctional efficiency was calculated. The rGO-TA-based composite films exhibited a multifunctional efficiency significantly higher than 1 (9.5 – 10.8 *vs.* 3.4 for rGO) when compared against epoxy and carbon aerogel indicating mass and volume savings.[44, 45]

At this point, it is worth mentioning research efforts elsewhere focused upon activated carbon fibers as structural supercapacitor electrodes. The carbon fiber-based electrodes exhibit significantly higher mechanical properties (tensile strength of 3960 MPa and Young's modulus of 207 GPa), but they suffer from low electrochemically active surface area leading to extremely poor electrochemical performance (*e.g.*, specific capacitance of 2.63 F/g).[46] Additionally, other researchers have focused on different device architectures such as spine-like or accordion-like batteries to combine good mechanical performance with energy storage.[47, 48]

A prototype flexible device was fabricated to display the energy storage capability of the electrodes while bearing mechanical loads. The rGO-TA/10 wt% BANF/Fe^{3+} composites were used as the electrodes, and H_3PO_4-polyvinyl(alcohol) (PVA) gel was the electrolyte, (Figure 4.10a). Electrochemical testing was conducted in flat and in bent states (bending radius: 0.6 cm) using cyclic voltammetry at a scan rate of 20 mV/s, as shown in Figure 4.9b. Cyclic bending up to 100 cycles had no significant effect on the CV curves and the initial specific capacitance (48 F/g), as shown in Figure 4.10c. The results indicate excellent electrochemical stability when mechanical loads are applied. Cyclic

voltammetry at lower scan rates showed significantly higher specific capacitances- up to 120 F/g at 1 mV/s, as shown in Figure 4.10d, 4.10e, and 4.10f.

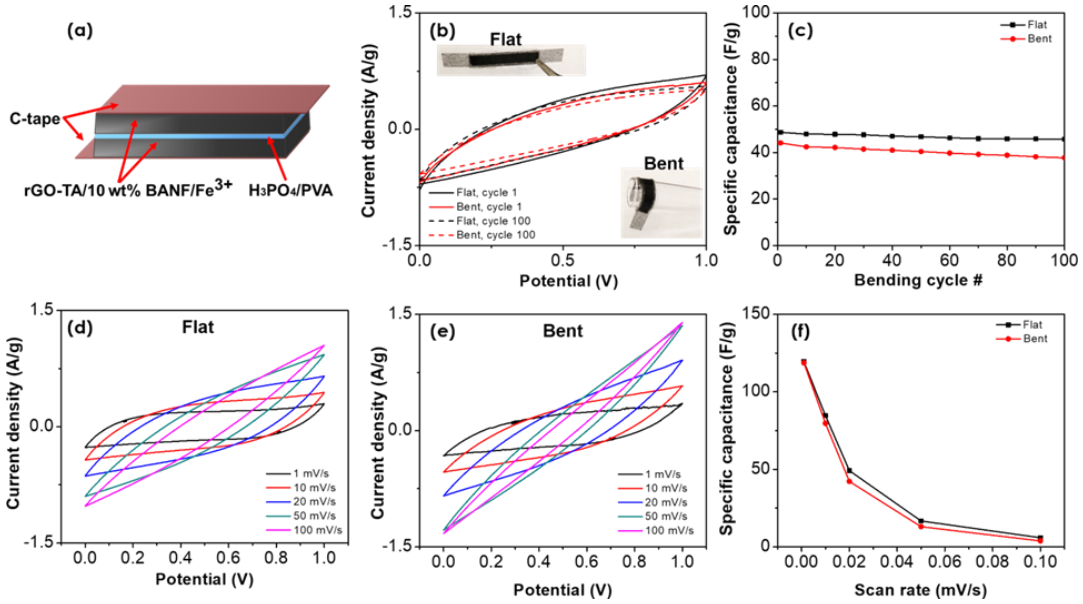

Figure 4.10 (a) Schematic representation of the flexible device. (b) Cyclic voltammetry curves for the rGO-TA/10 wt% BANF/Fe^{3+} flexible supercapacitor at 20 mV/s in flat and bent states. (c) Specific capacitance *vs.* bending cycle. Cyclic voltammetry curves at variant scan rates (1 - 100 mV/s) in (d) flat and (e) bent states. (f) Specific capacitance *vs.* scan rate for the rGO-TA/10 wt% BANF/Fe^{3+} flexible device in flat and bent states.

4.4. Conclusions

Mechanically strong electrodes were fabricated by simultaneously leveraging hydrogen bonding and metal ion coordination bonding interactions. rGO/BANF electrodes were modified with tannic acid to enhance the hydrogen bonding interactions and multivalent ions were introduced to create coordination bonding. The modified electrodes exhibited a five-fold increase in Young's modulus and a four-fold increase in

tensile strength compared to pure rGO (no BANFs) as a result of the synergy of the different interfacial interactions. Moreover, the electrodes maintained high electrical conductivity and capacitance making them ideal candidates for structural or even flexible electrodes. These results demonstrate that synergistic bonding leads to enhancements in mechanical performance while maintaining the energy storage ability of the next-generation electrodes.

4.5. References

1. Flouda, P.; Shah, S. A.; Lagoudas, D. C.; Green, M. J.; Lutkenhaus, J. L., Highly Multifunctional Dopamine-Functionalized Reduced Graphene Oxide Supercapacitors. *Matter* **2019,** *1* (6), 1532-1546.
2. Flouda, P.; Feng, X. Y.; Boyd, J. G.; Thomas, E. L.; Lagoudas, D. C.; Lutkenhaus, J. L., Interfacial Engineering of Reduced Graphene Oxide for Aramid Nanofiber-Enabled Structural Supercapacitors. *Batteries Supercaps* **2019,** *2* (5), 464-472.
3. Zhou, T.; Boyd, J. G.; Loufakis, D.; Lutkenhaus, J. L.; Lagoudas, D. C., Fabrication, characterization and micromechanics modeling of the electrical conductivity of reduced graphene oxide/aramid nanofiber nanocomposites. *Smart Materials and Structures* **2019,** *28* (9), 094001.
4. Kwon, S. R.; Harris, J.; Zhou, T.; Loufakis, D.; Boyd, J. G.; Lutkenhaus, J. L., Mechanically Strong Graphene/Aramid Nanofiber Composite Electrodes for Structural Energy and Power. *ACS Nano* **2017,** *11* (7), 6682-6690.
5. Liu, R.-Y.; Xu, A.-W., Byssal threads inspired ionic cross-linked narce-like graphene oxide paper with superior mechanical strength. *RSC Advances* **2014,** *4* (76), 40390-40395.
6. Wu, C.; Li, T.; Liao, C.; Li, L.; Yang, J., Tea polyphenol-inspired tannic acid-treated polypropylene membrane as a stable separator for lithium–oxygen batteries. *Journal of Materials Chemistry A* **2017,** *5* (25), 12782-12786.
7. Lim, M.-Y.; Shin, H.; Shin, D. M.; Lee, S.-S.; Lee, J.-C., Poly(vinyl alcohol) nanocomposites containing reduced graphene oxide coated with tannic acid for humidity sensor. *Polymer* **2016,** *84*, 89-98.
8. Jia, M.-Y.; Xu, L.-S.; Li, Y.; Yao, C.-L.; Jin, X.-J., Synthesis and characterization of graphene/carbonized paper/tannic acid for flexible composite electrodes. *New Journal of Chemistry* **2018,** *42* (17), 14576-14585.
9. Pan, L.; Wang, H.; Wu, C.; Liao, C.; Li, L., Tannic-Acid-Coated Polypropylene Membrane as a Separator for Lithium-Ion Batteries. *ACS Applied Materials & Interfaces* **2015,** *7* (29), 16003-16010.

10. Hummers, W. S.; Offeman, R. E., Preparation of Graphitic Oxide. *J. Am. Chem. Soc.* **1958,** *80* (6), 1339-1339.
11. Zhu, J.; Yang, M.; Emre, A.; Bahng, J. H.; Xu, L.; Yeom, J.; Yeom, B.; Kim, Y.; Johnson, K.; Green, P.; Kotov, N. A., Branched Aramid Nanofibers. *Angew. Chem. Int. Ed.* **2017,** *56* (39), 11744-11748.
12. Dreyer, D. R.; Park, S.; Bielawski, C. W.; Ruoff, R. S., The chemistry of graphene oxide. *Chem. Soc. Rev.* **2010,** *39* (1), 228-240.
13. Park, S.; Lee, K.-S.; Bozoklu, G.; Cai, W.; Nguyen, S. T.; Ruoff, R. S., Graphene Oxide Papers Modified by Divalent Ions—Enhancing Mechanical Properties via Chemical Cross-Linking. *ACS Nano* **2008,** *2* (3), 572-578.
14. Kudin, K. N.; Ozbas, B.; Schniepp, H. C.; Prud'homme, R. K.; Aksay, I. A.; Car, R., Raman spectra of graphite oxide and functionalized graphene sheets. *Nano Lett.* **2008,** *8* (1), 36-41.
15. Ferrari, A. C.; Basko, D. M., Raman spectroscopy as a versatile tool for studying the properties of graphene. *Nature Nanotechnology* **2013,** *8* (4), 235-246.
16. Lei, Y.; Tang, Z.; Liao, R.; Guo, B., Hydrolysable tannin as environmentally friendly reducer and stabilizer for graphene oxide. *Green Chemistry* **2011,** *13* (7), 1655-1658.
17. Flouda, P.; Shah, S. A.; Lagoudas, D. C.; Green, M. J.; Lutkenhaus, J. L., Highly Multifunctional Dopamine-Functionalized Reduced Graphene Oxide Supercapacitors. *Matter* **2019**.
18. Wan, S.; Xu, F.; Jiang, L.; Cheng, Q., Superior Fatigue Resistant Bioinspired Graphene-Based Nanocomposite via Synergistic Interfacial Interactions. *Adv. Funct. Mater.* **2017,** *27* (10), 1605636.
19. Benselfelt, T.; Nordenström, M.; Lindström, S. B.; Wågberg, L., Explaining the Exceptional Wet Integrity of Transparent Cellulose Nanofibril Films in the Presence of Multivalent Ions—Suitable Substrates for Biointerfaces. *Advanced Materials Interfaces* **2019,** *6* (13), 1900333.
20. Liu, L.; Gao, Y.; Liu, Q.; Kuang, J.; Zhou, D.; Ju, S.; Han, B.; Zhang, Z., High Mechanical Performance of Layered Graphene Oxide/Poly(vinyl alcohol) Nanocomposite Films. *Small* **2013,** *9* (14), 2466-2472.
21. Gao, Y.; Liu, L.-Q.; Zu, S.-Z.; Peng, K.; Zhou, D.; Han, B.-H.; Zhang, Z., The Effect of Interlayer Adhesion on the Mechanical Behaviors of Macroscopic Graphene Oxide Papers. *ACS Nano* **2011,** *5* (3), 2134-2141.
22. Kuila, T.; Bose, S.; Mishra, A. K.; Khanra, P.; Kim, N. H.; Lee, J. H., Chemical functionalization of graphene and its applications. *Prog. Mater Sci.* **2012,** *57* (7), 1061-1105.
23. Tianyang, Z.; James, G. B.; Dimitrios, L.; Jodie, L.; Dimitris, C. L., Fabrication, characterization and micromechanics modeling of the electrical conductivity of reduced graphene oxide/aramid nanofiber nanocomposites. *Smart Mater. Struct.* **2019**.
24. Sasso, C.; Zeno, E.; Petit-Conil, M.; Chaussy, D.; Belgacem, M. N.; Tapin-Lingua, S.; Beneventi, D., Highly Conducting Polypyrrole/Cellulose Nanocomposite Films with Enhanced Mechanical Properties. *Macromolecular Materials and Engineering* **2010,** *295* (10), 934-941.

25. Blighe, F. M.; Diamond, D.; Coleman, J. N.; Lahiff, E., Increased response/recovery lifetimes and reinforcement of polyaniline nanofiber films using carbon nanotubes. *Carbon* **2012,** *50* (4), 1447-1454.
26. Han, X.; Lv, L.; Yu, D.; Wu, X.; Li, C., Conductive Core–Shell Aramid Nanofibrils: Compromising Conductivity with Mechanical Robustness for Organic Wearable Sensing. *ACS Applied Materials & Interfaces* **2019,** *11* (3), 3466-3473.
27. Hou, M.; Xu, M.; Li, B., Enhanced Electrical Conductivity of Cellulose Nanofiber/Graphene Composite Paper with a Sandwich Structure. *ACS Sustainable Chemistry & Engineering* **2018,** *6* (3), 2983-2990.
28. Wan, S.; Hu, H.; Peng, J.; Li, Y.; Fan, Y.; Jiang, L.; Cheng, Q., Nacre-inspired integrated strong and tough reduced graphene oxide–poly(acrylic acid) nanocomposites. *Nanoscale* **2016,** *8* (10), 5649-5656.
29. Li, S.; Zhao, C.; Shu, K.; Wang, C.; Guo, Z.; Wallace, G. G.; Liu, H., Mechanically strong high performance layered polypyrrole nano fibre/graphene film for flexible solid state supercapacitor. *Carbon* **2014,** *79*, 554-562.
30. Cheng, Y.; Lu, S.; Zhang, H.; Varanasi, C. V.; Liu, J., Synergistic effects from graphene and carbon nanotubes enable flexible and robust electrodes for high-performance supercapacitors. *Nano Lett.* **2012,** *12* (8), 4206-11.
31. Gong, S.; Jiang, L.; Cheng, Q., Robust bioinspired graphene-based nanocomposites via synergistic toughening of zinc ions and covalent bonding. *Journal of Materials Chemistry A* **2016,** *4* (43), 17073-17079.
32. Wen, Y.; Wu, M.; Zhang, M.; Li, C.; Shi, G., Topological Design of Ultrastrong and Highly Conductive Graphene Films. *Advanced Materials* **2017,** *29* (41), 1702831.
33. Wan, S.; Li, Y.; Mu, J.; Aliev, A. E.; Fang, S.; Kotov, N. A.; Jiang, L.; Cheng, Q.; Baughman, R. H., Sequentially bridged graphene sheets with high strength, toughness, and electrical conductivity. *Proceedings of the National Academy of Sciences* **2018,** *115* (21), 5359-5364.
34. Wan, S.; Chen, Y.; Wang, Y.; Li, G.; Wang, G.; Liu, L.; Zhang, J.; Liu, Y.; Xu, Z.; Tomsia, A. P.; Jiang, L.; Cheng, Q., Ultrastrong Graphene Films via Long-Chain π-Bridging. *Matter* **2019**.
35. Kim, S. Y.; Hong, J.; Kavian, R.; Lee, S. W.; Hyder, M. N.; Shao-Horn, Y.; Hammond, P. T., Rapid fabrication of thick spray-layer-by-layer carbon nanotube electrodes for high power and energy devices. *Energ Environ Sci* **2013,** *6* (3), 888-897.
36. Che, J. F.; Chen, P.; Chan-Park, M. B., High-strength carbon nanotube buckypaper composites as applied to free-standing electrodes for supercapacitors. *J Mater Chem A* **2013,** *1* (12), 4057-4066.
37. Zhang, L. L.; Zhao, X. S., Carbon-based materials as supercapacitor electrodes. *Chem. Soc. Rev.* **2009,** *38* (9), 2520-31.
38. Sumboja, A.; Foo, C. Y.; Wang, X.; Lee, P. S., Large Areal Mass, Flexible and Free-Standing Reduced Graphene Oxide/Manganese Dioxide Paper for Asymmetric Supercapacitor Device. *Adv. Mater.* **2013,** *25* (20), 2809-2815.
39. Ma, Y.; Li, P.; Sedloff, J. W.; Zhang, X.; Zhang, H.; Liu, J., Conductive Graphene Fibers for Wire-Shaped Supercapacitors Strengthened by Unfunctionalized Few-Walled Carbon Nanotubes. *ACS Nano* **2015,** *9* (2), 1352-1359.

40. Li, Y. N.; Ren, G. Y.; Zhang, Z. Q.; Teng, C.; Wu, Y. Z.; Lu, X. Y.; Zhu, Y.; Jiang, L., A strong and highly flexible aramid nanofibers/PEDOT:PSS film for all-solid-state supercapacitors with superior cycling stability. *J Mater Chem A* **2016,** *4* (44), 17324-17332.
41. Whitten, P. G.; Spinks, G. M.; Wallace, G. G., Mechanical properties of carbon nanotube paper in ionic liquid and aqueous electrolytes. *Carbon* **2005,** *43* (9), 1891-1896.
42. Barisci, J. N.; Wallace, G. G.; Baughman, R. H., Electrochemical studies of single-wall carbon nanotubes in aqueous solutions. *J. Electroanal. Chem* **2000,** *488* (2), 92-98.
43. Rigueur, J. L.; Hasan, S. A.; Mahajan, S. V.; Dickerson, J. H., Buckypaper fabrication by liberation of electrophoretically deposited carbon nanotubes. *Carbon* **2010,** *48* (14), 4090-4099.
44. O'Brien, D.; Baechle, D.; Wetzel, E. J. J. o. C. M., Design and performance of multifunctional structural composite capacitors. *J. Compos. Mater.* **2011,** *45* (26), 2797-2809.
45. Snyder, J.; Gienger, E.; Wetzel, E. J. J. o. C. M., Performance metrics for structural composites with electrochemical multifunctionality. *J. Compos. Mater.* **2015,** *49* (15), 1835-1848.
46. Qian, H.; Diao, H.; Shirshova, N.; Greenhalgh, E. S.; Steinke, J. G. H.; Shaffer, M. S. P.; Bismarck, A., Activation of structural carbon fibres for potential applications in multifunctional structural supercapacitors. *J. Colloid Interface Sci.* **2013,** *395*, 241-248.
47. Shi, C.; Wang, T.; Liao, X.; Qie, B.; Yang, P.; Chen, M.; Wang, X.; Srinivasan, A.; Cheng, Q.; Ye, Q.; Li, A. C.; Chen, X.; Yang, Y., Accordion-like stretchable Li-ion batteries with high energy density. *Energy Storage Materials* **2019,** *17*, 136-142.
48. Qian, G.; Zhu, B.; Liao, X.; Zhai, H.; Srinivasan, A.; Fritz, N. J.; Cheng, Q.; Ning, M.; Qie, B.; Li, Y.; Yuan, S.; Zhu, J.; Chen, X.; Yang, Y., Bioinspired, Spine-Like, Flexible, Rechargeable Lithium-Ion Batteries with High Energy Density. *Advanced Materials* **2018,** *30* (12), 1704947.

5. STRUCTURAL LITHIUM-ION BATTERY ELECTRODES REINFORCED WITH KEVLAR ARAMID NANOFIBERS*

5.1. Introduction

In this chapter, we sought to expand the previous work on reduced graphene oxide (rGO)/branched aramid nanofiber (BANF) structural supercapacitor electrodes to lithium-ion battery systems. The reported rGO/BANF composite electrodes demonstrated a balanced combination of mechanical and energy storage properties.[1-5] These intriguing results led us to speculate that BANFs and rGO may be combined with redox active materials, such as lithium iron phosphate (LFP, cathode) and silicon (Si, anode), to fabricate lithium-ion battery electrodes with enhanced mechanical properties and good energy storage performance.

Lithium metal oxides such as $LiCoO_2$ (LCO), $LiMnO_2$ (LMO), and $LiFePO_4$ (LFP) have been extensively studied as cathode materials for lithium-ion batteries. Out of those, LFP is of great interest due to its high theoretical capacity (170 mAh/g), long cycle life, low cost, and abundancy.[6-8] However, a typical LFP-based cathode has a capacity of 124 mAh/g_{LFP} (at 0.5 C), a tensile strength as low as 0.2 MPa, and a Young's modulus of only 0.02 GPa.[9] Reports on structural metal oxide-based cathodes are extremely limited due to their inherently poor mechanical performance. Free-standing LFP/carbon nanotube (CNT) cathodes exhibited a capacity of 150 mAh/g_{LFP} at 0.1 C with a tensile strength of 2.5 MPa

*Modified and reprinted from "Structural lithium-ion battery electrodes reinforced with Kevlar aramid nanofibers" by Paraskevi Flouda, Suyash Oka, Dimitrios Loufakis, Dimitris C. Lagoudas and Jodie L. Lutkenhaus, *In preparation*

and a Young's modulus of 0.1 GPa.[10] Despite the high capacities of the metal oxide-based cathodes, their extremely poor mechanical performance hinders their use in structural applications.

Similarly, commercial graphite anodes (theoretical capacity 372 mAh/g) demonstrate a capacity of 330 mAh/$g_{graphite}$ (at 0.1 C) with a tensile strength of 3.7 MPa, and a Young's modulus of 0.7 GPa.[11] Higher capacity values may be achieved using silicon (Si) - based anodes. Si has been widely explored in lithium-ion battery anodes due to its abundancy and high theoretical capacity (3579 mAh/g, for $Li_{3.7}Si$), almost ten times higher than the theoretical capacity of graphite (372 mAh/g).[12, 13] Si/MXene/sodium alginate anodes exhibited capacity values of 900 mAh/g_{Si} at 0.5 C.[14] Despite the high capacities of the Si-based anodes several challenges need to be addressed. The large volumetric expansion of Si during lithiation/de-lithiation typically leads to particle pulverization, loss of electrical contact, and even delamination.[15] Additionally, free-standing structural silicon-based electrodes are challenging to fabricate and typically suffer from a brittle behaviour. Only a handful of studies on mechanically strong Si-based anodes have been reported.[16-18] Si nanoparticles/poly acrylic acid (PAA)/acetylene black (AC) composite electrodes exhibited capacity values of 2500 mAh/g_{Si} at 0.09 C with a low tensile strength of 12 MPa and a Young's modulus of 1.1 GPa.[18] Further improvement in the mechanical performance of the Si-based anodes is necessary for integration in structural applications.

Here, we report the design of mechanically strong lithium-ion battery cathodes and anodes using BANFs. More specifically, free-standing cathodes and anodes consisting of LFP (cathode) or Si (anode) particles, rGO, and BANFs were fabricated utilizing vacuum-

assisted filtration. LFP and Si acted as the active materials and were chosen due to their high theoretical capacities. rGO provided the electrical conductivity and BANFs served to bind all components together and provide structural support. Hydrogen bonding interactions between rGO and BANFs were harnessed to transfer mechanical loads within the electrodes. Electrical, mechanical, and electrochemical properties for all composite electrodes were evaluated as a function of composition. The BANF-containing electrodes exhibited improved mechanical performance with similar energy storage to commercial electrodes and other structural electrodes from the literature. The improved performance was further evaluated using electrochemical impedance spectroscopy (EIS), scanning electron microscopy (SEM), and x-ray photoelectron microscopy (XPS) before and after electrochemical cycling. This work demonstrates the utilization of Kevlar nanofibers for the design of lithium-ion battery cathodes and anodes with enhanced mechanical properties.

5.2. Materials and Methods

Graphite was purchased from Bay Carbon and Kevlar®69 from Thread Exchange. Sulfuric acid (H_2SO_4), potassium hydroxide (KOH), dimethyl sulfoxide (DMSO), potassium permaganese ($KMnO_4$), sodium nitrate ($NaNO_3$), poly(acrylic acid) (Mv ~ 3,000,000 g/mol), carboxymethylcellulose, 1 M lithium hexafluorophosphate ($LiPF_6$) in ethylene carbonate (EC) : diethyl carbonate (DEC) (1:1, v/v) were purchased from Sigma-Aldrich. polyvinylidene fluoride (PVDF, 5130) was purchased from Solef. Celgard 3501 was provided by Celgard. Silicon nanoparticles (diameter: 50 - 70 nm, 98+% purity) and

lithium iron phosphate ($LiFePO_4$) were purchased from US Research Nano Materials and MTI, respectively. Li foil (0.75 mm x 19 mm) was purchased from Alfa Aesar.

Branched aramid nanofibers (BANFs) were fabricated by the dissolution of chopped Kevlar (0.5 g) fiber in DMSO (50 ml) and KOH (0.5 g), as previously reported.[19] The mixture was stirred for 7-14 days until a dark red dispersion (10 mg/ml) was obtained. Graphene oxide (GO) was synthesized from graphite using a modified Hummers method as reported before.[20]

Desired amounts of Si or LFP dispersions in DMSO (1 mg/ml) were mixed with GO/DMSO (1 mg/ml) and BANF/DMSO (0.2 mg/ml). The total mass of solids was kept at 15 mg. The mixture was stirred for 1h at room temperature, followed by heating at 80 ^oC for 2h. During this step, deionized water (1 ml for every mg of BANFs) was added to reprotonate the BANF amide groups. Finally, vacuum filtration was performed using a Nylon filter membrane (pore size: 0.2 μm and diameter: 47 mm). The electrodes were peeled off the membrane, air-dried overnight, and dried under vacuum at 80 ^oC for three days. The composite films were placed between two heavy tiles to avoid bubble formation and thermally reduced at 200 ^oC for 2h under vacuum to yield reduced graphene oxide (rGO). Finally, the samples were cut to desired shapes (rectangular strips of 2 mm x 20 mm for mechanical testing and circular discs of 16 mm in diameter for electrochemical characterization).

Scanning electron microscopy (SEM) and energy dispersive X-ray spectroscopy (EDS) were performed using a JEOL SM-7500 SEM with an Oxford EDS detector. The thickness of the electrodes was measured using a gauge height (Tesa μ-Hite) and verified

using cross-sectional SEM. X-ray diffraction and Raman spectroscopy were performed using a Brucker D8 X-ray with a Cu (Kα, λ = 1.541 Å) and a Horiba Jobin-Yvon Lab Ram HR microscope with 633 nm excitation, respectively. X-ray photoelectron spectroscopy (XPS) was performed utilizing an Omicron ESCA Probe with Mg Kα radiation (hm = 1253.6 eV). Survey scans were performed with steps of 1.0 eV and 50 ms dwell time within a range of 10 – 1100 eV. High resolution scans were performed with steps of 0.05 eV and 250 ms dwell time. All spectra were calibrated using the C1s peak for sp^2-hybridized carbon atoms (284.5 eV). Furthermore, gaussian-lorentzian peak shape fitting and Shirley background correction were performed and the FWHM of the deconvoluted peaks was constrained.

Static uniaxial tensile tests were performed using a DMA Q800 (TA Instruments) at strain mode with a strain rate of 0.1 %/min and preload force of 0.01 Nt. Electrical conductivity measurements were conducted using a Keithley 2110 digital multimeter. Silver paste was used to attach four copper wires on the surface of the electrodes and conductivity values were calculated based on the measured resistance and film geometry. Tensile tests and electrical conductivity measurements were conducted at room temperature (~ 23 ^{o}C) and humidity (35-45%).

Electrochemical testing for the composite electrodes (diameter: 16 mm, thickness: 3 – 8 μm, and mass: ~ 6 mg) was performed in half-cells using a lithium metal foil (diameter: 16 mm, thickness: 0.75 mm, and mass: 0.08 g) as the reference/counter electrode at room temperature (~ 23 ^{o}C). Two Celgard 3501 membranes (diameter: 19 mm, thickness: ~ 21 μm, and mass: ~ 3 mg) were used as the separators, a stainless steel disk (diameter: 16

mm, thickness: 1 mm, and mass: 2.5 g) as the current collector, a stainless steel spring (diameter: ~ 16 mm, thickness: ~ 1 mm, and mass: 0.7 g), stainless steel top and bottom gaskets (diameter: 7.6 cm, thickness: ~ 16 mm, and mass: ~ 437 g), and 200 µl of 1 M $LiPF_6$ in EC:DEC (1:1 v/v) as the electrolyte. Si-containing electrodes were tested at a potential window of 0.01 – 2 V *vs.* Li/Li^+, while LFP-containing electrodes at 2.5 – 4.2 V *vs.* Li/Li^+. Cyclic voltammetry at different scan rates (0.1 – 50 mV/s) and galvanostatic cycling at varying C-rates (0.3 – 6 C) were conducted using Solatron potentiostats (Solatron Interface 1287 and Solatron 1470E). Charge-discharge currents for each C-rate were calculated from the theoretical capacity of LFP (170 mAh/g) and Si (3579 mAh/g). Prior to testing all cells were preconditioned using cyclic voltammetry at 20 mV/s for 10 cycles. Electrochemical impedance spectroscopy (EIS) was conducted on new and cycled electrodes for 5, 10, and 200 cycles using a Gamry interface 1000. For Si-containing electrodes a 10 mV AC amplitude with a frequency range of 100 kHz to 10 mHz at 0.2 V *vs.* Li/Li^+ was used. For LFP-containing electrodes a 10 mV AC amplitude with a frequency range of 100 kHz to 10 mHz at 3.5 V *vs.* Li/Li^+ was used.

5.3. Results and Discussion

Free-standing lithium-ion battery electrodes were fabricated using vacuum-assisted filtration. Dispersions of LFP and Si particles for the cathode and anode, respectively, were mixed with GO and BANFs in dimethyl sulfoxide followed by vacuum filtration. The formed thin films were thermally reduced at 200 ^oC to restore GO's electrical conductivity. Reduced GO (rGO) serves as the conductive additive while BANFs provide the structural support and act as a binder, ensuring good contact between all components

(Figure 5.1). More specifically, BANFs interact with rGO mainly though hydrogen bonding interactions between the rGO oxygen-containing groups and BANF amide groups allowing for load transfer within the composite electrodes.[2, 5]

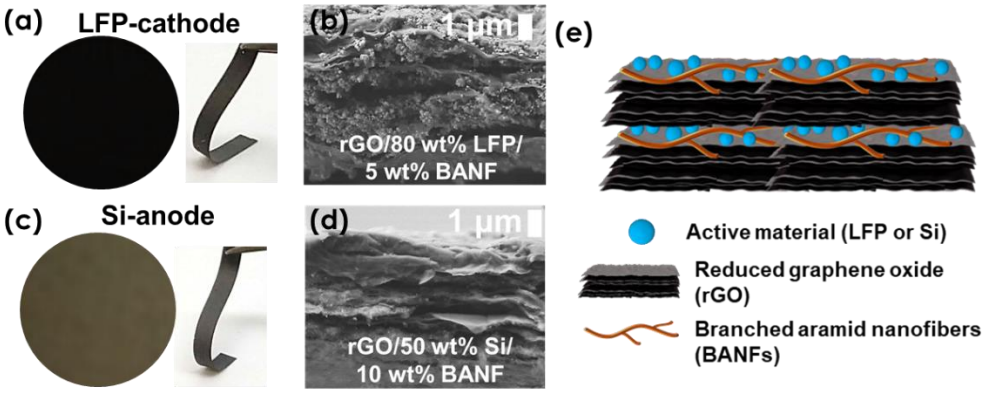

Figure 5.1 (a) Digital images and (b) cross-sectional scanning electron microscopy images for rGO/BANF/LFP cathodes. (c) Digital images and (d) cross-sectional scanning electron microscopy images for rGO/BANF/Si anodes. (e) Schematic representation for rGO/BANF lithium-ion battery electrodes.

The composite electrodes demonstrated qualitatively good mechanical properties and highly layered structures, Figure 5.1. rGO flakes and LFP/Si particles were visible from the cross-sectional SEM images. The highest LFP content for the rGO/LFP (without BANFs) cathodes was 50 wt%, while BANF addition allowed for LFP contents up to 80 wt%. Similarly, the highest Si content achieved for the rGO/Si (without BANFs) anodes was 50 wt%. Higher active material contents led to brittle films that cracked upon air-drying.

The addition of BANFs, LFP, and Si in rGO films was verified using XPS, Raman spectroscopy, and XRD. Figure 5.2 depicts the XPS survey scans and elemental analysis for the composite rGO/LFP cathodes and rGO/Si anodes. More specifically, rGO was composed of 87 atomic percent (at%) carbon and 13 at% oxygen. rGO/50 wt% LFP had 78 at% carbon, 14 at% oxygen, and small amounts (< 4 at%) of lithium, iron, and phosphorus. Upon addition of BANFs an additional peak at 396 – 402 eV appeared corresponding to 3 at% nitrogen. Similarly, the Si-based anodes contained 6 – 12 at% silicon. The low contents of lithium, iron, phosphorus, and silicon on the surface of the composites obtained using XPS are attributed to its low penetration depth (up to 10 nm).

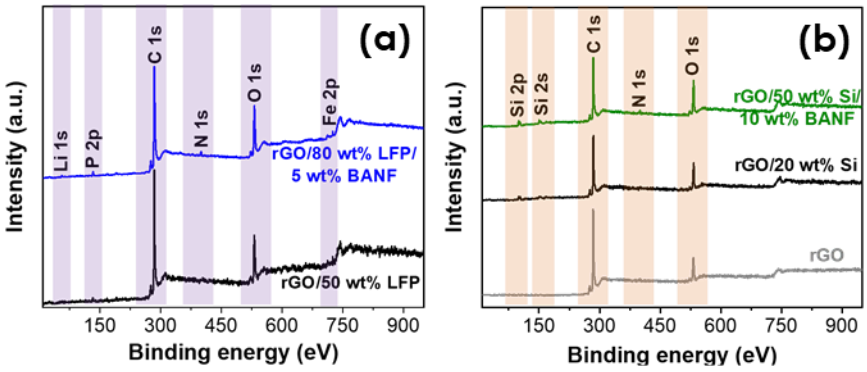

Figure 5.2 XPS survey scans for (a) rGO/LFP/BANF cathodes and (b) rGO/Si/BANF anodes with different compositions.

The modifications were further verified using Raman spectroscopy (Figure 5.3a) and XRD (Figure 5.3b-5.3c). rGO exhibited the two characteristic bands for carbon-based materials, the D-band at ~1318 cm^{-1} and G-band at ~1585 cm^{-1}. The D-band arises from the sp^3-hybridized carbon atoms, while the G-band from the sp^2-hybridized carbon atoms.[21] The intensity ratio (I_D/I_G) reveals qualitatively the amount of disorder and for

rGO it was equal to 1.0. Upon addition of LFP and Si, the I_D/I_G values remained similar (I_D/I_G = 1.0 - 1.2) indicating no changes in the rGO graphitic structure. The LFP-cathodes showed an additional band of peaks at < 320 cm^{-1} attributed to vibrations of Fe-O, while a peak at ~ 486 cm^{-1} appeared for the Si-anodes due to the Si addition.[21, 22] Figure 5.3b-5.3c shows the X-ray diffractograms for dried electrodes before reduction (after reduction it is difficult to determine the GO peaks). GO exhibited a broad diffraction peak at 2θ = 19.3° (002). LFP and Si addition led to additional diffraction peaks attributed to orthorhombic (*Pnma*) olivine $LiFePO_4$ (COD No. 7222394) and Si, respectively. The addition of 20 wt% Si led to a decrease in d-spacing from 4.6 Å to 4.3 Å, while further increase in Si to 50 wt% and BANF addition (10 wt%) led to a d-spacing of 4.0 Å. The decreasing d-spacing indicates that BANFs and Si wrap around the rGO flakes reducing the interplanar distance between GO sheets. The d-spacing was not calculated for the cathodes as the GO (002) diffraction peak was no longer visible due to the low GO content and the location of the LFP peaks.

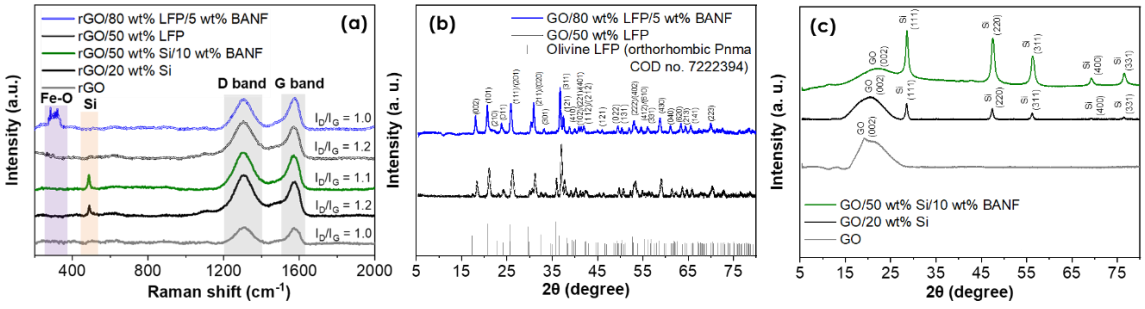

Figure 5.3 (a) Raman spectra for rGO, rGO/20 wt% Si, rGO/50 wt% Si/10 wt% BANF, rGO/50 wt% LFP, and rGO/80 wt% LFP/5 wt% BANF. XRD patterns for (b) LFP-cathodes and (c) Si-anodes.

The mechanical performance of the LFP-based cathodes was evaluated using tensile tests, as shown in Figure 5.4a. Addition of 50 wt% LFP in pure rGO films did not lead to significant changes in the mechanical performance. More specifically, rGO/50 wt% LFP cathodes exhibited a Young's modulus of 5.4 ± 0.5 GPa (*vs.* 5.0 ± 1.0 GPa for rGO)[5], tensile strength of 32 ± 3 MPa (*vs.* 35 ± 6 MPa for rGO)[5], ultimate strain of 0.7 ± 0.1 % (*vs.* 0.8 ± 0.1 % for rGO)[5], and toughness of 105 ± 5 kJ/m^3 (*vs.* 120 ± 30 kJ/m^3 for rGO)[5]. This may be attributed to the highly layered structures that were maintained upon LFP addition, as discussed in following paragraphs, which allows for efficient load transfer within the composites.[23] Addition of more LFP (80 wt%) and BANFs (5 wt%) led to improved mechanical performance resulting from the strong and stiff BANFs that bind all components together. More specifically, hydrogen bonding interactions between the rGO oxygen-containing groups and the BANF amide groups as well as π-π stacking interactions were harnessed and served to efficiently transfer mechanical loads within the composite electrodes. rGO/80 wt% LFP/5 wt% BANF cathodes showed a 44 % improvement in tensile strength (46 ± 4 MPa), 72 % in ultimate strain (1.2 ± 0.1 %), and 176 % in toughness (290 ± 30 kJ/m^3). Young's modulus remained within the initial range due to the high LFP content. Further addition of BANFs up to 10 wt% led to a deteriorated performance, as also observed in our previous studies for rGO/BANF supercapacitors,[2, 5] due to possible agglomerations of the BANFs.

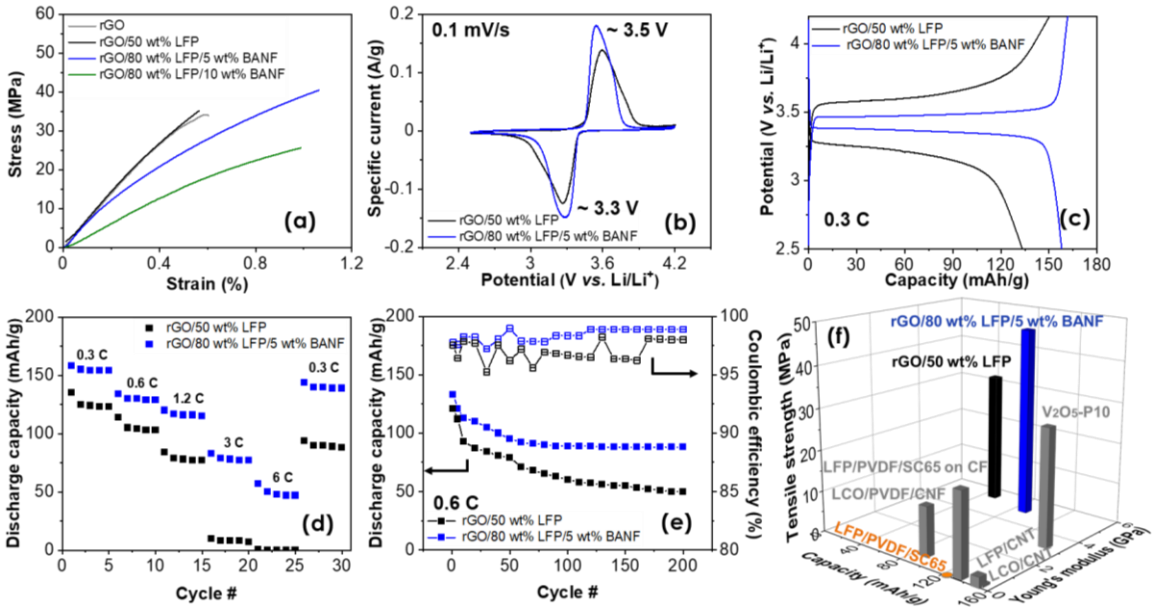

Figure 5.4 (a) Representative stress-strain curves for rGO[5], rGO/50 wt% LFP, rGO/80 wt% LFP/5 wt% BANF, and rGO/80 wt% LFP/10 wt% BANF. (b) Cyclic voltammograms at 0.1 mV/s, (c) potential profiles at 0.3 C, (d) galvanostatic cycling at different C-rates (0.3 C- 6 C), and (e) prolonged galvanostatic cycling at 0.6 C for 200 cycles for rGO/50 wt% LFP and rGO/80 wt% LFP/5 wt% BANF in a lithium metal half-cell. (f) Ashby plot for tensile strength *vs.* Young's modulus *vs.* capacity. Grey bars correspond to data obtained from the literature for lithium-ion batteries and the orange cylinder is the equivalent to a commercial LFP cathode. All capacities were calculated based on active material (LFP, LCO, or V_2O_5) mass loadings.

Four-point probe measurements were used to evaluate the electrical conductivity of the LFP-based cathodes. Addition of 50 wt% LFP led to an electrical conductivity of 19 ± 2 S/cm (*vs.* 28 ± 2 S/cm for rGO). Despite the high LFP content, the obtained

electrical conductivity values were similar to pure rGO electrodes indicating the formation of homogeneous electrodes. LFP particles do not disrupt the layered structure of the conductive rGO networks maintaining high electrical conductivity values. Further increase in LFP content up to 80 wt% and addition of BANFs led to lower electrical conductivity values, due to addition of non-conductive materials. Overall, the obtained electrical conductivity values are comparable to other LFP-based cathodes.[24] rGO/50 wt% LFP and rGO/80 wt% LFP/5 wt% BANF were selected to be tested as cathodes as they led to the best combination of mechanical and electrical properties.

The electrochemical performance of the LFP-based structural cathodes was investigated in a two-electrode lithium metal half-cell using 1M $LiPF_6$ in EC:DEC (1:1 v/v) as the electrolyte. All data are reported based on LFP mass loading. Figure 5.4b shows the cyclic voltammograms at a scan rate of 0.1 mV/s in a potential window of 2.5 – 4.2 V *vs.* Li/Li^+. rGO/50 wt% LFP and rGO/80 wt% LFP/5 wt% BANF exhibited a couple of peaks at ~3.5 V (anodic) and ~3.3 V (cathodic) attributed to the Fe^{2+}/Fe^{3+} redox reaction with a midpoint of ~3.4 V which is in accordance with the literature for LFP-based cathodes.[25, 26] rGO/80 wt% LFP/5 wt% BANF demonstrated slightly narrower peaks with higher specific current values compared to rGO/50 wt% LFP. The results indicate smaller diffusion limitations, as well as higher electrochemical activity.[25] Furthermore, the separation potential for rGO/50 wt% LFP was 0.33 V while for rGO/80 wt% LFP/5 wt% BANF it was 0.26 V, indicating improved reversibility.[25, 27]

Additionally, galvanostatic cycling was conducted at varying C-rates (0.3 C – 6 C), as shown in Figure 5.4c-5.4d. More specifically, both electrodes exhibited plateaus at

~ 3.4 V *vs.* Li/Li^+ which are attributed to the Fe^{2+}/Fe^{3+} redox reactions.[25] rGO/50 wt% LFP showed a capacity of 135 mAh/g at 0.3 C and 70 % of the initial capacity was recovered after testing at 6 C. rGO/80 wt% LFP/5 wt% BANF demonstrated a capacity of 158 mAh/g at 0.3 C with a capacity retention of 91 %. Furthermore, prolonged galvanostatic cycling at 0.6 C up to 200 cycles was conducted, as shown in Figure 5.4e. The BANF-containing cathodes exhibited a capacity retention of 66 % after 200 cycles with a coulombic efficiency of 98.9% (*vs.* 97.5 % for the first cycle), while rGO/50 wt% LFP demonstrated a lower capacity retention of 41 % with a coulombic efficiency of 98 % (*vs.* 96.4 % for the first cycle). The results are consistent with the cyclic voltammograms and further support the initial assessment of the enhanced energy storage performance of the BANF-containing cathodes. Indicative of the more stable cycling performance of the BANF-containing cathodes is also the slope of the capacity *vs.* cycling number plot starting from the 50^{th} cycle, with the slope decreasing from 2 to 0.05 upon BANF addition. The higher capacity values of the BANF-containing cathodes (158 mAh/g at 0.3 C *vs.* theoretical capacity of 170 mAh/g) result from the higher LFP content while the enhanced capacity retention with C-rate and cycling number result from the BANFs that act as a binder maintaining the structural integrity of the cathodes. To further support this, in depth characterization such as EIS, SEM, and XPS, before and after cycling are shown in following sections.

The energy storage performance of the LFP-cathodes was compared against high energy storage performing rGO/LFP cathodes, as well as commercial LFP-based cathodes from the literature (Figure 5.5). More specifically, Figure 5.5a shows the Ragone plot for

specific energy (Wh/kg) *vs.* specific power (W/kg) based on LFP mass loading. To our knowledge there are limited reports on rGO/LFP cathodes and most reports refer to electrodes containing also additional binders and conductive additives. rGO/LFP electrodes were compared against rGO/LFP/carbon black (CB)/polytetra fluoroethylene (PTFE) (3:72:10:5 wt/wt)[28], rGO decorated LFP/CB/polyvinylidene fluoride (PVDF) (2:78:15:5 wt/wt),[29] rGO/LFP doped with Mg^{2+}(LFMP)/CB/PVDF (2:78:10:10 wt/wt)[30], and LFP/CB/PVDF (90:5:5, wt/wt) (which is equivalent to commercial LFP-cathodes)[9] slurry electrodes coated on aluminum foil, as well as rGO/LFP (20:80 wt/wt)[31] electrodes sprayed on aluminum foil. rGO/50 wt% LFP exhibited deteriorated performance with a specific energy of 229.5 Wh/kg at a specific power of 85 W/kg and 0.34 Wh/kg at 1700 W/kg. The BANF containing cathodes demonstrated a specific energy of 268.6 Wh/kg at 85 W/kg and 79.9 Wh/kg at 1700 W/kg. Traditional rGO/LFP electrodes and commercial LFP cathodes, exhibited comparable specific energy values but with improved rate capability.[28-30] For example, rGO decorated LFP/CB/polyvinylidene fluoride (PVDF) (2:78:15:5 wt/wt) coated on Al foil demonstrated a specific energy of 263.5 Wh/kg at 57.8 W/kg and 163.2 Wh/kg at 5780 W/kg.[29] Similar trends were also observed based on total electrode mass, as shown in Figure 5.5b. Ragone plots for energy density (Wh/L) *vs.* power density (W/L) are shown in Figure 5.5c-5.5d. All literature reported rGO/LFP cathodes were coated on Al foil for structural support and their mechanical performance was not reported.

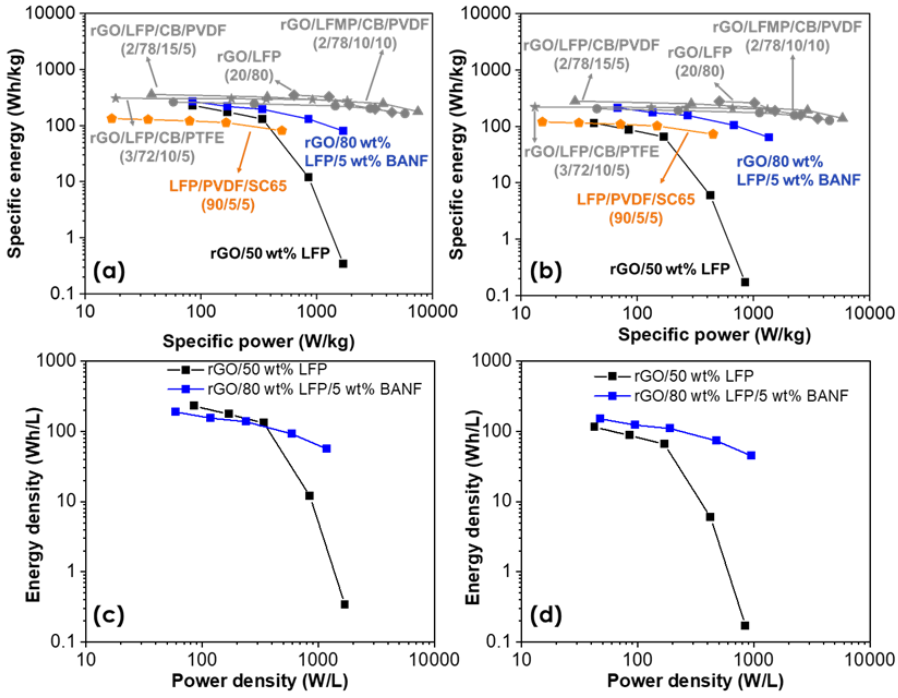

Figure 5.5 Ragone plots for (a, b) specific energy (Wh/kg) *vs.* specific power (W/kg) and (c, d) energy density (Wh/L) *vs.* power density (W/L) for rGO/50 wt% LFP and rGO/80 wt% LFP/5 wt% BANF compared against traditional rGO/LFP cathodes for lithium-ion batteries from the literature (grey) based on (a, c) LFP mass loading and (b, d) total electrode mass. Orange data correspond to commercial LFP cathodes as obtained from the literature. Numbers in parenthesis indicate the weight fractions for each component for data obtained from the literature.

Furthermore, the energy storage and mechanical performance of our structural LFP-cathodes were compared against commercial LFP cathodes and other structural cathodes, as shown in Figure 5.4f. Reports on structural cathodes are limited due to their inherently bad mechanical performance. We compared the LFP-cathodes with commercial

LFP/CB/PVDF (90:5:5, wt/wt),[9] LFP/CNT,[10] LFP/CB/PVDF (90:5:5, wt/wt) coated on carbon fiber fabric (CF),[9] LCO/CF/PVDF (82:7:11, wt/wt),[32] LCO/CNT,[33] and V_2O_5/P3HT-b-PEO (P10, 90:10 wt/wt) in an Ashy plot of tensile strength *vs.* Young's modulus *vs.* capacity.[34] The capacities reported are based on active mass loading and correspond to the last cycle after prolonged galvanostatic cycling to account also for structural robustness after cycling. Our LFP-cathodes demonstrated the best mechanical performance with comparable energy storage performance to other structural cathodes. Only V_2O_5-P10 demonstrated similar but worse mechanical performance with a Young's modulus of 3.2 GPa, tensile strength of 28.5 MPa, and a capacity of 145 mAh/g (based on V_2O_5 mass).[34] Commercial LFP cathodes,[9] LFP/CNT,[10] LFP/CB/PVDF coated on CF,[9] LCO/CF/PVDF,[32] and LCO/CNT[33] demonstrated significantly worse mechanical performance with a maximum overall Young's modulus of 0.65 GPa and tensile strength of 20 MPa *vs.* a Young's modulus of 5 ± 0.4 GPa and tensile strength of 46 ± 5 MPa for rGO/80 wt% LFP/5 wt% BANF. The enhanced mechanical performance of the BANF-containing cathodes is attributed to the strong and stiff BANFs, as well as the extensive interfacial interactions between BANFs and rGO that facilitate load transfer. The good energy storage performance results from the high LFP content, the rGO flakes that ensure good electrical conductivity, and the BANFs that bind all components together offering enhanced structural stability under prolonged cycling. At this point it is worth mentioning recent reports on CF-based batteries coated with active materials such as LFP.[35-38] These studies were not included in the Ashby plots as they report mechanical properties for the whole device and not just for the electrodes.

Tensile tests were conducted also for the Si-based anodes to evaluate their mechanical performance, as shown in Figure 5.6a. Overall, the mechanical performance was maintained similar to rGO. More specifically, addition of 20 wt% Si led to small deteriorations in Young's modulus (4 ± 0.5 GPa) and tensile strength (34 ± 3 MPa) with improved ultimate strain (1.2 ± 0.2 %) and toughness (290 ± 50 kJ/m^3). The deterioration in Young's modulus and strength is attributed to the brittle nature of the Si nanoparticles, while the enhanced ultimate strain and toughness result from the hydrogen bonding interactions between rGO and Si that allow for rGO flakes to slide leading to larger displacements.[39-42] More specifically, Si nanoparticles interact with rGO through hydrogen bonding interactions between the Si surface hydroxyl groups and the rGO oxygen-containing groups.[43] Furthermore, addition of BANFs up to 15 wt% led to improved Youngs's modulus (6.8 ± 0.3 GPa) and tensile strength (45 ± 3 MPa) values with similar ultimate strain (0.7 ± 0.1 %) and toughness (190 ± 20 kJ/m^3). In addition to the BANF hydrogen bonding and π-π interactions with rGO, the improvement is also attributed to the BANF hydrogen bonding interactions with the Si nanoparticles between the BANF amide groups and the Si hydroxyl groups. Similarly, to the LFP-cathodes, higher BANFs contents led to significantly deteriorated performance due to aggregations of the BANFs.

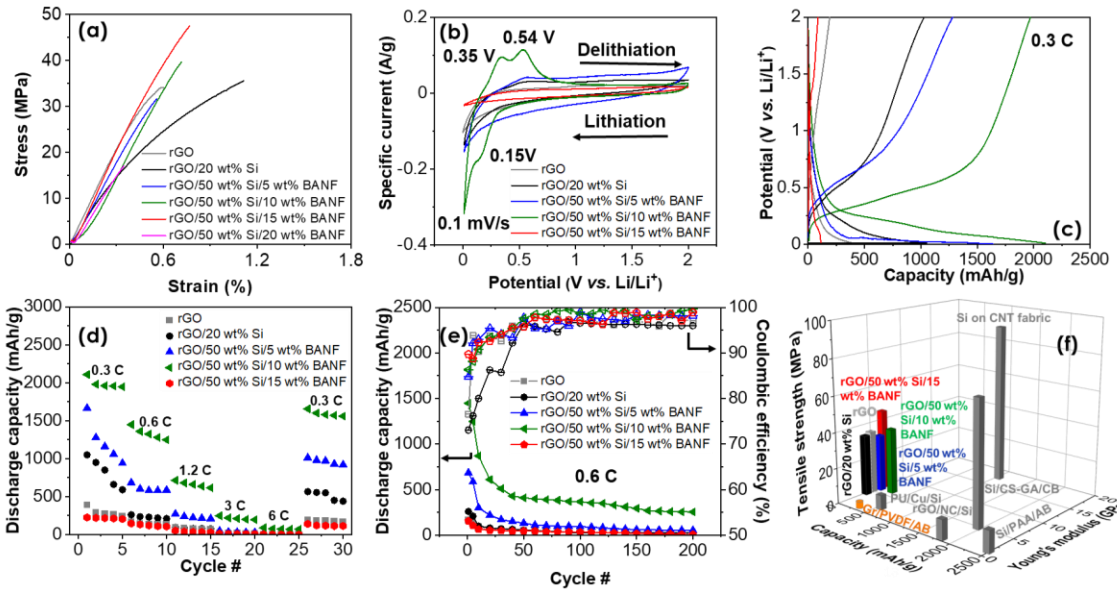

Figure 5.6 (a) Representative stress-strain curves for rGO,[5] rGO/20 wt% Si, rGO/50 wt% Si/5 wt% BANF, rGO/50 wt% Si/10 wt% BANF, rGO/50 wt% Si/15 wt% BANF, and rGO/50 wt% Si/20 wt% BANF. (b) Cyclic voltammograms at 0.1 mV/s, (c) potential profiles at 0.3 C, (d) galvanostatic cycling at different C-rates (0.3 C - 6 C), and (e) prolonged galvanostatic cycling at 0.6 C for 200 cycles for rGO, rGO/20 wt% Si, rGO/50 wt% Si/5 wt% BANF, rGO/50 wt% Si/10 wt% BANF, rGO/50 wt% Si/15 wt% BANF in a lithium metal half-cell. (f) Ashby plot for tensile strength *vs.* Young's modulus *vs.* capacity. Grey bars correspond to data for lithium-ion battery anodes obtained from the literature and the orange cylinder is the equivalent to a commercial anode. All capacities were calculated based on active material (Si) mass loadings.

The electrical conductivities of the Si-based anodes were measured using a four-point probe. Upon Si addition electrical conductivity deteriorated due to the dilution of the electrically conductive material, rGO.[44, 45] More specifically, rGO exhibited the highest

conductivity (28 ± 2 S/cm),[46] while addition of 20 wt% Si led to a conductivity of 5 ± 1 S/cm. Increasing the Si content to 50 wt% and adding BANFs (5 - 20 wt%) led to slightly lower electrical conductivity values (2 - 4 S/cm). Notwithstanding the deterioration in electrical conductivity, the structural Si-anodes exhibited comparable conductivity values to other reported Si-based anodes.[47-51] It is worth mentioning, the electrical conductivity of the LFP-based cathodes was higher than the Si-based anodes despite the higher content of non-conductive components for the LFP-cathodes. More specifically, rGO/50 wt% Si/5 wt% BANF electrodes exhibited an electrical conductivity of 4 ± 0.2 S/cm, whereas rGO/80 wt% LFP/5 wt% BANF showed conductivity values of 8.5 ± 2.5 S/cm. The higher electrical conductivity of the LFP-cathodes is indicative of formation of more homogeneous electrodes. All anodes were used for electrochemical testing except from rGO/50 wt% Si/20 wt% BANF due to its low conductivity and mechanical performance.

The energy storage performance was evaluated in lithium metal half cells using 1M $LiPF_6$ in EC:DEC (1:1 v/v) as the electrolyte. Figure 5.6b shows cyclic voltammograms obtained at 0.1 mV/s in a potential window of 0.01 – 2 V *vs*. Li/Li^+. The shape of the CV for rGO is similar to previous reports in the literature.[52] Upon addition of 20 wt% Si only a broad anodic peak at 0.54 V *vs*. Li/Li^+ appeared, underlining diffusion limitations.[53] Further increase in Si content up to 50 wt% and addition of 5 wt% BANFs led to an increase in the intensity of the anodic peak due to the higher active material content. rGO/50 wt% Si/10 wt% BANF exhibited similar CV curves to other reported Si-anodes with all Si features apparent.[54, 55] More specifically, a small cathodic peak at 0.15 V *vs*. Li/Li^+ which is attributed to the formation of metastable amorphous Li_xSi phases.[56]

Additionally, two anodic peaks at 0.35 V and 0.54 V *vs*. Li/Li^+ were observed due to the dealloying (conversion of Li_xSi to Si).[56] Higher BANF contents (15 wt%) led to a deteriorated performance as a result of low electrical conductivity values (2 ± 0.2 S/cm) and possible ion diffusion limitations.

Galvanostatic charging at different C-rates (0.3 C- 6 C) is shown in Figure 5.6c-5.6d. rGO and Si-based anodes exhibited steep curves similar to the literature.[17, 55] Moreover, capacity rapidly decreased with C-rate as it has also been reported before for such anodes due to structural changes, large volumetric expansion, during delithiation/lithiation and SEI formation.[54, 55] rGO/50 wt% Si/10 wt% BANF exhibited the highest capacity values (2108 mAh/g at 0.3 C) followed by rGO/50 wt% Si/5 wt% BANF (1160 mAh/g at 0.3 C). Higher BANFs content (> 10 wt%) led to deteriorated performance, as also observed from the CVs. After cycling at 6 C, we decreased the C-rate to 0.3 C. BANF (up to 10 wt%) - containing anodes recovered > 79 % of their initial capacity (*vs.* 49% and 54 % for rGO and rGO/20 wt% Si, respectively), indicating BANFs hindered electrode structural degradation. Prolonged cycling at 0.6 C up to 200 cycles is shown in Figure 5.6e. All structural anodes exhibited low capacity retention with rGO/50 wt% Si/10 wt% BANF demonstrating the highest capacity retention of 17.6 % with a coulombic efficiency of 99.6 % (*vs.* 86 % for the first cycle) and with a capacity *vs.* cycling number slope (starting from the 50^{th} cycle) of 1.4. The low capacity retention and high slope with cycling is common for Si-based anodes and typically arises from large volumetric expansion (up to 400 % for Si) and SEI formation.[54, 55] The improved performance of the rGO/50 wt% Si/10 wt% BANF compared to the other structural anodes

stems from the high active material content, good electrical conductivity, and the BANFs that serve as a binder and create less dense structures that allow for lithium-ion diffusion.

The energy storage performance was compared against other high performing rGO/Si anodes and a commercial anode from the literature, as shown in the Ragone plots in Figure 5.7. The BANF anodes were compared against rGO/Si (75:25, wt/wt)[57], rGO/Si (60:40, wt/wt)[58], rGO/Si (30:70, wt/wt),[59] and graphite/PVDF/AB (88.8:8:3.2, wt/wt)[11] – the equivalent to a commercial anode. From our work, rGO/50 wt% Si/10 wt% BANF demonstrated the best performance with a specific energy of 4216 Wh/kg at 2520 W/kg and 176 Wh/kg at 50400 W/kg. From the literature, the best performing was rGO/Si (30:70, wt/wt)[59] with a specific energy of 6716 Wh/kg at 285.7 W/kg and 2212 Wh/kg at 22857 W/kg. All reported rGO/Si electrodes were free-standing, however, the mechanical performance for the rGO/Si anodes was not reported.

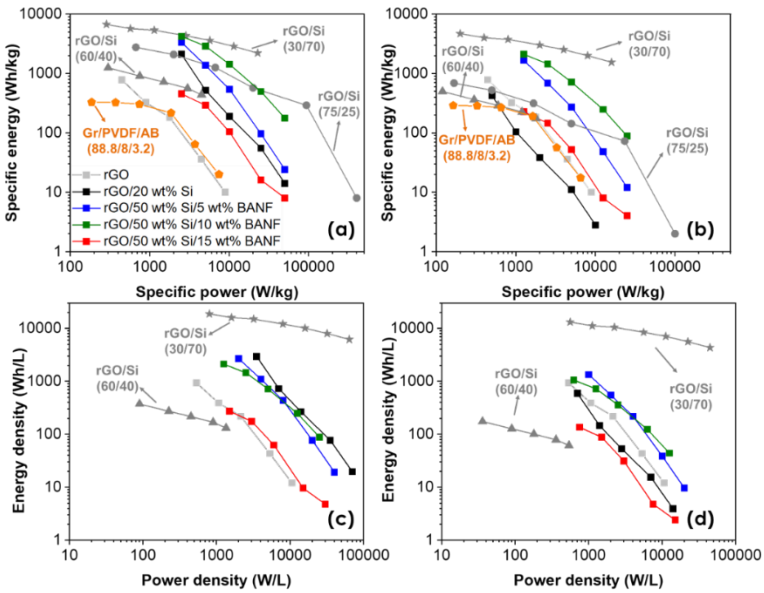

Figure 5.7 Ragone plots for (a, b) specific energy (Wh/kg) *vs.* specific power (W/kg) and (c, d) energy density (Wh/L) *vs.* power density (W/L) for rGO, rGO/20 wt% Si, rGO/50

wt% Si/5 wt% BANF, rGO/50 wt% Si/10 wt% BANF, and rGO/50 wt% Si/15 wt% compared against other rGO/Si anodes for lithium-ion batteries from the literature based on (a, c) Si mass loading and (b, d) total electrode mass. Numbers in parenthesis indicate the weight fractions for each component for data obtained from the literature. Legend in panel (a) applies also in panel (b). Orange data correspond to commercial anodes as obtained from the literature.

Finally, we compared the energy storage and mechanical performance of our structural anodes with other from the literature in an Ashby plot of tensile strength *vs.* Young's modulus *vs.* capacity after prolonged cycling (Figure 5.6f). More specifically, our Si-anodes were compared against graphite/PVDF/AB (88.8:8:3.2, wt/wt)[11] – the equivalent to a commercial anode, polyurethane (PU)/Cu/Si (12:79.7:8.3, wt/wt)[60], Si coated on CNT fabric (47:53, wt/wt)[17], rGO/NC/68 wt% Si[61], Si/PAA/AB (78:2:20, wt/wt)[18], and Si/CS-GA (60:20:20, wt/wt)[62]. Overall, our anodes demonstrated intermediate mechanical performance with relatively low capacity values. More specifically, Si coated on CNT fabric[17] and Si/CS-GA[62] exhibited the best mechanical performance followed by our Si-anodes. The superior mechanical performance of the Si-coated on CNT fabric[17] is attributed to the CNT fabric provides the structural support, while the performance of the Si/CS-GA[62] is attributed to the CS-GA crosslinkers that strongly bind with Si. Graphite/PVDF/AB,[11] PU/Cu/Si[60], rGO/NC/Si[61], and Si/PAA/AB[18] demonstrated inferior mechanical performance with comparable electrochemical properties to our Si-anodes. The relatively low electrochemical performance of our

structural anodes may be attributed to the low Si-content compared to most of the literature reports and the higher C-rate used for testing (0.6 C *vs.* 0.04 – 0.1 C for the literature data).

To investigate further the improved performance of the BANF-containing electrodes, the electrodes were characterized before and after electrochemical testing using EIS, SEM-EDS, and XPS. EIS tests provide information regarding ion and electron transport and are necessary for battery electrodes as ion-diffusion limitations are more prominent than in supercapacitors. Here, EIS was performed for all electrodes before cycling, after 10 cycles, and 200 cycles of galvanostatic charging at 0.6 C. Figure 5.8a displays the electrochemical impedance spectra after cycling for each cathode at 3.5 V *vs.* Li/Li^+. The impedance spectra for the anodes at 0.2 V *vs.* Li/Li^+ are shown in Figure 5.8b. Before cycling, the Nyquist plots exhibited a depressed semicircle and a long diffusion tail at the high and low frequency region, respectively. After cycling, two depressed semicircles became apparent in the high and medium frequency region with a Warburg tail at the low frequency region. The depressed semicircle at the high frequency region is indicative of SEI formation.[54, 63] The semicircle at the medium range is attributed to the charge transfer resistance between the electrode and the electrolyte, while the Warburg tail is indicative of lithium-ion diffusion in the electrode.[54, 63] An increase in the angle of the Warburg tail indicates enhanced ion transport.[64]

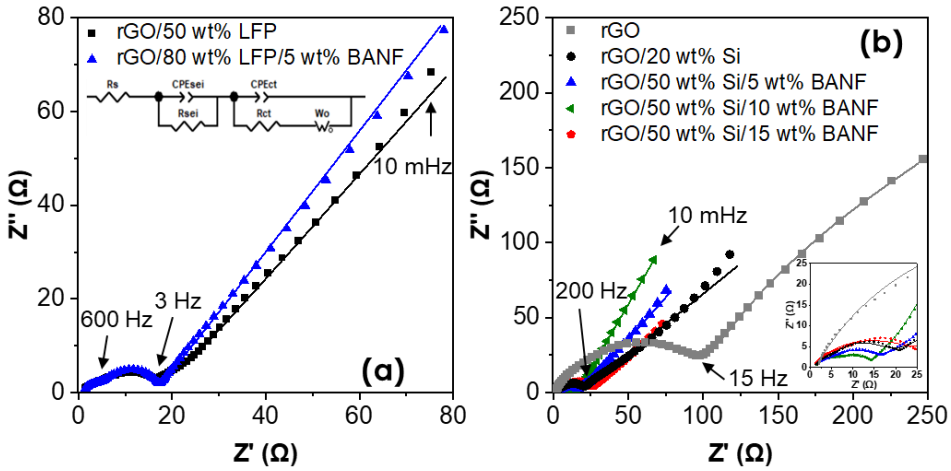

Figure 5.8 Nyquist plots for (a) LFP-cathodes and (b) Si-anodes after 200 cycles of galvanostatic charging at 0.6 C. The points represent the raw data and the solid lines the fitted data based on the equivalent circuit. Insets show the equivalent circuit used to model the data and a zoomed view of high frequency regions.

Two different equivalent circuits were used to fit the EIS data before and after cycling. After cycling, the circuit consisted of an ohmic resistance (R_s) attributed to the electrolyte resistance, a resistance due to the SEI layer (R_{SEI}) with a constant phase element (CPE_{SEI}), and a charge transfer resistance (R_{CT}) with a CPE_{CT} attributed to the electrode-electrolyte interface and a Warburg impedance (W_o) due to lithium-ion diffusion in the electrode. rGO exhibited the highest electrode resistance ($R_{SEI} + R_{CT} = 106.4\ \Omega$) resulting from its compact structure that hinders the lithium-ion diffusion within the electrode. The LFP-based cathodes exhibited similar resistance values (< 43 Ω) for the different compositions. All Si-based anodes exhibited similar resistance values (< 27.5 Ω), with rGO/50 wt% Si/10 wt% BANF demonstrating the highest Warburg tail angle indicating enhanced ionic conductivity. Overall, a slight decrease in electrode resistance was

observed after 10 cycles, while after 200 cycles resistance remained similar or even increased. This increase is attributed to the SEI formation.[54]

SEM images for the surface and cross-section before and after cycling are shown in Figure 5.9, respectively. All electrodes were thoroughly washed with dimethyl chloride to remove any residual electrolyte. Before electrochemical testing, all electrodes exhibited layered structures with thicknesses of 3 – 8 μm. After cycling the thickness of all electrodes increased due to volumetric expansion resulting from the electrolyte wetting and the lithiation/delithiation processes. Severe crack formation was observed for the LFP-cathodes and Si-anodes that did not contain BANFs. On the contrary the BANF electrodes maintained their layered structure and no cracks were visible despite their higher active material content. The results indicate that BANFs acted as a binder holding all components together and maintaining the structural integrity of the electrodes. Here, it is worth mentioning that attempts on fabricating anodes and cathodes with the same compositions but with traditional binders instead of BANFs failed. All films cracked upon air-drying. Furthermore, EDS mapping of the electrodes' surface revealed a decrease in Fe and Si elements with cycling for the LFP-cathodes and Si-anodes, respectively. These results indicate the formation of SEI in both anodes and cathodes.

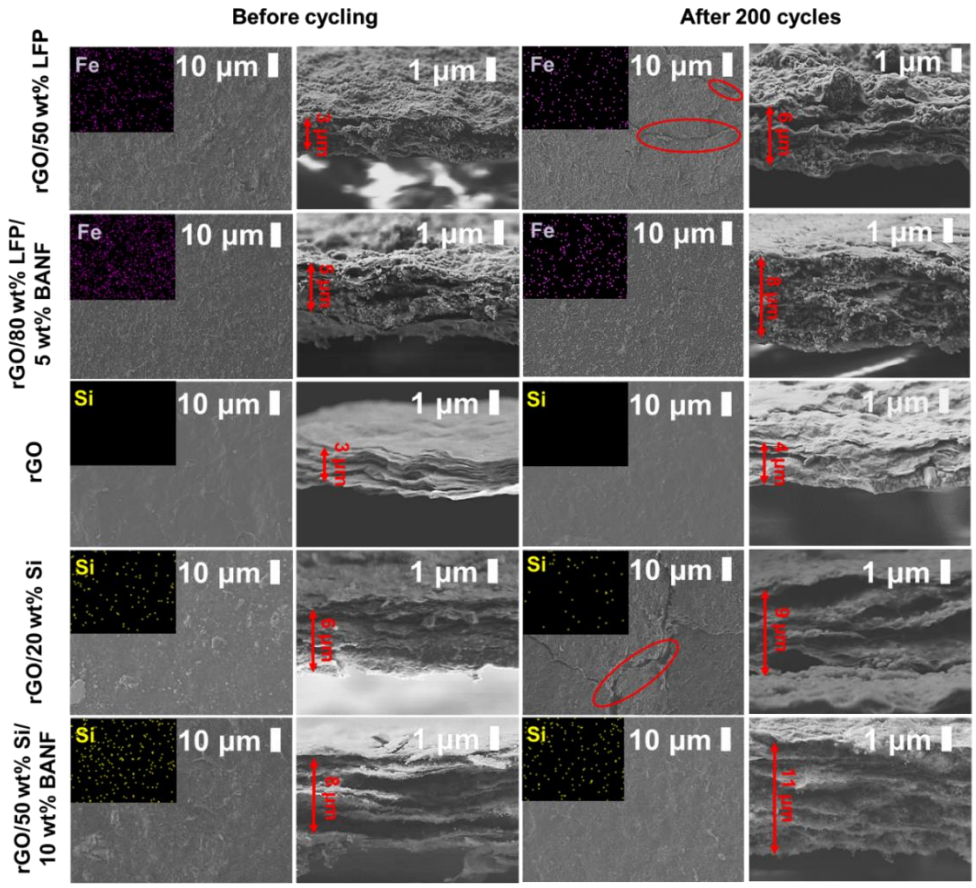

Figure 5.9 SEM images for LFP-cathodes and Si-anodes before and after electrochemical cycling. Insets show EDS mapping for Fe element for LFP-cathodes and Si element mapping for Si-anodes.

To better investigate the SEI formation, XPS before and after electrochemical cycling was utilized. In addition to C, O, Si that were observed before cycling, peaks due to F, P, and Li were detected after cycling. Figure 5.10 depicts the high-resolution peaks for C1s, F1s, and Li 1s for rGO/50 wt% LFP and rGO/80 wt% LFP/5 wt% BANF. More specifically for C1s, the appearance of -CH_2OCO_2Li at 288.7 eV, -Li_2CO_3 at 290.2 eV, and -CF_3 at 292.7 eV was observed and these peaks are derived from the reduction of

EC:DEC.[63] Similar observations were made for the F1s spectra and Li1s, with the appearance of Li-F (685.5 eV and 56.7 eV), $Li_xPO_yF_w/Li_xPF_y$ (688 eV), and $ROCO_2Li$ (54.6 eV). Figure 5.11 shows the high-resolution peaks C1s, F1s, Si 2p, and Li 1s for rGO, rGO/20 wt% Si, and rGO/50 wt% Si/10 wt% BANF after galvanic cycling. Similar observations with the cathodes were made.

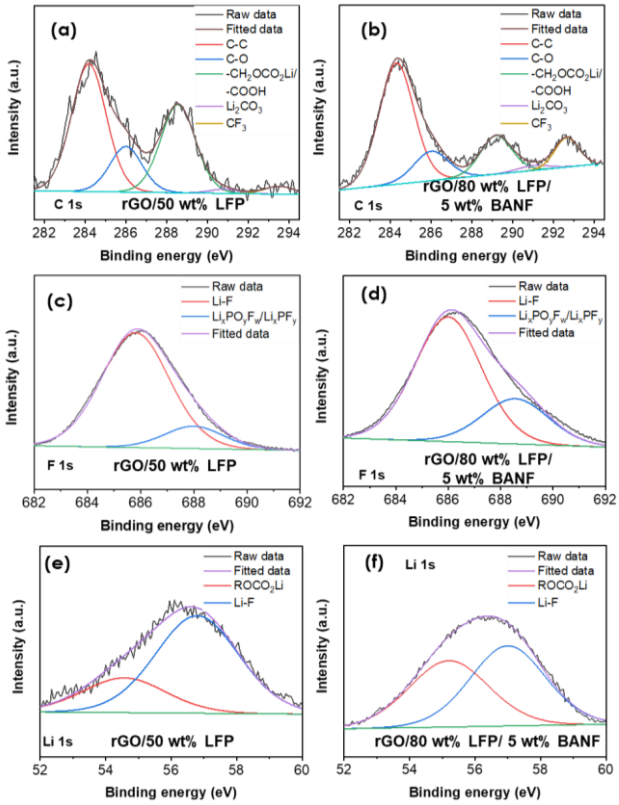

Figure 5.10 High resolution XPS spectra for C1s (a, b), F1s (c, d) and Li 1s (e, f) for rGO/50 wt% LFP (a, c, e) and rGO/80 wt% LFP/5 wt% BANF (b, d, f) after galvanic cycling.

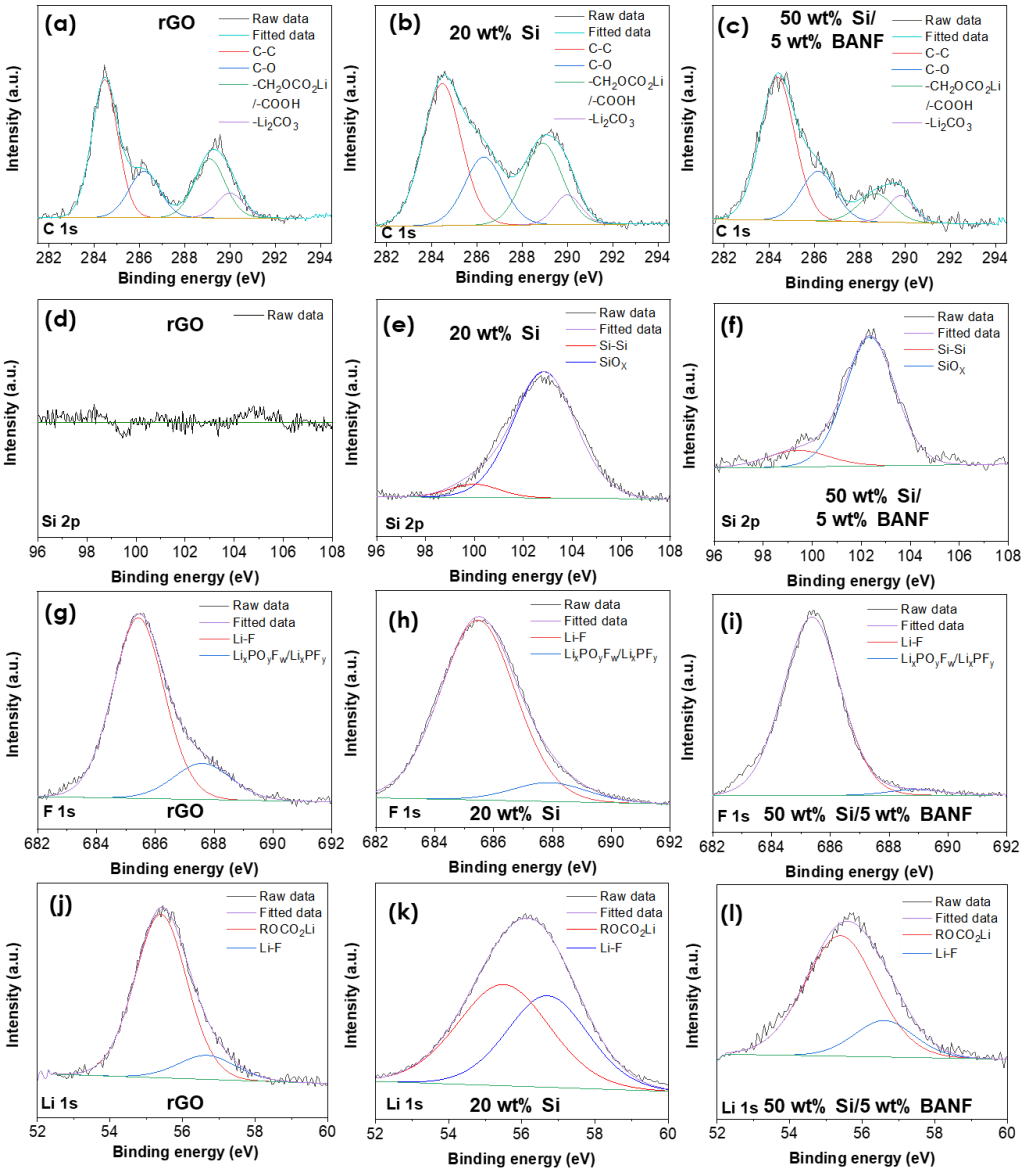

Figure 5.11 High resolution XPS spectra for C1s (a-c), Si 2p (d-f), F1s (g-i), and Li 1s (j-l) for rGO (a, d, g, j), rGO/20wt% Si (b, e, h, k), and rGO/50 wt% Si/10 wt% BANF (c, f, i, l) after galvanic cycling.

5.4. Conclusions

In this work, we demonstrated for the first time the utilization of BANFs as binders for lithium-ion battery cathodes and anodes. Mechanically strong lithium-ion battery cathodes and anodes based on branched aramid nanofibers (BANF) were fabricated using vacuum filtration. BANFs were combined with rGO, Si (anode) or LFP (cathode). BANF containing electrodes exhibited improved mechanical performance with good energy storage. Overall, an improvement up to two orders of magnitude in Young's modulus and tensile strength (Young's modulus ≥ 5 GPa and tensile strength ≥ 37 MPa for the BANF-based electrodes *vs.* a Young's modulus of 0.02 – 3.7 GPa and a tensile strength of 0.2 – 0.7 MPa for commercial cathodes and anodes) with similar energy storage compared to commercial battery electrodes was achieved. This is attributed to the BANFs that act as a binder, provide structural support, and allow for higher active material loadings leading to electrodes with enhanced structural stability. This work provides a route for the development of mechanically strong lithium-ion battery electrodes.

5.5. References

1. Kwon, S. R.; Harris, J.; Zhou, T.; Loufakis, D.; Boyd, J. G.; Lutkenhaus, J. L., Mechanically Strong Graphene/Aramid Nanofiber Composite Electrodes for Structural Energy and Power. *ACS Nano* **2017,** *11* (7), 6682-6690.
2. Flouda, P.; Shah, S. A.; Lagoudas, D. C.; Green, M. J.; Lutkenhaus, J. L., Highly Multifunctional Dopamine-Functionalized Reduced Graphene Oxide Supercapacitors. *Matter* **2019,** *1* (6), 1532-1546.
3. Flouda, P.; Feng, X. Y.; Boyd, J. G.; Thomas, E. L.; Lagoudas, D. C.; Lutkenhaus, J. L., Interfacial Engineering of Reduced Graphene Oxide for Aramid Nanofiber-Enabled Structural Supercapacitors. *Batteries Supercaps* **2019,** *2* (5), 464-472.
4. Patel, A. G.; Johnson, L.; Arroyave, R.; Lutkenhaus, J. L., Design of multifunctional supercapacitor electrodes using an informatics approach. *Mol Syst Des Eng* **2019,** *4*, 654-663.

5. Flouda, P.; Yun, J.; Loufakis, D.; Shah, S. A.; Green, M. J.; Lagoudas, D. C.; Lutkenhaus, J. L., Structural reduced graphene oxide supercapacitors mechanically enhanced with tannic acid. *Sustainable Energy & Fuels* **2020,** *4* (5), 2301-2308.
6. Zhang, W.-J., Structure and performance of LiFePO4 cathode materials: A review. *Journal of Power Sources* **2011,** *196* (6), 2962-2970.
7. Yuan, L.-X.; Wang, Z.-H.; Zhang, W.-X.; Hu, X.-L.; Chen, J.-T.; Huang, Y.-H.; Goodenough, J. B., Development and challenges of LiFePO4 cathode material for lithium-ion batteries. *Energy & Environmental Science* **2011,** *4* (2), 269-284.
8. Ellis, B. L.; Makahnouk, W. R. M.; Makimura, Y.; Toghill, K.; Nazar, L. F., A multifunctional 3.5 V iron-based phosphate cathode for rechargeable batteries. *Nature Materials* **2007,** *6* (10), 749-753.
9. Boaretto, N.; Almenara, J.; Mikhalchan, A.; Marcilla, R.; Vilatela, J. J., A Route to High-Toughness Battery Electrodes. *ACS Applied Energy Materials* **2019,** *2* (8), 5889-5899.
10. Wu, Y.; Wu, H.; Luo, S.; Wang, K.; Zhao, F.; Wei, Y.; Liu, P.; Jiang, K.; Wang, J.; Fan, S., Entrapping electrode materials within ultrathin carbon nanotube network for flexible thin film lithium ion batteries. *RSC Advances* **2014,** *4* (38), 20010-20016.
11. Zheng, H.; Zhang, L.; Liu, G.; Song, X.; Battaglia, V. S., Correlationship between electrode mechanics and long-term cycling performance for graphite anode in lithium ion cells. *Journal of Power Sources* **2012,** *217*, 530-537.
12. Zuo, X.; Zhu, J.; Müller-Buschbaum, P.; Cheng, Y.-J., Silicon based lithium-ion battery anodes: A chronicle perspective review. *Nano Energy* **2017,** *31*, 113-143.
13. Casimir, A.; Zhang, H.; Ogoke, O.; Amine, J. C.; Lu, J.; Wu, G., Silicon-based anodes for lithium-ion batteries: Effectiveness of materials synthesis and electrode preparation. *Nano Energy* **2016,** *27*, 359-376.
14. Sarang, K.; Zhao, X.; Holta, D.; Radovic, M.; Green, M.; Oh, E.-S.; Lutkenhaus, J., Minimizing Two-Dimensional Ti3C2Tx MXene Nanosheet Loading in Carbon-free Silicon Anodes. *Nanoscale* **2020**.
15. McDowell, M. T.; Lee, S. W.; Nix, W. D.; Cui, Y., 25th Anniversary Article: Understanding the Lithiation of Silicon and Other Alloying Anodes for Lithium-Ion Batteries. *Advanced Materials* **2013,** *25* (36), 4966-4985.
16. Li, J.-Y.; Xu, Q.; Li, G.; Yin, Y.-X.; Wan, L.-J.; Guo, Y.-G., Research progress regarding Si-based anode materials towards practical application in high energy density Li-ion batteries. *Materials Chemistry Frontiers* **2017,** *1* (9), 1691-1708.
17. Evanoff, K.; Benson, J.; Schauer, M.; Kovalenko, I.; Lashmore, D.; Ready, W. J.; Yushin, G., Ultra Strong Silicon-Coated Carbon Nanotube Nonwoven Fabric as a Multifunctional Lithium-Ion Battery Anode. *ACS Nano* **2012,** *6* (11), 9837-9845.
18. Assresahegn, B. D.; Bélanger, D., Effects of the Formulations of Silicon-Based Composite Anodes on their Mechanical, Storage, and Electrochemical Properties. *ChemSusChem* **2017,** *10* (20), 4080-4089.
19. Zhu, J.; Yang, M.; Emre, A.; Bahng, J. H.; Xu, L.; Yeom, J.; Yeom, B.; Kim, Y.; Johnson, K.; Green, P.; Kotov, N. A., Branched Aramid Nanofibers. *Angewandte Chemie* **2017,** *129* (39), 11906-11910.

20. Hummers, W. S.; Offeman, R. E., Preparation of Graphitic Oxide. *J. Am. Chem. Soc.* **1958,** *80* (6), 1339-1339.
21. Li, J.; Zhang, L.; Zhang, L.; Hao, W.; Wang, H.; Qu, Q.; Zheng, H., In-situ growth of graphene decorations for high-performance LiFePO4 cathode through solid-state reaction. *Journal of Power Sources* **2014,** *249*, 311-319.
22. Wang, J.-Z.; Zhong, C.; Chou, S.-L.; Liu, H.-K., Flexible free-standing graphene-silicon composite film for lithium-ion batteries. *Electrochem. Commun.* **2010,** *12* (11), 1467-1470.
23. Podsiadlo, P.; Kaushik, A. K.; Arruda, E. M.; Waas, A. M.; Shim, B. S.; Xu, J.; Nandivada, H.; Pumplin, B. G.; Lahann, J.; Ramamoorthy, A.; Kotov, N. A., Ultrastrong and Stiff Layered Polymer Nanocomposites. *Science* **2007,** *318* (5847), 80-83.
24. Wu, H.; Liu, Q.; Guo, S., Composites of Graphene and LiFePO4 as Cathode Materials for Lithium-Ion Battery: A Mini-review. *Nano-Micro Letters* **2014,** *6* (4), 316-326.
25. Lei, X.; Zhang, H.; Chen, Y.; Wang, W.; Ye, Y.; Zheng, C.; Deng, P.; Shi, Z., A three-dimensional LiFePO4/carbon nanotubes/graphene composite as a cathode material for lithium-ion batteries with superior high-rate performance. *Journal of Alloys and Compounds* **2015,** *626*, 280-286.
26. Yu, D. Y. W.; Fietzek, C.; Weydanz, W.; Donoue, K.; Inoue, T.; Kurokawa, H.; Fujitani, S., Study of LiFePO[sub 4] by Cyclic Voltammetry. *Journal of The Electrochemical Society* **2007,** *154* (4), A253.
27. Bi, H.; Huang, F.; Tang, Y.; Liu, Z.; Lin, T.; Chen, J.; Zhao, W., Study of LiFePO4 cathode modified by graphene sheets for high-performance lithium ion batteries. *Electrochimica Acta* **2013,** *88*, 414-420.
28. Zhu, X.; Hu, J.; Wu, W.; Zeng, W.; Dai, H.; Du, Y.; Liu, Z.; Li, L.; Ji, H.; Zhu, Y., LiFePO4/reduced graphene oxide hybrid cathode for lithium ion battery with outstanding rate performance. *Journal of Materials Chemistry A* **2014,** *2* (21), 7812-7818.
29. Wang, X.; Feng, Z.; Huang, J.; Deng, W.; Li, X.; Zhang, H.; Wen, Z., Graphene-decorated carbon-coated LiFePO4 nanospheres as a high-performance cathode material for lithium-ion batteries. *Carbon* **2018,** *127*, 149-157.
30. Wang, B.; Xu, B.; Liu, T.; Liu, P.; Guo, C.; Wang, S.; Wang, Q.; Xiong, Z.; Wang, D.; Zhao, X. S., Mesoporous carbon-coated LiFePO4 nanocrystals co-modified with graphene and Mg2+ doping as superior cathode materials for lithium ion batteries. *Nanoscale* **2014,** *6* (2), 986-995.
31. Jeon, J.-W.; Biswas, M. C.; Patton, C. L.; Wujcik, E. K., Water-processable, sprayable LiFePO4/graphene hybrid cathodes for high-power lithium ion batteries. *Journal of Industrial and Engineering Chemistry* **2020,** *84*, 72-81.
32. Liu, P.; Sherman, E.; Jacobsen, A., Design and fabrication of multifunctional structural batteries. *Journal of Power Sources* **2009,** *189* (1), 646-650.
33. Luo, S.; Wang, K.; Wang, J.; Jiang, K.; Li, Q.; Fan, S., Binder-Free LiCoO2/Carbon Nanotube Cathodes for High-Performance Lithium Ion Batteries. *Advanced Materials* **2012,** *24* (17), 2294-2298.

34. An, H.; Mike, J.; Smith, K. A.; Swank, L.; Lin, Y.-H.; L. Pesek, S.; Verduzco, R.; Lutkenhaus, J. L., Highly Flexible Self-Assembled V2O5 Cathodes Enabled by Conducting Diblock Copolymers. *Scientific Reports* **2015,** *5* (1), 14166.
35. Moyer, K.; Ait Boucherbil, N.; Zohair, M.; Eaves, J.; Pint, C., Polymer Reinforced Carbon Fiber Interfaces for High Energy Density Structural Lithium-Ion Batteries. *Sustainable Energy & Fuels* **2020**.
36. Moyer, K.; Meng, C.; Marshall, B.; Assal, O.; Eaves, J.; Perez, D.; Karkkainen, R.; Roberson, L.; Pint, C. L., Carbon fiber reinforced structural lithium-ion battery composite: Multifunctional power integration for CubeSats. *Energy Storage Materials* **2020,** *24*, 676-681.
37. Carlstedt, D.; Marklund, E.; Asp, L. E., Effects of state of charge on elastic properties of 3D structural battery composites. *Composites Science and Technology* **2019,** *169*, 26-33.
38. Xu, J.; Johannisson, W.; Johansen, M.; Liu, F.; Zenkert, D.; Lindbergh, G.; Asp, L. E., Characterization of the adhesive properties between structural battery electrolytes and carbon fibers. *Composites Science and Technology* **2020,** *188*, 107962.
39. Park, S.; Lee, K.-S.; Bozoklu, G.; Cai, W.; Nguyen, S. T.; Ruoff, R. S., Graphene Oxide Papers Modified by Divalent Ions—Enhancing Mechanical Properties via Chemical Cross-Linking. *ACS Nano* **2008,** *2* (3), 572-578.
40. Lee, D. H.; Kim, J. E.; Han, T. H.; Hwang, J. W.; Jeon, S.; Choi, S.-Y.; Hong, S. H.; Lee, W. J.; Ruoff, R. S.; Kim, S. O., Versatile Carbon Hybrid Films Composed of Vertical Carbon Nanotubes Grown on Mechanically Compliant Graphene Films. *Advanced Materials* **2010,** *22* (11), 1247-1252.
41. Shin, M. K.; Lee, B.; Kim, S. H.; Lee, J. A.; Spinks, G. M.; Gambhir, S.; Wallace, G. G.; Kozlov, M. E.; Baughman, R. H.; Kim, S. J., Synergistic toughening of composite fibres by self-alignment of reduced graphene oxide and carbon nanotubes. *Nature Communications* **2012,** *3* (1), 650.
42. Zhang, N.; Deng, Q.; Hong, Y.; Xiong, L.; Li, S.; Strasberg, M.; Yin, W.; Zou, Y.; Taylor, C. R.; Sawyer, G.; Chen, Y., Deformation mechanisms in silicon nanoparticles. *Journal of Applied Physics* **2011,** *109* (6), 063534.
43. Shan, C.; Wu, K.; Yen, H.-J.; Narvaez Villarrubia, C.; Nakotte, T.; Bo, X.; Zhou, M.; Wu, G.; Wang, H.-L., Graphene Oxides Used as a New "Dual Role" Binder for Stabilizing Silicon Nanoparticles in Lithium-Ion Battery. *ACS Applied Materials & Interfaces* **2018,** *10* (18), 15665-15672.
44. Zhang, C.; Park, S.-H.; Seral-Ascaso, A.; Barwich, S.; McEvoy, N.; Boland, C. S.; Coleman, J. N.; Gogotsi, Y.; Nicolosi, V., High capacity silicon anodes enabled by MXene viscous aqueous ink. *Nature Communications* **2019,** *10* (1), 849.
45. Ashuri, M.; He, Q.; Shaw, L. L., Silicon as a potential anode material for Li-ion batteries: where size, geometry and structure matter. *Nanoscale* **2016,** *8* (1), 74-103.
46. Flouda, P.; Yun, J.; Loufakis, D.; Shah, S. A.; Green, M. J.; Lagoudas, D. C.; Lutkenhaus, J. L., Structural reduced graphene oxide supercapacitors mechanically enhanced with tannic acid. *Sustainable Energy & Fuels* **2020**.

47. Park, B. H.; Jeong, J. H.; Lee, G.-W.; Kim, Y.-H.; Roh, K. C.; Kim, K.-B., Highly conductive carbon nanotube micro-spherical network for high-rate silicon anode. *Journal of Power Sources* **2018,** *394*, 94-101.
48. Wang, L.; Liu, T.; Peng, X.; Zeng, W.; Jin, Z.; Tian, W.; Gao, B.; Zhou, Y.; Chu, P. K.; Huo, K., Highly Stretchable Conductive Glue for High-Performance Silicon Anodes in Advanced Lithium-Ion Batteries. *Advanced Functional Materials* **2018,** *28* (3), 1704858.
49. Wang, C.; Wu, H.; Chen, Z.; McDowell, M. T.; Cui, Y.; Bao, Z., Self-healing chemistry enables the stable operation of silicon microparticle anodes for high-energy lithium-ion batteries. *Nature Chemistry* **2013,** *5* (12), 1042-1048.
50. Cho, H.; Kim, K.; Park, C.-M.; Jeong, G., In situ fabrication of nanohybrid carbon/polyamide film providing robust binding and conductive network in silicon anode for lithium-ion battery. *Journal of Power Sources* **2019,** *410-411*, 25-30.
51. Lee, K.; Kim, T.-H., Poly(aniline-co-anthranilic acid) as an electrically conductive and mechanically stable binder for high-performance silicon anodes. *Electrochimica Acta* **2018,** *283*, 260-268.
52. Wang, G.; Shen, X.; Yao, J.; Park, J., Graphene nanosheets for enhanced lithium storage in lithium ion batteries. *Carbon* **2009,** *47* (8), 2049-2053.
53. Zeng, W.; Wang, L.; Peng, X.; Liu, T.; Jiang, Y.; Qin, F.; Hu, L.; Chu, P. K.; Huo, K.; Zhou, Y., Enhanced Ion Conductivity in Conducting Polymer Binder for High-Performance Silicon Anodes in Advanced Lithium-Ion Batteries. *Advanced Energy Materials* **2018,** *8* (11), 1702314.
54. Sarang, K. T.; Li, X.; Miranda, A.; Terlier, T.; Oh, E.-S.; Verduzco, R.; Lutkenhaus, J. L., Tannic Acid as a Small-Molecule Binder for Silicon Anodes. *ACS Applied Energy Materials* **2020,** *3* (7), 6985-6994.
55. Chan, C. K.; Peng, H.; Liu, G.; McIlwrath, K.; Zhang, X. F.; Huggins, R. A.; Cui, Y., High-performance lithium battery anodes using silicon nanowires. *Nature Nanotechnology* **2008,** *3* (1), 31-35.
56. Chen, X.; Li, X.; Ding, F.; Xu, W.; Xiao, J.; Cao, Y.; Meduri, P.; Liu, J.; Graff, G. L.; Zhang, J.-G., Conductive Rigid Skeleton Supported Silicon as High-Performance Li-Ion Battery Anodes. *Nano Letters* **2012,** *12* (8), 4124-4130.
57. Sun, F.; Huang, K.; Qi, X.; Gao, T.; Liu, Y.; Zou, X.; Wei, X.; Zhong, J., A rationally designed composite of alternating strata of Si nanoparticles and graphene: a high-performance lithium-ion battery anode. *Nanoscale* **2013,** *5* (18), 8586-8592.
58. Jiang, H.; Zhou, X.; Liu, G.; Zhou, Y.; Ye, H.; Liu, Y.; Han, K., Free-Standing Si/Graphene Paper Using Si Nanoparticles Synthesized by Acid-Etching Al-Si Alloy Powder for High-Stability Li-Ion Battery Anodes. *Electrochimica Acta* **2016,** *188*, 777-784.
59. Zhao, X.; Hayner, C. M.; Kung, M. C.; Kung, H. H., In-Plane Vacancy-Enabled High-Power Si–Graphene Composite Electrode for Lithium-Ion Batteries. *Advanced Energy Materials* **2011,** *1* (6), 1079-1084.
60. Liu, L.; Li, M.; Chu, L.; Jiang, B.; Lin, R., Facile fabrication of flexible Si-based nanocomposite films as high-rate anodes by layer-by-layer self-assembly. *Applied Surface Science* **2019,** *476*, 501-512.

61. Zhou, X.; Liu, Y.; Du, C.; Ren, Y.; Li, X.; Zuo, P.; Yin, G.; Ma, Y.; Cheng, X.; Gao, Y., Free-Standing Sandwich-Type Graphene/Nanocellulose/Silicon Laminar Anode for Flexible Rechargeable Lithium Ion Batteries. *ACS Applied Materials & Interfaces* **2018,** *10* (35), 29638-29646.
62. Chen, C.; Lee, S. H.; Cho, M.; Kim, J.; Lee, Y., Cross-Linked Chitosan as an Efficient Binder for Si Anode of Li-ion Batteries. *ACS Applied Materials & Interfaces* **2016,** *8* (4), 2658-2665.
63. Bordes, A.; Eom, K.; Fuller, T. F., The effect of fluoroethylene carbonate additive content on the formation of the solid-electrolyte interphase and capacity fade of Li-ion full-cell employing nano Si–graphene composite anodes. *Journal of Power Sources* **2014,** *257*, 163-169.
64. An, H.; Li, X.; Chalker, C.; Stracke, M.; Verduzco, R.; Lutkenhaus, J. L., Conducting Block Copolymer Binders for Carbon-Free Hybrid Vanadium Pentoxide Cathodes with Enhanced Performance. *ACS Applied Materials & Interfaces* **2016,** *8* (42), 28585-28591.

6. BRANCHED ARAMID NANOFIBER-POLYANILINE ELECTRODES FOR STRUCTURAL ENERGY STORAGE*

6.1. Introduction

In this chapter, we further investigate the utilization of branched aramid nanofibers (BANFs) in both structural supercapacitor electrodes and lithium-ion battery structural cathodes using polyaniline (PANI). PANI is a promising electrode material for electrochemical energy storage due to its tuneable morphology and pseudocapacitive response.[1] However, PANI has poor mechanical properties and, as a result, is unfit to support mechanical loads in devices.[2] Here, we present a strategy for mechanically strong PANI-based electrodes for structural supercapacitors and Li-ion batteries by taking advantage of composite structures.

PANI, a p-type conjugated polymer, has been extensively studied as an electrode material due to its high electrical conductivity (2-5 S/cm when in emeraldine salt form) and high theoretical capacity (147 mAh/g, assuming one electron exchange for every two repeat units), as well as its low cost and ease of synthesis.[3-8] PANI is redox active and stores charge though a reversible doping-dedoping mechanism, which depends strongly on the anion in the electrolyte.[3-5, 9] As a result, PANI and its composite derivatives have been explored as pseudocapacitive electrode materials in supercapacitors and Li-ion batteries.[10] As a supercapacitor electrode, PANI/reduced graphene oxide (rGO) exhibited

---

*Modified and reprinted with permission from "Branched aramid nanofiber-polyaniline electrodes for structural energy storage" by Paraskevi Flouda, Alexander H. Quinn, Anish G. Patel, Dimitrios Loufakis, Dimitris C. Lagoudas, and Jodie L. Lutkenhaus, *Nanoscale* 2020, 12 (32), 16840-16850. Copyright 2020, Royal Society of Chemistry

an electrical conductivity of 5.5 S/cm and specific capacitance of 210 F/g.[11] Carbon nanotube (CNT)/PANI electrodes demonstrated electrical conductivities up to 150 S/cm and specific capacitances up to 424 F/g.[12] Additionally, PANI has been studied as a cathode material for Li-ion batteries. Most battery-based studies focus on PANI-coated on conductive substrates using layer-by-layer (LbL) methods.[5, 8, 13, 14] PANI/rGO LbL electrodes exhibited electrical conductivities of 1.84 S/cm and capacities of 188 mAh/g, whereas PANI/MXene LbL electrodes showed capacities up to 145 mAh/g.[8, 15] Although there are limited number reports on free-standing PANI films,[16-18] there are no examples of PANI-based electrodes for structural batteries.

Despite the extensive studies on the electrical and electrochemical performance of PANI, there are only a handful of studies on its mechanical performance.[19] Single PANI fibers exhibited electrical conductivities of 600 S/cm, Young's moduli of 2 GPa, and tensile strength of 105 MPa after doping.[20] Pure PANI films are generally plagued by brittleness and low ductility.[21] However, studies on PANI composite films show promise. For instance, PANI/cellulose membranes exhibited a Young's modulus of 5.6 GPa and tensile strength of 95.7 MPa, but the electrical conductivities were as low as 0.05 S/cm.[22]

We hypothesized that the mechanical performance of PANI composites may be improved by the addition of strong polymers such as branched aramid nanofibers (BANFs). This hypothesis is motivated by our prior work, in which BANFs dramatically improved the mechanical properties of rGO-based electrodes.[23-30] PANI/ANF composites (using un-branched ANFs) have been previously explored for sensors, EMI shielding, and flexible supercapacitor electrodes.[31-34] PANI filtered through a premade matrix of ANF

exhibited high electrical conductivities of 20-300 S/cm and good mechanical properties with a Young's modulus of ~5 GPa and a tensile strength of 179 MPa.[31] Similarly, PANI/ANF core-shell composites demonstrated electrical conductivities of $0.05 \cdot 10^{-2}$ S/cm, Young's moduli of 1.3 GPa, and tensile strengths of 50 MPa.[33] PANI grown directly on ANF premade films showed a Young's modulus of 4 GPa, tensile strength of 233 MPa, and a specific capacitance of 138 F/g in a two-electrode symmetric solid state cell.[34] We expect branched ANFs to lead to further improvements in mechanical performance as it has also been demonstrated in our prior work on rGO/ANF and rGO/BANF structural electrodes due to the higher surface area available for hydrogen bonding and π-π stacking interactions. [25, 26, 35] Despite progressive studies on the mechanical properties of PANI/ANF composites, the effects of BANF on the mechanical and energy storage performance of PANI in both supercapacitors and batteries are still unexplored.

Here, aniline was polymerized in the presence of BANFs and single walled carbon nanotubes (SWCNTs) to create strong and conductive networks for structural capacitors and batteries. Free-standing thin film electrodes of high BANF content (50 - 80 wt%) were fabricated using vacuum filtration of the three components. PANI acted as the redox-active component for energy storage, and PANI's combination with CNTs leads to more accessible redox sites.[36] Furthermore, CNTs were chosen due to their high electrical conductivity (~ 10^3 S/cm) and high surface area (120 – 500 m^2/g),[37-39] which we hypothesized might further enhance the electrochemical performance of the structural electrodes. As it has been demonstrated before in rGO/Co_9S_8 and rGO/MnO_2/CNTs electrodes for Li-ion batteries and supercapacitors, the combination of redox active

materials with high surface area conductive materials leads to improved energy storage performance.[40, 41] The morphology and composition were investigated using scanning electron microscopy (SEM), transmission electron microscopy (TEM), energy dispersive spectroscopy (EDS), and Raman spectroscopy. The mechanical properties were assessed using uniaxial tensile testing. Finally, the PANI/BANF/CNT electrodes were investigated in symmetric supercapacitors and in Li-ion batteries. An electrochemical analysis of the charge-storage mechanism was also applied. Altogether, this work demonstrates the first design of structural electrodes based on PANI for both supercapacitors and Li-ion batteries.

6.2. Materials and Methods

Aniline, ammonium persulfate (APS), hydrochloric acid (HCl), dimethyl sulfoxide (DMSO), 1 M lithium hexafluorophosphate ($LiPF_6$) in ethylene carbonate:dimethylene cabonate:diethylene carbonate (EC:DMC:DEC) (1:1:1 v/v), Li metal foil, branched polyethyleneimine (b-PEI, MW = 25,000 g/mol, MN = 10,000 g/mol), sodium nitrate ($NaNO_3$), hydrogen peroxide (H_2O_2), potassium permanganate ($KMnO_4$), and sulfuric acid (H_2SO_4) were purchased from Sigma-Aldrich. Kevlar®69 thread was purchased from Thread Exchange. Carbon paper was purchased from Alfa Aesar. Celgard 3501 was provided by Celgard. Spectra/Por dialysis tubes of 12-14 kD molecular weight cut-off were purchased from VWR. Single-walled carbon nanotubes (SWCNTs, diameter: 1.8 nm), carboxylated multi-walled carbon nanotubes (MWCNTs-COOH), and graphite (SP-1) were purchased from Tuball, CheapTubes, and Bay Carbon, respectively.

Chopped Kevlar fiber (0.5 g) was mixed with KOH (0.5 g) in DMSO (50 ml).[42] The mixture was stirred for seven days to obtain a dark red viscous dispersion of BANF/DMSO (10 mg/ml). Dialysis of a BANF/DMSO (1 mg/ml) mixture was performed for 3 days to exchange water for DMSO.

PANI and PANI:poly(2-acrylamido-2-methyl-1-propanesulfonic acid) (PAAMPSA) complexes were prepared following prior reports from our group.[5, 15, 43] Initially, dispersions of PANI and PANI:PAAMPSA (1 mg/ml) in water/DMSO were directly vacuum filtered using a Nylon filter paper (pore size: 0.2 μm and diameter: 47 mm). BANF-containing composites were fabricated by mixing and stirring for 2 h desired amounts of PANI or PANI:PAAMPSA dispersions with BANF dispersions (1 mg/ml) in water/DMSO followed by vacuum filtration. Layered PANI/BANF composites were fabricated using sequential vacuum filtration. More specifically, desired amounts of BANFs/DMSO (1 mg/ml) were filtered to form thin films of BANFs. Subsequently, PANI/water (1 mg/ml) mixtures were filtered through the BANF premade membrane. Finally, composites containing PANI:PAAMPSA, 10 wt% BANFs, and 10 wt% of a third component (b-PEI, MWCNT-COOH, or GO) were fabricated by directly mixing and stirring for 2 h dispersions of the components (1 mg/ml) in water followed by vacuum filtration. GO dispersions (1 mg/ml) in water were prepared following previous reports using the modified Hummers' method.[30, 44] All composites were washed with a 1M HCl solution and dried under vacuum at 60 ^{o}C for 3 days. Composites containing MWCNT-COOH and GO were thermally reduced at 200 ^{o}C for 2 h under vacuum. The total mass of the composites was kept constant at ~20 mg.

To fabricate BANF/CNT/PANI composites, BANF/water dispersions (1 mg/ml) were mixed with SWCNTs/water (1 mg/ml) dispersions at desired ratios. The mixture was ultrasonicated for 5 min and stirred for 1 h to form homogeneous BANF/CNT dispersions. Aniline monomer (30 mg) was mixed with the BANF/CNT dispersion (20 ml of 1 mg/ml) for 1 h under nitrogen. APS (0.69 g) was added in 1M HCl (20 ml) and stirred for 1 h under nitrogen. The two dispersions were rapidly mixed together under nitrogen for 24h.[33] Thin films were fabricated through vacuum filtration using a Nylon filter paper (pore size: 0.2 μm and diameter: 47 mm). The total mass of the composites was kept constant at ~20 mg. Finally, the films were washed with a 1M HCl solution and dried under vacuum at 60 ^{o}C for 3 days.

Raman spectra were collected using a Horiba JobinYvon spectrometer with excitation at 514 nm. FT-IR/ATR was conducted using IR Prestige 21 system, equipped with a diamond ATR lens (Shimadzu). Scanning electron microscopy images were obtained using a JEOL, SM-7500F SEM with an Oxford EDS system. Electrical conductivity measurements were obtained using a four-point probe.

Tensile testing was conducted using a DMA Q8OO (TA Instruments) with a strain rate of 0.1 %/min and preload force of 0.02 Nt. All measurements were conducted at room temperature and humidity (~23 ^{o}C and 30-35 %).

Two-electrode symmetric coin cells were used for supercapacitor testing. Electrodes of mass loadings of 1.5 - 2 mg/cm^2 (per total electrode mass) were used. 1 M H_2SO_4 was used as the aqueous electrolyte, Celgard 3501 as the separator, and carbon paper as the current collector. Two stainless steel spacers and a spring were used. The electrochemical

testing was conducted using a potentiostat (Gamry Interface 1000, Gamry Instruments). Cyclic voltammetry tests were conducted at a potential window of -0.2-0.8 V and varying scan rates (1-100 mV/s). Galvanostatic cycling experiments were conducted at the same potential window under different specific currents (0.2-2 A/g). The specific capacitance was calculated as described previously.[24] Half-cell battery testing was conducted using a two-electrode setup (Tomcell). The electrochemical test was conducted using a Solatron (Electrochemical Interface 1287). The working electrodes (same mass ladings as with the supercapacitor electrodes) were further dried under vacuum overnight at 60 ^{o}C. Li metal foil was used as the counter/reference electrode and 1M $LiPF_6$ in 1:1:1 (v/v) EC:DEC:DMC was used as the electrolyte. Celgard 3501 was used as the separator. Cyclic voltammetry tests were performed at various scan rates (1 – 100) mV/s and galvanostatic cycling tests at varying specific currents (50 – 1000 mA/g). All electrodes were preconditioned with 50 cycles of cyclic voltammetry at 20 mV/s. Electrochemical impedance spectroscopy (EIS) was performed using a potentiostat (Gamry Interface 1000, Gamry Instruments) at 3.3 V *vs.* Li/Li^+ with a 5 mV amplitude and frequency range of 1 MHz - 100 mHz.

6.3. Results and Discussion

Fabricating PANI-containing free-standing electrodes is challenging due to PANI's poor mechanical properties and inability to disperse in various solvents.[5, 19] Initially, PANI/water dispersions were directly vacuum filtrated, however, brittle films that cracked upon drying were formed. To improve the mechanical performance of the films, BANFs (10 wt%) were added to the PANI dispersions followed by vacuum filtration. However,

the poor stability of the PANI/BANF dispersion led to inhomogeneous films that also cracked while drying.[5] To avoid this, a two-layer vacuum filtration (1st layer BANF and 2nd layer PANI) was performed, but the obtained electrodes exhibited inferior electrochemical performance resulting from poor electrical percolation. Further attempts were made using PANI:poly(2-acrylamido-2-methyl-1-propanesulfonic acid) (PAAMPSA) as PANI:PAAMPSA complexes form more stable dispersions.[5] Various third components were also added to alleviate the brittleness, such as branched polyethyleneimine (b-PEI), carboxyl functionalized multi-walled carbon nanotubes (MWCNTs-COOH), and graphene oxide (GO). Finally, polymerization of aniline in the presence of BANF and single walled carbon nanotubes (SWCNTs) was selected as it led to homogeneous electrodes with desirable mechanical and electrical properties.

Preparation of the electrode first proceeded by slow dialysis of the BANF/DMSO mixture to exchange water for DMSO. Then, desired amounts of pristine SWCNTs were added to the BANF/water dispersion followed by ultrasonication. Aniline was polymerized in the presence of BANFs (diameter = 15-30 nm)[26] and SWCNTs (diameter = 1.8 nm) to obtain a network morphology. Figure 6.1b-6.1d shows SEM and TEM images of PANI/BANF/CNT bundles forming continuous networks. The shadow in Figure 6.1d is indicative of PANI, as observed before in similar structures.[33, 45] However, we cannot distinguish BANFs from SWCNTs. Additionally, PANI formation was confirmed using EDS and Raman spectroscopy as discussed in more detail below.

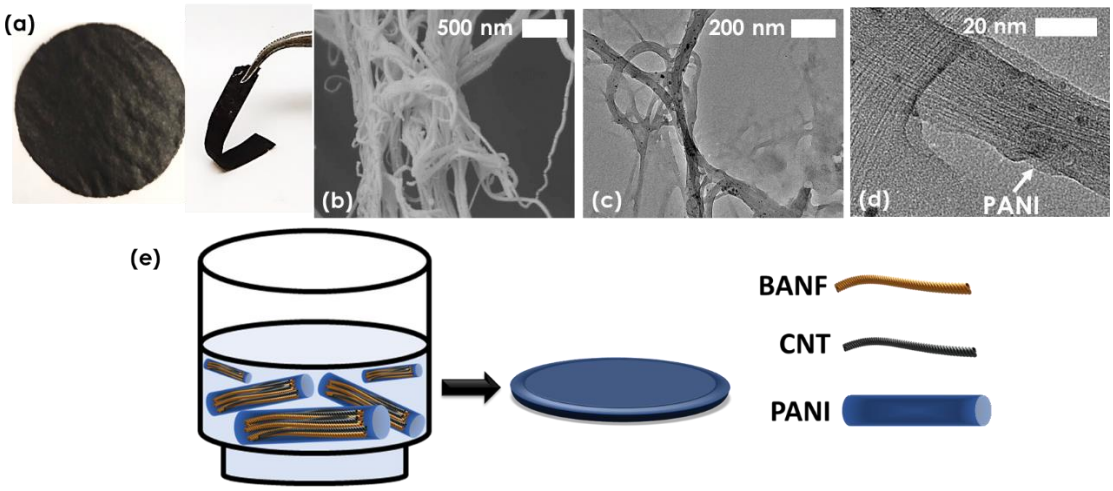

Figure 6.1 (a) Digital image of the PANI/BANF/CNT electrode. SEM (b) and TEM (c and d) images of PANI/BANF/CNT bundles. (e) Schematic representation for the vacuum filtration of the PANI/BANF/CNT bundles.

Mechanically strong electrodes were fabricated using vacuum-assisted filtration, as shown in Figure 6.1. The electrodes were composed of ~15 wt% PANI, whereas the remaining ~85 wt% was divided among BANFs and SWCNTs at desired ratios. Unless otherwise specified, "PANI/BANF/CNT" corresponds to an electrode having a composition of 15 wt% PANI, 73 wt% BANF, and 12 wt% SWCNT.

SWCNT and PANI addition were verified using EDS, Raman spectroscopy, and FT-IR spectroscopy on BANF, BANF/CNT, and PANI/BANF/CNT composites, as shown in Figure 6.2a-c and Figure 6.3. EDS mapping of the N element of the composite surface (Figure 6.2a-c) qualitatively showed a decrease in N content upon addition of SWCNT (BANF/CNT *vs.* BANF). Furthermore, PANI addition (PANI/BANF/CNT)

caused an increase in N, indicating the successful aniline polymerization in the presence of BANF/CNT.

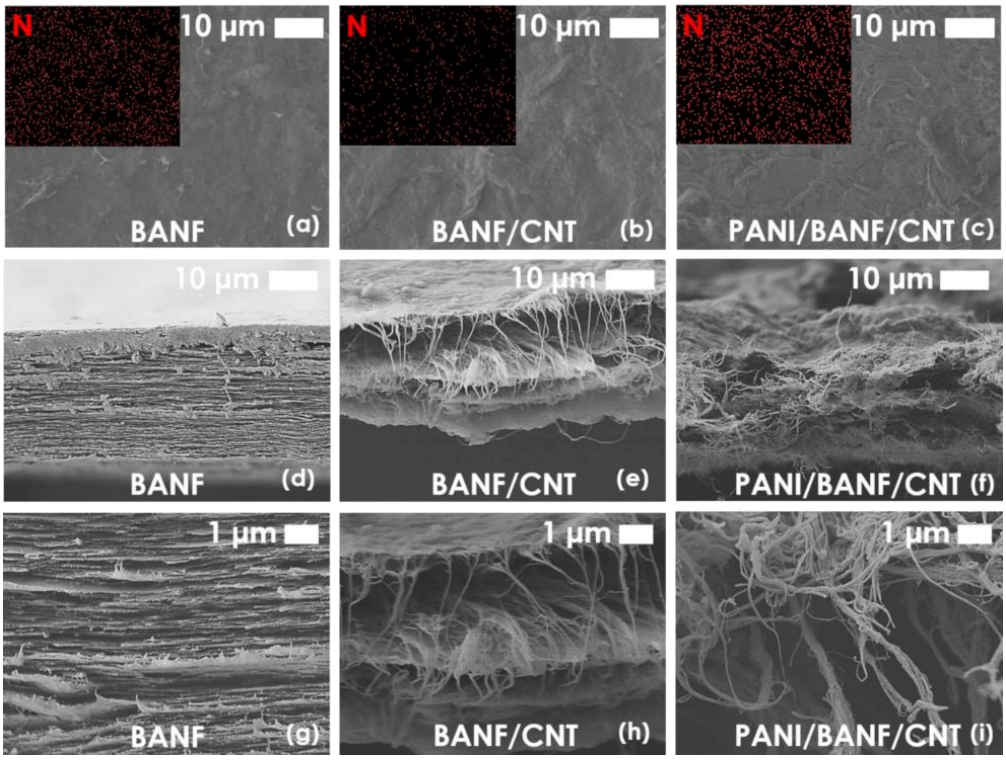

Figure 6.2 (a-c) SEM images and EDS mapping of the N element for BANF, BANF/CNT, and PANI/BANF/CNT surfaces. Cross-sectional SEM images for BANF (d, g), BANF/CNT (e, h), and PANI/BANF/CNT (f, i) at low (d-f) and high (g-i).

Raman spectra are shown in Figure 6.3a. More specifically, BANFs exhibited peaks due to C=C stretching (1176, 1267, 1508, and 1608 cm^{-1}), C-H in-plane bending (1321 cm^{-1}), N-H bending/C-N stretching (1564 cm^{-1}), and C=O stretching (1650 cm^{-1}) modes.[23, 46] BANF/CNT exhibited the G-band at 1588 cm^{-1} resulting from the SWCNT's sp^2-hybrized carbon atoms.[47] PANI/BANF/CNT spectra showed two broad peaks at 1260

– 1450 cm^{-1} and 1490 – 1610 cm^{-1} resulting from the additional contribution of the PANI C-N stretching (1331 cm^{-1}) and C=N stretching (1496 cm^{-1}) modes.[4, 15, 48] These observations demonstrate that SWCNTs and PANI were successfully incorporated in the BANF composites.

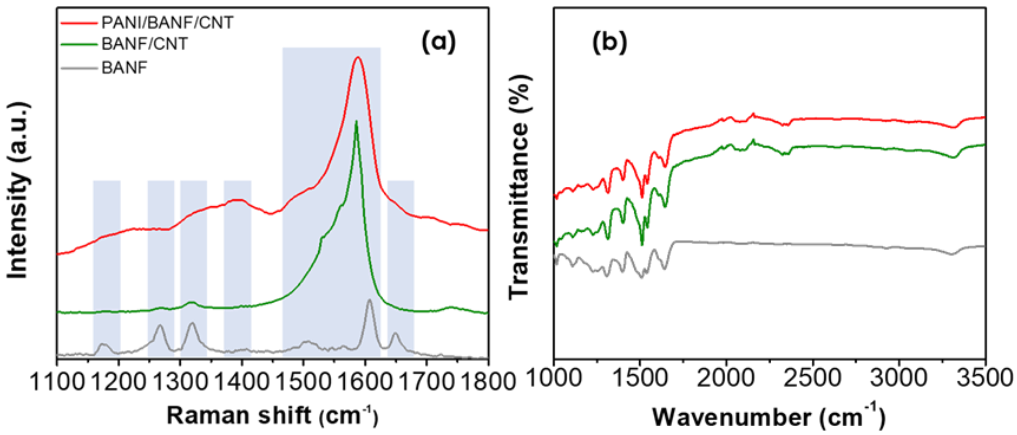

Figure 6.3 (a) Raman and (b) FT-IR spectra for BANF, BANF/CNT, and PANI/BANF/CNT. Legend in panel (a) applies also in panel (b). The shaded regions refer to peaks of interest

The addition of SWCNTs and PANI was also confirmed using FT-IR spectroscopy, as shown in Figure 6.3b. BANF exhibited peaks due to C-H in-plane deformation (1173 cm^{-1}), C-N stretching of secondary aromatic amines (1318 cm^{-1}), C-H bending (1490 cm^{-1}), C=C stretching (1515 cm^{-1}), N-H deformation and C-N stretching coupled modes (1545 cm^{-1}), C=O stretching (1645 cm^{-1}), and N-H stretching (3300 cm^{-1}).[49] Upon addition of SWCNTs (BANF/CNT) the intensity of the C=C peak increased as a result of the additional SWCNT sp^2-hybrized carbon atoms.[50] Furthermore,

PANI/BANF/CNT exhibited peaks due to C-N stretching of secondary aromatic amines (1173 cm^{-1}) and N-B-N stretching (1490 cm^{-1}), where B represents benzenoid and Q quinoid moieties in PANI.[31] The PANI peaks are difficult to distinguish in the FT-IR spectra due to the low PANI composition (~15 wt%) and the location of the peaks.

The morphology of the composites with different compositions was investigated using SEM, as shown in Figure 6.2d – 6.2i and Figure 6.4. BANF films showed a highly layered structure and thicknesses varying from 22-30 μm. The layered structure was maintained upon addition of SWCNT (BANF/CNT) and PANI (PANI/CNT) as shown in Figure 6.2e and Figure 6.4, respectively. In both cases the SWCNTs were visible from the cross-sectional SEM images; however, the addition of PANI led to a less distinguishable layered structure. BANF/CNT, PANI/CNT, and PANI/BANF/CNT composites displayed thicknesses of 5-15 μm.

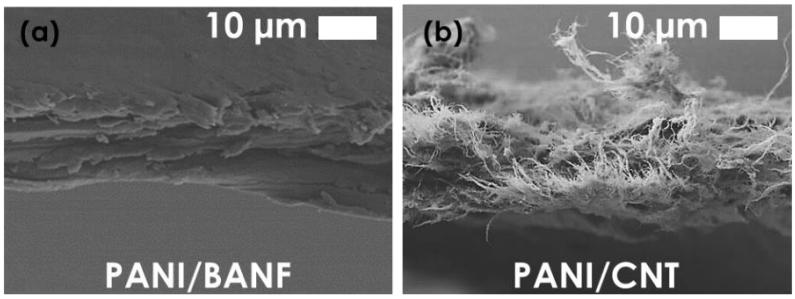

Figure 6.4 Cross-sectional SEM images for (a) PANI/BANF and (b) PANI/CNT.

Tensile tests were conducted to evaluate the mechanical properties of the composites, as shown in Figure 6.5a-6.5c. BANF films exhibited the highest tensile strength (138 ± 5.3 MPa), stain to failure (8.5 ± 0.2 %), and toughness (7100 ± 175 kJ/m^3)

with an intermediate Young's modulus of 3.0 ± 0.1 GPa. The mechanical performance of the BANF films was similar to other ANF-based films reported in the literature.[51-56] Addition of 14 wt% SWCNTs (BANF/CNT) led to a deteriorated mechanical performance due to the dilution of the strong and stiff BANFs. More specifically, tensile strength decreased by 54 % (to 64 ± 6 MPa), Young's modulus by 17 % (to 2.5 ± 0.2 GPa), ultimate strain by 36 % (to 5.4 ± 0.9 %), and toughness by 73 % (to 1900 ± 350 kJ/m^3). PANI/BANF and PANI/BANF/CNT electrodes exhibited lower tensile strength, ultimate strain, and toughness but higher Young's modulus as compared to BANF/CNT. Specifically, PANI/BANF (15 wt% PANI) possessed the highest Young's modulus (5.4 ± 0.6 GPa) with a tensile strength of 58 ± 1.4 MPa, an ultimate tensile strain of 1.9 ± 0.4%, and a toughness of 770 ± 270 kJ/m^3. PANI/BANF/CNT demonstrated a Young's modulus of 4.0 ± 0.5 GPa, tensile strength of 40.0 ± 4.0 MPa, strain of 1.7 ± 0.2 %, and toughness of 430 ± 40 kJ/m^3. This can be attributed to the combined effect of the dilution of the BANFs, the strong interactions between PANI and BANFs, and the high rigidity of the PANI molecules.[3, 31] The rigid PANI molecules interact with the BANFs and SWCNTs through hydrogen bonding and π-π stacking interactions. More specifically, the PANI amine groups hydrogen-bond with the BANF amide groups, while PANI interacts with the BANF aromatic groups and the SWCNT sp^2-hybridized carbon atoms through π-π stacking interactions.[32, 57] The extensive hydrogen bonding and π-π stacking interactions facilitate load transfer within the BANF composites.[58]

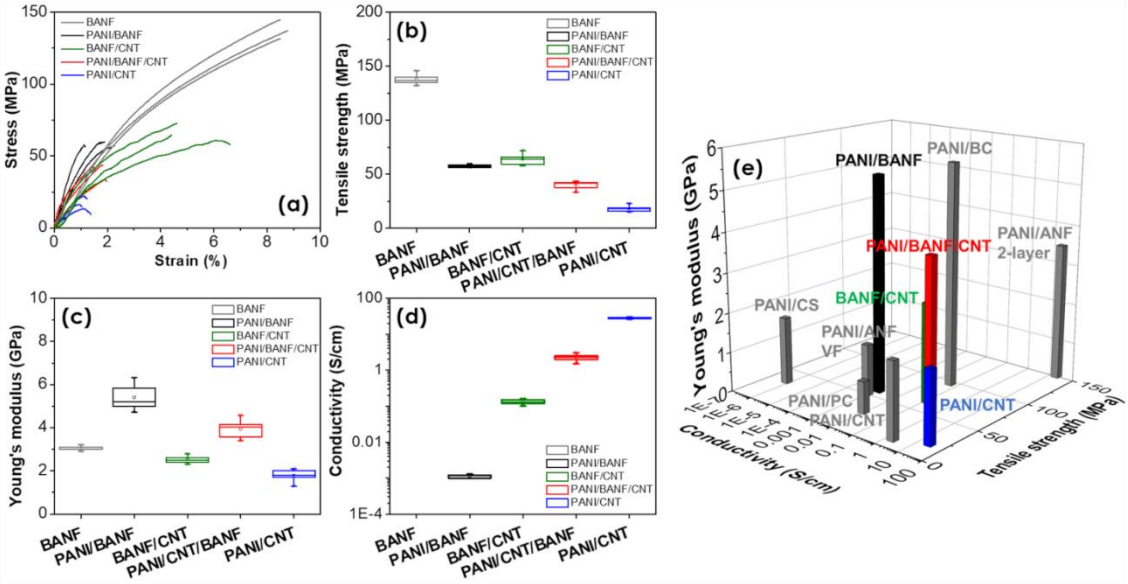

Figure 6.5 Representative stress-stain curves for BANF, BANF/CNT, PANI/BANF, PANI/BANF/CNT, and PANI/CNT. Box plots for (b) tensile strength, (c) Young's modulus, and (d) electrical conductivity. (e) Ashby plot of Young's modulus *vs.* tensile strength *vs.* electrical conductivity for PANI containing free-standing conductive composites. Grey bars represent data obtained from the literature.

The electrical conductivity of the composite films was measured using the four-point probe method, as shown in Figure 6.5d. PANI/BANF composites demonstrated the lowest conductivity ($1.14 \cdot 10^{-3} \pm 0.1 \cdot 10^{-3}$ S/cm) due to poor percolation. Electrical conductivity increased to 2.5 ± 0.4 S/cm upon addition of SWCNTs (PANI/BANF/CNT). Overall, the PANI/BANF/CNT composites exhibited the second highest conductivity despite the high BANF (73 wt%) content. BANF/CNT films demonstrated conductivity values of 0.13 ± 0.02 S/cm while PANI/CNT exhibited the highest conductivity with a value of 28 ± 1.4 S/cm. These results underline the significance of SWCNTs in the

composites as they serve to create an electrically conductive network, assuring good electrical connectivity between PANI and BANF.[59]

Furthermore, the effect of SWCNT content in the PANI/BANF/CNT electrodes on the electrical and mechanical performance was investigated. The PANI content was kept constant (~15 wt%) while the BANF/CNT ratio varied from ~ 11 (7 wt% SWCNT) to ~ 2 (29 wt% SWCNT). Upon decreasing the BANF/CNT ratio from ~11 to ~ 6, electrical conductivity increased from 0.21 ± 0.03 S/cm to 2.5 ± 0.4 S/cm. Further decrease in the BANF/CNT ratio (from ~ 6 to ~ 2) did not lead to significant changes in electrical conductivity, indicating that percolation had already been achieved. In contrast, mechanical performance drastically deteriorated at lower BANF/CNT ratios. BANF/CNT ratios of ~11 (7 wt% SWCNT) led to a tensile strength of 48 ± 4.5 MPa, strain of 1.8 ± 0.2 %, Young's modulus of 4.6 ± 0.4 GPa, and toughness of 508 ± 20 kJ/m^3. Decreasing the BANF/CNT ratio to ~ 2 (29 wt% SWCNT) led to a tensile strength of 10.8 ± 1.7 MPa, strain of 1.2 ± 0.2 %, a Young's modulus of 1.4 ± 0.2 GPa, and a toughness of 81 ± 20 kJ/m^3. These results show that BANFs are critical to maintaining good mechanical properties in the composite electrodes. PANI/BANF/CNT electrodes containing 12 wt% CNT were selected for further electrochemical testing as they led to the best combination of mechanical and electrical properties.

Comparisons against other PANI-containing free-standing composites in the literature are shown in Figure 6.5e. To date, only a handful of reports focus on free-standing PANI films due to PANI's low mechanical performance.[19] Herein, the composite electrodes were compared against two-layer PANI/ANF, PANI/polycarbonate (PC),

PANI/bacterial cellulose (BC), PANI/chitosan (CS), PANI/ANF fabricated using vacuum filtration (VF), and PANI/CNT.[3, 21, 22, 31, 33, 60] All composites contained similar amounts of PANI (10 - 15 wt%). Our PANI/BANF/CNT composites exhibited a good combination of electrical and mechanical properties in the comparison. Two-layer PANI/ANF exhibited the highest reported electrical conductivity (19.3 S/cm) and tensile strength (150 MPa) with a Young's modulus of 3.4 MPa.[31] The premade ANF layer served as the structural support while the impregnated layer of PANI ensured good electrical conductivity.[31] PANI/CS and PANI/CNT were fabricated by directly mixing PANI with CS and CNTs, respectively, leading to inhomogeneous films and as a result to an inferior mechanical performance.[21, 60] PANI/BC, PANI/PC, and PANI/ANF VF were prepared by polymerizing aniline in the presence of the other components, similar to our approach.[3, 22, 33] PANI/PC and PANI/ANF VF demonstrated relatively high tensile strengths but the electrical conductivities and Young's moduli were significantly inferior to the PANI/BANF/CNT composites.[3, 33] PANI/BC exhibited higher mechanical properties but with a lower electrical conductivity.[22] This comparison shows that the superior electrical conductivity of our PANI/BANF/CNT composites results from the continuous SWCNT conductive networks whereas the enhanced mechanical performance results from the extensive hydrogen bonding and π-π stacking interactions between BANFs, PANI, and SWCNTs. The good mechanical and electrical properties of the PANI/BANF/CNT make them ideal candidates for structural electrodes.

The electrochemical performance of the composite electrodes was evaluated in a two-electrode symmetric coin cell configuration using 1 M H_2SO_4 aqueous electrolyte.

More specifically, cyclic voltammetry (CV) was performed for PANI/CNT, PANI/BANF, PANI/BANF/12 wt% CNT, and BANF/CNT at 1 mV/s, as shown in Figure 6.6a. The shapes of the CV curves for the PANI-containing electrodes indicate a pseudo-capacitive behaviour resulting from the redox-active nature of PANI.[61] PANI/CNT and PANI/BANF/12 wt% CNT exhibited two broad pairs of redox peaks attributed to the leucoemeraldine/emeraldine and emeraldine/pernigraniline transitions of PANI.[59, 62]

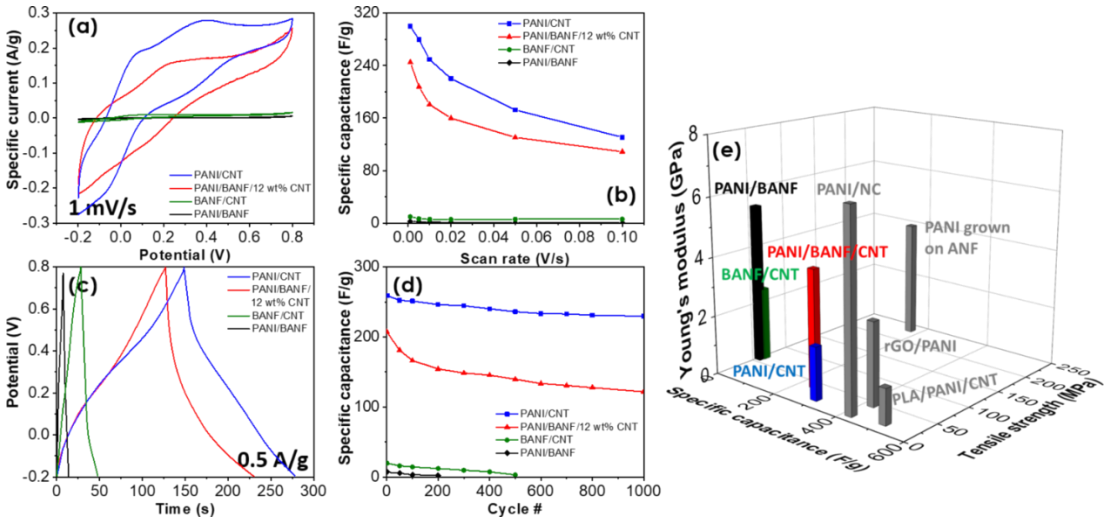

Figure 6.6 (a) Cyclic voltammograms at 1 mV/s and (b) specific capacitance *vs.* scan rate for PANI/BANF, BANF/CNT, PANI/ BANF/12 wt% CNT, and PANI/CNT. (c) Galvanostatic charge-discharge curves and (d) specific capacitance *vs.* cycle number for all electrodes at 0.5 A/g. (e) Ashby plot of Young's modulus *vs.* specific capacitance *vs.* tensile strength for PANI-containing free-standing supercapacitor electrodes. Specific capacitance values were calculated per active mass (PANI, CNT, and rGO mass).

The specific capacitance (based on active mass) for all electrodes was calculated at varying scan rates (1 – 100 mV/s) (Figure 6.6b). BANF/CNT and PANI/BANF

exhibited an inferior performance attributed to the low electrical conductivity and low content of the electrochemically active materials. PANI/CNT exhibited the highest specific capacitance values, with a specific capacitance of 299.1 ± 1.2 F/g at 1 mV/s. PANI/BANF/12 wt% CNT electrodes showed a similar behaviour despite the high content of BANFs (73 wt%), with a specific capacitance of 245.4 ± 2.6 F/g at 1 mV/s. CNTs and PANI form together a network that allows for fast electron and ion transport with increased surface area, facilitating fast redox reactions.[63] Specific capacitance decreased with scan rate for all electrodes resulting from diffusion limitations, as expected.[59,64]

Furthermore, galvanostatic cycling was conducted at 0.5 A/g. The curves exhibited quasi-triangular shapes resulting from the pseudocapacitive nature of PANI and the double-layer behaviour of CNTs, as shown in Figure 6.6c. Prolonged galvanostatic cycling experiments were conducted up to 1,000 cycles (Figure 6.6d). PANI/BANF and BANF/CNT electrodes did not reach 1,000 cycles due to their poor performance. The results are in agreement with the cyclic voltammetry tests. PANI/CNT and PANI/BANF/12 wt% CNT exhibited capacitance retentions of ~90 % and ~60 %, respectively. The lower capacitance retention of the BANF containing electrodes may be attributed to possible structural changes during cycling resulting from the swelling of BANFs in the electrolyte, as observed before in the literature.[65] Swelling of BANFs may close open pores, preventing the electrolyte penetration, and as a result leading to reduced cycling stability.

Finally, the structural supercapacitor electrodes were compared against other PANI containing free-standing electrodes from the literature, as shown in Figure 6.6e.

More specifically, PANI/BANF/12 wt% CNT electrodes were compared against rGO/PANI, polylactic acid (PLA)/CNT/PANI, PANI/nanocellulose (NC), and PANI grown on ANF.[17, 18, 34, 66] rGO/PANI, PLA/CNT/PANI, and PANI/NC exhibited higher specific capacitance values.[18, 66, 67] The enhanced energy storage performance of the rGO/PANI electrodes can be attributed to the higher PANI content (25.4 wt%).[67] The exact PANI content of the PANI/NC and PLA/CNT/PANI electrodes was not reported.[12, 18] Our PANI/BANF/12 wt% CNT electrodes exhibited a better combination of high energy storage, Young's modulus, and tensile strength. The better mechanical performance (tensile strength and Young's modulus) of the PANI/BANF/12 wt% CNT electrodes results from the strong BANFs and the extensive interfacial interactions (hydrogen bonding and π-π stacking interactions) within the composites. The PANI/BANF/12 wt% CNT electrodes exhibited a good combination of mechanical properties with a decent electrochemical performance in two electrode symmetric cells. At this point, it is worth mentioning the recent report on PANI grown on ANF premade films.[34] These electrodes exhibited a high tensile strength (233.3 MPa) with a similar Young's modulus (~4 GPa) to our electrodes, resulting from the strong premade ANF films/substrates.[34] The reported specific capacitance values in a two-electrode symmetric solid state device (~168 F/g based on active mass and 138 F/g based on total electrode mass) are comparable to our PANI/BANF/12 wt% CNT electrodes.[34] However, it is not possible to draw any further concrete conclusions regarding the energy storage performance (*i.e.* rate capability and cycling stability) as different testing configurations were used.

Besides being redox-active in aqueous media, as demonstrated above, PANI may also be utilized as the cathode in a non-aqueous Li-ion battery.[68] Towards this idea, the performance of a PANI/BANF/12 wt% CNT cathode in a Li-ion battery was investigated in a lithium metal half-cell. Specifically, Li metal foil was the anode and 1 M $LiPF_6$ in EC:DEC:DMC (1:1:1 v/v) was the electrolyte. Cyclic voltammetry was conducted at a scan rate of 1 mV/s in a 1.5 to 4 V *vs.* Li/Li^+ voltage range, as shown in Figure 6.7a. The PANI/BANF/12 wt% CNT cell exhibited one pair of wide peaks due to the leucoemeraldine/emeraldine transformation,[15 7, 63] whereas BANF/CNT showed no peaks. Capacitive plateaus are attributed to the CNTs.[69]

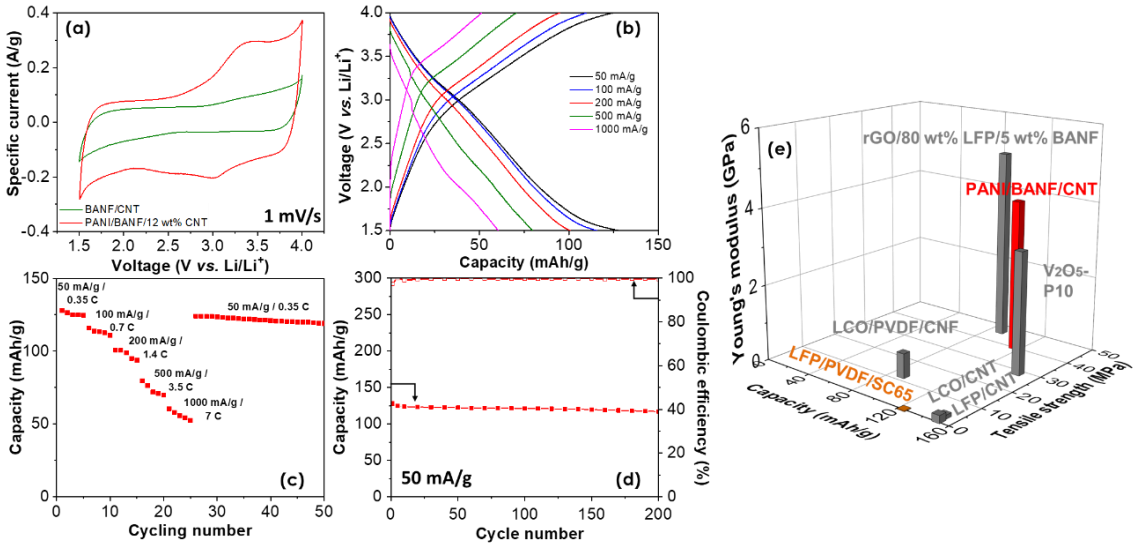

Figure 6.7 (a) Cyclic voltammograms at 1 mV/s for BANF/CNT (green) and PANI/BANF/12 wt% CNT (red) electrodes in a lithium metal half-cell. (b) Galvanostatic charge-discharge curves at varying specific currents (50 – 1000 mA/g), (c) rate capability, and (d) prolonged galvanostatic cycling at 50 mA/g for 200 cycles for a PANI/BANF/12 wt% CNT cathode. (e) Ashby plot for tensile strength *vs.* Young's modulus *vs.* capacity.

Grey bars correspond to data obtained from the literature for lithium-ion battery cathodes and the orange cylinder is the equivalent to a commercial LFP cathode. All capacities were calculated based on active material (PANI, LFP, LCO, or V_2O_5) mass loadings.

Figure 6.7b and 6.7c presents the charge-discharge voltage profiles at varying specific currents (50 – 1000 mA/g) and the rate capability, respectively. The discharge capacity at 50 mA/g was 128 mAh/g, whereas at 1000 mA/g the discharge capacity dropped to 61 mAh/g. Subsequently, a capacity of 124 mAh/g was recovered at 50 mA/g, indicating the high stability of the electrodes. Prolonged charge-discharge tests at 50 mA/g were conducted for 200 cycles, Figure 6.7d. After 200 cycles, the discharge capacity was maintained at 116 mAh/g with a coulombic efficiency of 99.1 % (*vs.* 97 % for the first cycle), with a low slope (starting from the 50^{th} cycle) of 0.03. The obtained capacity values are comparable with the theoretical capacity of PANI (147 mAh/g for one electron transferred per two repeat units), underlining the exceptional energy storage performance of the PANI/BANF/12 wt% CNT cathodes.

Furthermore, we conducted electrochemical impedance spectroscopy (EIS) before and after 25 cycles at 3.3 V *vs.* Li/Li^+. Figure 6.8 shows the Nyquist plot, while the inset shows the equivalent circuit used to analyse the EIS data. The Nyquist plots before and after cycling exhibited a similar behaviour, with one semicircle at high frequency and a long diffusive tail at low frequency. In the equivalent circuit, R_S (intercept with the real axis) is attributed to the electrolyte resistance, R_{CT} represents the charge transfer impedance, *CPE* represents the non-ideal electric double layer capacitance, and W_o represents the Warburg impedance due to the lithium ion diffusion in the bulk of the

electrode.[70] Before cycling the fitted value of R_{CT} was 25 Ω and after 25 cycles R_{CT} decreased to 12 Ω. The angle of the diffusive tail which is indicative of lithium ion diffusion[71] decreased slightly from 74° to 66°. The low R_{CT} values[72] and the relatively small variation in the EIS data with cycling indicate the good electronic conductivity and structural stability of the PANI/BANF/12 wt% CNT cathodes.

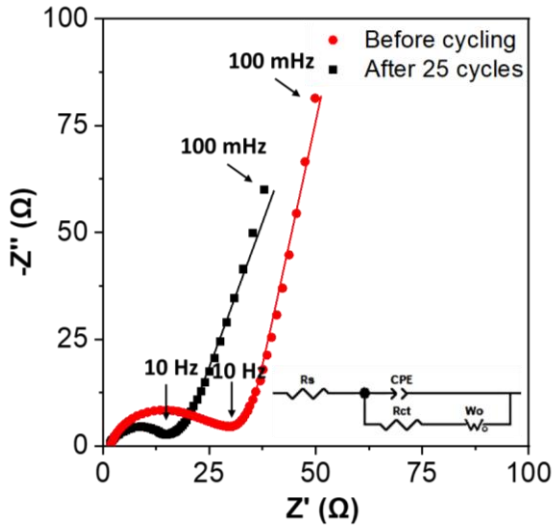

Figure 6.8 Nyquist plot of PANI/BANF/12 wt% CNT cathode obtained by performing EIS before cycling and after 25 cycles. The inset shows the equivalent circuit used to model the data. EIS was conducted at 3.3 V *vs.* Li/Li^+ with a 5 mV amplitude and a frequency range of 1 MHz - 100 mHz.

Ragone plots of specific power *vs.* specific energy and power density *vs.* energy density are shown in Figure 6.9. The PANI/BANF/CNT electrodes exhibited a maximum specific energy value of 320 mWh/g at a specific power of 8,000 mW/g, and a maximum specific power of 9,166 mW/g at a specific energy of 138 mWh/g. Similarly, the highest energy density was 243 mWh/L at a power density of 11,550 mW/L and the maximum

power density was 13,250 mW/L at an energy density of 105 mWh/L. PANI/BANF/CNT exhibited comparable performance with other PANI-based non-structural electrodes coated on conductive substrates, such as PANI/V_2O_5 and PANI/rGO.[15, 73]

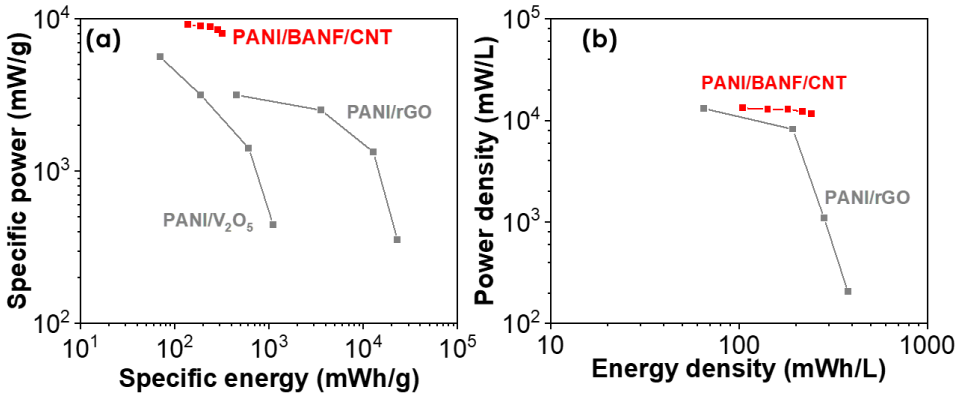

Figure 6.9 (a) Specific power *vs.* specific energy and (b) power density *vs.* energy density (based on active mass) for PANI/BANF/12 wt% CNT cathodes in a lithium metal half-cell. Grey data correspond to PANI-based electrodes from the literature.

Our electrodes were compared against other PANI-based battery electrodes such as PANI/MXene, PANI/rGO, PANI/SWCNTs aerogels, PANI/MWCNTs, and PANI/polyoxometalate.[8, 15, 74-76] Despite the low PANI content (~15 wt%), the PANI/BANF/12 wt% CNT electrodes exhibited comparable but lower capacities as compared to the literature. However, notably, our electrodes were free-standing with good mechanical properties, whereas the mechanical properties were not reported for these prior reports. Further, most of the prior electrodes were coated onto conductive substrates for structural support.[8, 15, 75, 76] Additionally, the PANI/BANF/CNT were compared with other cathodes from the literature, such as commercial LFP/CB/PVDF (90:5:5, wt/wt),[77]

LFP/CNT,[78] LCO/CF/PVDF (82:7:11, wt/wt),[79] LCO/CNT,[80] and V_2O_5/P3HT-b-PEO (P10, 90:10 wt/wt), as shown in Figure 6.7e. This comparison demonstrates that the PANI/BANF/12 wt% CNT electrodes are potential candidates for structural cathode materials in Li-ion batteries due to their high capacity, good rate charge-discharge performance, good cycle performance, and mechanical performance.

Since PANI is a pseudocapacitive material, unlike the materials studied in the previous chapters, with both Faradaic and non-Faradaic contributions, we further investigated the charge storage mechanism of the PANI/BANF/12 wt% CNT cathodes in the Li-ion battery environment, and the Faradaic and non-Faradaic contributions were distinguished using equation 6.1:

$$I = a \cdot v^b \tag{6.1}$$

where I is the specific current (A/g), v the scan rate (mV/s), and a and b are adjustable parameters.[15, 73, 81] The redox process is considered as an ideal Faradaic process when b is 0.5, whereas when b is 1 the process is considered to be a non-Faradaic process. Values between 0.5 and 1 indicate a mixed mechanism.[8, 13, 15, 81] The b-values for the PANI/BANF/12 wt% CNT cathodes were obtained from the slope of the log (I) *vs.* log (v) graphs for scan rates of 1 – 20 mV/s. Figure 6.10 shows the b-values obtained from the anodic and cathodic scans from 1.5 to 4 V. More specifically, in the cathodic scans, the b-value reached a minimum of b = 0.47 at 3 V, which is in accordance with the Faradaic peak observed in the CV curves. Similarly, in the anodic scans the b-value reached a minimum of b = 0.46 at 3.3 V. The results indicate qualitatively that charge storage within

the PANI/BANF/12 wt% CNT electrodes occurred with mixed Faradaic (due to PANI's leucoemeraldine/emeraldine transformation) and non-Faradaic contributions.

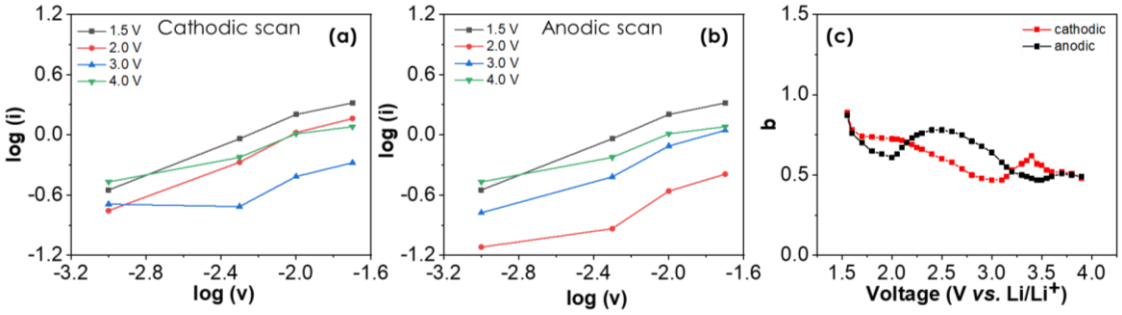

Figure 6.10 Plot of log(I) *vs.* log(v) for (a) cathodic and (b) anodic scans in cyclic voltammetry for PANI/BANF/12 wt% CNT cathodes. (c) Plot of b-value *vs.* potential (V *vs.* Li/Li^+) as calculated from $\log(I) = b \cdot \log(v) + \log(a)$.

Additionally, the relative contributions of Faradaic and non-Faradaic charge storage were calculated using equation 6.2 (power law for b = 1, ideal Faradaic process and b = ½, non-Faradaic process):

$$I = a_1 \cdot v + a_2 \cdot v^{0.5} \tag{6.2}$$

where I is the specific current (A/g) and a_1 and a_2 are the relative contributions of the non-Faradaic and Faradaic processes, respectively.[8, 15, 70] The values of a_1 and a_2 were obtained from the slopes and intercepts of the $I/v^{0.5}$ *vs.* $v^{0.5}$ plots. From this analysis, we reconstructed the cyclic voltammetry plot at 1 mV/s, as shown in Figure 6.11a. The blue line corresponds to the non-Faradaic processes, the green to the Faradaic, and the red to the total specific current. The results indicate that the charge storage mechanism is dominated by Faradaic processes. Figure 6.11b shows the percentage contributions of non-

Faradaic and Faradaic mechanisms at various scan rates (1 mV/s – 20 mV/s). The Faradaic charge storage decreased from 84 % to 51 % with scan rate, which is typical for PANI-based electrodes due to diffusion limitations.[8]

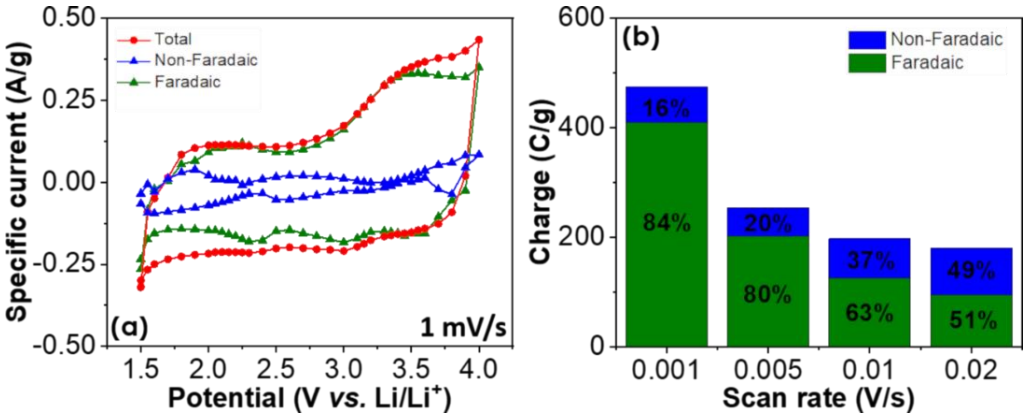

Figure 6.11 Cyclic voltammetry (a) at 1 mV/s for PANI/BANF/12 wt% CNT cathodes and (b) charge stored at different scan rates displaying the Faradaic (green) and non-Faradaic (blue) contribution.

6.4. Conclusions

Structural electrodes for supercapacitors and batteries based on PANI, BANFs, and CNTs were developed. BANFs served as the load bearing component while CNTs and PANI facilitated fast electronic transport. Further, PANI stored charge through its conversion among leucoemeraldine, emeraldine, and pernigraniline states. Extensive hydrogen bonding and π-π stacking interactions within the composite electrodes were harnessed, leading to high mechanical performance (tensile strength and Young's modulus). The continuous networks created by BANFs, CNTs, and PANI led to a good combination of energy storage and mechanical performance as compared to the literature,

making them ideal candidates for structural electrodes in both supercapacitors and lithium-ion batteries. The structural electrodes exhibited capacity values (128 ± 5 mAh/g) comparable to the theoretical capacity of PANI (147 mAh/g), indicating the PANI was nearly fully utilized. The charge storage mechanism was further investigated by distinguishing the Faradaic and non-Faradaic contributions. As expected for PANI-based electrodes mixed contributions were obtained. This work demonstrates an efficient route for designing and fabricating structural electrodes for both supercapacitors and lithium-ion batteries based on conjugated polymers with high energy storage performance.

6.5. References

1. Fusalba, F.; Gouérec, P.; Villers, D.; Bélanger, D., Electrochemical Characterization of Polyaniline in Nonaqueous Electrolyte and Its Evaluation as Electrode Material for Electrochemical Supercapacitors. *J. Electrochem. Soc.* **2001,** *148* (1), A1-A6.
2. Long, Y.-Z.; Li, M.-M.; Gu, C.; Wan, M.; Duvail, J.-L.; Liu, Z.; Fan, Z., Recent advances in synthesis, physical properties and applications of conducting polymer nanotubes and nanofibers. *Prog. Polym. Sci.* **2011,** *36* (10), 1415-1442.
3. Jeon, B. H.; Kim, S.; Choi, M. H.; Chung, I. J., Synthesis and characterization of polyaniline–polycarbonate composites prepared by an emulsion polymerization. *Synth. Met.* **1999,** *104* (2), 95-100.
4. Jeon, J.-W.; Kwon, S. R.; Li, F.; Lutkenhaus, J. L., Spray-On Polyaniline/Poly(acrylic acid) Electrodes with Enhanced Electrochemical Stability. *ACS Applied Materials & Interfaces* **2015,** *7* (43), 24150-24158.
5. Jeon, J.-W.; O'Neal, J.; Shao, L.; Lutkenhaus, J. L., Charge Storage in Polymer Acid-Doped Polyaniline-Based Layer-by-Layer Electrodes. *ACS Applied Materials & Interfaces* **2013,** *5* (20), 10127-10136.
6. MacDiarmid, A. G.; Epstein, A. J., The concept of secondary doping as applied to polyaniline. *Synth. Met.* **1994,** *65* (2), 103-116.
7. MacDiarmid, A. G.; Yang, L. S.; Huang, W. S.; Humphrey, B. D., Polyaniline: Electrochemistry and application to rechargeable batteries. *Synth. Met.* **1987,** *18* (1), 393-398.
8. Yun, J.; Echols, I.; Flouda, P.; Wang, S.; Easley, A.; Zhao, X.; Tan, Z.; Prehn, E.; Zi, G.; Radovic, M.; Green, M. J.; Lutkenhaus, J. L., Layer-by-Layer Assembly of Polyaniline Nanofibers and MXene Thin-Film Electrodes for Electrochemical Energy Storage. *ACS Applied Materials & Interfaces* **2019**.

9. Ghenaatian, H. R.; Mousavi, M. F.; Rahmanifar, M. S., High performance hybrid supercapacitor based on two nanostructured conducting polymers: Self-doped polyaniline and polypyrrole nanofibers. *Electrochim. Acta* **2012,** *78*, 212-222.
10. Kwon, S. R.; Jeon, J.-W.; Lutkenhaus, J. L., Sprayable, paintable layer-by-layer polyaniline nanofiber/graphene electrodes. *RSC Advances* **2015,** *5* (20), 14994-15001.
11. Wu, Q.; Xu, Y.; Yao, Z.; Liu, A.; Shi, G., Supercapacitors Based on Flexible Graphene/Polyaniline Nanofiber Composite Films. *ACS Nano* **2010,** *4* (4), 1963-1970.
12. Meng, C.; Liu, C.; Fan, S., Flexible carbon nanotube/polyaniline paper-like films and their enhanced electrochemical properties. *Electrochem. Commun.* **2009,** *11* (1), 186-189.
13. Shao, L.; Jeon, J.-W.; Lutkenhaus, J. L., Polyaniline nanofiber/vanadium pentoxide sprayed layer-by-layer electrodes for energy storage. *Journal of Materials Chemistry A* **2014,** *2* (35), 14421-14428.
14. Moon, S.; Jung, Y. H.; Kim, D. K., Enhanced electrochemical performance of a crosslinked polyaniline-coated graphene oxide-sulfur composite for rechargeable lithium–sulfur batteries. *J. Power Sources* **2015,** *294*, 386-392.
15. Jeon, J.-W.; Kwon, S. R.; Lutkenhaus, J. L., Polyaniline nanofiber/electrochemically reduced graphene oxide layer-by-layer electrodes for electrochemical energy storage. *Journal of Materials Chemistry A* **2015,** *3* (7), 3757-3767.
16. Yanilmaz, M.; Dirican, M.; Asiri, A. M.; Zhang, X., Flexible polyaniline-carbon nanofiber supercapacitor electrodes. *Journal of Energy Storage* **2019,** *24*, 100766.
17. Hsu, H. H.; Khosrozadeh, A.; Li, B.; Luo, G.; Xing, M.; Zhong, W., An Eco-Friendly, Nanocellulose/RGO/in Situ Formed Polyaniline for Flexible and Free-Standing Supercapacitors. *ACS Sustainable Chemistry & Engineering* **2019,** *7* (5), 4766-4776.
18. Wang, Q.; Wang, H.; Du, P.; Liu, J.; Liu, D.; Liu, P., Porous polylactic acid/carbon nanotubes/polyaniline composite film as flexible free-standing electrode for supercapacitors. *Electrochim. Acta* **2019,** *294*, 312-324.
19. Valentová, H.; Stejskal, J., Mechanical properties of polyaniline. *Synth. Met.* **2010,** *160* (7), 832-834.
20. Mottaghitalab, V.; Spinks, G. M.; Wallace, G. G., The influence of carbon nanotubes on mechanical and electrical properties of polyaniline fibers. *Synth. Met.* **2005,** *152* (1), 77-80.
21. Blighe, F. M.; Diamond, D.; Coleman, J. N.; Lahiff, E., Increased response/recovery lifetimes and reinforcement of polyaniline nanofiber films using carbon nanotubes. *Carbon* **2012,** *50* (4), 1447-1454.
22. Hu, W.; Chen, S.; Yang, Z.; Liu, L.; Wang, H., Flexible Electrically Conductive Nanocomposite Membrane Based on Bacterial Cellulose and Polyaniline. *The Journal of Physical Chemistry B* **2011,** *115* (26), 8453-8457.
23. Kwon, S. R.; Elinski, M. B.; Batteas, J. D.; Lutkenhaus, J. L., Robust and Flexible Aramid Nanofiber/Graphene Layer-by-Layer Electrodes. *ACS Appl Mater Interfaces* **2017,** *9* (20), 17125-17135.

24. Kwon, S. R.; Harris, J.; Zhou, T.; Loufakis, D.; Boyd, J. G.; Lutkenhaus, J. L., Mechanically Strong Graphene/Aramid Nanofiber Composite Electrodes for Structural Energy and Power. *ACS Nano* **2017,** *11* (7), 6682-6690.
25. Flouda, P.; Feng, X. Y.; Boyd, J. G.; Thomas, E. L.; Lagoudas, D. C.; Lutkenhaus, J. L., Interfacial Engineering of Reduced Graphene Oxide for Aramid Nanofiber-Enabled Structural Supercapacitors. *Batteries & Supercaps* **2019,** *2* (5), 464-472.
26. Flouda, P.; Shah, S. A.; Lagoudas, D. C.; Green, M. J.; Lutkenhaus, J. L., Highly Multifunctional Dopamine-Functionalized Reduced Graphene Oxide Supercapacitors. *Matter* **2019,** *1* (6), 1532-1546.
27. Sun, W.; Shah, S. A.; Lowery, J. L.; Oh, J. H.; Lutkenhaus, J. L.; Green, M. J., Lightweight Kevlar-Reinforced Graphene Oxide Architectures with High Strength for Energy Storage. *Advanced Materials Interfaces 0* (0), 1900786.
28. Shah, S. A.; Kulhanek, D.; Sun, W.; Zhao, X.; Yu, S.; Parviz, D.; Lutkenhaus, J. L.; Green, M. J., Aramid nanofiber-reinforced three-dimensional graphene hydrogels for supercapacitor electrodes. *J. Colloid Interface Sci.* **2019**.
29. Patel, A. G.; Johnson, L.; Arroyave, R.; Lutkenhaus, J. L., Design of multifunctional supercapacitor electrodes using an informatics approach. *Mol Syst Des Eng* **2019,** *4*, 654-663.
30. Flouda, P.; Yun, J.; Loufakis, D.; Shah, S. A.; Green, M. J.; Lagoudas, D. C.; Lutkenhaus, J. L., Structural reduced graphene oxide supercapacitors mechanically enhanced with tannic acid. *Sustainable Energy & Fuels* **2020,** *4* (5), 2301-2308.
31. Lyu, J.; Zhao, X.; Hou, X.; Zhang, Y.; Li, T.; Yan, Y., Electromagnetic interference shielding based on a high strength polyaniline-aramid nanocomposite. *Compos. Sci. Technol.* **2017,** *149*, 159-165.
32. Zhao, Y.; Zhang, S.; Hu, F.; Li, J.; Chen, H.; Lin, J.; Yan, B.; Gu, Y.; Chen, S., Electrochromic polyaniline/aramid nanofiber composites with enhanced cycling stability and film forming property. *Journal of Materials Science: Materials in Electronics* **2019,** *30* (13), 12718-12728.
33. Han, X.; Lv, L.; Yu, D.; Wu, X.; Li, C., Conductive Core–Shell Aramid Nanofibrils: Compromising Conductivity with Mechanical Robustness for Organic Wearable Sensing. *ACS Applied Materials & Interfaces* **2019,** *11* (3), 3466-3473.
34. Yin, Q.; Jia, H.; Mohamed, A.; Ji, Q.; Hong, L., Highly flexible and mechanically strong polyaniline nanostructure @ aramid nanofiber films for free-standing supercapacitor electrodes. *Nanoscale* **2020,** *12* (9), 5507-5520.
35. Zhu, J.; Yang, M.; Emre, A.; Bahng, J. H.; Xu, L.; Yeom, J.; Yeom, B.; Kim, Y.; Johnson, K.; Green, P.; Kotov, N. A., Branched Aramid Nanofibers. *Angewandte Chemie* **2017,** *129* (39), 11906-11910.
36. Eftekhari, A.; Li, L.; Yang, Y., Polyaniline supercapacitors. *Journal of Power Sources* **2017,** *347*, 86-107.
37. Zhang, L. L.; Zhao, X. S., Carbon-based materials as supercapacitor electrodes. *Chemical Society Reviews* **2009,** *38* (9), 2520-2531.

38. Kim, Y. J.; Shin, T. S.; Choi, H. D.; Kwon, J. H.; Chung, Y.-C.; Yoon, H. G., Electrical conductivity of chemically modified multiwalled carbon nanotube/epoxy composites. *Carbon* **2005,** *43* (1), 23-30.
39. Marinho, B.; Ghislandi, M.; Tkalya, E.; Koning, C. E.; de With, G., Electrical conductivity of compacts of graphene, multi-wall carbon nanotubes, carbon black, and graphite powder. *Powder Technology* **2012,** *221*, 351-358.
40. Wang, H.; Lu, S.; Chen, Y.; Han, L.; Zhou, J.; Wu, X.; Qin, W., Graphene/Co9S8 nanocomposite paper as a binder-free and free-standing anode for lithium-ion batteries. *Journal of Materials Chemistry A* **2015,** *3* (47), 23677-23683.
41. Cheng, Y.; Lu, S.; Zhang, H.; Varanasi, C. V.; Liu, J., Synergistic Effects from Graphene and Carbon Nanotubes Enable Flexible and Robust Electrodes for High-Performance Supercapacitors. *Nano Letters* **2012,** *12* (8), 4206-4211.
42. Xu, L.; Zhao, X.; Xu, C.; Kotov, N. A., Water-Rich Biomimetic Composites with Abiotic Self-Organizing Nanofiber Network. *Adv. Mater* **2018,** *30* (1), 1703343-n/a.
43. Jeon, J.-W.; Ma, Y.; Mike, J. F.; Shao, L.; Balbuena, P. B.; Lutkenhaus, J. L., Oxidatively stable polyaniline:polyacid electrodes for electrochemical energy storage. *Physical Chemistry Chemical Physics* **2013,** *15* (24), 9654-9662.
44. Hummers, W. S.; Offeman, R. E., Preparation of Graphitic Oxide. *Journal of the American Chemical Society* **1958,** *80* (6), 1339-1339.
45. Kim, J. Y.; Park, Y. J., Carbon nanotube/Co3O4 nanocomposites selectively coated by polyaniline for high performance air electrodes. *Scientific Reports* **2017,** *7* (1), 8610.
46. Penn, L.; Milanovich, F., Raman spectroscopy of Kevlar 49 fibre. *Polymer* **1979,** *20* (1), 31-36.
47. Konyushenko, E. N.; Stejskal, J.; Trchová, M.; Hradil, J.; Kovářová, J.; Prokeš, J.; Cieslar, M.; Hwang, J.-Y.; Chen, K.-H.; Sapurina, I., Multi-wall carbon nanotubes coated with polyaniline. *Polymer* **2006,** *47* (16), 5715-5723.
48. Kim, S. Y.; Hong, J.; Kavian, R.; Lee, S. W.; Hyder, M. N.; Shao-Horn, Y.; Hammond, P. T., Rapid fabrication of thick spray-layer-by-layer carbon nanotube electrodes for high power and energy devices. *Energ Environ Sci* **2013,** *6* (3), 888-897.
49. Yang, M.; Cao, K.; Sui, L.; Qi, Y.; Zhu, J.; Waas, A.; Arruda, E. M.; Kieffer, J.; Thouless, M. D.; Kotov, N. A., Dispersions of aramid nanofibers: a new nanoscale building block. *ACS Nano* **2011,** *5* (9), 6945-54.
50. He, S.; Wei, J.; Guo, F.; Xu, R.; Li, C.; Cui, X.; Zhu, H.; Wang, K.; Wu, D., A large area, flexible polyaniline/buckypaper composite with a core–shell structure for efficient supercapacitors. *Journal of Materials Chemistry A* **2014,** *2* (16), 5898-5902.
51. Xiao, G.; Di, J.; Li, H.; Wang, J., Highly thermally conductive, ductile biomimetic boron nitride/aramid nanofiber composite film. *Composites Science and Technology* **2020,** *189*, 108021.
52. Yang, B.; Ding, X.; Zhang, M.; Wang, L.; Huang, X., A flexible, strong, heat- and water-resistant zeolitic imidazolate framework-8 (ZIF-8)/ aramid nanofibers (ANFs) composite nanopaper. *Composites Communications* **2020,** *17*, 192-196.

53. Xie, F.; Jia, F.; Zhuo, L.; Lu, Z.; Si, L.; Huang, J.; Zhang, M.; Ma, Q., Ultrathin MXene/aramid nanofiber composite paper with excellent mechanical properties for efficient electromagnetic interference shielding. *Nanoscale* **2019,** *11* (48), 23382-23391.
54. Luo, J.; Zhang, M.; Nie, J.; Liu, G.; Tan, J.; Yang, B.; Song, S.; Zhao, J. R., A deep insight into the structure and performance evolution of aramid nanofiber films induced by UV irradiation. *Polymer Degradation and Stability* **2019,** *167*, 170-178.
55. Yang, B.; Wang, L.; Zhang, M.; Luo, J.; Ding, X., Timesaving, High-Efficiency Approaches To Fabricate Aramid Nanofibers. *ACS Nano* **2019,** *13* (7), 7886-7897.
56. Wang, F.; Wu, Y.; Huang, Y.; Liu, L., Strong, transparent and flexible aramid nanofiber/POSS hybrid organic/inorganic nanocomposite membranes. *Composites Science and Technology* **2018,** *156*, 269-275.
57. Yao, Q.; Chen, L.; Zhang, W.; Liufu, S.; Chen, X., Enhanced Thermoelectric Performance of Single-Walled Carbon Nanotubes/Polyaniline Hybrid Nanocomposites. *ACS Nano* **2010,** *4* (4), 2445-2451.
58. Guan, Y.; Li, W.; Zhang, Y. L.; Shi, Z. Q.; Tan, J.; Wang, F.; Wang, Y. H., Aramid nanofibers and poly (vinyl alcohol) nanocomposites for ideal combination of strength and toughness via hydrogen bonding interactions. *Composites Science and Technology* **2017,** *144*, 193-201.
59. Liu, F.; Luo, S.; Liu, D.; Chen, W.; Huang, Y.; Dong, L.; Wang, L., Facile Processing of Free-Standing Polyaniline/SWCNT Film as an Integrated Electrode for Flexible Supercapacitor Application. *ACS Applied Materials & Interfaces* **2017,** *9* (39), 33791-33801.
60. Thanpitcha, T.; Sirivat, A.; Jamieson, A. M.; Rujiravanit, R., Preparation and characterization of polyaniline/chitosan blend film. *Carbohydr. Polym.* **2006,** *64* (4), 560-568.
61. Simon, P.; Gogotsi, Y.; Dunn, B., Where Do Batteries End and Supercapacitors Begin? *Science* **2014,** *343* (6176), 1210-1211.
62. Miao, F.; Shao, C.; Li, X.; Wang, K.; Lu, N.; Liu, Y., Electrospun Carbon Nanofibers/Carbon Nanotubes/Polyaniline Ternary Composites with Enhanced Electrochemical Performance for Flexible Solid-State Supercapacitors. *ACS Sustainable Chemistry & Engineering* **2016,** *4* (3), 1689-1696.
63. Liu, P.; Han, J.-J.; Jiang, L.-F.; Li, Z.-Y.; Cheng, J.-N., Polyaniline/multi-walled carbon nanotubes composite with core-shell structures as a cathode material for rechargeable lithium-polymer cells. *Appl. Surf. Sci.* **2017,** *400*, 446-452.
64. Lee, J.-S. M.; Briggs, M. E.; Hu, C.-C.; Cooper, A. I., Controlling electric double-layer capacitance and pseudocapacitance in heteroatom-doped carbons derived from hypercrosslinked microporous polymers. *Nano Energy* **2018,** *46*, 277-289.
65. Patel, A.; Wilcox, K.; Li, Z.; George, I.; Juneja, R.; Lollar, C. T.; Lazar, S.; Grunlan, J. C.; Tenhaeff, W. E.; Lutkenhaus, J. L., High Modulus, Thermally Stable, and Self-Extinguishing Aramid Nanofiber Separators. *ACS Applied Materials & Interfaces* **2020**.
66. Zheng, W.; Lv, R.; Na, B.; Liu, H.; Jin, T.; Yuan, D., Nanocellulose-mediated hybrid polyaniline electrodes for high performance flexible supercapacitors. *Journal of Materials Chemistry A* **2017,** *5* (25), 12969-12976.

67. Hu, R.; Zhao, J.; Zhu, G.; Zheng, J., Fabrication of flexible free-standing reduced graphene oxide/polyaniline nanocomposite film for all-solid-state flexible supercapacitor. *Electrochimica Acta* **2018,** *261*, 151-159.
68. Novák, P.; Müller, K.; Santhanam, K. S. V.; Haas, O., Electrochemically Active Polymers for Rechargeable Batteries. *Chemical Reviews* **1997,** *97* (1), 207-282.
69. Hyder, M. N.; Lee, S. W.; Cebeci, F. Ç.; Schmidt, D. J.; Shao-Horn, Y.; Hammond, P. T., Layer-by-Layer Assembled Polyaniline Nanofiber/Multiwall Carbon Nanotube Thin Film Electrodes for High-Power and High-Energy Storage Applications. *ACS Nano* **2011,** *5* (11), 8552-8561.
70. Sarang, K. T.; Miranda, A.; An, H.; Oh, E.-S.; Verduzco, R.; Lutkenhaus, J. L., Poly(fluorene-alt-naphthalene diimide) as n-Type Polymer Electrodes for Energy Storage. *ACS Applied Polymer Materials* **2019,** *1* (5), 1155-1164.
71. An, H.; Li, X.; Chalker, C.; Stracke, M.; Verduzco, R.; Lutkenhaus, J. L., Conducting Block Copolymer Binders for Carbon-Free Hybrid Vanadium Pentoxide Cathodes with Enhanced Performance. *ACS Applied Materials & Interfaces* **2016,** *8* (42), 28585-28591.
72. Yang, L.; Wang, S.; Mao, J.; Deng, J.; Gao, Q.; Tang, Y.; Schmidt, O. G., Hierarchical MoS2/Polyaniline Nanowires with Excellent Electrochemical Performance for Lithium-Ion Batteries. *Advanced Materials* **2013,** *25* (8), 1180-1184.
73. Shao, L.; Jeon, J.-W.; Lutkenhaus, J. L., Porous polyaniline nanofiber/vanadium pentoxide layer-by-layer electrodes for energy storage. *Journal of Materials Chemistry A* **2013,** *1* (26), 7648-7656.
74. Ge, D.; Yang, L.; Honglawan, A.; Li, J.; Yang, S., In Situ Synthesis of Hybrid Aerogels from Single-Walled Carbon Nanotubes and Polyaniline Nanoribbons as Free-Standing, Flexible Energy Storage Electrodes. *Chemistry of Materials* **2014,** *26* (4), 1678-1685.
75. He, B.-L.; Dong, B.; Wang, W.; Li, H.-L., Performance of polyaniline/multi-walled carbon nanotubes composites as cathode for rechargeable lithium batteries. *Materials Chemistry and Physics* **2009,** *114* (1), 371-375.
76. Yang, H.; Song, T.; Liu, L.; Devadoss, A.; Xia, F.; Han, H.; Park, H.; Sigmund, W.; Kwon, K.; Paik, U., Polyaniline/Polyoxometalate Hybrid Nanofibers as Cathode for Lithium Ion Batteries with Improved Lithium Storage Capacity. *The Journal of Physical Chemistry C* **2013,** *117* (34), 17376-17381.
77. Boaretto, N.; Almenara, J.; Mikhalchan, A.; Marcilla, R.; Vilatela, J. J., A Route to High-Toughness Battery Electrodes. *ACS Applied Energy Materials* **2019,** *2* (8), 5889-5899.
78. Wu, Y.; Wu, H.; Luo, S.; Wang, K.; Zhao, F.; Wei, Y.; Liu, P.; Jiang, K.; Wang, J.; Fan, S., Entrapping electrode materials within ultrathin carbon nanotube network for flexible thin film lithium ion batteries. *RSC Advances* **2014,** *4* (38), 20010-20016.
79. Liu, P.; Sherman, E.; Jacobsen, A., Design and fabrication of multifunctional structural batteries. *Journal of Power Sources* **2009,** *189* (1), 646-650.
80. Luo, S.; Wang, K.; Wang, J.; Jiang, K.; Li, Q.; Fan, S., Binder-Free LiCoO2/Carbon Nanotube Cathodes for High-Performance Lithium Ion Batteries. *Advanced Materials* **2012,** *24* (17), 2294-2298.

81. Lindström, H.; Södergren, S.; Solbrand, A.; Rensmo, H.; Hjelm, J.; Hagfeldt, A.; Lindquist, S.-E., Li+ Ion Insertion in TiO2 (Anatase). 2. Voltammetry on Nanoporous Films. *The Journal of Physical Chemistry B* **1997,** *101* (39), 7717-7722.

7. CONCLUSIONS AND FUTURE DIRECTIONS

7.1. Conclusions

In this dissertation, we developed nanocomposite structural electrodes for supercapacitors and lithium-ion batteries based on Kevlar® aramid nanofibers. Initially, aramid nanofibers (ANFs) were combined with functionalized reduced graphene oxide (f-rGO) to yield structural supercapacitor electrodes. We investigated the role of non-covalent interfacial interactions and their effect on mechanical and electrochemical performance. ANFs and rGO interact with each other through hydrogen bonding interactions between the ANF amide groups and the rGO oxygen-containing groups, as well as π-π stacking interactions. Hydrogen bonding interactions were enhanced by functionalizing rGO with carboxylic acid groups (-COOH), amine groups (-NH_2), dopamine, tannic acid, and also by branching the ANFs (BANFs). Additionally, coordination bonding was induced by the addition of divalent (Ca^{2+}) and trivalent (Fe^{3+}) ions. Metal ions chelate strongly with the carboxylic acid groups of f-rGO and also interact with the carbonyl and hydroxyl groups on the basal planes of f-rGO. The structural energy storage properties for the f-rGO/ANF or BANF composites were investigated as a function of composition.

The performance of the rGO/ANF structural supercapacitor electrodes in terms of specific Young's modulus, specific energy, and multifunctional efficiency (benchmark materials: carbon aerogel and epoxy) is demonstrated in Figure 7.1a. Pure rGO (black star) exhibited the lowest multifunctional efficiency (n_{mf} = 3.4) resulting from poor mechanical

performance. Addition of ANFs (rGO/ANF composites, black bubble) led to higher multifunctional efficiency values (n_{mf} = 4 – 6) with deteriorations in energy storage resulting from the addition of the strong ANFs and dilution of the electrochemically active material (rGO). Overall, the highest multifunctional efficiency values (n_{mf} = 5.3 – 13.6) were achieved by the BANF-containing composites (rGO/BANFs, grey bubble). Branching ANFs led to enhanced hydrogen bonding interactions between rGO and ANFs without the disadvantages of functionalization (*i.e.* introduction of defects). This resulted to simultaneously high specific Young's modulus (11 – 35 GPa·cm^3/g) and specific energy values (14 – 17 Wh/kg).

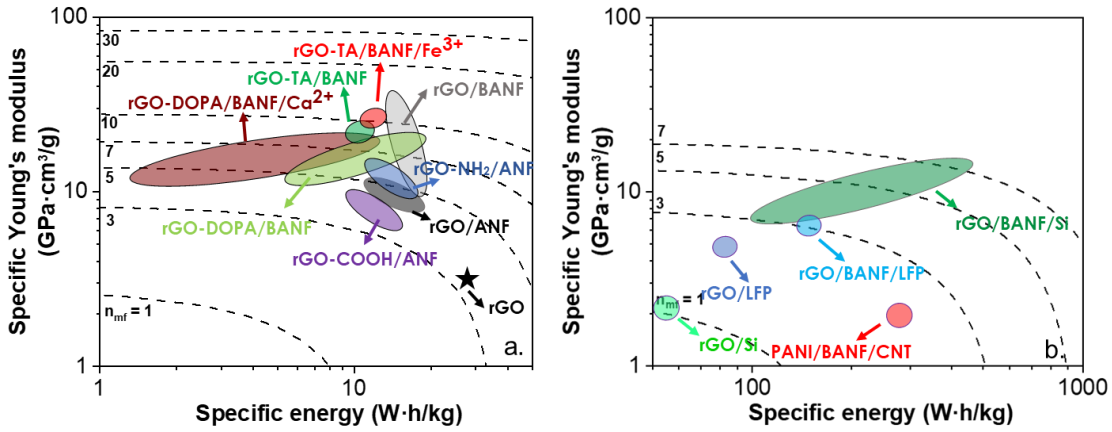

Figure 7.1 Specific Young's modulus *vs.* specific energy for all (a) supercapacitor electrodes and (b) lithium-ion battery electrodes investigated in this dissertation. The dashed lines represent constant multifunctional efficiency (η_{mf}) traces. Epoxy and carbon aerogel were used as the benchmark materials for panel (a), and epoxy and graphite/LFP commercial battery were used for panel (b). Ashby plots using the same benchmark materials for supercapacitors and batteries are shown in Appendix A.

Additionally, we investigated the effect of different functionalizations. Tannic acid functionalization (rGO-TA/BANF composites, dark green bubble) led to the highest multifunctional efficiencies (n_{mf} = 9.5) followed by the dopamine functionalized electrodes (rGO-DOPA/BANF composites, light green bubble) with multifunctional efficiencies values of 5.5 – 8.2. The good performance of the tannic acid and dopamine functionalized composites was attributed to the extensive hydrogen bonding interactions induced by tannic acid and dopamine – molecules with high density of functional groups – and the mild functionalization process. Functionalization with amine groups (rGO-NH_2/ANF composites, blue bubble) led to only small improvements compared to the rGO/ANF composites, while functionalization with carboxylic acid groups (rGO-COOH/ANF, purple bubble) led to deteriorations (n_{mf} = 3.1 – 4) due to the introduction of defects during the functionalization process resulting from the use of harsh chemicals. Furthermore, coordination bonding induced by divalent ions (rGO-DOPA/BANF/Ca^{2+}, maroon bubble) and trivalent ions (rGO-TA/BANF/Fe^{3+}, red bubble) led to only small improvements in multifunctional efficiency compared against the same electrodes without the addition of metal ions. The improvement was attributed to the coordination bonding of the metal ions with the rGO flakes that led to improved mechanical performance, however, the introduction of defects and ion-diffusion limitations deteriorated the energy storage performance.

Using the lessons learnt from the structural supercapacitor electrodes, we developed structural lithium-ion battery electrodes. rGO/BANFs were combined with silicon (Si) for the anodes and lithium iron phosphate (LFP) for the cathodes. BANF-

containing electrodes exhibited improved multifunctional efficiency values (benchmark materials: carbon aerogel and graphite/LFP commercial lithium-ion battery), as shown in Figure 7.1b. More specifically, rGO/BANF/LFP cathodes (light blue bubble) and rGO/BANF/Si anodes (dark green bubble) demonstrated multifunctional efficiency values of ~ 3.3 and 3.2 – 7.1, respectively, which is almost double the efficiency for rGO/LFP (no BANFs, dark blue bubble) and rGO/Si (no BANFs, light green bubble). Hydrogen bonding interactions between rGO and BANFs were harnessed leading to electrodes with improved mechanical performance and also higher active material loadings, which resulted to also improved energy storage performance. Overall, an improvement of two orders of magnitude in tensile strength and Young's modulus with similar energy storage compared to commercial battery electrodes was achieved.

Finally, we developed structural supercapacitor and lithium-ion battery cathodes using PANI, a conjugated redox active polymer. PANI had been utilized before as an electrode material, however, its brittle nature hindered the use of PANI in structural applications. Aniline was polymerized in the presence of BANFs and single-walled carbon nanotubes (SWCNTs). Hydrogen bonding and π-π stacking interactions within the composite electrodes were harnessed, leading to enhanced mechanical performance (tensile strength and Young's modulus) compared to other PANI-containing electrodes. Continuous networks of BANFs, CNTs, and PANI led to a good combination of energy storage and mechanical performance with high-capacity values (128 ± 5 mAh/g *vs.* a theoretical capacity of 147 mAh/g), leading to multifunctional efficiency values of ~ 2.1.

In conclusion, structural nanocomposite electrodes reinforced with Kevlar® aramid nanofibers were developed. We specifically emphasized on the role of interfacial interactions on energy storage and mechanical performance. The highest multifunctional efficiency, to date, for rGO-based structural supercapacitor electrodes was reported. It was shown that favourable interfacial interactions can lead to nanocomposites with desirable multifunctional properties and improved multifunctional efficiency values. The strategies presented in this dissertation may be translated to other nanocomposite systems, as well as to other applications (*e.g.* mechanically strong nanocomposites for EMI shielding).

7.2. Future Directions

As demonstrated in the previous sections, the rGO/BANF composite electrodes exhibited a balanced combination of mechanical and electrochemical performance compared to other structural electrodes from the literature (Figure 7.2). The high multifunctional efficiency values of the rGO/BANF composites indicate that the utilization of such materials may lead to mass savings in real-life applications. However, to realize such technologies several other aspects need to be taken into consideration. First, the mechanical properties of the rGO/BANF composites are still considered low for structural applications, and as a result new multifunctional materials need to be developed and investigated. New battery chemistries should also be investigated as the utilization of lithium-ion batteries comes with serious safety concerns that may hinder their use in structural applications. Finally, the efficacy of the composite electrodes while mechanical loads are simultaneously applied is crucial for their performance. Investigating this, will

require the development of new characterization techniques, as well as new performance metrics.

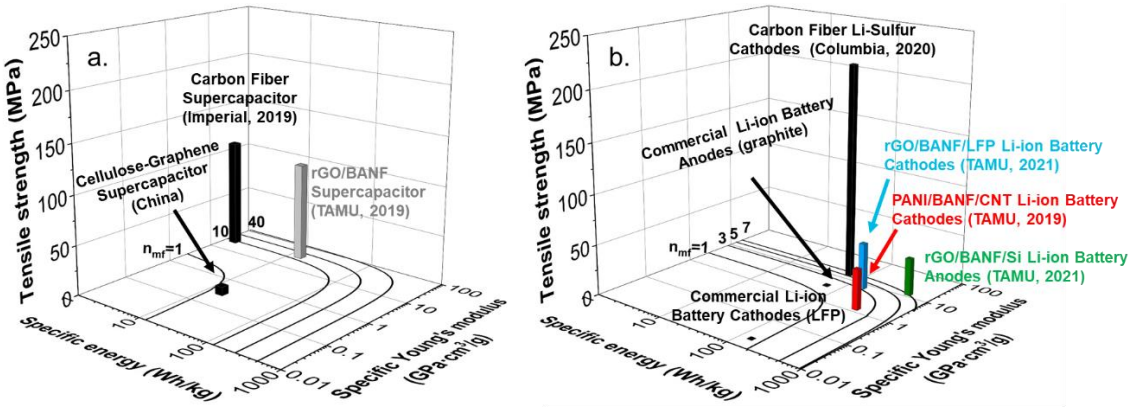

Figure 7.2 Ashby plots of (a) specific Young's modulus *vs.* specific energy *vs.* tensile strength for structural (a) supercapacitors and (b) batteries. Black bars correspond to data obtained from the literature. Solid lines represent constant multifunctional efficiency (η_{mf}) traces. Epoxy and carbon aerogel were used as the benchmark materials for panel (a), and epoxy and graphite/LFP commercial battery were used for panel (b). Ashby plots using the same benchmark materials for supercapacitors and batteries are shown in Appendix A.

New materials, such as carbon fibers, need to be investigated in more depth to improve mechanical performance. Carbon fiber (CF) fabrics have been explored before as structural electrodes for supercapacitors and batteries, as shown in Figure 7.2.[1-5] In general, CF-based systems tend to have excellent mechanical properties but struggle with energy storage performance when compared to conventional, non-structural supercapacitors and batteries.[1, 2] The approaches presented in this dissertation for

improving interfacial interactions may be also be translated to CF-based electrodes. Functionalizing CF fabrics and even combining them with BANFs could improve adhesion not only between the CFs, but also between the CFs and the active materials, avoiding delamination of the active materials, allowing for higher active material loadings, and improved electrochemical cycling life. This could potentially lead to nanocomposite electrodes with similar mechanical properties to traditional CF-based composites but with also improved energy storage performance.

Furthermore, several safety concerns related to the utilization of lithium-ion batteries need to be addressed as they may prohibit the large-scale deployment of multifunctional batteries in structural applications. For example, lithium dendritic growth formed during charging may puncture the separator leading to short-circuiting.[6, 7] Additionally, traditional electrolytes are highly flammable and as a result overcharging or short-circuiting a lithium-ion battery can lead to catastrophic failure. These concerns further increase for the case of structural systems that large external mechanical loads will also be applied. To address the safety concerns, several other battery chemistries that require aqueous electrolytes have been explored such as Na-ion, K-ion, and Zn-ion batteries.[8, 9] Out of those, Zn metal batteries show promise due to zinc's high abundance, low cost, and non-toxicity.[8, 9] The rGO/BANF electrodes can be combined with α-MnO_2 particles to create structural cathodes for Zn metal batteries. Zn may be electrodeposited onto strong conductive substrates (*e.g.* rGO/BANF, and CF fabrics) to create structural anodes. We expect similar mechanical performance with slightly deteriorated energy storage (theoretical capacity of 308 mAh/g) compared to the lithium-ion battery electrodes

presented in the previous sections. However, by translating the structural electrodes in safer battery systems, important safety concerns will be addressed allowing for their utilization in real-life applications.

Additionally, the energy storage performance of structural electrodes while under mechanical loads and elevated temperatures needs to be carefully evaluated. Such experiments, require new testing approaches such as *in-situ* testing. Evaluating energy storage performance while external mechanical loads are applied and/or at elevated temperatures would give us a better understanding of the electrodes' performance in real-life applications. Additionally, internal stresses developed during electrochemical cycling need to be evaluated. The movement of ions within the electrodes causes volumetric changes and internal stresses which may severely affect the mechanical integrity of the nanocomposite electrodes. It is expected that coupling effects will be more apparent for the case of the lithium-ion battery systems compared to supercapacitors. This is attributed to the different energy storage mechanisms. Lithium-ion intercalation/de-intercalation taking place during charging/discharging in batteries, leads to large volumetric expansions within the electrodes that may affect the electrodes' mechanical integrity, making them more susceptible to external mechanical loads.

Finally, new performance metrics are required to better capture the multifunctional performance and coupling effects. The currently used expression for the multifunctional efficiency is a simplified and easy tool that accounts for mass savings. However, it fails to capture the need for simultaneously both good mechanical and electrochemical performances, as well as the effect of complicated loading conditions and electrode

structures. Several efforts on developing a new expression for the multifunctional efficiency that captures some of these parameters were recently made.[10-12] These efforts need to continue to develop a metric that accommodates the current needs of the field.

7.3. References

1. Asp, L. E.; Greenhalgh, E. S., Structural power composites. *Composites Science and Technology* **2014,** *101*, 41-61.
2. Asp, L. E.; Johansson, M.; Lindbergh, G.; Xu, J.; Zenkert, D., Structural battery composites: a review. *Functional Composites and Structures* **2019,** *1* (4), 042001.
3. Moyer, K.; Ait Boucherbil, N.; Zohair, M.; Eaves, J.; Pint, C., Polymer Reinforced Carbon Fiber Interfaces for High Energy Density Structural Lithium-Ion Batteries. *Sustainable Energy & Fuels* **2020**.
4. Moyer, K.; Meng, C.; Marshall, B.; Assal, O.; Eaves, J.; Perez, D.; Karkkainen, R.; Roberson, L.; Pint, C. L., Carbon fiber reinforced structural lithium-ion battery composite: Multifunctional power integration for CubeSats. *Energy Storage Materials* **2020,** *24*, 676-681.
5. Huang, W.; Wang, P.; Liao, X.; Chen, Y.; Borovilas, J.; Jin, T.; Li, A.; Cheng, Q.; Zhang, Y.; Zhai, H.; Chitu, A.; Shan, Z.; Yang, Y., Mechanically-robust structural lithium-sulfur battery with high energy density. *Energy Storage Materials* **2020,** *33*, 416-422.
6. Lin, D.; Yuen, P. Y.; Liu, Y.; Liu, W.; Liu, N.; Dauskardt, R. H.; Cui, Y., A Silica-Aerogel-Reinforced Composite Polymer Electrolyte with High Ionic Conductivity and High Modulus. *Advanced Materials* **2018,** *30* (32), 1802661.
7. Lutkenhaus, J. L.; Flouda, P., Ceramic Electrolytes Get "Tough" on Lithium Metal Batteries. *Matter* **2020,** *3* (1), 14-15.
8. Kundu, D.; Adams, B. D.; Duffort, V.; Vajargah, S. H.; Nazar, L. F., A high-capacity and long-life aqueous rechargeable zinc battery using a metal oxide intercalation cathode. *Nature Energy* **2016,** *1* (10), 16119.
9. Jia, H.; Wang, Z.; Tawiah, B.; Wang, Y.; Chan, C.-Y.; Fei, B.; Pan, F., Recent advances in zinc anodes for high-performance aqueous Zn-ion batteries. *Nano Energy* **2020,** *70*, 104523.
10. Patel, A. G.; Johnson, L.; Arroyave, R.; Lutkenhaus, J. L., Design of multifunctional supercapacitor electrodes using an informatics approach. *Mol Syst Des Eng* **2019,** *4*, 654-663.
11. Sun, W.; Shah, S. A.; Lowery, J. L.; Oh, J. H.; Lutkenhaus, J. L.; Green, M. J., Lightweight Kevlar-Reinforced Graphene Oxide Architectures with High Strength for Energy Storage. *Advanced Materials Interfaces* **2019,** *6* (21), 1900786.

12. Zhou, T.; Dickinson, E.; Boyd, J. G.; Lutkenhaus, J. L.; Lagoudas, D. C., Multifunctional efficiency metric for structural supercapacitors. *Multifunctional Materials* **2021,** *3* (4), 044002.
13. Rigueur, J. L.; Hasan, S. A.; Mahajan, S. V.; Dickerson, J. H., Buckypaper fabrication by liberation of electrophoretically deposited carbon nanotubes. *Carbon* **2010,** *48* (14), 4090-4099.
14. Kim, S. Y.; Hong, J.; Kavian, R.; Lee, S. W.; Hyder, M. N.; Shao-Horn, Y.; Hammond, P. T., Rapid fabrication of thick spray-layer-by-layer carbon nanotube electrodes for high power and energy devices. *Energ Environ Sci* **2013,** *6* (3), 888-897.
15. Whitten, P. G.; Spinks, G. M.; Wallace, G. G., Mechanical properties of carbon nanotube paper in ionic liquid and aqueous electrolytes. *Carbon* **2005,** *43* (9), 1891-1896.
16. Barisci, J. N.; Wallace, G. G.; Baughman, R. H., Electrochemical studies of single-wall carbon nanotubes in aqueous solutions. *J. Electroanal. Chem* **2000,** *488* (2), 92-98.
17. Weng, Z.; Su, Y.; Wang, D.-W.; Li, F.; Du, J.; Cheng, H.-M., Graphene–Cellulose Paper Flexible Supercapacitors. *Advanced Energy Materials* **2011,** *1* (5), 917-922.
18. Wang, D.-W.; Li, F.; Zhao, J.; Ren, W.; Chen, Z.-G.; Tan, J.; Wu, Z.-S.; Gentle, I.; Lu, G. Q.; Cheng, H.-M., Fabrication of Graphene/Polyaniline Composite Paper via In Situ Anodic Electropolymerization for High-Performance Flexible Electrode. *ACS Nano* **2009,** *3* (7), 1745-1752.
19. Sumboja, A.; Foo, C. Y.; Wang, X.; Lee, P. S., Large areal mass, flexible and free-standing reduced graphene oxide/manganese dioxide paper for asymmetric supercapacitor device. *Advanced materials* **2013,** *25* (20), 2809-2815.
20. Ma, Y.; Li, P.; Sedloff, J. W.; Zhang, X.; Zhang, H.; Liu, J., Conductive Graphene Fibers for Wire-Shaped Supercapacitors Strengthened by Unfunctionalized Few-Walled Carbon Nanotubes. *ACS Nano* **2015,** *9* (2), 1352-1359.
21. Li, S.; Zhao, C.; Shu, K.; Wang, C.; Guo, Z.; Wallace, G. G.; Liu, H., Mechanically strong high performance layered polypyrrole nano fibre/graphene film for flexible solid state supercapacitor. *Carbon* **2014,** *79*, 554-562.
22. Che, J. F.; Chen, P.; Chan-Park, M. B., High-strength carbon nanotube buckypaper composites as applied to free-standing electrodes for supercapacitors. *J Mater Chem A* **2013,** *1* (12), 4057-4066.
23. Cheng, Y.; Lu, S.; Zhang, H.; Varanasi, C. V.; Liu, J., Synergistic Effects from Graphene and Carbon Nanotubes Enable Flexible and Robust Electrodes for High-Performance Supercapacitors. *Nano Letters* **2012,** *12* (8), 4206-4211.
24. Lee, W. S. V.; Peng, E.; Choy, D. C.; Xue, J. M., Mechanically robust glucose strutted graphene aerogel paper as a flexible electrode. *Journal of Materials Chemistry A* **2015,** *3* (37), 19144-19147.
25. Li, Y.; Ren, G.; Zhang, Z.; Teng, C.; Wu, Y.; Lu, X.; Zhu, Y.; Jiang, L., A strong and highly flexible aramid nanofibers/PEDOT:PSS film for all-solid-state supercapacitors with superior cycling stability. *Journal of Materials Chemistry A* **2016,** *4* (44), 17324-17332.

26. Hu, R.; Zhao, J.; Zhu, G.; Zheng, J., Fabrication of flexible free-standing reduced graphene oxide/polyaniline nanocomposite film for all-solid-state flexible supercapacitor. *Electrochim. Acta* **2018,** *261*, 151-159.
27. Yanilmaz, M.; Dirican, M.; Asiri, A. M.; Zhang, X., Flexible polyaniline-carbon nanofiber supercapacitor electrodes. *Journal of Energy Storage* **2019,** *24*, 100766.
28. Zheng, W.; Lv, R.; Na, B.; Liu, H.; Jin, T.; Yuan, D., Nanocellulose-mediated hybrid polyaniline electrodes for high performance flexible supercapacitors. *Journal of Materials Chemistry A* **2017,** *5* (25), 12969-12976.
29. Hsu, H. H.; Khosrozadeh, A.; Li, B.; Luo, G.; Xing, M.; Zhong, W., An Eco-Friendly, Nanocellulose/RGO/in Situ Formed Polyaniline for Flexible and Free-Standing Supercapacitors. *ACS Sustainable Chemistry & Engineering* **2019,** *7* (5), 4766-4776.
30. Wang, J.; Cheng, Q.; Tang, Z., Layered nanocomposites inspired by the structure and mechanical properties of nacre. *Chemical Society Reviews* **2012,** *41* (3), 1111-1129.
31. Callister, W. D., Jr., *Materials science and engineering : an introduction*. 4th ed. ed.; John Wiley & Sons: New York, 1997.
32. Gojny, F.; Wichmann, M.; Fiedler, B.; Schulte, K., Influence of different carbon nanotubes on the mechanical properties of epoxy matrix composites – A comparative study. *Compos Sci Technol.* **2005,** *65* (15-16), 2300-2313.
33. Lin, J.; Bang, S. H.; Malakooti, M. H.; Sodano, H. A., Isolation of Aramid Nanofibers for High Strength and Toughness Polymer Nanocomposites. *ACS Applied Materials & Interfaces* **2017,** *9* (12), 11167-11175.
34. Ji, B. H.; Gao, H. J., Mechanical properties of nanostructure of biological materials. *J Mech Phys Solids* **2004,** *52* (9), 1963-1990.
35. Cui, W.; Li, M.; Liu, J.; Wang, B.; Zhang, C.; Jiang, L.; Cheng, Q., A Strong Integrated Strength and Toughness Artificial Nacre Based on Dopamine Cross-Linked Graphene Oxide. *ACS Nano* **2014,** *8* (9), 9511-9517.
36. Wan, S.; Xu, F.; Jiang, L.; Cheng, Q., Superior Fatigue Resistant Bioinspired Graphene-Based Nanocomposite via Synergistic Interfacial Interactions. *Adv. Funct. Mater.* **2017,** *27* (10), 1605636.
37. Guan, Y.; Li, W.; Zhang, Y.; Shi, Z.; Tan, J.; Wang, F.; Wang, Y., Aramid nanofibers and poly (vinyl alcohol) nanocomposites for ideal combination of strength and toughness via hydrogen bonding interactions. *Compos Sci Technol.* **2017,** *144*, 193-201.
38. Wang, J.; Cheng, Q.; Tang, Z., Layered nanocomposites inspired by the structure and mechanical properties of nacre. *Chem. Soc. Rev.* **2012,** *41* (3), 1111-29.
39. Zhu, J.; Cao, W.; Yue, M.; Hou, Y.; Han, J.; Yang, M., Strong and Stiff Aramid Nanofiber/Carbon Nanotube Nanocomposites. *ACS Nano* **2015,** *9* (3), 2489-2501.
40. Sasso, C.; Zeno, E.; Petit-Conil, M.; Chaussy, D.; Belgacem, M. N.; Tapin-Lingua, S.; Beneventi, D., Highly Conducting Polypyrrole/Cellulose Nanocomposite Films with Enhanced Mechanical Properties. *Macromolecular Materials and Engineering* **2010,** *295* (10), 934-941.
41. Blighe, F. M.; Diamond, D.; Coleman, J. N.; Lahiff, E., Increased response/recovery lifetimes and reinforcement of polyaniline nanofiber films using carbon nanotubes. *Carbon* **2012,** *50* (4), 1447-1454.

42. Han, X.; Lv, L.; Yu, D.; Wu, X.; Li, C., Conductive Core–Shell Aramid Nanofibrils: Compromising Conductivity with Mechanical Robustness for Organic Wearable Sensing. *ACS Applied Materials & Interfaces* **2019,** *11* (3), 3466-3473.
43. Cheng, Y.; Lu, S.; Zhang, H.; Varanasi, C. V.; Liu, J., Synergistic effects from graphene and carbon nanotubes enable flexible and robust electrodes for high-performance supercapacitors. *Nano Lett.* **2012,** *12* (8), 4206-11.
44. Flouda, P.; Feng, X.; Boyd, J. G.; Thomas, E. L.; Lagoudas, D. C.; Lutkenhaus, J., Interfacial Engineering of Reduced Graphene Oxide for Aramid Nanofiber-Enabled Structural Supercapacitors. *Batteries & Supercaps 0* (ja).
45. Hou, M.; Xu, M.; Li, B., Enhanced Electrical Conductivity of Cellulose Nanofiber/Graphene Composite Paper with a Sandwich Structure. *ACS Sustainable Chemistry & Engineering* **2018,** *6* (3), 2983-2990.
46. Wan, S.; Xu, F.; Jiang, L.; Cheng, Q., Superior Fatigue Resistant Bioinspired Graphene-Based Nanocomposite via Synergistic Interfacial Interactions. *Adv. Funct. Mater.* **2017,** *27* (10), 1605636.
47. Wen, Y.; Wu, M.; Zhang, M.; Li, C.; Shi, G., Topological Design of Ultrastrong and Highly Conductive Graphene Films. *Adv. Mater.* **2017,** *29* (41), 1702831.
48. Gong, S.; Jiang, L.; Cheng, Q., Robust bioinspired graphene-based nanocomposites via synergistic toughening of zinc ions and covalent bonding. *Journal of Materials Chemistry A* **2016,** *4* (43), 17073-17079.
49. Wan, S.; Hu, H.; Peng, J.; Li, Y.; Fan, Y.; Jiang, L.; Cheng, Q., Nacre-inspired integrated strong and tough reduced graphene oxide–poly(acrylic acid) nanocomposites. *Nanoscale* **2016,** *8* (10), 5649-5656.
50. Wan, S.; Li, Y.; Mu, J.; Aliev, A. E.; Fang, S.; Kotov, N. A.; Jiang, L.; Cheng, Q.; Baughman, R. H., Sequentially bridged graphene sheets with high strength, toughness, and electrical conductivity. *Proceedings of the National Academy of Sciences* **2018,** *115* (21), 5359-5364.
51. Wan, S.; Chen, Y.; Wang, Y.; Li, G.; Wang, G.; Liu, L.; Zhang, J.; Liu, Y.; Xu, Z.; Tomsia, A. P.; Jiang, L.; Cheng, Q., Ultrastrong Graphene Films via Long-Chain π-Bridging. *Matter* **2019**.
52. Lyu, J.; Zhao, X.; Hou, X.; Zhang, Y.; Li, T.; Yan, Y., Electromagnetic interference shielding based on a high strength polyaniline-aramid nanocomposite. *Compos. Sci. Technol.* **2017,** *149*, 159-165.
53. Jeon, B. H.; Kim, S.; Choi, M. H.; Chung, I. J., Synthesis and characterization of polyaniline–polycarbonate composites prepared by an emulsion polymerization. *Synth. Met.* **1999,** *104* (2), 95-100.
54. Hu, W.; Chen, S.; Yang, Z.; Liu, L.; Wang, H., Flexible Electrically Conductive Nanocomposite Membrane Based on Bacterial Cellulose and Polyaniline. *The Journal of Physical Chemistry B* **2011,** *115* (26), 8453-8457.
55. Thanpitcha, T.; Sirivat, A.; Jamieson, A. M.; Rujiravanit, R., Preparation and characterization of polyaniline/chitosan blend film. *Carbohydr. Polym.* **2006,** *64* (4), 560-568.

APPENDIX A

ASHBY PLOT DATA

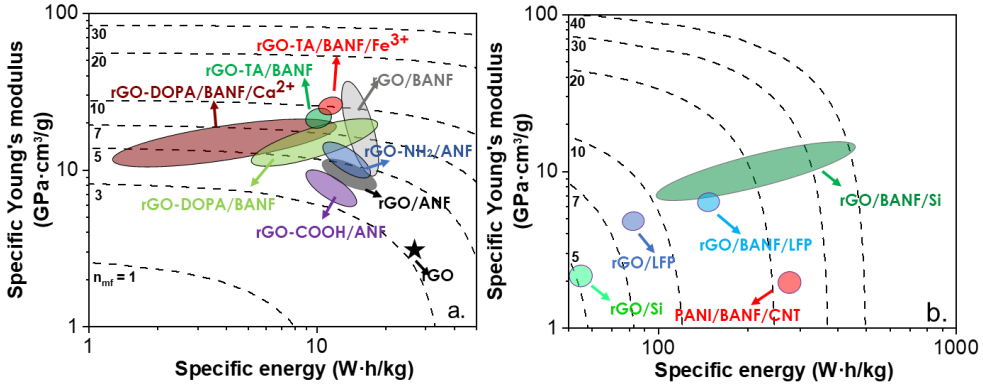

Figure A.1 Specific Young's modulus *vs.* specific energy for all (a) supercapacitor electrodes and (b) lithium-ion battery electrodes investigated in this dissertation. The dashed lines represent constant multifunctional efficiency (η_{mf}) traces. Epoxy and carbon aerogel were used as the benchmark materials.

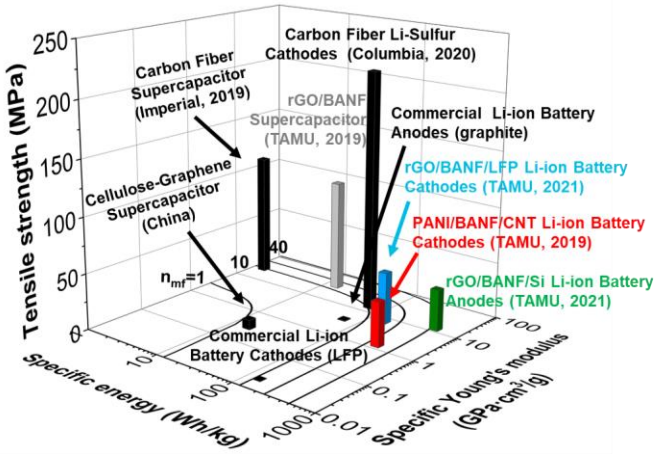

Figure A.2 Ashby plots of (a) specific Young's modulus *vs.* specific energy *vs.* tensile strength for structural (a) supercapacitors and (b) batteries. Black bars correspond to data obtained from the literature. Solid lines represent constant multifunctional efficiency (η_{mf}) traces. Epoxy and carbon aerogel were used as the benchmark materials.

Table A.1 Data from this dissertation used for Ashby plots in chapters 2, 3, 4, 5, 6 and 7.

Materials (chapter #)	Strength [MPa]	Young's modulus [GPa]	Specific Young's modulus [GPa]	Specific capacitance [F/g] or *capacity [mAh/g]	Specific energy [Wh/kg]	nmf (epoxy and carbon aerogel)
rGO (2)	33.0	4.8	3.4	216.2	27.0	3.4
rGO/10wt% ANF (2)	55.3	7.5	7.5	137.6	17.2	4.1
rGO/25wt% ANF (2)	79.0	9.9	11.0	120	15.0	5.1
rGO-COOH (2)	35.0	4.4	2.8	127.2	15.9	2.3
rGO-COOH/10wt% ANF (2)	59.6	8.1	5.8	104.4	13.1	3.1
rGO-COOH/25wt% ANF (2)	72.6	8.8	8.0	97.8	12.2	3.8
rGO-NH_2 (2)	46.9	7.0	4.1	126.0	15.8	2.7
rGO-NH_2/10wt% ANF (2)	74.8	9.0	8.1	116.3	14.5	4.1
rGO-NH_2/25wt% ANF (2)	98.0	12.2	12.2	104.6	13.2	5.4
rGO/10wt% BANF (3)	80.6	6.6	11.8	135.6	17.0	5.3
rGO/25wt% BANF (3)	99.8	10.6	35.0	110.5	14.0	13.6
rGO-1wt% DOPA/10wt% BANF (3)	96.3	9.7	19.0	127.9	16.0	8.2
rGO-1wt% DOPA/25wt% BANF (3)	116.4	8.5	14.1	49.1	6.1	5.5
rGO-1wt% DOPA/10wt% BANF/Ca^{2+} (3)	116.9	15.4	19.3	83.2	10.4	7.7
rGO-1wt% DOPA/25wt% BANF/Ca^{2+} (3)	142.3	13.1	13.1	10.6	1.3	4.8
rGO-TA/10 wt% BANF (4)	140.0	17	24.3	120	10.5	9.5
rGO-TA/10 wt% BANF/Fe^{3+} (4)	140.0	25	27.8	145	11.6	10.8
rGO/50 wt% LFP (5)	32.0	5.4	5.4	50.0*	85.0	8.7
rGO/80 wt% LFP/5 wt% BANF (5)	46.0	5.0	7.1	90.0*	153.0	14.8
rGO/20 wt% Si (5)	34.0	4.0	2.7	25.0*	50.0	5.0
rGO/50 wt% Si/5 wt% BANF (5)	32.0	6.0	7.5	54.0*	108.0	11.3
rGO/50 wt% Si/10 wt% BANF (5)	37.0	6.2	12.4	255.0*	510.0	45.2
PANI/73 wt% BANF/12 wt% SWCNT (6)	40.0	4.0	1.3	128.0*	320.0	26.1

Table A.2 Literature data used for supercapacitor electrodes for Ashby plots in chapters 2, 3, 4, and 6.

Materials	Strength [MPa]	Young's modulus [GPa]	Specific Young's modulus [GPa·cm^3/g]	Specific capacitance [F/g]	Specific energy [Wh/kg]	Multifunctional efficiency
MWCNT paper[13, 14]	14.5	3.3	4.0	104	13	2.5
SWCNT paper[15, 16]	11.2	2.15	-	40.7	-	-
rGO-cellulose paper[17]	8.67	2.4	-	120	16.7	-
rGO-polyaniline[18]	12.6	-	-	233	-	-
rGO/MnO_2[19]	8.79	9.84	-	243	-	-
Wire shaped rGO/CNT composite[20]	385.7	5.3	4.9	35.9	2.9	2.0
Polypyrrole nanofibre/rGO paper[21]	35	0.0021	-	345	-	-
SWCNT-Ppy-CE composite paper[22]	68.73	17.84	21.5	320	25.6	9.7
rGO/MnO_2/CNTs[23]	48	2.3	-	372	-	-
Glucose strutted rGO aerogel paper[24]	0.6	-	-	311	-	-
ANFs/PEDOT:PSS[25]	76.4	4.7	-	111.5	-	-
rGO/PANI[26]	43	2.8	-	424.4 (active mass)	-	-
PANI/CNF[27]	0.5	1.7	-	-	-	-
PANI/NC[28]	12.4	6.6	-	421.5 (active mass)	-	-
PANI/rGO/NC[29]	5.8	0.64	-	-	-	-

Table A.3 Literature data for mechanically strong composites for Ashby plot (Young's modulus *vs.* ultimate strength) used in chapter 3.

			Fabrication method
Materials	**Young's modulus [GPa]**	**Tensile strength [MPa]**	**Mechanical**
MWCNT paper[13]	3.3	14.5	Electrophoretically deposited on stainless steel substrate
SWCNT paper[15]	2.15	11.2	Vacuum filtration
MTM/Chitosan [30]	10.7	76.0	Vacuum filtration
Wood[31]	14	112	-
Epoxy[32]	2.6	64	Mold casting
ANF/epoxy[33]	3.25	83.3	Mold casting
Nacre[30]	70	105	-
Bone[34]	20	100	-
rGO-DOPA[35]	6	205	Evaporation-induced assembly process
rGO-DOPA/Ni^{2+}[36]	3	298	Vacuum filtration
ANF/PVA[37]	5.2	126.5	Solution casting
GO/Chitosan[38]	6.3	206	Vacuum filtration
GO/PVA[30]	4.8	110	Vacuum filtration
ANF/CNT[39]	35	383	Vacuum filtration

Table A.4 Literature data for mechanically strong conductive materials used in Ashby plot (Young's modulus *vs.* tensile strength *vs.* electrical conductivity) for chapters 3 and 6.

Materials	Young's modulus [GPa]	Electrical conductivity [S/cm]	Tensile strength (MPa)	Fabrication method
PPY/cellulose[40]	0.38	7.9	15	Cast on teflon mould
PANI/CNT[41]	1.8	1.9	9.9	Vacuum filtration
ANF/PPY[42]	1.4	0.1	57	Vacuum filtration
MWCNTs[14]	3.3	200	14.5	Spray layer-by-layer MWNTNH_3^+ /MWNT-COO^- on carbon paper
PPY/rGO[21]	2.6	142.1	35	Vacuum filtration
rGO/MnO2/CNT[43]	2.3	67	48	Vacuum filtration
rGO[44]	4.8	28 ± 2	33	Vacuum filtration
rGO/Cellulose[45]	4.8	44	72.2	Vacuum filtration
rGO-PDA	4.6	155.3	173.6	Vacuum filtration
rGO-PDA/Ni^{2+}[46]	6.2	180.3	227.1	Vacuum filtration
rGO-CNC[47]	6.13	1105	765	Cast-drying
rGO-PCO/Zn^{2+}[48]	11.2	131.8	439.1	Vacuum filtration
SWCNT-Ppy-CE composite paper[22]	17.84	171	68.73	Ppy deposition on SWCNT buckypaper[22]
rGO-PAA[49]	18.2	108.9	206	Vacuum filtration
SBG[50]	15.6	512.3	944.5	Vacuum filtration
pBG[51]	23.3	1192.2	1054.3	Vacuum filtration
2-layer PANI/ANF [52]	3.4	19.3	150	Layer by layer filtration
PANI/PC[53]	0.8	0.01	28	Pressurized powder
PANI/BC[54]	5.6	0.05	95.7	In-situ polymerization on premade BC films
PANI/CS[55]	1.7	7.69x10-7	32.3	Drop-casting
PANI/ANF VF[42]	1.3	0.001	50	Vacuum filtration
PANI/CNT[41]	1.9	1.9	9.9	Vacuum filtration

Table A.5 Literature comparison for Li-ion battery cathodes used in section 5.

Sample	Mass loading (LFP or LCO or V_2O_5) [mg/cm^2]	Cycle number	Potential window [V]	Capacity [mAh/g], based on LFP mass	Capacity [mAh/g], based on total mass	Tensile strength [MPa]	Young's modulus [GPa]	Electrode fabrication method
rGO/LFP/CB/PFTE (3:72:10:5, wt/wt)[1]	-	50	2 - 3.8	168 (at 10 mA/g or 0.06 C)	121 (at 7.2 mA/g or 0.04 C)	-	-	Doctor blading
rGO/LFP/CB/PVDF (2:78:15:5, wt/wt)[2]	-	500	2.5 – 4.0	71.3 (at 1872 mA/g or 10 C)	56 (at 1469 mA/g or 7.8 C)	-	-	Doctor blading of LFP decorated GO
rGO/LFMP/CB/PVDF (2:78:10:10, wt/wt)[3]	1.6	1000	2.5 – 4.2	341 (at 4001 mA/g or 21 C)	266 (at 3120 mA/g or 16 C)	-	-	Doctor blading of LFP doped with Mg^{2+}
rGO/LFP (20:80, wt/wt)[4]	-	1000	1.5 – 4.5	82.5 (at 212.5 or 1.3 C)	66 (at 170 mA/g or 1C)	-	-	Spraying
Commercial LFP:SC65:PVDF (90:5:5, wt/wt)[5]	3.3	100	3 - 3.8	124 (at 80 mA/g or 0.5 C)	111.6 (at 72 mA/g or 0.45 C)	0.2	0.02	Doctor blading
LFP:SC65:PVDF coated on CF (90:5:5, wt/wt)[5]	3.6	100	3 - 3.8	133 (at 80 mA/g or 0.5 C)	119.7 (at 72 mA/g or 0.45 C)	20	0.17	Doctor blading
LFP/ CNT (95:5, wt/wt)[6]	-	50	2.5 – 4.2	150 (at 17 mA/g or 0.1 C)	142.5 (at 16.1 mA/g or 0.095 C)	2.5	0.1	Spraying on CNT films

Table A5 (continued) Literature comparison for Li-ion battery cathodes used in section 5.

Sample	**Mass loading (LFP or LCO or V_2O_5) [mg/cm^2]**	**Cycle number**	**Potential window [V]**	**Capacity [mAh/g], based on LFP mass**	**Capacity [mAh/g], based on total mass**	**Tensile strength [MPa]**	**Young's modulus [GPa]**	**Electrode fabrication method**
$LiCO_2$/CF/PVDF (82:7:11, wt/wt)[7]	-	1	3 – 4.2	90 (at 0.1 mA/cm^2)	x	12	0.65	Slurry-casting
LCO/CNT (95:5, wt/wt)[8]	~ 0.5	50	3 – 4.3	151 (at 27.4 mA/g or 0.1 C)	143.5 (at 26.03 mA/g or 0.095 C)	0.5	0.2	Casting
V_2O_5-P10 (90:10, wt/wt)[9]	-	200	2 – 3.8	145 (at 44.3 mA/g or 1 C)	130.5 (at 39.9 mA/g or 0.9 C)	28.5	3.2	Casting
rGO/50 wt% LFP (this work)	~ 1.5	200	2.5 – 4.2	50 (at 100 mA/g or 0.6 C)	25 (at 50 mA/g or 0.3 C)	32 ± 3	5.4 ± 0.5	Vacuum filtration
rGO/80 wt% LFP/5 wt% Si (this work)	~ 1.7	200	2.5 – 4.2	90 (at 100 mA/g or 0.6 C)	72 (at 80 mA/g or 0.5 C)	46 ± 4	5 ± 0.4	Vacuum filtration

Table A.6 Literature comparison for Li-ion battery anodes used in section 5.

Sample	Mass loading (Si/graphite) [mg/cm^2]	Cycle number	Potential window [V]	Capacity [mAh/g], based on active mass	Capacity [mAh/g], based on total mass	Tensile strength [MPa]	Young's modulus [GPa]	Electrode fabrication method
rGO/Si (75:25, wt/wt)[10]	-	100	0.02 – 2	1500 (at 1350 mA/g or 0.4 C)	375 (at 337.5 mA/g or 0.09 C)	-	-	Layer by layer vacuum filtration
rGO/Si (60:40, wt/ wt)[11]	0.5	100	0.005 – 1.5	1500 (at 100 mA/g or 0.03 C)	600 (at 60 mA/g or 0.02 C)	-	-	Vacuum filtration and acid etching of Al-Si
rGO/Si (30:70, wt/wt)[12]	1.0	150	0.02 - 2	3714 (at 1428 mA/g or 0.4 C)	2600 (at 1000 mA/g or 0.3 C)	-	-	Vacuum filtration
Commercial graphite/PVDF/AB (88.8:8:3.2, wt/wt)[13]	-	1	0.01 - 1	330 (at 37.2 mA/g or 0.1 C)	293 (at 33 mAh/g or 0.09 C)	3.7	0.7	Doctor blading
PU/Cu/Si[14] (12:79.7:8.3, wt/wt)	-	300	0.01 – 2	574 (at 357.9 mA/g or 0.1C)	47.6 (at 29.7 mA/g or 0.008 C)	2	8.2	Layer by layer
Si on CNT fabric[15] (47:53 wt/wt)	-	150	0.01 – 1	1051 (426 mA/g or 0.1C)	494 (at 200 mA/g or 0.06 C)	90	17.5	Chemical vapor deposition
rGO/NC/Si[16] (-:-:68, wt/wt)	-	100	0.02 – 2	1839 (at 147 mA/g or 0.04 C)	1251 (at 100 mA/g or 0.03 C)	11.2	0.4	Layer by layer

Table A.6 (continued) Literature comparison for Li-ion battery anodes used in section 5.

Sample	Mass loading (Si/graphite) [mg/cm^2]	Cycle number	Potential window [V]	Capacity [mAh/g], based on active mass	Capacity [mAh/g], based on total mass	Tensile strength [MPa]	Young's modulus [GPa]	Electrode fabrication method
Si/PAA/AB[17] (78:2:20, wt/wt)	1.0	340	0.01 – 1	2500 (at 340 mA/g or 0.09 C)	1950 (at 265.2 mA/g or 0.07 C)	12	1.1	Slurry casting
Si/CS-GA/CB[18] (60:20:20, wt/wt)	-	100	0.03 – 3	1969 (at 500 mA/g or 0.1 C)	1181.4 (at 300 mA/g or 0.08 C)	68.8	4.7	Doctor blading
rGO (this work)	~ 1.5	200	0.01 – 2	10 (at 2147.4 mA/g or 0.6 C)	10 (at 2147.4 mA/g or 0.6 C)	35 ± 6	5 ± 1	Vacuum filtration
rGO/20 wt% Si (this work)	~ 1.8	200	0.01 – 2	25 (at 2147.4 mA/g or 0.6 C)	5 (at 429.5 mA/g or 0.1 C)	34 ± 3	4 ± 0.5	Vacuum filtration
rGO/50 wt% Si/5 wt% BANF (this work)	~ 1.5	200	0.01 – 2	54 (at 2147.4 mA/g or 0.6 C)	27 (at 1073.7mA/g or 0.3 C)	32 ± 3	6 ± 0.1	Vacuum filtration
rGO/50 wt% Si/10 wt% BANF (this work)	~ 1.5	200	0.01 – 2	255 (at 2147.4 mA/g or 0.6 C)	127.5 (at 1073.7mA/g or 0.3 C)	37 ± 3	6.2 ± 0.4	Vacuum filtration
rGO/50 wt% Si/15 wt% BANF (this work)	~ 1.5	200	0.01 – 2	9 (at 2147.4 mA/g or 0.6 C)	4.5 (at 1073.7mA/g or 0.3 C)	45 ± 3	6.8 ± 0.3	Vacuum filtration

Table A.7 Data used for 3D Ashby plots in chapter 7.

Materials	Strength [MPa]	Specific Young's modulus [GPa·cm^3/g]	Specific energy [Wh/kg]	nmf (epoxy and carbon aerogel)	nmf (epoxy and graphite/LFP battery)
rGO/25wt% BANF (chapter 3)	99.8	35	14	13.6	-
rGO/50 wt% Si/10 wt% BANF (chapter 5)	37	12.4	510	45.2	7.1
rGO/80 wt% LFP/5 wt% BANF (chapter 5)	46	7.1	153	14.8	3.3
PANI/73 wt% BANF/12 wt% SWCNT (chapter 6)	40	1.3	320	26.1	2.1
Commercial LFP cathode (LFP:SC65:PVDF (90:5:5, wt/wt)[5])	0.2	0.02	140	11.2	0.7
Commercial graphite anode (Commercial graphite/PVDF/AB (88.8:8:3.2, wt/wt)[13])	0.7	3.7	66	6.6	1.7
Sulfur/Carbon nanofiber boron nitride/PVDF-Li/carbon nanofiber[19]	214	15	65	10.6	5.7
ST carbon fiber-carbon aerogel/polyethylene terephthalate (Imperial 2019)	110	26	1.4	2.7	-
rGO-cellulose paper[20]	8.67	1.4	21	2.2	-

References

1. Zhu, X.; Hu, J.; Wu, W.; Zeng, W.; Dai, H.; Du, Y.; Liu, Z.; Li, L.; Ji, H.; Zhu, Y., LiFePO4/reduced graphene oxide hybrid cathode for lithium ion battery with

outstanding rate performance. *Journal of Materials Chemistry A* **2014,** *2* (21), 7812-7818.
2. Wang, X.; Feng, Z.; Huang, J.; Deng, W.; Li, X.; Zhang, H.; Wen, Z., Graphene-decorated carbon-coated LiFePO4 nanospheres as a high-performance cathode material for lithium-ion batteries. *Carbon* **2018,** *127*, 149-157.
3. Wang, B.; Xu, B.; Liu, T.; Liu, P.; Guo, C.; Wang, S.; Wang, Q.; Xiong, Z.; Wang, D.; Zhao, X. S., Mesoporous carbon-coated LiFePO4 nanocrystals co-modified with graphene and Mg2+ doping as superior cathode materials for lithium ion batteries. *Nanoscale* **2014,** *6* (2), 986-995.
4. Jeon, J.-W.; Biswas, M. C.; Patton, C. L.; Wujcik, E. K., Water-processable, sprayable LiFePO4/graphene hybrid cathodes for high-power lithium ion batteries. *Journal of Industrial and Engineering Chemistry* **2020,** *84*, 72-81.
5. Boaretto, N.; Almenara, J.; Mikhalchan, A.; Marcilla, R.; Vilatela, J. J., A Route to High-Toughness Battery Electrodes. *ACS Applied Energy Materials* **2019,** *2* (8), 5889-5899.
6. Wu, Y.; Wu, H.; Luo, S.; Wang, K.; Zhao, F.; Wei, Y.; Liu, P.; Jiang, K.; Wang, J.; Fan, S., Entrapping electrode materials within ultrathin carbon nanotube network for flexible thin film lithium ion batteries. *RSC Advances* **2014,** *4* (38), 20010-20016.
7. Liu, P.; Sherman, E.; Jacobsen, A., Design and fabrication of multifunctional structural batteries. *Journal of Power Sources* **2009,** *189* (1), 646-650.
8. Luo, S.; Wang, K.; Wang, J.; Jiang, K.; Li, Q.; Fan, S., Binder-Free LiCoO2/Carbon Nanotube Cathodes for High-Performance Lithium Ion Batteries. *Advanced Materials* **2012,** *24* (17), 2294-2298.
9. An, H.; Mike, J.; Smith, K. A.; Swank, L.; Lin, Y.-H.; L. Pesek, S.; Verduzco, R.; Lutkenhaus, J. L., Highly Flexible Self-Assembled V2O5 Cathodes Enabled by Conducting Diblock Copolymers. *Scientific Reports* **2015,** *5* (1), 14166.
10. Sun, F.; Huang, K.; Qi, X.; Gao, T.; Liu, Y.; Zou, X.; Wei, X.; Zhong, J., A rationally designed composite of alternating strata of Si nanoparticles and graphene: a high-performance lithium-ion battery anode. *Nanoscale* **2013,** *5* (18), 8586-8592.
11. Jiang, H.; Zhou, X.; Liu, G.; Zhou, Y.; Ye, H.; Liu, Y.; Han, K., Free-Standing Si/Graphene Paper Using Si Nanoparticles Synthesized by Acid-Etching Al-Si Alloy Powder for High-Stability Li-Ion Battery Anodes. *Electrochimica Acta* **2016,** *188*, 777-784.
12. Zhao, X.; Hayner, C. M.; Kung, M. C.; Kung, H. H., In-Plane Vacancy-Enabled High-Power Si–Graphene Composite Electrode for Lithium-Ion Batteries. *Advanced Energy Materials* **2011,** *1* (6), 1079-1084.
13. Zheng, H.; Zhang, L.; Liu, G.; Song, X.; Battaglia, V. S., Correlationship between electrode mechanics and long-term cycling performance for graphite anode in lithium ion cells. *Journal of Power Sources* **2012,** *217*, 530-537.
14. Liu, L.; Li, M.; Chu, L.; Jiang, B.; Lin, R., Facile fabrication of flexible Si-based nanocomposite films as high-rate anodes by layer-by-layer self-assembly. *Applied Surface Science* **2019,** *476*, 501-512.

15. Evanoff, K.; Benson, J.; Schauer, M.; Kovalenko, I.; Lashmore, D.; Ready, W. J.; Yushin, G., Ultra Strong Silicon-Coated Carbon Nanotube Nonwoven Fabric as a Multifunctional Lithium-Ion Battery Anode. *ACS Nano* **2012,** *6* (11), 9837-9845.
16. Zhou, X.; Liu, Y.; Du, C.; Ren, Y.; Li, X.; Zuo, P.; Yin, G.; Ma, Y.; Cheng, X.; Gao, Y., Free-Standing Sandwich-Type Graphene/Nanocellulose/Silicon Laminar Anode for Flexible Rechargeable Lithium Ion Batteries. *ACS Applied Materials & Interfaces* **2018,** *10* (35), 29638-29646.
17. Assresahegn, B. D.; Bélanger, D., Effects of the Formulations of Silicon-Based Composite Anodes on their Mechanical, Storage, and Electrochemical Properties. *ChemSusChem* **2017,** *10* (20), 4080-4089.
18. Chen, C.; Lee, S. H.; Cho, M.; Kim, J.; Lee, Y., Cross-Linked Chitosan as an Efficient Binder for Si Anode of Li-ion Batteries. *ACS Applied Materials & Interfaces* **2016,** *8* (4), 2658-2665.
19. Huang, W.; Wang, P.; Liao, X.; Chen, Y.; Borovilas, J.; Jin, T.; Li, A.; Cheng, Q.; Zhang, Y.; Zhai, H.; Chitu, A.; Shan, Z.; Yang, Y., Mechanically-robust structural lithium-sulfur battery with high energy density. *Energy Storage Materials* **2020,** *33*, 416-422.
20. Weng, Z.; Su, Y.; Wang, D.-W.; Li, F.; Du, J.; Cheng, H.-M., Graphene–Cellulose Paper Flexible Supercapacitors. *Advanced Energy Materials* **2011,** *1* (5), 917-922.

APPENDIX B

DATA FOR RAGONE PLOTS

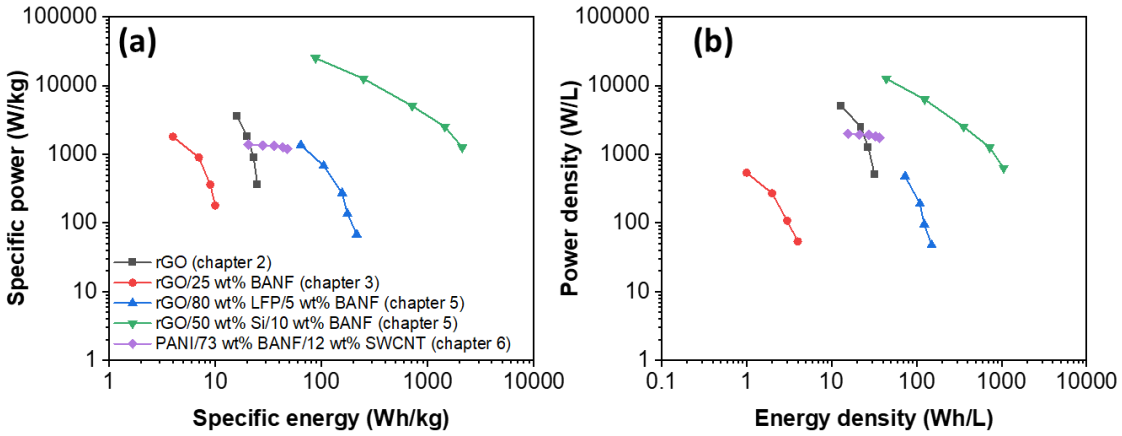

Figure B.1 Ragone plots for (a) specific power (W/kg) *vs.* specific energy (Wh/kg) and (b) power density (W/L) *vs.* energy density (Wh/L) for rGO (supercapacitor, chapter 2) compared to electrodes with the highest multifunctional efficiency values developed in this dissertation, such as rGO/25 wt% BANF (supercapacitor, chapter 3), rGO/80 wt% LFP/5 wt% BANF (lithium-ion battery cathode, chapter 5), rGO/50 wt% Si/10 wt% BANF (lithium-ion battery anode, chapter 5), and PANI/BANF/CNT (lithium-ion battery cathode, chapter 6). Legend in panel (a) also applies in panel (b).

Table B.1 Ragone plot data for rGO and rGO-COOH/ANF composites for chapter 2

rGO				rGO/ 10 wt% ANF				rGO/ 25 wt% ANF			
Specific energy (Wh/kg)	**Specific power (W/kg)**	**Energy density (Wh/L)**	**Power density (W/L)**	**Specific energy (Wh/kg)**	**Specific power (W/kg)**	**Energy density (Wh/L)**	**Power density (W/L)**	**Specific energy (Wh/kg)**	**Specific power (W/kg)**	**Energy density (Wh/L)**	**Power density (W/L)**
25	360	32	504	15	360	15	360	11	360	324	20
23	900	27	1260	15	900	15	900	10	900	810	17
20	1800	22	2510	12	1800	12	1800	8	1800	1620	14
16	3600	13	5040	10	3600	10	3600	6	3600	3240	8
rGO-COOH				**rGO-COOH/ 10 wt% ANF**				**rGO-COOH/ 25 wt% ANF**			
Specific energy (Wh/kg)	**Specific power (W/kg)**	**Energy density (Wh/L)**	**Power density (W/L)**	**Specific energy (Wh/kg)**	**Specific power (W/kg)**	**Energy density (Wh/L)**	**Power density (W/L)**	**Specific energy (Wh/kg)**	**Specific power (W/kg)**	**Energy density (Wh/L)**	**Power density (W/L)**
14	360	22	576	12	360	17	504	10	360	11	396
12	900	19	1440	10	900	15	1260	7	900	8	990
10	1800	16	2880	9	1800	12	2510	4	1800	4	1980
6	3600	9	5760	6	3600	8	5040	0	3600	0	3960

Table B.2 Ragone plot data for rGO-NH2/ANF and rGO/BANF composites for chapters 2 and 3, respectively.

rGO-NH_2				**rGO-NH_2/ 10 wt% ANF**				**rGO-NH_2/ 25 wt% ANF**			
Specific energy (Wh/kg)	**Specific power (W/kg)**	**Energy density (Wh/L)**	**Power density (W/L)**	**Specific energy (Wh/kg)**	**Specific power (W/kg)**	**Energy density (Wh/L)**	**Power density (W/L)**	**Specific energy (Wh/kg)**	**Specific power (W/kg)**	**Energy density (Wh/L)**	**Power density (W/L)**
14.4	360	38.896	612	11.7	360	25.168	396	12.2	360	12.2	360
13	900	33.32	1530	10.25	900	21.56	990	10	900	10	900
11.5	1800	27.2	3060	9	1800	17.6	1980	7	1800	7	1800
9	3600	16.32	6120	8	3600	10.56	3960	0	3600	0	3600
rGO				**rGO/ 10 wt% BANF**				**rGO/ 25 wt% BANF**			
Specific energy (Wh/kg)	**Specific power (W/kg)**	**Energy density (Wh/L)**	**Power density (W/L)**	**Specific energy (Wh/kg)**	**Specific power (W/kg)**	**Energy density (Wh/L)**	**Power density (W/L)**	**Specific energy (Wh/kg)**	**Specific power (W/kg)**	**Energy density (Wh/L)**	**Power density (W/L)**
35	180	49	252	16	180	9	108	10	180	4	54
25	360	32	504	15	360	9	216	9	360	3	108
23	900	27	1260	15	900	9	540	7	900	2	270
20	1800	22	2510	12	1800	7	1080	4	1800	1	540
16	3600	13	5040	10	3600	6	2160	-	-	-	-

Table B.3 Ragone plot data for rGO-DOPA/BANF and rGO-TA/BANF composites for chapters 3 and 4, respectively.

rGO-DOPA / 10 wt% BANF				rGO-DOPA / 25 wt% BANF				rGO-DOPA / 10 wt% BANF/Ca^{2+}				rGO-DOPA / 10 wt% BANF/Ca^{2+}			
Specific energy (Wh/kg)	**Specific power (W/kg)**	**Energy density (Wh/L)**	**Power density (W/L)**	**Specific energy (Wh/kg)**	**Specific power (W/kg)**	**Energy density (Wh/L)**	**Power density (W/L)**	**Specific energy (Wh/kg)**	**Specific power (W/kg)**	**Energy density (Wh/L)**	**Power density (W/L)**	**Specific energy (Wh/kg)**	**Specific power (W/kg)**	**Energy density (Wh/L)**	**Power density (W/L)**
15	180	7	90	3	180	1.8	108	9	180	7	144	1	180	1	180
14	360	7	180	2	360	1.4	216	8	360	6	288	0.8	360	0.8	360
13	900	6	450	1	900	0.6	540	7	900	6	720	-	-	-	-
12	1800	-	-	-	-	-	-	3	1800	2	1440	-	-	-	-
9	3600	-	-	-	-	-	-	-	-	-	-	-	-	-	-
rGO-TA / 10 wt% BANF				**rGO-TA / 10 wt% BANF/Ta^{3+}**											
Specific energy (Wh/kg)	**Specific power (W/kg)**	**Energy density (Wh/L)**	**Power density (W/L)**	**Specific energy (Wh/kg)**	**Specific power (W/kg)**	**Energy density (Wh/L)**	**Power density (W/L)**								
9	180	7	144	1	180	1	180								
8	360	6	288	0.8	360	0.8	360								
7	900	6	720	-	-	-	-								
3	1800	2	1440	-	-	-	-								
-	-	-	-	-	-	-	-								

Table B.4 Ragone plot data for our rGO/BANF/LFP and literature LFP-containing composites for chapter 5 (based on LFP mass).

rGO/50 wt% LFP				rGO/80 wt% LFP / 5 wt% BANF				rGO/LFP/CB/PVDF (2:78:15:5, wt/wt)[1]				rGO/LFP/CB/PFTE (3:72:10:5, wt/wt)[2]			
Specific energy (Wh/kg)	**Specific power (W/kg)**	**Energy density (Wh/L)**	**Power density (W/L)**	**Specific energy (Wh/kg)**	**Specific power (W/kg)**	**Energy density (Wh/L)**	**Power density (W/L)**	**Specific energy (Wh/kg)**	**Specific power (W/kg)**	**Energy density (Wh/L)**	**Power density (W/L)**	**Specific energy (Wh/kg)**	**Specific power (W/kg)**	**Energy density (Wh/L)**	**Power density (W/L)**
229.5	85	229.5	85	268.6	85	188.0	59.5	306	18.36	-	-	360.36	37.4	-	-
175.1	170	175.1	170	219.3	170	153.5	119	302.4	183.6	-	-	323.62	374	-	-
130.9	340	130.9	340	195.5	340	136.9	238	297	367.2	-	-	247.06	3740	-	-
11.9	850	11.9	850	130.9	850	91.6	595	291.6	918	-	-	178.64	7480	-	-
0.34	1700	0.34	1700	79.9	1700	55.9	1190	279	1836	-	-	360.36	37.4	-	-

rGO/LFMP/CB/PVDF (2:78:10:10, wt/wt)[3]				rGO/LFP (20:80, wt/wt)[4]				Commercial LFP:SC65:PVDF (90:5:5, wt/wt)[5]			
Specific energy (Wh/kg)	**Specific power (W/kg)**	**Energy density (Wh/L)**	**Power density (W/L)**	**Specific energy (Wh/kg)**	**Specific power (W/kg)**	**Energy density (Wh/L)**	**Power density (W/L)**	**Specific energy (Wh/kg)**	**Specific power (W/kg)**	**Energy density (Wh/L)**	**Power density (W/L)**
263.5	57.8	-	-	348.75	637.5	-	-	133	17	-	-
244.8	289	-	-	326.25	1275	-	-	128	35	-	-
224.4	1445	-	-	236.25	1912.5	-	-	121	80	-	-
202.3	2890	-	-	198.75	3187.5	-	-	113	165	-	-
163.2						-	-	81	500	-	-

Table B.5 Ragone plot data for our rGO/BANF/Si and literature Si-containing composites for chapter 5 (based on Si mass).

rGO				rGO/20 wt% Si				rGO/50 wt% Si / 5 wt% BANF				rGO/50 wt% Si / 10 wt% BANF			
Specific energy (Wh/kg)	**Specific power (W/kg)**	**Energy density (Wh/L)**	**Power density (W/L)**	**Specific energy (Wh/kg)**	**Specific power (W/kg)**	**Energy density (Wh/L)**	**Power density (W/L)**	**Specific energy (Wh/kg)**	**Specific power (W/kg)**	**Energy density (Wh/L)**	**Power density (W/L)**	**Specific energy (Wh/kg)**	**Specific power (W/kg)**	**Energy density (Wh/L)**	**Power density (W/L)**
780	446.4	936	535.7	2100	2520	2940	3528	3332	2520	2665.6	2016	4216	2520	2108	1260
324	892.8	388.8	1071.4	520	5040	728	7056	1368	5040	1094.4	4032	2896	5040	1448	2520
182	1785.6	218.4	2142.7	190	10080	266	14112	544	10080	435.2	8064	1428	10080	714	5040
36	4464	43.2	5356.8	55	25200	77	35280	96	25200	76.8	20160	496	25200	248	12600
10	8928	12	10713.6	14	50400	19.6	70560	24	50400	19.2	40320	176	50400	88	25200
rGO/50 wt% Si / 15 wt% BANF				**rGO/Si (75:25, wt/wt)[6]**				**rGO/Si (60:40, wt/wt)[7]**				**rGO/Si (30:70, wt/wt)[8]**			
Specific energy (Wh/kg)	**Specific power (W/kg)**	**Energy density (Wh/L)**	**Power density (W/L)**	**Specific energy (Wh/kg)**	**Specific power (W/kg)**	**Energy density (Wh/L)**	**Power density (W/L)**	**Specific energy (Wh/kg)**	**Specific power (W/kg)**	**Energy density (Wh/L)**	**Power density (W/L)**	**Specific energy (Wh/kg)**	**Specific power (W/kg)**	**Energy density (Wh/L)**	**Power density (W/L)**
452	2520	271.2	1512	2756.6	670	-	-	1248	300	374.4	90	6716	285.7	800	18804.8
292	5040	175.2	3024	2090.5	2001	-	-	907.5	750	272.25	225	5716	571.4	1600	16004.8
104	10080	62.4	6048	1258.3	6700	-	-	721.5	1500	216.45	450	5358	1142.8	3200	15002.4
16	25200	9.6	15120	573	20000	-	-	562.5	3000	168.75	900	4320	2857.1	8000	12096
8	50400	4.8	30240	291	93800	-	-	439.5	4500	131.85	1350	3608	5714.2	16000	10102.4

Table B.6 Ragone plot data for our commercial Si-containing composites and our PANI composites for chapters 5 and 6 (based on graphite and PANI mass).

Commercial graphite/PVDF/AB (88.8:8:3.2, wt/wt)[9]				PANI/73 wt% BANF/12 wt% SWCNT				PANI/V_2O_5 [10]				PANI/rGO[11]			
Specific energy (Wh/kg)	**Specific power (W/kg)**	**Energy density (Wh/L)**	**Power density (W/L)**	**Specific energy (Wh/kg)**	**Specific power (W/kg)**	**Energy density (Wh/L)**	**Power density (W/L)**	**Specific energy (Wh/kg)**	**Specific power (W/kg)**	**Energy density (Wh/L)**	**Power density (W/L)**	**Specific energy (Wh/kg)**	**Specific power (W/kg)**	**Energy density (Wh/L)**	**Power density (W/L)**
328	186	-	-	320	8000	243	11552	1103	446	-	-	22999	354	65.1	13092
325	372	-	-	287	8455	218	12210	612	1412	-	-	12776	1333	193.5	8182
304	744	-	-	240	8888	182	12835	189	3162	-	-	3574	2511	283	1091
217	1860	-	-	187	8928	142	12892	70	5623	-	-	456	3162	379	205
64	3720	-	-	137	9166	104	13236	-	-	-	-	-	-	-	-
20	7440	-	-	-				-	-	-	-	-	-	-	-

References

1. Wang, X.; Feng, Z.; Huang, J.; Deng, W.; Li, X.; Zhang, H.; Wen, Z., Graphene-decorated carbon-coated LiFePO4 nanospheres as a high-performance cathode material for lithium-ion batteries. *Carbon* **2018,** *127*, 149-157.
2. Zhu, X.; Hu, J.; Wu, W.; Zeng, W.; Dai, H.; Du, Y.; Liu, Z.; Li, L.; Ji, H.; Zhu, Y., LiFePO4/reduced graphene oxide hybrid cathode for lithium ion battery with outstanding rate performance. *Journal of Materials Chemistry A* **2014,** *2* (21), 7812-7818.
3. Wang, B.; Xu, B.; Liu, T.; Liu, P.; Guo, C.; Wang, S.; Wang, Q.; Xiong, Z.; Wang, D.; Zhao, X. S., Mesoporous carbon-coated LiFePO4 nanocrystals co-modified with graphene and Mg2+ doping as superior cathode materials for lithium ion batteries. *Nanoscale* **2014,** *6* (2), 986-995.
4. Jeon, J.-W.; Biswas, M. C.; Patton, C. L.; Wujcik, E. K., Water-processable, sprayable LiFePO4/graphene hybrid cathodes for high-power lithium ion batteries. *Journal of Industrial and Engineering Chemistry* **2020,** *84*, 72-81.
5. Boaretto, N.; Almenara, J.; Mikhalchan, A.; Marcilla, R.; Vilatela, J. J., A Route to High-Toughness Battery Electrodes. *ACS Applied Energy Materials* **2019,** *2* (8), 5889-5899.
6. Sun, F.; Huang, K.; Qi, X.; Gao, T.; Liu, Y.; Zou, X.; Wei, X.; Zhong, J., A rationally designed composite of alternating strata of Si nanoparticles and graphene: a high-performance lithium-ion battery anode. *Nanoscale* **2013,** *5* (18), 8586-8592.
7. Jiang, H.; Zhou, X.; Liu, G.; Zhou, Y.; Ye, H.; Liu, Y.; Han, K., Free-Standing Si/Graphene Paper Using Si Nanoparticles Synthesized by Acid-Etching Al-Si Alloy Powder for High-Stability Li-Ion Battery Anodes. *Electrochimica Acta* **2016,** *188*, 777-784.
8. Zhao, X.; Hayner, C. M.; Kung, M. C.; Kung, H. H., In-Plane Vacancy-Enabled High-Power Si–Graphene Composite Electrode for Lithium-Ion Batteries. *Advanced Energy Materials* **2011,** *1* (6), 1079-1084.
9. Zheng, H.; Zhang, L.; Liu, G.; Song, X.; Battaglia, V. S., Correlationship between electrode mechanics and long-term cycling performance for graphite anode in lithium ion cells. *Journal of Power Sources* **2012,** *217*, 530-537.